Analysis, Design Optimisation and Experimental Performance of Synchronous Reluctance and Permanent Magnet Assisted Synchronous Reluctance Machines

Thushanthan Mohanarajah
School of Engineering
Western Sydney University

A thesis submitted for the degree of Doctor of Philosophy

November 2019

STATEMENT OF AUTHENTICATION

I hereby declare that except where referenced explicitly of others work, the content of this thesis is my work, and which have not been used for other degrees or qualifications. The content of this thesis, including but not limited to simulation models, and experimental results, are entirely original, and that does not include contents of collaborative work or such a material. The previously published materials such as journals and conference papers are my original works, and neither duplicated nor used for other purposes.

Thushanthan Mohanarajah

11/10/2019

ACKNOWLEDGMENT

I would like to take this opportunity to thank my direct supervisor Dr Jamal Rizk for giving me this opportunity to work on the electrical machines throughout this research process as well as the guidance and support. I also take this opportunity to pass my sincere gratitude and special thanks to Prof. Nagrial Mahmood, for his assistance, guidance on technical & non-technical issues, encouragement on publications, and organising funds to make this journey a smooth & motivating. I also would to like express my sincere thanks to Dr Ali Hellany for the precise guidance during the challenging time. They are incredible and inspiring mentors, and their in-depth knowledge of electrical machines is priceless. I also pass my sincere thanks to Western Sydney University's technical services cluster manager Dr Tosin Famakinwa, technical team lead Moses Oyeku, and technical officers Ajak Deng and Matthew Kessanis for their supports, organising logistics and giving me the freedom to use the electrical lab.

I cannot miss thanking Zhong Lin, for her effort in helping to cut prototypes not just one, but ten of them each needed new wire-cutting, and Alexy. K. for the lessons in using macros in Ansys Electronics Desktop even though it was a short session, it was priceless, and Nicole Yeng, for her tireless effort to manufacture the test bench and delivered. Without their assistance, my work would have been a lot more complicated. Finally, my aunt Irene Chithra Thayaparan, whose care, support and love must be acknowledged throughout the entire course of my studies in Australia. I also like to take this opportunity to acknowledge the previous researchers who have worked over the years and published such key journals, papers, and keynotes on this topic not only to make Synchronous Reluctance Machine a viable alternative to Inductance Machine but also for documenting their works for the future generations.

" If someone feels that they had never made a mistake in their life, then it means they had never tried a new thing in their life" **- Albert Einstein.**

ABSTRACT

The research studies, in detail, the synchronous reluctance machine (SynRM) and permanent magnet assisted synchronous reluctance machine (PMSynRM) to improve the machine performances. In this study, the SynRM analytical models are revisited, and functional characteristics are mathematically developed to improve the machine performance. The performance parameters such as torque density, power factor, and efficiency are investigated along with torque ripples. SynRM is known for its high torque density in a compact size. Its improvement is analytically studied further by optimising rotor properties. The power factor of these machines is rather low compared with its equivalent AC machines. Although the machine's power factor can be improved using control techniques, it is still not high enough. The machine has gone through significant development over the years since J.K Kostko published the first paper on reluctance machines back in 1923. The researchers have tested various types of anisotropies, such as axially laminated and transversally laminated. The machine torque and power factor depend on its saliency ratio.

Although the axially laminated structure offers high saliency ratio due to the naturally distributed flux barrier structure, it has mechanical constraints. The axial rotor segments are fixed together by specially designed bolts that are conductive material in nature. This mechanical arrangement increases quadrature axis inductance, consequently reduces the saliency ratio of the machine. On the other hand, the transversally laminated structure is more mechanically feasible and offers comparatively high performance. One of the primary focus of this study is to improve the power factor. It has been comprehensively investigated. The SynRM machine is also known for high torque ripples. The non-linear structure and its reluctance path along the air-gap make the machine highly susceptible to torque pulsation.

The cross induction due to the D and Q axis along the air-gap increases the machine's ripples. Besides, poor stator winding (both sinusoidal and step excitation) also increases the machine torque ripples. The existing ripple reduction

practices are revisited in this study to further understand the torque ripples of this machine. The rotor of SynRM is redesigned and optimised to reduce the ripples effect. The causes of ripples are also analytically studied in detail, and mathematical models are developed and presented for understanding the phenomena. Two different ways of analysing the ripple effects are considered, and the pros and cons of both methods are discussed. The SynRM is simulated using an advanced finite element analysis (FEM) software to verify the analytical models as well as optimise the machine performance. Firstly, primitive rotor structures are developed so that they can be automatically varied during parameterisation and optimisation. Four flux barrier shapes are analysed to determine the optimum shape for high performance by investigating flux's natural path. From the results, a multi-barrier arrangement is studied with an advanced algorithm for three and four-layer designs, and an optimum rotor is proposed based on the simulations.

Using a single-objective and multi-objective optimisation techniques, the SynRM is optimised from the simulated design. An advanced topology is developed for automated optimisation that can offer flexibility in varying optimisation variables as part of this research. The optimised design's performance is analysed in detail and compared with analytical models. The torque ripples are discussed in detail, and an advanced torque ripple minimisation topology is developed. Then the design is optimised for two types of barrier shapes. A number of designs are prototyped for experimental verification.

Finally, the current trend in rare-earth magnets is investigated with its cost per volume ratio. The rare-earth neodymium magnets are focused on this study for improved performance with optimum volume. The analytical model of PM assisted design is studied in detail, and its performance parameters are compared with SynRM. A PMSynRM with a linear-barrier is simulated for a detailed analysis of the machine that discusses different PM volumes and the impact on machine performance due to the volume of PM and location. The performance parameters, discussed in the analytical model, are compared with the simulation results. The improvement in power factor and torque density is investigated using various designs.

The optimisation is performed in two ways. The first one is adding PMs to the optimised SynRM. Single-objective and multi-objective optimisation are performed using an advanced optimisation algorithm. Secondly, the topology of SynRM is modified for PMSynRM in such a way the entire machine can be automated during optimisation by adding the PM's variables to the existing one. The performances of the two optimised designs have been compared. PMSynRM prototypes are developed to verify the simulation results. The eight SynRM designs are prototyped to report the practical results. Six of them are to verify various performance parameters of SynRM and two of them to test the ripples effect. Moreover, two PMSynRM prototypes are fabricated to verify the simulation results. The saliency of each SynRM is measured and compared with simulated results. Then, each design is tested experimentally in all possible scenarios and compared. Extensive testing is performed on all prototypes under various operating conditions and reported.

CONTENTS

LIST OF ABBREVIATION

2D	Two Dimensional
3D	Three Dimensional
3ph	Three Phase
AC	Alternating Current
ALA	Axially Laminated Anisotropy
EMF	Electromotive Force
DC	Direct Current
DTC	Direct Torque Control
FEM	Finite Element Method
FEA	Finite Element Analysis
IM	Induction Motor
IPM	Interior Permanent Magnet Machine
mmf	Magneto Motive Force
MOO	Multi-objective Optimisation
MTPA	Maximum Torque Per Ampere
PF	Power Factor
PM	Permanent Magnets
PMSynRM	Permanent Magnet Assisted SynRM
p.u.	Per Unit
PWM	Pulse Width Modulation
QN	Quasi-Newton algorithm
rpm	Revolution Per Minute
SNLP	Sequential Non-Linear Programming Algorithm
SOO	Single-Objective Optimisation
SPM	Surface-Mounted Permanent Magnet Machines
SRM	Switch Reluctance Machine
SynRM	Synchronous Reluctance Machine
TLA	Transversally Laminated Anisotropy
VFD	Variable Frequency Drive
VSD	Variable Speed Drive

LIST OF SYMBOLS

λ_d	D – Axis flux linkage	i_d	Stator current in direct axis
λ_q	Q – Axis flux linkage	i_m	Peak to peak current
λ_{md}	D – Axis magnetising flux linkage	i_q	Stator current in Q – axis
λ_{mq}	Q – Axis magnetising flux linkage	I_s	The magnitude of the current space vector
λ_l	Leakage flux linkage	J	Current density
λ_m	Q – Axis PM-induced flux linkage	$K_s(\vartheta_s)$	Periodic function
λ_s	The magnitude of flux linkage space vector	k_w	Rotor Insulation ratio
ξ	Saliency ratio	L_d	Inductance in the D - axis
ξ_i	Intrinsic saliency ratio	L_{dq}	DQ inductance
μ	Permeability	L_{ls}	Winding leakage induction
γ	Torque angle	L_{md}	Magnetising inductance in the D axis
ϑ	Load angle	L_{mq}	Magnetising inductance in the Q axis
θ	Current angle	L_q	Inductance in the Q axis
ϑ_r	Rotor angular coordinate	p	Number of poles
$\vartheta_{(r)}$	Rotor position angle	q	Number of stator slots per pole pair
ϑ_s	Stator angular coordinate	R	Radius of air-gap
ω	Angular frequency	r_s	Stator winding resistance
B	Magnetic flux density	R_{cmr}	Rotor iron losses resistance
$\cos(\phi)$	Power factor	$R_{cr-loss}$	Machine's per phase core loss

$\frac{d\lambda_{ds}}{dt}$	Transient changes in voltages in the D- axis	t	Lamination thickness
$\frac{d\lambda_{qs}}{dt}$	Transient changes in voltages in the Q- axis	V	Per phase stator terminal voltage
e_{Int_s}	Stator internal voltage	$v_a, v_b \& v_c$	Three phase voltages
g	Radial air-gap	v_d	Stator Voltage in D–Axis
$i_a, i_b \& i_c$	Three-phase Currents	v_q	Stator Voltage in Q-axis
v_m	Peak to peak voltage		
V_s	voltage space vector		

1 INTRODUCTION

1.1 Background

The efficiency of electrical machines has been the trend in recent times due to the ever-increasing demand for electrical energy. An efficient electrical motor uses less power with reduced losses compared with a poor efficient machine. Induction machines (IM) have long operational life, rugged structure, and are known for reliable operation but with relatively poor efficiency when compared to the latest efficiency standards. The combination of recent energy consumption legislation (IEC/EN60034-30:2008) around the world especially in the developed countries and cost of running poor electrical machine has triggered the search for an alternative to the induction machine which has been well-known for decades in the power industry due to its robustness and reliability [1, 2].

Although the induction machine has been developed to nearly its maximum potential, its efficiency is always a concern. It has rotor coils so that it can develop rotational force due to the rotating magnetic field. The coil comes with resistance, associated copper losses, and other losses such as frictional losses. Therefore, the efficiency of this machine is limited, especially in small range machines. Industry uses 42 % of the world's electrical energy and two-third of that is used by electrical motors [1, 3]. Over 90 % of the 300 million electrical motors installed worldwide are induction motors [2, 4]. Thus, an alternative to the induction machine is needed now than ever before. Hence, researchers have been collaborating with industry to improve the efficiency of the electrical machines in recent time.

The SynRM has been given significant attention in the past two decades due to high torque density in a compact size, high efficiency, and better pull-out torque in a magnet free structure. The history of the reluctance machine goes back nearly a century [5]. The earlier SynRMs were equipped with rotor cage for starting purpose. The rotor cage significantly reduced the machine's performance. Moreover, its power factor was quite low compared with other generic electrical machines. The early machines were designed with axial segments and called axially laminated design. The ALA (axially laminated anisotropy) design had few advantages such as high saliency ratio due to its distributed barrier structure. However, the segments are mechanically connected via radial support which act as flux guides in the Q axis, resulting in poor machine performance. Thus, this machine was only used in special applications and not considered for mass production. The lack of starting mechanism and manufacturing technology, the proper understanding of the machine's potential, the domination of other machines such as induction machine did not attract either the researchers or industry.

Digital computer evolution in the mid-90s, development of vector-oriented controllers and innovation in machine design such as transversally laminated design allowed the researches to re-visit the machine [6-8]. Advanced electronic controllers allowed the researchers to remove rotor cage and re-design the machine with multi-barrier in TLA design [9-11]. The latest technology and machine design tools improved the performance significantly. The researchers had demonstrated that a SynRM could out-perform an equivalent induction machine [12-14]. Researchers confirmed that the machine's efficiency is significantly high compared to an equivalent induction machine in a compact size [15]. Its magnet free rotor with high torque density in compact size allowed the researchers to consider the machine for electric vehicle in recent times [16-19]. Its ability to operate with high speed in the field-weakening region with relatively less structural deformation due to the absence of rotor coil make this machine a potential candidate for electric vehicle application.

Further, its pull-out torque is nearly double of the rated torque. The simple and rugged rotor structure makes the machine to be maintenance-free and reliable for long-lasting operation. Although the machine's torque density is slightly lower than an equivalent PM machine, the rotor is considerably less-expensive and no demagnetisation issues to consider. In addition, the compact size and high torque density coupled with precise control at lower speed make this machine an excellent choice for robotic applications. Unlike switched reluctance machine, SynRM can adopt the existing stator of any conventional AC machine. As this is a conventional type electrical machine, it requires a generic sinusoidally excited stator. Hence, the stator and controller of an induction machine can be used in the same frame sizes without developing new standards.

Nonetheless, its power factor and torque ripples are still a concern for the machine designers. SynRM is already in mass production starting as low as 0.75 kW and as high as 370 kW [20]. Although its efficiency has increased compared with an equivalent induction machine, the power factor have room for improvement. This thesis explicitly studies the machine's design characteristics to improve the machine performances such as torque, power factor, efficiency, and torque ripples without complicating the manufacturing. It compares an off-the-shelf SynRM with numerous prototypes exclusively made for this study. It has been shown that the machine's performances can be substantially increased by optimising the rotor dimensions such as barrier profile. The study focuses primarily on rotor optimisation for high performance. The flux barrier shapes, end barrier profiles, barrier location insulation ratio are explicitly investigated for premium performance. A series of scenarios are studied with respect to the machine performances. On the other hand, the PMSynRM is rather new machine. The SynRM researchers have proposed to use permanent magnets to improve its performance.

It was proposed to improve the performance of ALA design, but it can still be applied for the TLA design. Although ferrite PMs were initially suggested to improve the SynRM performance, but the PMSynRM can be designed with either rare-earth or ferrite permanent magnets depending on the requirements. The PMs in the barrier cavities along the negative Q axis can saturate the ribs in a transversally laminated design. The saturation will increase the reluctance in the axis resulting in high saliency ratio. It will increase the performance such as torque density and importantly, power factor. The two machines share quite similar characteristics. The temperature rise is quite low due to the absence of rotor coils in this machine. It cuts-down the fan size, resulting in low losses. Thus, the rotor deformation is no longer an issue in this machine even in high-speed application.

The hybrid design is rather new and still yet to be developed. The rapid price increase in rare-earth permanent magnet in the early 2010s, depletion of rare-earth magnet materials and environmental considerations reduce the interest of using a high volume of permanent magnets for electrical machines in recent times [21]. However, these types of machines have been exclusively considered for electrical vehicle application besides other special application such as in military and space industry. The electric vehicle industry is yet to boom in the coming years. Thus, the interest shifts towards an alternative hybrid machine with an optimised amount of permanent magnet that can produce similar performance as PM machines. The PMSynRM development at this point is crucial due to its potential as a hybrid electrical machine.

The PMSynRM is not only used for regular application but also can be used in sustainable energy development. It is an excellent choice for windmill application as a generator. The only concern of this machine is its cogging torque. This thesis shows that the cogging torque issues can easily be solved with proper optimisation. Thus, PMSynRM can be a viable alternative to PM machines due to its dual torques capability, *i.e.* reluctance, and PM torque with significantly high-power factor if it is optimised. The high-cost PMs Increase the manufacturing cost of PM machines. However, the PMSynRM can be designed with an optimum volume of rare-earth PMs for specific characteristic that can reduce the cost significantly.

This thesis focuses on developing topologies to optimise PMSynRM. It also extensively studies the characteristics of the machine at both operational regions maximum torque per ampere (MTPA), and field-weakening regions. It then compares the performances with an equivalent SynRM. Moreover, the machine is analytically modelled, simulated using innovative approaches and the results are explicitly discussed. Finally, a design process is suggested for improved machine performance.

1.2 Evolution of SynRM

J.K Kostko developed a theory for the reluctance (Kostko called it "reaction") motors in 1923 [5]. Since then, it was given various names such as polyphase reluctance motor, reluctance motor, reluctance synchronous motor and subsequently called synchronous reluctance motor by various researchers [10, 22-24]. Kostko developed not only the theory but also clearly articulated the challenges the machine had at the time. Although he did not believe that the machine will ever be extensively used, he pointed out the advantages of SynRM such as simplified rotor structure and variable speed and excellent operating characteristics at the time. Kostko also pointed out that high saliency should be reached to have better machine performance by producing multiple rotor segments, with multiple barriers. His proposal for achieving high saliency ratio is shown in Figure 1-1. Even the modern SynRM machine with hybrid barriers nearly follows the similar design procedures that Kostko proposed nearly a century ago.

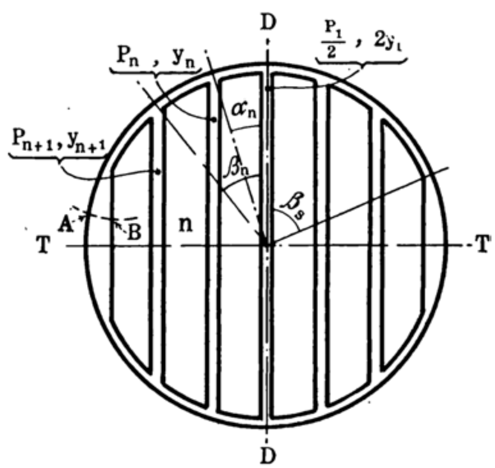

Figure 1-1: J.K Kostko's proposal for achieving high saliency

1.2.1 Reluctance machine in the mid-20th century

Another reluctance machine called the doubly salient reluctance machine was also developed in parallel in the middle of the last century. The doubly salient machine is named switched reluctance motor [25, 26]. The switched reluctance motor is generally considered as a separate type from synchronous reluctance machine. Since Kostko's introduction, the reluctance machine was ignored for quite a long time. However, industrial revolution across the globe in the early-1950s and specific characteristics of SynRM such as high pull-in load torque and variable speed operation attracted many researchers [27-33]. SynRM had been significantly developed during this time due to innovative work by Trickey and followed by C. Lin, M.E. Talaat, P.J. Lawrenson, A.J.O. Cruickshank, V.B. Honsinger, W. Fong, T.A. Lipo, I. Boldea and M.H. Nagrial [9, 28, 33-40]. The challenges of developing this machine due to lack of literature are acknowledged by M.E. Talaat [27, 28, 34].

Around the same time, few researchers developed a machine that had combined synchronous machine with a reluctance rotor and called it "synchronous motor without field excitation" [22, 27]. It is because the salient pole synchronous machine of that time shared the same principle except it had field excitation. The researchers confronted challenges in starting the machine and bring to synchronism, resulted in introducing field excitation which, to a certain extent compromised machine performance. Later, the machine was equipped with a squirrel cage in the rotor to produce starting torque. The reluctance machine of that time was designed particularly for line start synchronous performance that used the same inverter [41-43]. A damper winding was also provided to keep the machine in synchronism during sudden load changes.

SynRM has never had a steady development during the early stages. The next phase of development came in the 1960s through P.J. Lawrenson, A.J Cruickshank, W. Fong, and T.A Lipo [36, 44-47]. Initially, Lawrenson proposed a two-pole reluctance motor with a segmental rotor and claimed it is a novel design of that time due to its low inertia [30, 44]. The low in iron peripheral segmental rotor was claimed to have the inertia of one-fifth of its counterparts as shown in Figure 1-2 (a & b).

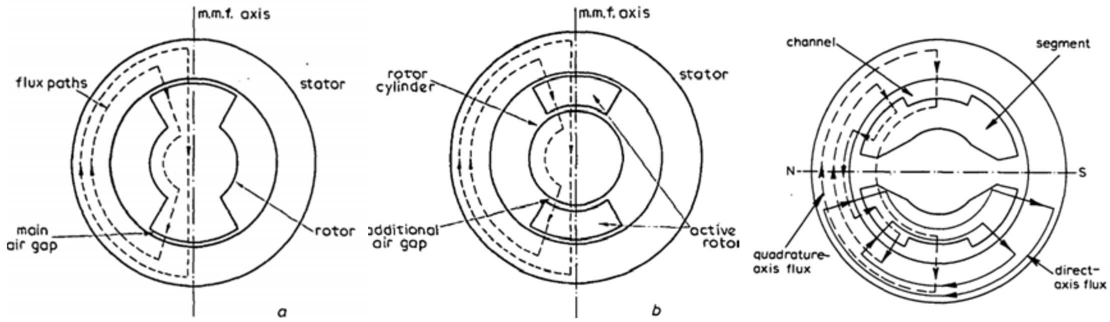

(a) (b) (c)

Figure 1-2: P.J Lawrenson's reluctance motors (a) standard inertia rotor (b) law inertia rotor and (c) segmental rotor with channel

Lawrenson and associates then improved the rotor with a shallow axial channel in the D – axis on purely segmental rotor, is shown in Figure 1-2 (c) [48]. The channel was filled with conductive materials to achieve synchronism and high machine performance such as power factor of 0.8 and efficiency of 90 % at that time. This machine had better maximum pull-out torque compared to an equivalent induction motor. It had used thyristor inverter supply to achieve low starting currents and variable speeds (only achieve two-speeds). Lawrenson also managed to implement the field-weakening technique of that time to run into 2:1.

This segmental design should be acknowledged and was considered the next step towards further development in SynRM. During this time, the segmental rotor machines were adopted by the electrical machine industry and available but only for a particular application due to its poor efficiency lasted until the mid-1990s [49-51]. Although this machine claimed to have excellent operating characteristics, high machine performance and substantially improved synchronous performance, the machine could not surpass its counterpart IM in many areas. Moreover, the construction was relatively complicated and less rugged and needed a non-magnetic shaft and other accessories.

T. A. Lipo published theory and simulation intensive paper for the first time with computer simulations on the SynRM stability analysis in 1967 [36]. He derived SynRM equations primarily using a salient pole synchronous machine of two-pole three-phase by removing the field excitation and provided a solution to convert it to the multi-phase system (1.1). He converted the 3 phase equations into a reference frame for the first time for SynRM using the park's transformation. Then, he applied the theory of small displacements to study the dynamic behaviour of SynRM to torque and damping over a wide speed range. Using a digital computer, he simulated the region of instability and using analogue computer-simulated transient characteristics of a SynRM. He had demonstrated that the SynRM has instability problem at lower speeds due to insufficient damping within the machine [36]. The issue was quite crucial due to the static converters of that time, which generates non-sinusoidal waves that can cause further instability in this machine. Lipo's contribution to SynRM development should be acknowledged who published his first work in 1967. Since, he has been either publishing or involved in SynRM development in one way or another till present.

$$T = \left(\frac{n}{2}\right)\left(\frac{p}{2}\right)\left(\lambda_{md} i_q - \lambda_{mq} i_d\right) \tag{1.1}$$

Around the same time, attempts were made to develop a controller for the SynRM motor. Lawrenson attempted but only managed 2-speed reluctance motor controller. W. Fong, who had been working on induction machine control, attempted to implement the latest control technique of that time called pole amplitude modulation onto SynRM. He had attempted not only the controller but also developed his version of 4/6 pole reluctance motor in the process with a rotor cage on the circumferential [33]. The rotor peripheral iron was milled out to distinguish the permeance in D and Q axis via peripheral grooves, as shown in Figure 1-3. In order to have permeance distribution along the air-gap, the flux fringing method was used, and the fringing coefficient was introduced. The angles of each cut-off were adjusted to achieve needed flux fringing coefficient. Although he has experimentally verified his findings and proved its potentials, but it was never further developed.

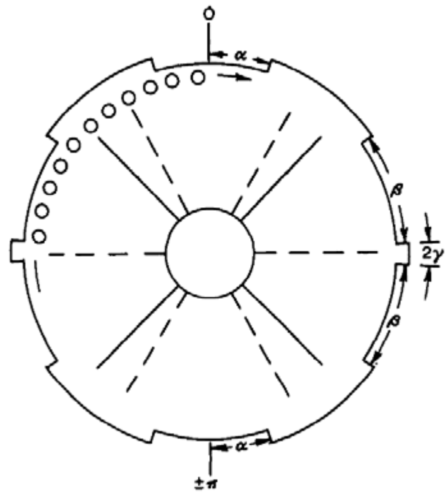

Figure 1-3: Reluctance rotor by W. Fong with rotor cage and peripheral cut-offs

Fong published a vital literature on the new rotor design with methods to organise flux barriers in the multipoles non-segmented reluctance rotor [52]. Although he had a superior flux barrier design similar to today's hybrid flux guides shown in Figure 1-4. He could not directly implement it in the practical rotor as he had other limitations such as starting torque requirements. Hence, he accommodated the multi-barriers in his novel rotor of that time with interpolar grooves and peripheral slots for rotor cage. During this period, the segmental rotor was dominating in reluctance machine. It is the first practical non-segmented design and can safely be considered as foundation for today's SynRM.

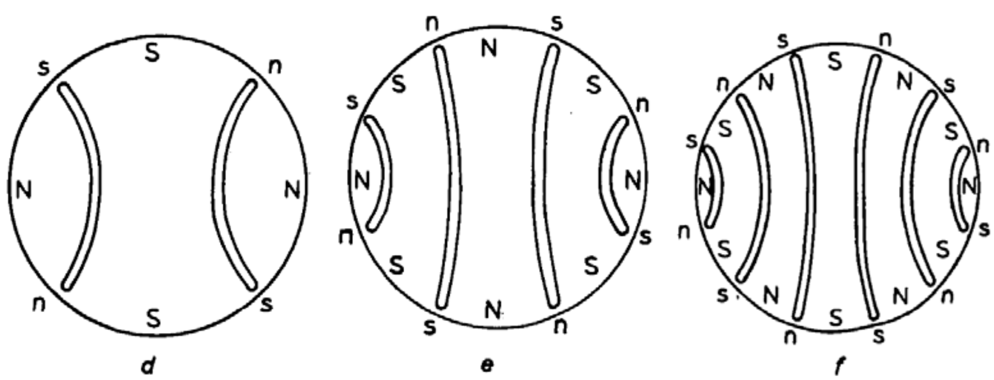

Figure 1-4: 1970's single, and multi-barriers proposed by W. Fong

Fong claimed that the new SynRM had more than 140% pull-out torque, around 80 % of full load torque and similar starting current and torque of its equivalent IM. This SynRM had higher torque density, pull-out torque to full load torque ratio. On the other hand, the full load power factor was only 0.7, while equivalent IM had 0.87. The efficiency was generally equal to the same size IM. However, one of the significant milestones of the SynRM design process is incorporating finite element method (FEM) for machine analysis. A. Wexler employed FEM to investigate SynRM for the first time in 1973 [53]. The FEM software was one of the early generations and had many limitations in modelling a highly complicated and non-linear SynRM.

1.2.2 Axially laminated anisotropy design

On the other hand, A.J Cruickshank worked on axially laminated reluctance rotor almost at the same time as Lawrenson. He designed and developed an ALA rotor using a technique called Cut-C cores. A graphical version of an ALA design is shown in Figure 1-5. In this design, the transversally laminated design is replaced by C formed axial anisotropy materials. He also articulated the essential parameters of reluctance machine to minimise torque ripples under all various operations, such as the importance of optimising reactance ratio (x_d/x_q) to achieve high output [45, 54]. Another type of ALA machine further investigated by S.C Rao in the mid-1970s [55]. Rao's ALA design was more or less similar to the Cruickshank's Cut-C design but with an axial hub and Q axis damper bar.

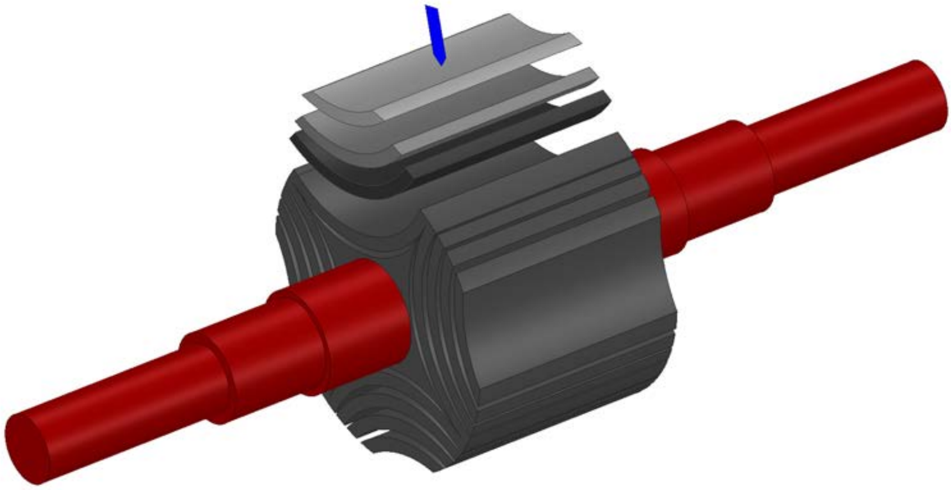

Figure 1-5: A 3D sketch of an ALA machine

The grain-oriented laminations were mounted on the axial hub, as shown in Figure 1-7. The damper circuit operated as field voltage inducer as well as sudden load absorber for better dynamic loading. The earlier ALA machines exhibited good operating characteristics, produced excellent pull-out and pull-in torques and better power factor over a transversally laminated design. However, due to the lack of sophisticated controller at the time, the rotor cage is needed for starting purposes. Therefore, the ALA saliency ratio could not be improved, which resulted in poor machine performance. Moreover, the complicated and unconventional design methodology did not attract the industry.

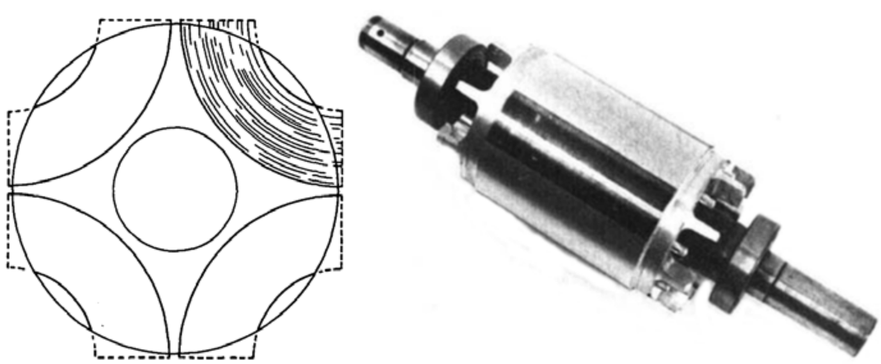

Figure 1-6: A.J Cruickshank's axially laminated rotor

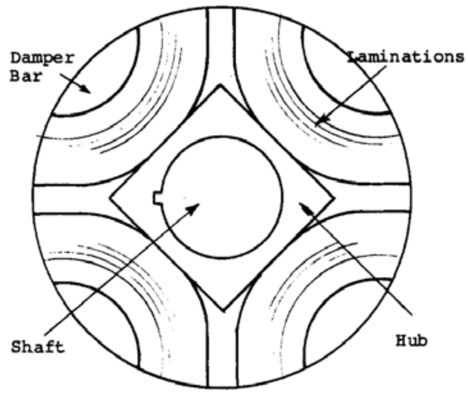

Figure 1-7: Rao's axially laminated anisotropy rotor

The ALA rotor design concept was forgotten for almost the next two decades until T.A Lipo, D.A Staton, and W.L Soong revisited in the early to mid-1990s [12, 50, 51]. Lipo clearly distinguished the differences in switched reluctance and SynRM machine and compared the two with IM and pointed out why SynRM stands out among the three [12]. He also developed the widely used torque relationship of SynRM for axially laminated design Eq. (1.2) through to (1.7). In the same reference, he introduced a new type of motor with axial lamination and axial permanent magnets and called it PM assisted SynRM, which will be discussed in the subsequent section.

$$L_d = L_l + L_{md} \tag{1.2}$$

$$L_q = L_l + L_{mq} \tag{1.3}$$

$$\begin{aligned} \lambda_d &= L_d i_d \\ \lambda m_d &= L_{md} i_d \end{aligned} \tag{1.4}$$

$$\begin{aligned} \lambda_q &= L_q i_q \\ \lambda_{mq} &= L_{mq} i_q \end{aligned} \tag{1.5}$$

$$T_{SynRM} = \frac{3}{2}\frac{p}{2}\left(\lambda_d i_q - \lambda_q i_d\right) \quad (1.6)$$

$$T_{SynRM} = \frac{3}{2}\frac{p}{2}\left(L_d - L_q\right)i_d i_q \quad (1.7)$$

D.A Staton et al. published a critical article on improving the saliency ratio of both ALA and TLA designs and used vector and field-oriented controller for SynRM [56]. It identified the importance of the saliency ratio and direct connection with machine performance parameters. It also recognised that the saliency ratio of the rotor cage compromised its performance and proposed to use a vector controller instead of the rotor cage for starting purposes [50]. For the first time, the SynRM was identified as a replacement for vector-controlled IM, especially ALA design. The reference goes further and develops a relationship of saliency ratio and lamination thickness, Eq. (1.8). Based on the new saliency ratio derivation, the authors claimed to have unsaturated maximum saliency ratio of 60 for their ALA machine, which is a lot more than the Kostko's prediction of 25.

$$\xi = \frac{tR}{g} + 1 \quad (1.8)$$

Where t is flux barrier as segment thickness and (R/g) is typically a constant

Although the authors distinguished that ALA design has better anisotropy compared to equivalent TLA, the ALA design performance only matches an equivalent IM using an inverter fed controller. However, the ALA machine has shown relatively good operating characteristics such as high torque density at low speed compared to an IM but in the order of 10-15 % with higher efficiency and wider speed range. W.L. Soong published a key article on ALA design which not only discussed the ALA rotor and other PM machines but also comprehensively analysed the field-weakening performance for a wide speed range of 7.5:1 [51]. He followed T.A. Lipo's suggestion on using PM assisted axially laminated synchronous reluctance machine. A four-pole 11 kW induction machine was de-rated to 7.5 kW to achieve 10:1 constant torque for his PM assisted ALA rotor experiments. The machine has pre-fabricated poles with interleaved laminations mounted on to the rotor shaft using bolts, as shown in Figure 1-8 for his experimental work. He identified the limitations on saliency ratio and defined requirement for field-weakening operation and also defined intrinsic magnetising saliency ratio as Eq. (1.9) which is the maximum possible saliency for a given rotor. He claimed that the unsaturated saliency of a machine is in the range of $0.2\xi_i < \xi < 0.4\xi_i$. His machine achieved an unsaturated saliency of 11.5 and successfully ran the machine with wide range field weakening region.

$$\xi_i = \frac{k_w R}{pg} \tag{1.9}$$

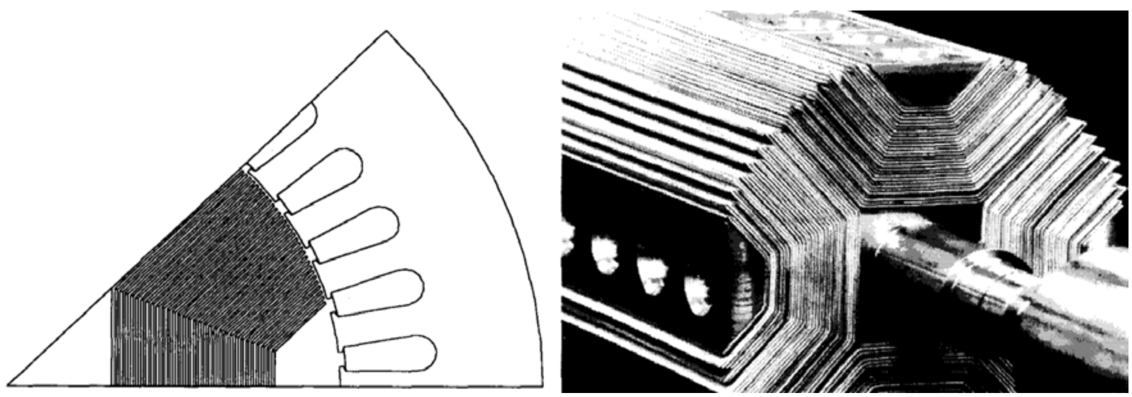

Figure 1-8: Axially laminated rotor topology and prototype rotor by W.L Soong

He also analysed designs with higher number of poles and its influence on rotor saliency and proposed four-pole for better practical construction and optimal saliency. Although he employed a four-pole machine, but suggested that larger machine sizes with a higher order of poles could yield better machine performance due to the smaller flux path and reduced saturation. However, due to the lack of advanced power electronics controller, he also could not achieve wider range field-weakening characteristics on SynRM instead suggested to use PMs in along the axial direction. Since the above-mentioned publications on axially laminated design, there has been numerous literature published on the same topic [51, 57-71].

The ALA anisotropy demonstrated reasonably good operating characteristics, better saliency ratio, better low-speed performance, high torque density, and power factor even without highly advanced controllers. Nevertheless, the design was not recognised by industry due to the challenges involved in manufacturing. This type of machine structure requires entirely new fabrication techniques, machining tools and new investment. However, all other AC machines, including PM synchronous machines, follows similar manufacturing technology as any other conventional AC machine which is stamping or wire-cutting.

1.2.3 Transversally laminated anisotropy SynRM

Traditional AC machines were manufactured using a technique called mould or stamping. In this process, the electrical machine laminations including for transformers, are cut, and transversally stacked as shown in a 3d sketch in Figure 1-9. When it comes to the reluctance machine in the 50s and 60s, the researchers seem to prefer axially laminated design due to the influence of segmental design during that time. The segmental design, although complicated for mass manufacturing, it was somehow easy to prepare for a prototype at labs which is acknowledged by T.J.E Miller and D.A. Staton [72].

On the other hand, the TLA design requires a proper mould or stamping tools to prepare which was costly, cannot be prepared at the lab and need good finishing in order to achieve precious air-gap length. With the introduction of flux barrier design with peripheral slots and circumferential grooves by W. Fong in the late 1960s, the TLA design was gradually presented. However, due to the challenges in controlling and achieving high torque density of the same or above IM and trend in ALA design, demotivated the interest in TLA.

Figure 1-9: A 3D sketch of a modern TLA machine

The next phase of development starts in the late 80s through three crucial researchers in the field of reluctance machine T.J.E Miller [10, 13], M. Nagrial *et. al*. [73-77] and A. Vagati. By this time, electrical machine control technology has been already developed with advanced power electronics and digital controllers while PWM, slip control and field-oriented control were already popular and widely used in IM and other PM machines.

Miller identified the gap in reluctance machine of that time and also recognised that so little development had been done in the cage-less reluctance motor. Although he was interested in control, but designed a rotor without a cage while controlling it using field-oriented control techniques [10, 13]. Contrary to the traditional convention, he used the low reluctance axis as quadrature axis and vice versa due to the selection of IPM rotor geometry to replace SynRM for experimental purposes. Although he claims it is more consistent with SynRM theory, the saliency ratio equation had to be inverted, and the phasor diagram also modified to suit the adopted convention [13]. His experimental results with a single barrier IPM rotor proved that SynRM had high torque density compared to IM and suggested to use the axially laminated design for better saliency ratio. He did not utilise the full potential of transversally laminated SynRM with multi-barrier. Miller and Staton published another article that investigated various parameters of SynRM and proposed practical suggestions to design rotor to achieve high saliency [72].

They have concluded that the multi-barrier transversally laminated rotor is impractical and proposed to use ALA structure due to its simplicity. The significant thing to note, those two articles employed FEM to simulate a practical problem. In the same time, Nagrial et al. had been working on both solid and TLA rotor types since the late 1980s, as shown in Figure 1-10. Their design focused on improving the torque density and pf by maximising the inductance ratio by employing a Q – axis grooves in the rotor peripheral, as shown in Figure 1-10 (a).

They have experimentally verified that the SynRM TLA rotor that employs flux guides and grooves can perform better than that of IM [9]. A few years later, a comprehensive FEM study was performed but on segmental design [74]. The literature, although dealing with the improvement of machine performance, primarily focused on enhancing saliency ratio through optimising magnetic circuit. Unsaturated saliency ratio of 16.2 was reported in a segmental design. Although their primary focus was testing a multi-barrier TLA rotor, they could not be able to test it on prototype due to the manufacturing difficulties.

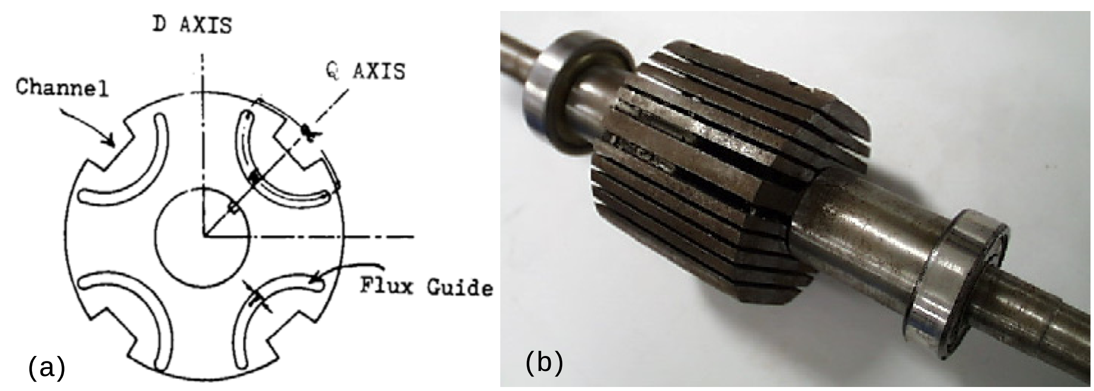

Figure 1-10: SynRM machine of Nagrial et al. in the 1990s (a) single flux guided rotor with peripheral grooves (b) prototype of the segmental rotor

The literature focusses on having higher reluctance in the Q axis and lower reluctance on the d axis instead of focusing on the placement of the barrier as they already had enough challenges in fabrication. They overlook the importance of the barrier placement, thickness, barrier to segment ratio, the optimum number of barriers, barrier to barrier thickness, insulation ratio, aligning barriers to stator teeth and importance of rotor ribs and webs.

Vagati who had been working on control and design of conventional AC machine, published a research paper on reluctance machine jointly with I. Marongiu in 1991 [78]. It, starts with, drawing the basic questions relevant to the challenges faced by SynRM developers of the time to improve its torque per volume and flux weakening feature above the equivalent IM. Those were, how to achieve L_d and method to minimise L_q, how to minimise the iron losses in the rotor due to stator slotting how to align the barrier to stator teeth. A mathematical model for a slotted stator and rotor anisotropy developed and a practical rotor with multi-barriers in two and four poles analysed in this paper. Their rotor design is shown in Figure 1-11. The rotor is somehow similar to W. Fong's rotor (Figure 1-4), without the rotor cage, peripheral grooves, and circumferential slots. Instead, they virtually introduce tangential ribs to connect the steel segments.

The vital features of this design are the varying barrier thickness, cut-off at the end of Q axis to increase the saliency ratio (even though it was not mentioned in the paper) and attempt to minimise ripples by strategically placing the barriers concerning stator teeth [79]. The flux linkage oscillation in the rotor peripheral was mainly attributed to the iron nearer to the rotor surface, which is the stator teeth. The mathematical theory intensive paper opened the doors for further development.

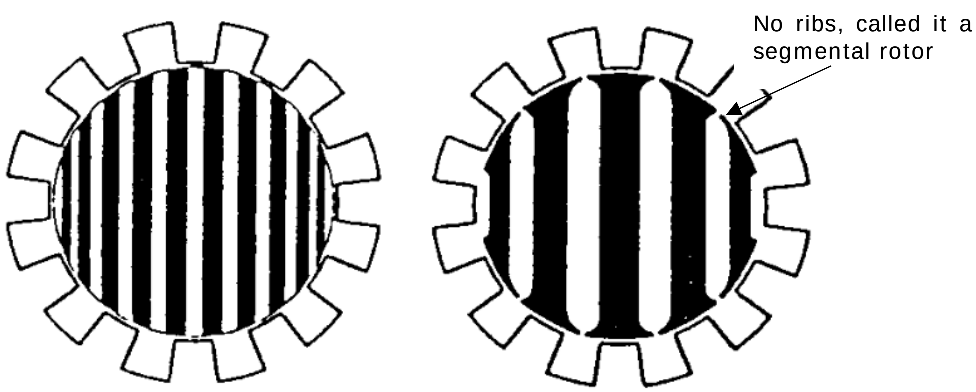

Figure 1-11: Vagati's five-barriers and two barriers per pole SynRM without rotor cage

He published another article where he categorised his rotor as segmental type [80]. Besides, he distinguished the difference between flux barrier design and distributed anisotropy due to the non-magnetic material distribution. A stator tooth distributed anisotropy, rotor segments, tangential ribs are introduced. The paper also highlighted concerns about the mechanical integrity of the rotor due to tiny ribs and compromising saliency ratio due to the rib size. It also introduced an optimisation technique to improve SynRM performance. Although he called it a segmental design in [80], it is transversal anisotropy due to the presence of rib, as shown in Figure 1-12. He had acknowledged this structure is transversally laminated anisotropy six years after in his paper [81]. Since then, he has published numerous papers on improvement, optimisation, and control of SynRM [78, 82-86].

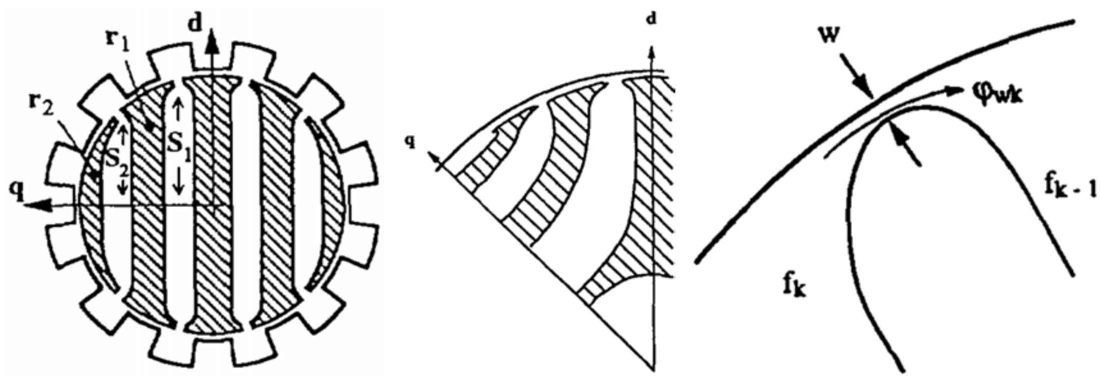

Figure 1-12: Vagati's realistic SynRM and rib profile in the early 1990s

In the meantime, he had continuously been working on the improvement of SynRM with his team. The theoretical estimation and improvement of torque ripples was published in 1993 [87] which investigated the ripple mechanism of a multi-segment structure. The fluctuations due to stator-rotor interaction was defined. The stator magnetic potential modulation had been derived concerning the modulated D-Q axes inductances Eq. (1.10) through to (1.15), where ΔL_d, ΔL_q and ΔL_{dq} defines the modulated stator potential behaviour with respect to rotor segment and stator tooth [87].

$$\begin{bmatrix}\lambda_d\\ \lambda_q\end{bmatrix} = \begin{bmatrix}L_d(\vartheta) & L_{dq}(\vartheta)\\ L_{dq}(\vartheta) & L_q(\vartheta)\end{bmatrix}\begin{bmatrix}i_d\\ i_q\end{bmatrix} \tag{1.10}$$

$$\frac{\partial \lambda_d}{\partial i_q} = \frac{\partial \lambda_q}{\partial i_d} \tag{1.11}$$

$$L_d(\vartheta) = L_{d0} + \Delta L_d \cos(pq\vartheta) \tag{1.12}$$

$$L_q(\vartheta) = L_{q0} + \Delta L_q \cos(pq\vartheta) \tag{1.13}$$

$$L_{dq}(\vartheta) = -\Delta L_{dq} \sin(pq\vartheta) \tag{1.14}$$

$$\lambda_{dq} = L(\vartheta) i_{dq} \tag{1.15}$$

In addition, the torque behaviour relationship was derived from co-energy by neglecting magnetic non-linearity for a 3ph as in Eq. (1.16). The second term corresponds to machine torque ripples. The first term corresponds to the average torque, and the second one is the torque pulsation with respect to the rotor angle. Although the skew method is attempted, a complete reduction of ripples in SynRM is impossible due to the anisotropy and has been theoretically proven by Vagati et al. Besides, he had drawn a new relationship between ripples and number of stator slots. He has proven that increasing slot number reduce the modulated D, Q and cross inductances.

$$T = \frac{\partial w`}{\partial \vartheta} = p\lambda_{dq} \times i_{dq} + \frac{1}{2} i_{dq}^{T} \frac{\partial \lambda_{dq}}{\vartheta} \tag{1.16}$$

1.2.4 Modern SynRM

Although many researchers have proposed TLA design, it was Vagati who established the mechanically rugged, high torque, acceptable pf with reasonably reduced ripples in 1998. Transversally laminated anisotropy was selected over axially laminated structure due to its simplicity and performance. While ALA has inherently more advantages over TLA design, the simplicity of TLA structure provides a higher degree of freedom to design various barrier shapes. TLA structure can be manufactured using either the same stamping technology (it has slightly high tolerance) or wire cutting techniques (medium speed wire-cutting can have tolerance of up to ± 0.01 mm) using the existing machining tools. Moreover, it uses the same stator, winding and frames. Thus, it does not require new investment. The tangential and radial ribs provide mechanical integrity to the segments of the rotor, as shown in Figure 1-13. The combination of TLA design and sophisticated field-oriented controllers provide greater freedom for designers to optimise rotor dimensions in such a way the direct and quadrature axes induction ratio can be maximised.

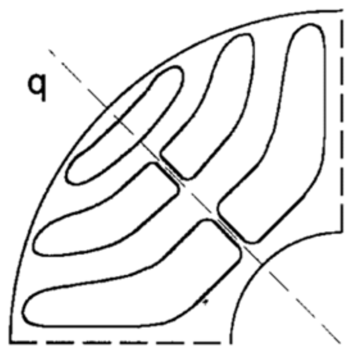

Figure 1-13: Vagati's first TLA design

The reference [81] revealed that SynRM could be designed to have a tolerable torque pulsation of 5 – 10 % without skewing or other additional arrangements while achieving full torque per volume with reasonably good power factor in a TLA structure [88]. Besides, the controlling of SynRM motor using a field-oriented controller exhibited superior dynamic behaviour in the wide field-weakening range [89]. One of the major electrical machine manufacturers, ABB introduced their complete SynRM product line, ranging from small as 1.1 kW to 350 kW [20].

However, the SynRM's drawback such as high torque ripples and low power factor still need to be improved to match other machines. The applications, such as electric or hybrid electric vehicle, require great low and high-speed characteristics with reduced torque ripples for smooth operation. It has been discussed and shown that the ripples of SynRM could be minimised to an acceptable level by optimising rotor dimensions and barrier placement [68, 90-94]. The distribution of air-gap mmf by proper barrier placement is critical to reduce the ripples [81, 88, 95].

The asymmetrical barrier design has also been suggested to reduce torque ripples [91, 96]. Another approach to reducing ripples is segmented lamination topology [97, 98]. Another technique is employing concentrated winding to minimise the ripples, which is not the scope of this thesis [99]. Lately, the researchers have suggested optimising the barrier dimension for better machine performance, including pf [100-103]. The reference [104] has shown that optimisation of torque density improves the power factor also, but it did not consider the torque ripples. Therefore, a single-objective optimisation either torque or power factor is not enough to yield a high-performance machine as discussed later in this thesis.

On the other hand, a single-objective optimisation for torque ripples improves the power factor and the torque. The high insulation ratio is also suggested for high power factor, but increasing the insulation ratio beyond a certain level reduces machine performance due to high reactance and saturation. High power factor, relatively low torque ripple and high torque density can be achieved by adding PMs to SynRM [21, 105-116] to produce a high-performance machine whose performance can be compared with brushless PM machines.

1.3 Evolution of PMSynRM

Although permanent magnet usage in electrical machines has a long history but it has been used in SynRM only from the early 1990s [12]. T.A. Lipo suggested to use PM in the axially laminated rotor barrier cavities in order to overcome the drawbacks of SynRM of that time as well as to enhance the machine performance. The SynRM was slowly getting attention during the early 1990s. The machine demonstrated high torque density and in fact, excess of an equivalent induction motor. However, the high torque density was achieved by increasing the current by $\sqrt{2}$ of the machine of that time. It imposed unwanted stress to the inverter and resulted in poor power factor [12]. Lipo suggested using sandwiched magnetic bars in axially laminated rotor between axial laminations sections to increase the torque of SynRM without increasing supplied current, as shown in Figure 1-14. However, the insertion of PMs has not only increased the torque density but also improved the power factor and reduced torque ripples [107, 117-125].

The new machine is called permanent magnet assisted synchronous reluctance machine (PMSynRM). The D – axis flux magnetises the SynRM core, and the PMs are merely used for obstruction of the Q – axis armature reaction in a typical PMSynRM. Ferrite magnet or a similar low-grade magnet was suggested with a relatively small amount of flux for the early version of PMSynRM.

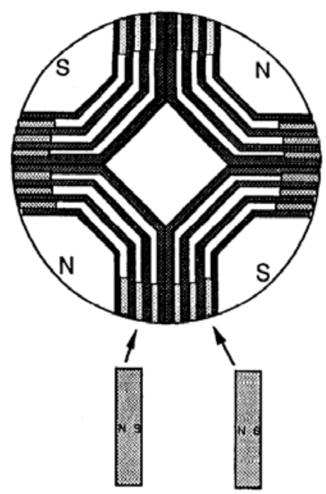

Figure 1-14: Lipo's first PM assisted synchronous reluctance machine

The torque density can be increased by 25 % to 30 % more if rare-earth PMs are used. The added PMs can push the resultant flux into the fourth quadrant that moves the voltage vector of the machine into the first quadrant. As a result, the angle between voltage and current vector can be minimised to almost 0°. Thus, the power factor of this machine can be quite high if rare-earth magnets are used. The addition of magnet in the quadrature axis reduces the resultant flux, which is given in Eq. (1.17). The PMSynRM torque is defined by Eq. (1.18) where the PM flux in negative Q axis direction is accounted.

$$\lambda_q = L_q i_q + \lambda_{pm} \tag{1.17}$$

$$T_{PMSynRM} = \frac{3}{2}\frac{p}{2}\left(\lambda_d i_q - (\lambda_q - \lambda_{pm}) i_d\right) \tag{1.18}$$

The PMs in an ALA design is rather challenging and complicated. It requires a separate mechanical arrangement but also require modification of PMs for proper bolting to strengthen its mechanical integrity, especially for high-speed applications. Researchers prefer TLA structure over ALA due to its simplicity in mounting PMs and ruggedness. The structure does not need an extra arrangement to mount PMs, and barriers can be sized to accommodate PMs, as shown in Figure 1-15.

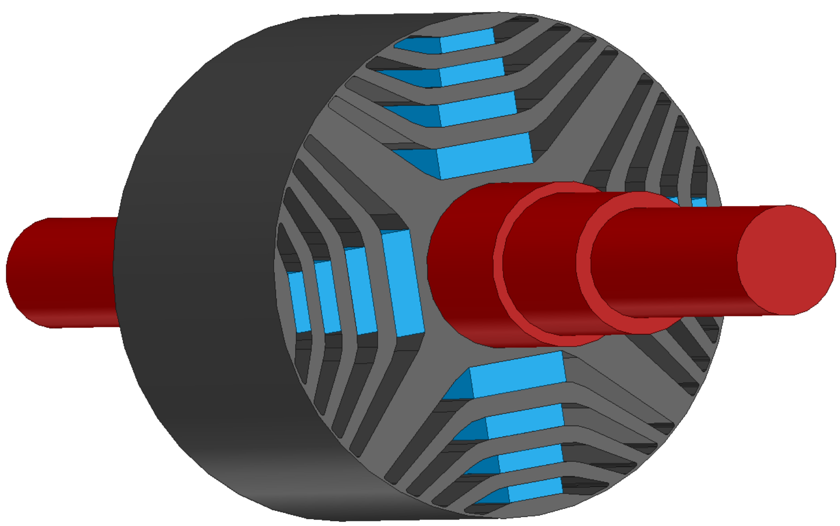

Figure 1-15: Arrangement of permanent magnets in the TLA rotor

Since the early 90s, the development of PMSynRM gained importance due to simplicity of the TLA rotor structure, increased torque, improved power factor and low-cost ferrite magnets. Although PMs were initially proposed to minimise the machine current to improve the inverter performance. They were used to improve machine power factor and torque ripples. T.M. Jahns and W.L. Soong proposed PMs for improving synchronous machine performance while reducing torque ripples [126]. Although it targeted conventional PM machines, it was also applicable to PMSynRM. Since then, PMs are used to enhance SynRM machine performance [105, 113, 127, 128].

One of the first literature on using PMs for high performance experimentally proved that the power factor of above 0.9 could be achieved [117]. The impact of PMs and hysteresis losses were studied using FEM and reported that losses due to PMs are negligible [118, 129]. A TLA PMSynRM was practically experimented in for various PM volume [130]. The PMSynRM was tested for 1:5 wide speed range and claimed that the machine could perform better than the SynRM with added PMs. It also distinguished the reluctance torque and magnet torque produced by the machine for each test with a change in PM quantity, as shown in Figure 1-16. It was claimed that the danger of uncontrolled generator mode stalling is less in this machine [131]. The researchers tried to reduce the Q axis flux linkage by providing relatively larger PM into barrier closer to the shaft in a four-barrier structure. The experiment intended to reduce the losses of SynRM and increase efficiency by inserting PMs, and claimed to achieved 3.6 % more efficiency.

Figure 1-16: PMSynRM of the early 2000s

In a key paper, they had calculated flux linkage by voltage integration in the field-weakening region and flux current by tracking rotor saliency in the low-speed region for sensor-less control of PMSynRM [132]. Low speed and field-weakening characteristics of the machine are experimentally presented. The literature claimed that PMSynRM could be controlled at standstill condition while the machine also demonstrated very large constant power range with accurate dynamic behaviour. The reference pointed out that the machine has a weak no-load characteristic. Instantaneous steady-state flux linkage, by added PMs at online, is an important parameter for design machine controller [133-135]. This method is virtuous for achieving fast dynamic controller for high-performance applications. Since then, the motor has been intensively researched for various application, especially electric and hybrid electric vehicles [135-140].

The effort by N. Bianchi et al for recent development in PMSynRM and SynRM are worth noting [108, 120, 141-147]. Their literature on asymmetry barrier design with alternative poles for torque ripples minimisation is critical [144]. They have provided a solution by combining asymmetry barriers of opposite poles to compensate 12^{th} order harmonic for further minimisation of ripples. He called it Machaon rotor topology. They have also employed multi-objective optimisation to optimise PM for wide constant power operation [120, 145].

The other PM machines such as surface-mounted and interior mounted permanent magnet machines, have extended history. They have already been in mass production and used in various applications including electric and hybrid electric vehicles and proven to be highly effective in certain applications. However, the development of PMSynRM has been rather slow in comparison to those machines. PMSynRMs can perform better due to its hybrid torques with degree of freedom in the design. It can be more cost-effective due to the usage of either low volume high-grade PMs or higher volume of ferrite magnets.

1.4 Synchronous Reluctance Machines (SynRM)

The synchronous reluctance machine (SynRM) unlike other conventional electrical machines, operates based on the difference in reluctance. SynRM has the same stator of AC conventional electrical machines with sinusoidally distributed flux. The rotor is the only difference which is a simplified, copper coil-less and rugged structure made of electromagnetic steel [31, 48, 85, 148]. It is an alternative to induction machine (IM) with high reliability and less maintenance for the long run [149-152]. SynRM is already available in as small as 1.1 kW to as high as 375 kW [21, 153]. Due to the absence of rotor cage and coils, the machine's inertia is reduced and losses cut by significant per cent resulting in high efficiency and high torque density in comparison to its counterpart induction machine. Moreover, the rotor heating effect is relatively low in this machine [153, 154].

The rotor can have two types of anisotropy one is axially laminated anisotropy (ALA), and the other is transversally laminated anisotropy (TLA). Although ALA exhibits better magnetic saliency than transversally laminated structure when used with grain-oriented electromagnetic thin steel laminated axially, but the construction is rather complicated and expensive [45, 51, 69, 70]. The TLA design exhibits similar machine performance through rugged rotor with high mechanical integrity and less manufacturing complexity [155-161].

The TLA design is manufactured by either circular wire cutting technology or stamped grain-oriented pieces stacked together and heat pressed on the shaft. A detail view of four-pole SynRM with the conventional stator, coils and four barrier rotors with radial and tangential ribs is shown in Figure 1-17. A practical stator, rotor and coil windings are shown in FEM program with precise details such as stator slot details, end coil winding, winding resistance, and inductance of end coil segments.

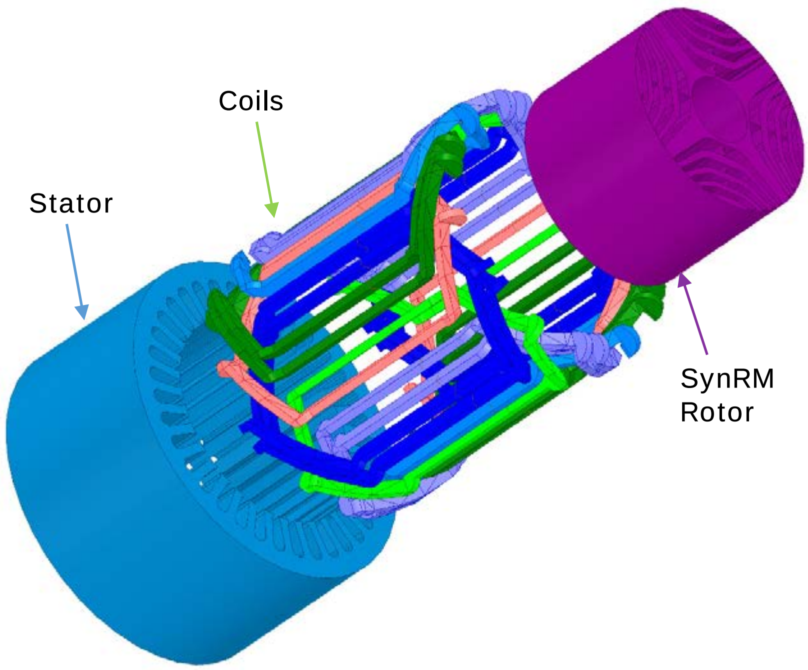

Figure 1-17: A detail view of synchronous reluctance motor

The primary machine design parameter is the saliency ratio or differences in saliency in the SynRM design process Eq. (1.19). The saliency ratio is the ratio of direct and quadrature axes inductance used as a machine design parameter for machines with magnetic saliency [50, 104, 152, 162-164]. As there are no rotor coils or PMs in the rotor, the only excitation is via multiphase sinusoidally distributed supply. The higher saliency means, better torque and pf in SynRM. Hence, it is the primary design intent in the machine design process to achieve high saliency. The D axis flux linkage should be increased as high as possible while minimising the Q axis flux linkage to as low as possible.

$$\xi = \frac{L_d}{L_q} \tag{1.19}$$

Figure 1-18(a) shows a rotor with high permeability or low reluctance in the direct axis and low permeability or high reluctance in the Q axis so that the flux linkage from air-gap can be entirely directed into D axis, as shown in Figure 1-18(b) [79, 165-171]. In order to achieve high reluctance in the Q axis, the axis space shall be barricaded by high insulation (non-magnetic gaps) to restrict the flux passage via this axis. Therefore, the SynRM rotor should be designed with multi flux guides (also called flux barriers) along the quadrature axis. Although eliminating the radial and tangential ribs are an ideal solution to increase the reluctance in the Q axis, but they are essential for the mechanical support between rotor segments, as shown in Figure 1-19. Therefore, the design of ribs and webs are significant in the design process to achieve both high mechanical integrity and high machine performance.

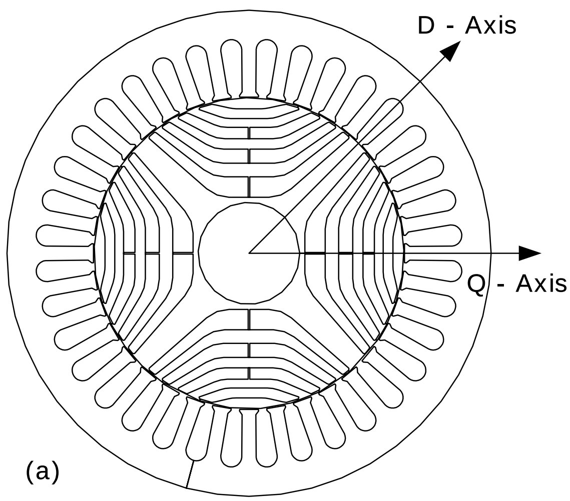

Figure 1-18: A four-pole SynRM with (a) primary D - Q axes and (b) D axis flux path are shown

On the other hand, the SynRM generally has a relatively low power factor and high torque ripples [101, 144, 172-174]. These drawbacks can be overcome by careful selection of rotor flux guides and optimising the rotor dimensions. Figure 1-18 shows a four barrier and four-pole reluctance rotors with the stator of 36 slots. The rotor has tangential ribs and radial webs arrangement. The magnetic D and Q axes are indicated in Figure 1-18a, and D axis flux path is shown in Figure 1-18b.

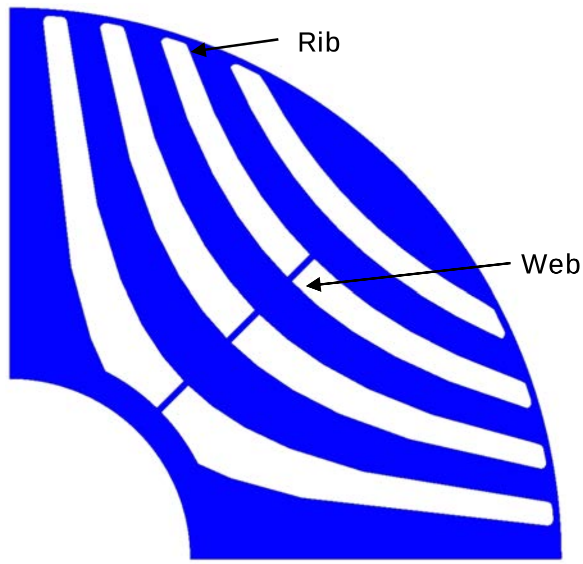

Figure 1-19: Tangential ribs and radial webs of a SynRM rotor

The control of a SynRM is generally precise, and faster in comparison to the induction machine due to the absence of slip. Its linearity in maximum torque per ampere (MTPA) region and good flux-weakening ability in the constant power region makes it a better candidate for direct torque control [62]. It can also be controlled using the conventional VFD/VSD, although a unique controller can also be used. The direct torque control method of SynRM has the ability to start the motor with reasonably high torque and fast response even at low speeds [175-180].

Figure 1-20 shows the control regions of selected SynRM where the torque is constant up to the rated speed and power is constant for speeds above rated speed (field weaken region). Its linearity with D and Q currents allows the torque to be linear at MTPA region (also known as constant torque region). However, the torque is decreased in the field-weakening region for increasing speed.

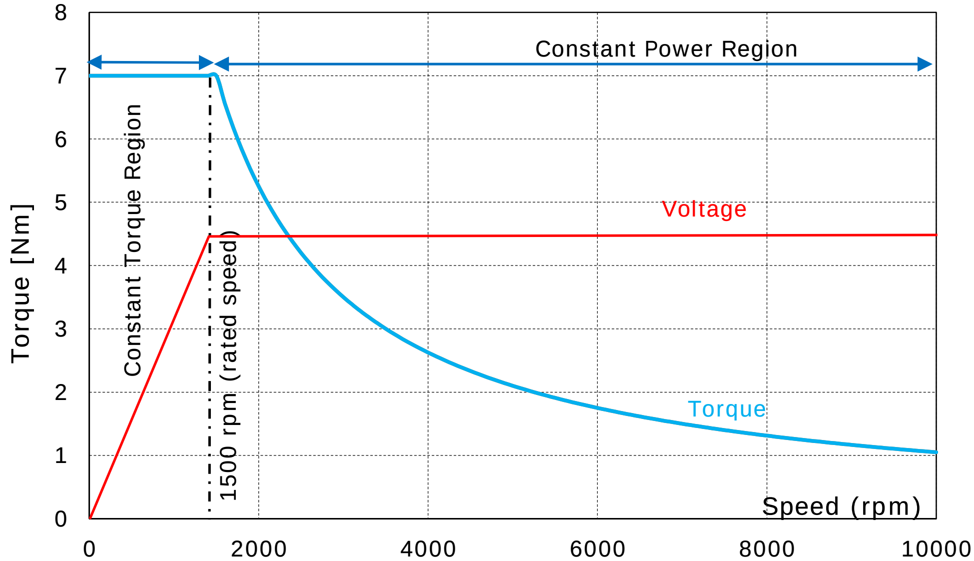

Figure 1-20: Constant speed constant power regions of SynRM

In constant power region, the machine voltage is maintained at maximum available from the inverter to maintain the constant power. Its fast and precise control over a wide speed range makes it a good candidate for electric vehicle applications [16-18, 181]. Figure 1-20 shows the torque-speed curve of the investigated machine (rated torque of 7 Nm and rated speed of 1500 rpm) at MTPA and field-weakening regions. The torque is constant between 0 and 1500 rpm, and it reduces with speed. On the other hand, the voltage is maintained at its maximum in the field-weakening region.

1.5 Permanent Magnet Assisted Synchronous Reluctance Machines

The SynRM machine becomes permanent magnet assisted synchronous reluctance machine (PMSynRM) when PMs are inserted into its flux barriers. PMs are introduced to obstruct flux in the Q axis direction. Hence, the radial and tangential ribs can be saturated. Consequently, the PMs improves the saliency ratio resulting in higher torque and power factor [112, 121, 125, 142, 182]. An appropriately sized PM at an optimised location can also improve the torque ripples [19, 106, 173]. The magnetic torque component is introduced along with reluctance torque by the addition of PMs. The resultant machine has a combination of reluctance and magnetic torque components.

Thus, there are numerous possible designs available for PMSynRM within the two extreme ends, one with just reluctance torque, and the other with only magnetic torque [21]. There is slight confusion between interior permanent magnet machines and PMSynRM. The interior permanent magnet machine is similar to PMSynRM in terms of the design process as well as structure [21]. However, both are distinguished by the magnitude of the PM flux. If the PM flux dominates, then the machine is called IPM and if the reluctance torque dominates, then the machine is called PMSynRM. In general, a PMSynRM has around 25 % to 30 % PM flux torque.

A PMSynRM has less PM volume compared with an equivalent IPM. Figure 1-21(a) shows a sketch of D and Q axes flux linkages in a PMSynRM and the PM-induced flux that opposes the Q axis flux at the air-gap. As a result, a high reluctance is created along axis, while PMs does not affect the D axis flux path. Figure 1-21b shows the D axis flux path in the simulated model where the PMs assist slightly to direct the flux towards the Q axis. An expanded view of saturation in ribs due to PM is shown in Figure 1-21c.

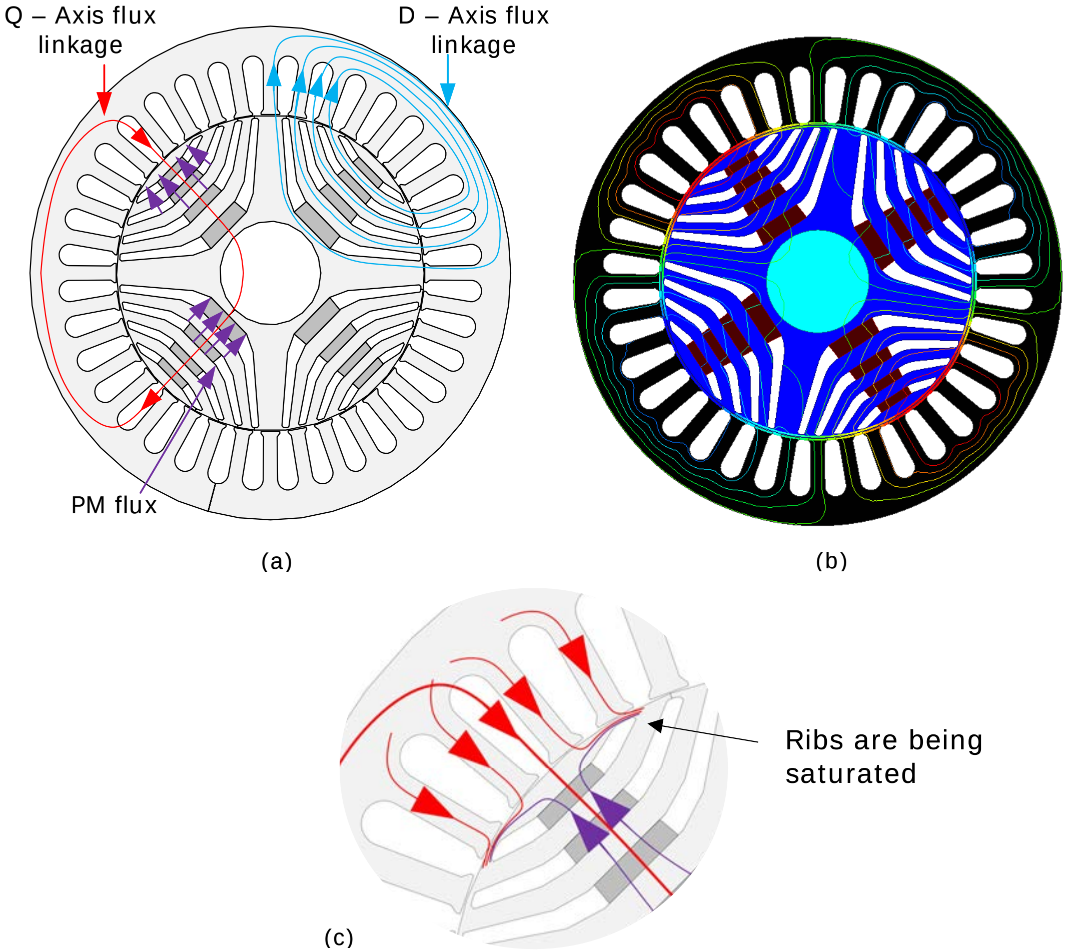

Figure 1-21: Flux path of PMSynRM shown in (a) sketch demonstrates D axis, Q axis flux path and PM flux (b) D axis flux linkage in a simulated environment (c) An expanded view shows how the tangential ribs are being saturated

The insertion of PMs reduced the Q axis flux linkage significantly, and it is shown in Figure 1-22 at a rated condition. The results are obtained from the same rotor, but one with PMs inserted. PMs in the flux barrier not only reduce the Q axis flux linkage but also slightly reduced D axis flux due to the residual PM flux along the D axis as can be seen in Figure 1-21b. The saturation and crossed saturation due to radial and tangential ribs, and for varying currents are shown in Figure 1-23. The saturation due to current is visible in the figure. SynRM's Q axis flux increases with current and experiences saturation at a specific current. Then the rate of change of the flux is quite low as the ribs are already saturated. Whereas, the D axis flux experiences saturation quite later than Q axis flux and experiences high saturation. Beyond this point, the increasing current does not contribute to machine efficiency.

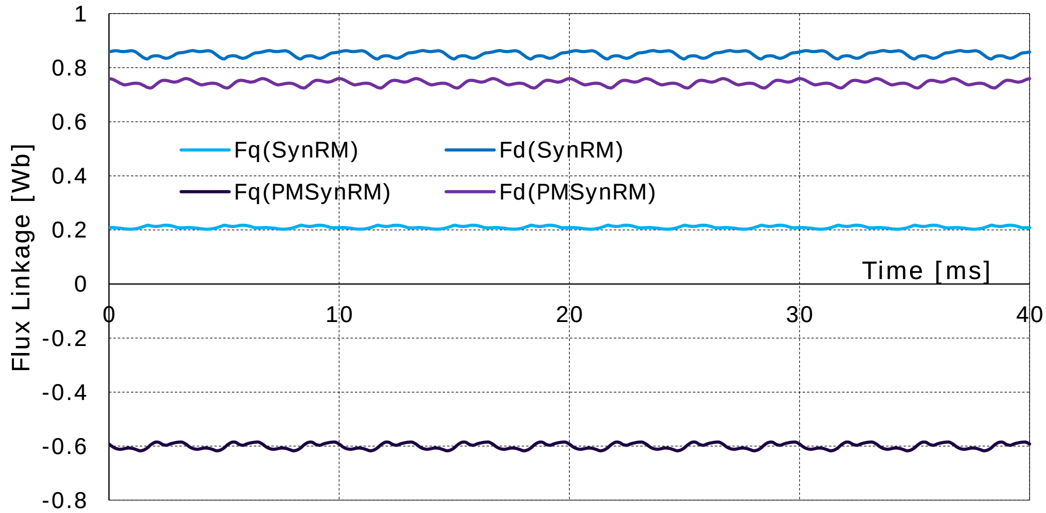

Figure 1-22: D and Q Axes flux linkages of both SynRM and PMSynRM

On the other hand, PMSynRM's Q axis flux is saturated even before the current is applied due to the added PM flux. D axis flux of this machine begins to saturate at lower current compared with SynRM and regularly experiences saturation. Thus, it should be operated with quite lower currents compared with an equivalent SynRM to have high efficiency. The DQ flux linkages are shown in Figure 1-22 and Figure 1-23 are obtained for a PMSynRM and equivalent SynRM at the rated condition and MTPA trajectory.

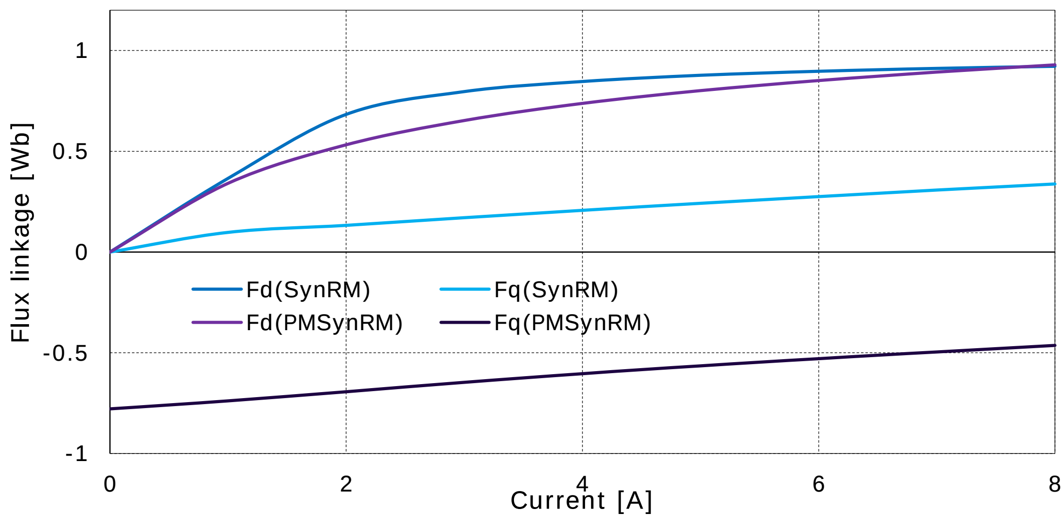

Figure 1-23: D and Q axis induction saturating as supply current increases

In general, a SynRM is controlled by current controllers, hence susceptible to saturation caused by the overcurrent. The currents, up to 8 A, are simulated and the saturation in SynRM is shown in Figure 1-23. Although the D axis flux linkage of PMSynRM is slightly lower at rated condition (I_{max}=4.1 A), it gradually increases with currents. On the other hand, F_d of SynRM experiences a high rate of change at lower currents due to the optimised magnetic path, but then suffers high saturation and decays to a constant value. F_q of SynRM suffers slight saturation before it becomes steady with currents. However, F_q of PMSynRM does not suffer saturation as the ribs have already been saturated due to PM flux before the current is applied.

Although PMs are suggested for minimisation of quadrature flux linkage, it can also be used to inject D axis flux linkage [108, 111, 115, 134, 183, 184]. The PMs along an intermediate axis can divide flux into longitudinal and transverse flux that can be distributed to both D and Q axes. Consequently, the addition of flux in the D axis can improve the saliency ratio of the machine.

1.6 Research Motivation and Goal

The ultimate goal of this research is to increase the performance of SynRM and PMSynRM. In recent times, local and international standards are tightened to improve the machine efficiency. The premium standard is also known as IE4 (adopted by most of the countries) requires significantly higher efficiency, as shown in Figure 1-24 [1, 2]. The efficiency of larger machines is already quite high, and above the 90 % mark. The machines of over 100 kW are already above the 95 % efficiency range, as shown in Figure 1-24. The larger machines have high degree of freedom in terms of design, with larger frame size so that the barriers and ribs can freely be designed. On the other hand, the smaller size machines (below 5 kW) does not have enough room in the rotor space to have optimal barrier widths.

The smaller machines often operate at the lower end of 80 % efficiency. These are the machines that dominate the industry as well as household applications. Thus, their efficiency must be increased as high as possible not only to comply with the international standards, but also to reduce the operational cost, and environmental impacts. On the other hand, as already discussed, the usage of rare-earth permanent magnets is not encouraged anymore.

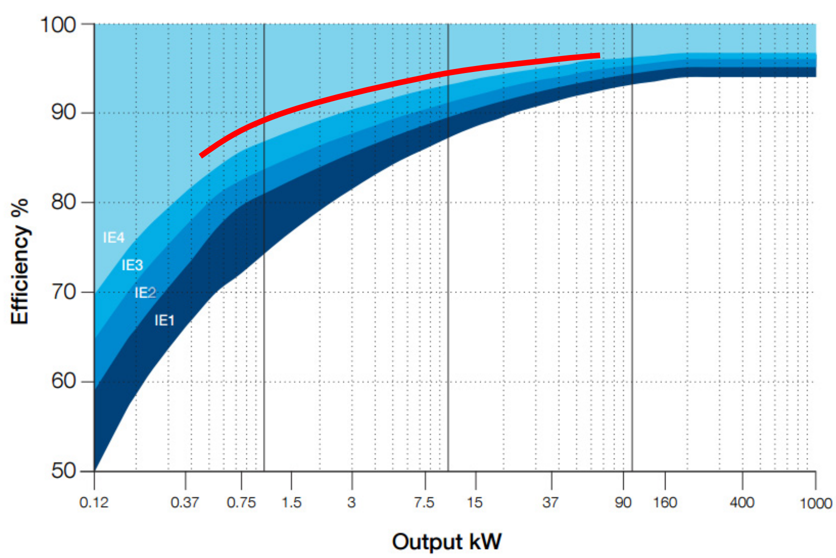

Figure 1-24: International efficiency standard of four-pole machines (extracted from ABB's manual)

The PM machine industry is looking for an alternative machine that can match the characteristics of IPM or SPM machines. The electric vehicle industry has been growing in recent times and expected to take over the internal combustion engine by 2030. The electric vehicle industry uses either surface-mounted PM machines or interior permanent magnet machines predominantly. Both machines are PM synchronous machines with a significant amount of rare-earth PMs. There are two types of rare-earth magnets available, one is neodymium, and the other is samarium cobalt magnets. Neodymium magnets are quite popular due to its high magnetic field and coercive force. A high-grade sintered neodymium magnet ($Nd_2Fe_{14}B$) can produce high magnetic fields.

As of 2018, over 120,000 tons of neodymium magnets are produced every year [185]. The electrical vehicle industry already uses over 30 % of neodymium magnets. The limitation of rare-earth magnets deposits and cost of production is not sustainable for the booming electric vehicle industry. Therefore, SynRM and PMSynRM's developments are inevitable. This study is directed to increase the smaller machine's efficiency to above the premium standard level defined by IEC/EN60034-30[1, 2]. The primary goal of this research is to increase the efficiency of those two machines above and beyond the standards proposed by international standards and local government legislation to the marked red line shown in Figure 1-24.

1.7 Publications and Scientific Contribution

As part of this research study, numerous conference papers and a journal are published at IEEE conferences and recognised journals. In addition, four journals are in the process of publication along with other two conference papers as listed below:

Published papers:

[1] T. Mohanarajah, J. Rizk, M. Nagrial et al., "Finite element analysis and design methodology for high-efficiency synchronous reluctance motors," Electric Power Components and Systems, 2018.

[2] T. Mohanarajah, J. Rizk, M. Nagrial et al., "Design optimisation of flux barrier synchronous reluctance machines," in Intl Aegean Conference on Electrical Machines & Power Electronics (ACEMP), 2015 Intl Conference on Optimisation of Electrical & Electronic Equipment (OPTIM) & Intl Symposium on Advanced Electromechanical Motion Systems (ELECTROMOTION), pp, 58-62, 2015.

[3] T. Mohanarajah, J. Rizk, M. Nagrial et al., "Optimisation of flux barrier parameters in synchronous reluctance machines," in IEEE Conference on Energy Conversion (CENCON), pp, 299-304, 2015.

[4] T. Mohanarajah, M. Nagrial, A. Hellany et al., "Effect of saturation on performance of synchronous reluctance machines," in IEEE International Conference on Power and Energy (PECon), pp, 802-807, 2016.

[5] T. Mohanarajah, J. Rizk, M. Nagrial et al., "Comparative analysis of synchronous reluctance machines with and without permanent magnets," in IEEE International Conference on Power System Technology (POWERCON), pp, 1-6, 2016.

[6] T. Mohanarajah, J. Rizk, M. Nagrial et al., "Design of synchronous reluctance motors with improved power factor," in 11th IEEE International Conference on Compatibility, Power Electronics and Power Engineering (CPE-POWERENG), pp, 340-345, 2017.

[7] T. Mohanarajah, J. Rizk, A. Hellany et al., "Torque ripple improvement in synchronous reluctance machines," in 2nd International Conference On Electrical Engineering (EECon), pp, 44-50, 2018.

[8] T. Mohanarajah, J. Rizk, M. Nagrial et al., "Permanent magnet optimisation in pm assisted synchronous reluctance machines," in IEEE 27th International Symposium on Industrial Electronics (ISIE), pp, 1347-1351, 2018.

[9] T. Mohanarajah, J. Rizk, M. Nagrial et al., "Analysis and design of high-performance synchronous reluctance machine," in IEEE 12th International Conference on Compatibility, Power Electronics and Power Engineering (CPE-POWERENG-2018), pp, 1-6, 2018.

Submitted Publications:

[1] T. Mohanarajah, J. Rizk, M. Nagrial, and A. Hellany, "Design and Torque Ripples Optimisation of Permanent Magnet Assisted Synchronous Reluctance Machines," IET Electric Power Applications, vol. TBC, no. TBC, 2019.

[2] T. Mohanarajah, J. Rizk, M. Nagrial, and A. Hellany, "Design Optimisation of Synchronous Reluctance Machines for Low Torque Ripples," IEEE Transactions on Industrial Electronics, vol. TBC, no. TBC, 2019.

[3] T. Mohanarajah, J. Rizk, M. Nagrial, and A. Hellany, "A Novel Method to Optimise Permanent Magnet Assisted Synchronous Reluctance Machines," Electric Power Components and Systems, vol. TBC, 2019.

[4] T. Mohanarajah, J. Rizk, M. Nagrial, and A. Hellany, "Design of Permanent Magnet Assisted Synchronous Reluctance Machines with Rare Earth Magnets" in 17th International Conference on Frontiers of Information Technology (FIT), Islamabad, Pakistan, TBC 2019: IEEE, p. TBC.

[5] T. Mohanarajah, J. Rizk, M. Nagrial, and A. Hellany, "Designing Highly Efficient Synchronous Reluctance Machines," in International Conference on Electrical Engineering Research and Practice (ICEERP2019) Sydney, Australia, TBC 2019: IEEE, p. TBC.

1.8 Organisation of the Thesis

The thesis begins with review of existing literature and recognising contribution to the development of SynRM. The thesis focuses on analytical model and FEM simulation of SynRM. A new optimisation approach is utilised for single-objective and multi-objective optimisation. The study also investigates the torque ripples of the machine. Then PMSynRM is analytically modelled and simulated in the same FEM environment and optimised with specially developed optimisation topologies. Finally, both SynRM and PMSynRM are experimentally verified using ten different prototypes exclusively fabricated for this study to back up the simulation results.

Chapter 02: This chapter concentrates on the analytical modelling of synchronous reluctance machines. A detailed and complete phasor diagram is developed, and machine parameters are defined and theoretically investigated. Various machine parameters are analytically studied, and saturation of this machine is demonstrated. The machine's non-linear magnetic circuit is also investigated in details. Moreover, electrical steel material with high anisotropy is discussed for high saliency ratio.

Chapter 03: This chapter investigates critical machine performances in a simulation environment using finite element method. The chapter starts with proposing an advanced meshing technique for rotating electrical machines and then analyses the optimum flux guide to yield maximum performance. The SynRM with multi-barrier is defined using the newly found barrier type, and numerous simulations are performed to investigate machine operational characteristics. The chapter investigates a method to use saturation and cross-saturation to improve the machine saliency.

Chapter 04: This chapter focuses on optimisation techniques for SynRM. Single and multi-objective optimisation algorithms have been discussed, and an advanced optimisation topology is developed for a generic SynRM optimisation. The machine is optimised using single, and multi-objective optimisation and the results are compared.

Chapter 05: Permanent magnet assisted synchronous reluctance machine is investigated both analytically and by simulation. The chapter reviews the rare-earth permanent magnets and their properties. The analytical model and the phasor diagram of the machine is presented. Further, two optimisation categories are studied one is optimising PMs in an already optimised SynRM, and the second one is optimising PMSynRM. The chapter also investigates the torque, power factor and efficiency of the machine.

Chapter 06: This chapter focuses on experimental verification of both synchronous reluctance and permanent magnet assisted reluctance machines. A newly designed test system is used for this study. Ten prototypes have been fabricated, six of them are SynRM, two for PMSynRM investigation, and the last two are for torque ripple studies. Thus, comparison of the FEM simulation can be verified and validated. The experimental results of SynRM and PMSynRM are presented and compared with FEM results. Moreover, the torque ripple investigation is also experimentally verified, and the simulation results are backed up by the test results.

Chapter 07: This chapter concludes the research and the findings of the thesis. It also lists recommendation for future works.

Part I: Synchronous Reluctance Machines

2 SYNCHRONOUS RELUCTANCE MACHINES

2.1 Introduction

This chapter presents the basic principles of SynRM and defines its operating characteristics. The SynRM studied in this thesis is a 3ph balanced system unless otherwise mentioned. Thus, the sum of the vector currents and voltages are zero. Hence, two magnetic axes in the DQ reference frame system is adequate to define the SynRM operating principle. Simplified SynRM characteristics are presented using the park's transformation in the DQ reference frame, and it is extended for analytically modelling the machine performances. SynRM is, in principle, a salient pole machine due to the differences in reluctance between D and Q axes. It can be described via a simplified reluctance theory. Let us consider a single salient pole rotor placed inside the magnetised core rotates around a pivot, as shown in Figure 2-1(a). When the rotor is rotated by some angle, as shown in Figure 2-1(b), the rotor will experience a torque towards the indicated direction as its conservation of energy state is disturbed.

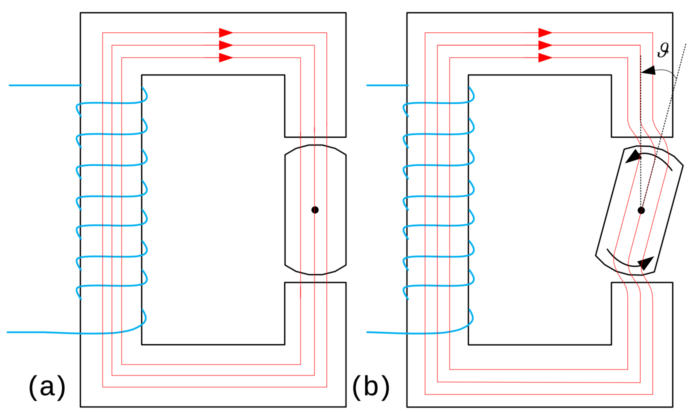

Figure 2-1: Basic single-phase magnetised stator and a single salient pole rotor depicting reluctance theory

$$\varphi = \frac{mmf}{R_{total}} \tag{2.1}$$

Where $R_{total} = R_{gap} + 2R_{core}$, R_{core} - core reluctance and R_{agp} - air-gap reluctance

In order to increase the field energy, the flux line should be shorter. Thus, the flux lines reach out to make the rotor straight so that the flux lines are shorter in length. The magnetic circuit of the system is shown in Figure 2-2. The magnetic flux in the core is given in Eq. (2.1). mmf of the coil is constant, therefore to increase φ the total reluctance should be reduced to maintain the field energy. The flux develops the torque due to the conservation of energy.

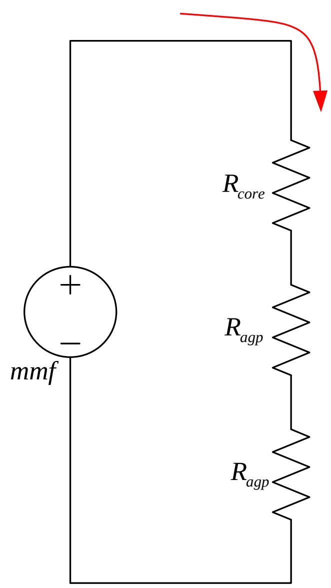

Figure 2-2: Magnetic circuit of a single salient system

2.1.1 Anisotropy structure

The design of SynRM requires an understanding of magnetic material anisotropy and its grain-oriented structure. The magnetic materials are an isotropic structure in nature, but the magnetic steel materials used as a grain-oriented structure in SynRM rotor is anisotropic. The incorporation of the anisotropy into the finite element method and software is vital in achieving precise results from its simulations. There are various topologies used for SynRM such as segmental, axially laminated, and transversally laminated structures.

In each design, the ultimate objective is to achieve high permeance along the D axis and minimise the Q axis permeance. The segmental structure is no longer considered due to construction constraints. Therefore, it is not discussed further in this study. The development of axially laminated anisotropy (page: 1-23) and transversally laminated anisotropy (page: 1-28) has been discussed. Understanding the two anisotropy structures is very crucial in understanding the non-linear magnetic circuit.

2.1.2 Axially laminated anisotropy rotors

The axially laminated structure (Figure 1-5) is one that has been considered since the late 70s but has never completely developed due to the complicated structure. Nonetheless, its high anisotropy is proven to be better than the transversally laminated structure. Besides, its inherent ability to have distributed flux barriers with minimum cross saturation (no ribs) helps to achieve better machine performance. Its saliency ratio is high in comparison to other structures. Hence, it offers excellent performance such as torque per volume, power factor and efficiency [67, 186].

Furthermore, the combination of interleaved and tiny laminated structure and optimisation technique can minimise its ripples effect better than that of TLA design. The disadvantage of the structure is that the design requires radial webs in between the flux barriers and steel segments to provide mechanical support against radial forces. The thicker the radial webs, the more mechanically stronger the rotor. However, the webs act as a flux carrier in the Q axis path and increase permeance along this axis. It increases the L_q, resulting in reduced saliency ratio and hence, performance.

2.1.3 Transversally laminated anisotropy rotors

The modern machines are transversally laminated anisotropy due to their ruggedness and simple structure. By merely producing laminations, preferred segments of flux guides and barriers are achieved via this anisotropy design, as shown in Figure 1-9. The required segments are achieved by introducing radial webs and tangential ribs that also provide a mechanical connection between each flux carrier. The introduction of ribs and webs also adds some Q axis flux linkage. Thus, the size is vital in TLA SynRM design process. Slightly oversized ribs can significantly improve the Q axis flux linkage while the undersized ribs can reduce the mechanical integrity of the rotor. The ribs shall be designed to saturate for lower current in order to minimise flux through.

Although the ribs and webs contribute a little amount of flux linkage, it is acceptable if they are appropriately sized and optimised. The ribs help to minimise ripples. Due to the ribs, the rotor is completed with circumference layer that minimises fluctuation of flux in air-gap. TLA structure offers saliency ratio of above 10 for multi-barrier designs when the number of poles is less than 6. The two structures differ in terms of machine performance, only by the ability to produce the right shape and size of barriers and flux carriers. Other than its anisotropy structure, they are similar in terms of machine characteristics.

2.2 SynRM Basic Operating Principles

In typical caged induction machine, the stator mmf induces the current in the rotor cage. The induced current produces rotor mmf that revolves with a slip in asynchronous with the stator mmf. The machine's air-gap mmf is the resultant of both stator and rotor mmf which is responsible for developing electromagnetic torque in IM. However, unlike IM, the SynRM torque is produced purely by differences in reluctance in the rotor geometry. It employs the same stator, but the rotor is a reluctance rotor with neither cage nor coils. Therefore, there is no rotor mmf, and the only mmf is by the stator. The D axis has high permeance, and the flux linkage via the air-gap finds a passage through this axis and the rotor with rotating magnetic flux. Thus, the machine is in synchronism with the stator mmf. The permeance and inductance of SynRM are further explained in detail in section 2.2.1.

As demonstrated in section 2.1, the rotor is locked into stator mmf at no-load condition. When the machine is loading, the rotor is dragged from its low energy state. In order to overcome the rotor, drag and to minimise field energy, the torque is produced in the system. The magnetising current i_q is developed to counteract against the drag. The magnitude of i_q depends on the load. The magnitude of i_q is 0 at no-load condition. The following section discusses 3ph to DQ transformation especially in SynRM. The three-phase sinusoidally distributed stator is typically converted to the reference frame for simplification called D and Q frame using Park's transformation. The system is transformed from 3ph to $\alpha\beta$ coordinate first and then it is converted to DQ frame for simplified analyses. A single salient pole, shown in Figure 2-3, is selected for the analysis. The electrical reference angle between α and DQ frame is ϑ. The rotating speed with respect to a reference angle can be derived as given in Eq. (2.2).

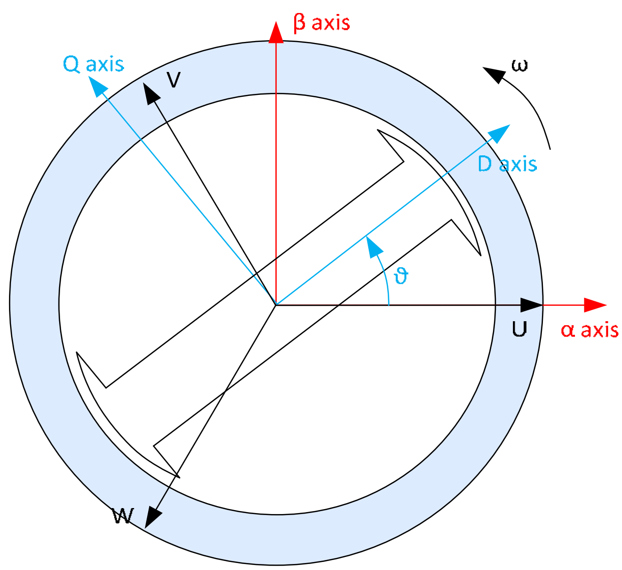

Figure 2-3: Simplified single salient pole system with 3ph $\alpha\beta$ and DQ frame is shown

$$\frac{d\vartheta}{dt} = \omega_e \tag{2.2}$$

The sinusoidally distributed 3ph system is given by Eq. (2.3) and (2.4).

$$\begin{bmatrix} i_a \\ i_b \\ i_c \end{bmatrix} = i_m \begin{bmatrix} \cos(\omega t) \\ \cos(\omega t - \frac{2\pi}{3}) \\ \cos(\omega t + \frac{2\pi}{3}) \end{bmatrix} \tag{2.3}$$

$$\begin{bmatrix} v_a \\ v_b \\ v_c \end{bmatrix} = v_m \begin{bmatrix} \cos(\omega t) \\ \cos(\omega t - \frac{2\pi}{3}) \\ \cos(\omega t + \frac{2\pi}{3}) \end{bmatrix} \tag{2.4}$$

The DQ and zero conversion of SynRM after removing rotor coils from Park's transformation is given in Eq. (2.5) to (2.7). A balance 3ph system is considered for the conversion. Therefore, zero term will be 0 and ignored in the conversion.

$$\begin{aligned} i_d &= \frac{2}{3}[i_a \cos(\omega t) + i_b \cos(\omega t - \frac{2\pi}{3}) + i_c \cos(\omega t + \frac{2\pi}{3})] \\ i_q &= \frac{2}{3}[i_a \sin(\omega t) + i_b \sin(\omega t - \frac{2\pi}{3}) + i_c \sin(\omega t + \frac{2\pi}{3})] \end{aligned} \tag{2.5}$$

$$\begin{aligned} v_d &= \frac{2}{3}[v_a \cos(\omega t) + v_b \cos(\omega t - \frac{2\pi}{3}) + v_c \cos(\omega t + \frac{2\pi}{3})] \\ v_q &= \frac{2}{3}[v_a \sin(\omega t) + v_b \sin(\omega t - \frac{2\pi}{3}) + v_c \sin(\omega t + \frac{2\pi}{3})] \end{aligned} \tag{2.6}$$

$$\lambda_d = \frac{2}{3}[\lambda_a \cos(\theta_T) + \lambda_b \cos(\theta_T - \frac{2\pi}{3}) + \lambda_c \cos(\theta_T + \frac{2\pi}{3})]$$
$$\lambda_q = \frac{2}{3}[\lambda_a \sin(\theta_T) + \lambda_b \sin(\theta_T - \frac{2\pi}{3}) + \lambda_c \sin(\theta_T + \frac{2\pi}{3})] \quad (2.7)$$

Where; $\theta_T = \alpha_i + \omega t$

2.2.1 Direct and Quadrature axis inductances and saliency

In order to improve the effectiveness of the reluctance concept, SynRM is designed to have high permeance along the D axis to allow magnetic flux passage while it should be opposite for Q axis. In other words, the reluctance of the D axis shall be reduced as low as possible. On the other hand, the flux linkage path of all other magnetic axes shall be obstructed. SynRM has only two magnetic axes, as shown in Figure 1-18. The reluctance in the Q axis must be reduced to as low as possible. It will increase the D axis inductance L_d and reduce L_q. Hybrid barrier structure in TLA rotor provides the required machine specification but only if it is properly designed. An increasing number of barriers will increase the insulation ratio of pole space and hence, increase the saliency ratio. However, the higher number of barriers will not help to achieve high machine performance, discussed in detail in the subsequent sections.

The inductances are derivative of flux linkage with respect to its current and given in Eq. (2.8). Because the inductances are a function of DQ currents, the saliency ratio can be written as a function of currents as in Eq. (2.9). Thus, the saliency ratio is a current dependent and affected by saturation and cross saturation.

$$L_d = \frac{d\lambda_d}{di_d}$$
$$L_q = \frac{d\lambda_q}{di_q} \quad (2.8)$$

$$\xi\left(i_d, i_q\right) = \frac{L_d\left(i_d, i_q\right)}{L_q\left(i_d, i_q\right)} \tag{2.9}$$

The primary parameter of SynRM that define the machine performance is its saliency ratio or the differences in the inductances. The power factor of SynRM is proportional to the saliency ratio, and the torque is a function of the difference in inductance as given in Eq. (1.7). Thus, the saliency ratio becomes a primary design parameter in SynRM. The higher saliency ratio will increase the differences in inductance, consequently machine power factor and torque. The low-speed control and sensor-less control techniques are possible in a SynRM with high saliency by tracking the stator current at low and high-speed regions [187].

2.2.2 Saliency comparison of electrical machines

Magnetic saliency produces reluctance torque in SynRM. On the other hand, PM machines have just magnetic torque where the saliency is not a significant parameter. A surface-mounted PM machine (Figure 2-4(a)) does not generate magnetic saliency. Its saliency is $\xi \cong 1$ (where $L_d \cong L_q$). The SPM does not have a barrier arrangement to obstruct the flux path in the Q axis. Therefore, the flux in this direction does not have to cross any barrier that causes higher L_q. Whereas, the D axis has incremental permeability towards the air-gap resulting in reduced L_d that leads to a non-magnetic salient rotor.

On the other hand, a SynRM that employs hybrid barriers, as shown in Figure 2-4(f) creates a distinguished flux path between D and Q axes. The self-explained name barrier, act to stop flux in the Q axis resulted in the different magnetic circuit within the two magnetic axes. The higher number of barriers increase the effectiveness of the generated magnetic saliency. SynRM can generate saliency ratio of above 10 to achieve high performance if the barriers are optimised. The other machines shown between those two extreme ends are PM machines (Figure 2-4(b-e)) and does not require high saliency as they are designed to have PM magnetic flux to develop torque.

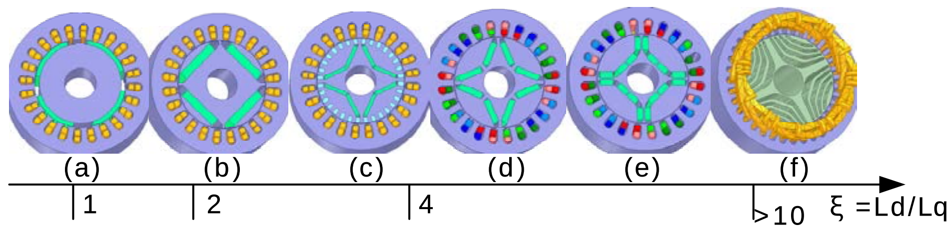

Figure 2-4: Saliency comparison of PM and SynRM

2.3 Non-Linear Magnetic Circuit of SynRM Rotor

A non-linear magnetic circuit of SynRM problem is simplified for an intuitive understanding. As explained earlier, the sinusoidally excited stator magnetic flux passes through the air-gap into the rotor via two magnetic axes, as shown in Figure 2-5. A single barrier SynRM is shown in the figure. The magnetic source for D and Q axes is shown as two separate stator components for better understanding, where the D axis source has the dominant magnetic flux, and the Q source also has undesirable flux which limits the saliency. The lines through the internal and external of barrier belong to the D axis, and the red flux lines are depicted as Q axis flux linkage. If the Q source is eliminated, the machine saliency will be infinity. However, it is impossible due to the rotor structure that is shown in Figure 2-5. However, the saliency can be increased by minimising the unwanted Q source by properly designing the rotor to reduce flux in the Q axis.

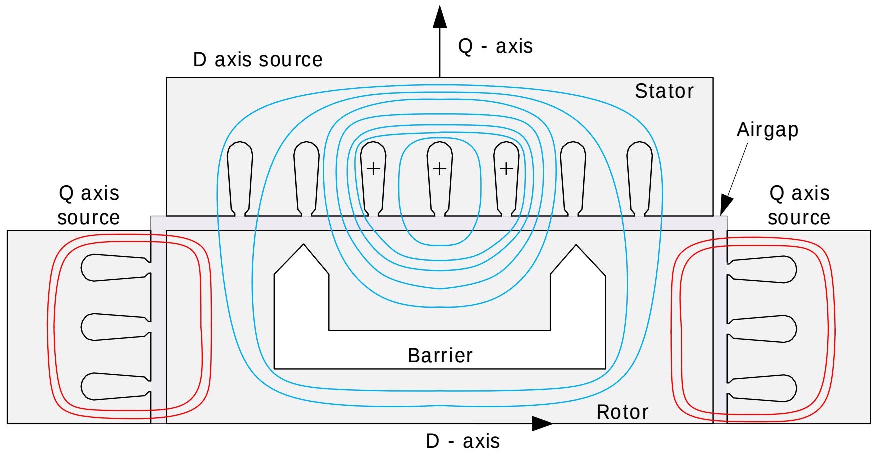

Figure 2-5: A simplified flux linkage path in D&Q frame of a SynRM with a single barrier

The design procedure to enhance saliency ratio should follow two directions, one is increasing the D axis flux linkage, and the other is minimising the Q axis flux. The field strength is high when the length of the flux line is shorter. As can be seen in Figure 2-5, the flux is high in the internal section of the barrier. Thus, having high iron segments along the circumference of the D axis is vital. The stator and rotor are magnetic steel with low reluctance material in comparison to the air-gap. As shown in Figure 2-2, the magnetic flux passes through from stator to rotor via the air-gap and back to the stator. Thus, the length of the air-gap must be reduced to as low as practically possible.

The current manufacturing technology can produce 0.01 mm tolerance. It ensures the integrity of the rotating part during high-speed rotation. However, at high speed, the mechanical components experience temperature rise resulting in some form of deformation. It is not a major issue in SynRM, and it does not produce much temperature as IMs due to the absence of rotor coils. Q axis flux can be minimised but requires a bit of effort. The most popular method is to have multiple barriers. From the above non-linear model, we can develop the equivalent circuit of SynRM.

2.4 SynRM Equivalent Circuit

There are no field excitation winding presents in the SynRM. The flux harmonics due to sinusoidally distributed stator winding adds an additional component to the stator leakage inductance. Since the SynRM is another synchronous reluctance machine without field winding and damper circuits, an equivalent circuit of SynRM can be obtained based on conventional machine analysis, as shown in Figure 2-6.

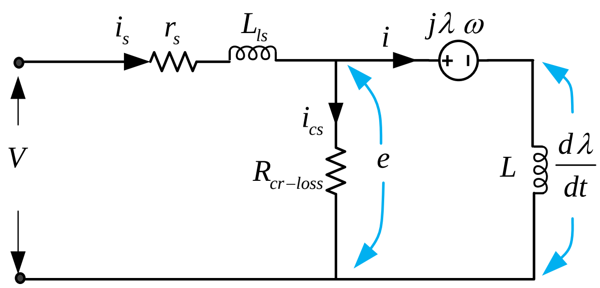

Figure 2-6: Per phase steady-state phasor of an equivalent circuit of SynRM

Based on the steady-state condition shown in Figure 2-6 of a SynRM, the vector equations can be written as given in Eq. (2.10) and (2.11). Similarly, the stator per phase terminal current can be given as in Eq. (2.12).

$$V = e + r_s i_s + j\omega L_{sl} i_s \tag{2.10}$$

$$e = \frac{d\lambda}{dt} + j\omega\bullet\lambda \tag{2.11}$$

$$i_s = i + i_c \tag{2.12}$$

Where V is per phase terminal voltage, ω is angular speed in the DQ frame and e is the back electromotive force (back emf).

Similarly, D and Q axes equivalent circuit can be obtained using the DQ frame at steady-state, as shown in Figure 2-7, where M_d and M_q are mutual inductance in the DQ frame and given in Eq. (2.13). The DQ voltage vectors comprise heat loss term $i_{dq}r_s$, and energy storage components in the form of $L_{dq}\left(di_{dq}/dt\right)+M_{dq}\left(di_{dq}/dt\right)$, and outputs $\left(\partial\lambda_{dq}/\partial\theta\right)\omega+\lambda_{dq}\omega$ [188].

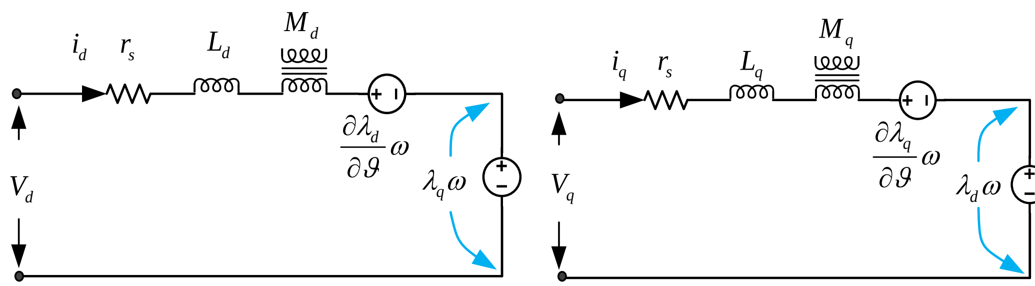

Figure 2-7: D and Q steady-state equivalent circuits

$$M_d = \left.\frac{\partial\lambda_d}{\partial i_q}\right|_{i_d=const}$$
$$M_q = \left.\frac{\partial\lambda_q}{\partial i_d}\right|_{i_q=const} \tag{2.13}$$

If the stator slotting effects are ignored in a modern SynRM machine with the round rotor (*i.e.* notch or grooves are not present in the rotor circumference), it can be assumed that there is no variance in the D and Q flux linkages. Hence, the terms $\left(\partial\lambda_{dq}/\partial\theta\right)\omega$ can be ignored. Thus, the final DQ steady-state equivalent circuit can be simplified, as shown in Figure 2-8.

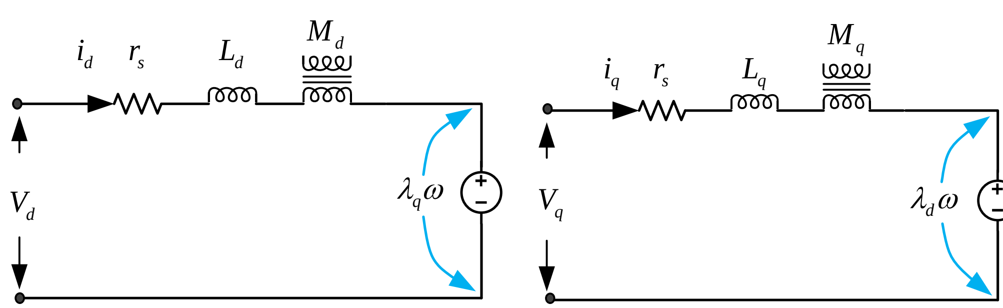

Figure 2-8: Simplified D and Q axes steady-state equivalent circuits

The per-phase terminal voltage and current of DQ vectors can be derived as given in Eq. (2.14) and (2.15). Using the simplified equivalent circuit in Figure 2-8 the D and Q axes voltage vectors can be derived as given in Eq. (2.16) and (2.17).

$$V_s = v_d + jv_q \tag{2.14}$$

$$I_s = i_d + ji_q \tag{2.15}$$

$$v_d = r_s i_d + L_d \frac{di_d}{dt} + M_d \frac{di_q}{dt} + \lambda_q \omega \tag{2.16}$$

$$v_q = r_s i_q + L_q \frac{di_q}{dt} + M_q \frac{di_d}{dt} + \lambda_d \omega \tag{2.17}$$

2.4.1 Phasor diagram of SynRM

From the above analogy, the phasor diagram of the SynRM can be obtained, as shown in Figure 2-9 where the core loss is ignored for the time being. SynRM is well known for poor power factor where the voltage vector significantly leads the current vector (by φ) as shown in the figure. The current vector I_s and voltage vector V_s are obtained from Eq. (2.14) and (2.15). The flux vector $\lambda_s$in the DQ frame is obtained using the sum of $L_d i_d$ and $L_q i_q$. The λ_s is generated by sinusoidally distributed field. Thus, the flux linkage is rotating with ω at sinusoidal distribution. If the rotor is dragged out of the conservation of energy state (a state it is aligned with the rotating field), the torque will be developed to minimise the dragged angle ϑ. The torque will act accordingly to minimise $\vartheta \to 0$ as discussed in section 2.1.

Therefore, the angle dragged out from the D axis is called the load angle, which is often confused with the current angle. In order to convert the electrical energy into mechanical energy, the angle should be kept non-zero. On the other hand, the current is responsible for magnetisation and torque generation. Thus, it becomes a control objective in SynRM controllers. The current (θ), load (ϑ) and torque (γ) angles are related by Eq. (2.18). The magnetic reactance in D and Q axes are given in Eq. (2.19).

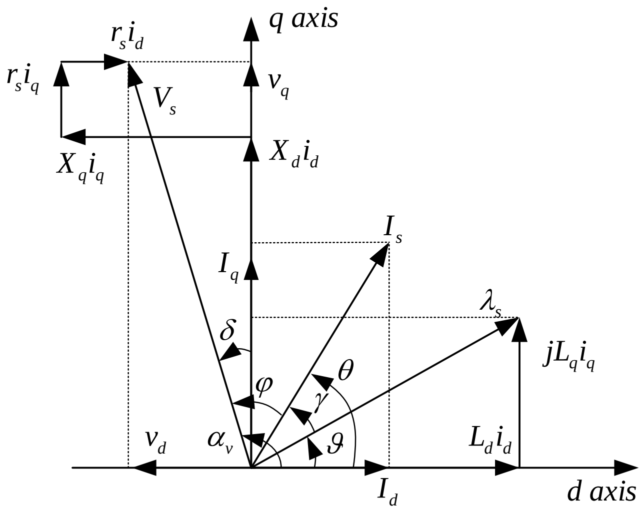

Figure 2-9: Phasor diagram of SynRM in DQ frame

$$\theta = \vartheta + \gamma \tag{2.18}$$

$$\begin{aligned} X_d &= j\lambda_d \omega \\ X_q &= j\lambda_q \omega \end{aligned} \tag{2.19}$$

$$\begin{aligned} v_d &= -V_s \sin(\delta) \\ v_q &= V_s \cos(\delta) \end{aligned} \tag{2.20}$$

$$\begin{aligned} I_d &= I_s \cos\theta \\ I_d &= \frac{V_s\left(X_q \cos\delta - R_s \sin\delta\right)}{R_s^2 + X_d X_q} \end{aligned} \tag{2.21}$$

$$I_q = I_s \sin\theta$$
$$I_q = \frac{V_s\left(R_s \cos\delta + X_d \sin\delta\right)}{R_s^2 + X_d X_q} \tag{2.22}$$

The induced electromotive voltage is given in Eq. (2.23). Using Eq. (2.8) and (2.23), the electromotive voltage can be further simplified to Eq. (2.24). The magnitude of flux linkage space vector can be derived as Eq. (2.25). However, if the cross saturation is considered in the analytical model, the DQ flux linkage becomes as in Eq. (2.26).

$$e = j\omega\lambda_s = j\omega\left(\lambda_d + j\lambda_q\right) \tag{2.23}$$

$$e = -\omega L_q.i_q + j\omega L_d i_d.i_q \tag{2.24}$$

$$\lambda_s = L_s i_s = \begin{bmatrix} L_d & 0 \\ 0 & L_q \end{bmatrix} i_{dq} \tag{2.25}$$

$$\lambda_{dq} = \begin{bmatrix} L_d & L_{dq} \\ L_{dq} & L_q \end{bmatrix} i_{dq} = \frac{L_d + L_q}{2} i_{dq} + \left(\frac{L_d - L_q}{2} + jL_{dq}\right) i_{dq}^{\bullet} \tag{2.26}$$

Where $i_{dq}^{\bullet}$ is complex conjugate with respect to the reference frame

2.5 Machine Performance Parameters

The quality of any electrical machine is determined by its machine performance parameters. The two key performance parameters of AC conventional machines are torque and power factor. Due to its saliency, the SynRM's torque ripples can be an additional performance parameter. Therefore, the three parameters are used to determine the functionality of a SynRM and PMSynRM. The importance of the three parameters is discussed in the subsequent section. The efficiency is the other highly important parameter as the ultimate goal of this study is to design a highly efficient machine.

2.5.1 Torque

The earlier SynRM had low torque density at starting. In order to tackle this drawback, a rotor cage was introduced to overcome the starting torque issue. However, it is no longer an issue in SynRM with modern controllers. The advances in power electronic controllers allow the designers to overcome the starting torque issue. The removal of the cage not only enhanced the efficiency of a machine due to the absence of rotor resistance but, also reduced rotor/shaft temperature. It results in a smaller cooling fan and higher reliability of the machine. SynRM has higher overload capacity almost three times its rated load in comparison to an IM [12, 187]. By means of elimination and reduction to vector form, the torque equation of SynRM can be readily obtained to a scaler version by applying the principle of arbitrary displacement to Eq. (1.1). The equation ignored slotting effects on the rotor inner surface and saturation on the core, for a three-phase machine $n = 3$, results in Eq. (2.27). For the steady-state condition, the torque can be approximated using the phasor diagram in Figure 2-9 to Eq. (2.28).

The torque can be derived using Eq. (1.4), (1.5) and (2.27) to (2.29). The SynRM machine torque changes as the square of the volts per Hz with the sine of twice the torque angle. Therefore, in theory, the maximum torque shall be reached at torque angle $45°$. The theoretical torque of SynRM is plotted as a function of torque angle in Figure 2-10 for variable voltage. The theoretical derivation does not include slotting effects, saturation, and cross-coupling effects into consideration. The practical torque and torque angle relationship is studied in detail in section 3. It can be further derived in terms of DQ inductances as given in Eq. (2.30) where the torque is related to the difference in inductances and torque angle ϑ.

Because the leakage inductance is isotropic, it does not add to the torque term. Therefore, the torque calculation considers only the magnetic inductance of the DQ frame. On the other hand, the power factor includes the leakage inductance, which is discussed in section 2.5.2. This is the primary reason why the current angle of the maximum torque (MTPA) and power factor is not the same. The differences in DQ flux and magnetising flux linkages are shown in vector space in Figure 2-11. As can be seen, the magnetising flux linkage (also inductance) is slightly smaller than the DQ flux linkage.

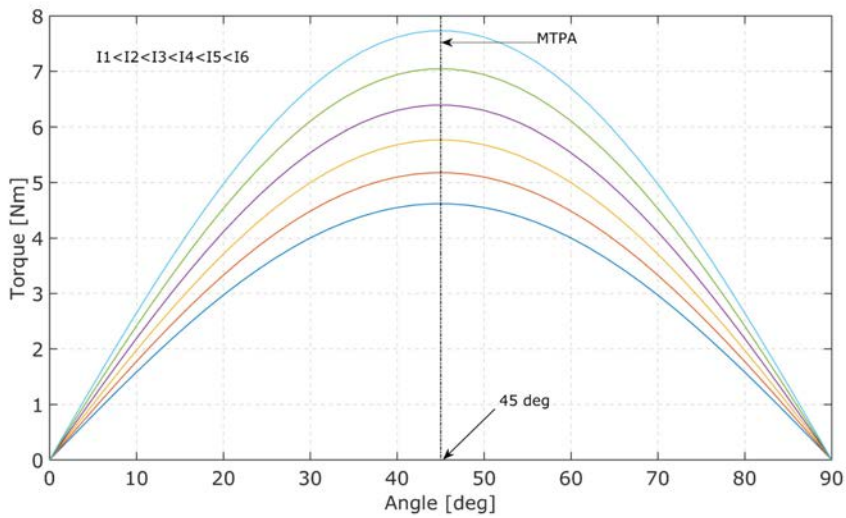

Figure 2-10: Torque as a function of load angle in the analytical model (assumptions)

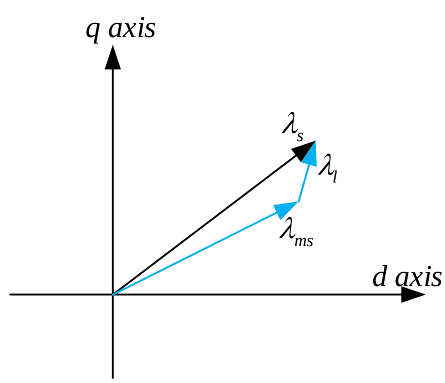

Figure 2-11: DQ flux linkage and magnetising flux linkage

$$T = \left(\frac{3}{2}\right)\left(\frac{p}{2}\right)\left(\lambda_{md} i_q - \lambda_{mq} i_d\right) \tag{2.27}$$

$$T_{SynRM} = \frac{3}{2}\frac{p}{2}\left(\frac{L_{md} - L_{mq}}{L_{md}L_{mq}}\right)\frac{V_d}{\omega}\frac{V_q}{\omega} \tag{2.28}$$

$$T_{SynRM} = \frac{3}{2}\frac{p}{2}\left(\frac{1}{L_{mq}} - \frac{1}{L_{md}}\right)\left(\frac{V_s}{\omega}\right)^2 \frac{\sin(2\vartheta)}{2} \tag{2.29}$$

$$T_{SynRM} = \frac{3}{2}\frac{p}{2}\left(L_{md} - L_{mq}\right) I^2 \sin(2\theta) \tag{2.30}$$

As most of the SynRM, as well as PMSynRM, are controlled by current controlled methods, Eq. (2.30) is very important. The torque can also be directly related by DQ currents as given in Eq. (2.31)

$$T_{SynRM} = \frac{3}{2}\frac{p}{2}\left(1 - \frac{L_{mq}}{L_{md}}\right) L_{md} i_d i_q \tag{2.31}$$

Theoretical characteristics that neglect the stator slotting effect and radial webs and tangential ribs of SynRM torque is plotted in Figure 2-10. In this case, the MTPA trajectory follows the current angle of $45°$ for change in currents. However, a realistic SynRM rotor carries slots in the inner circumference that causes reluctance fluctuation, saturation and its ribs and webs cause cross-saturation due to the magnetic potential difference on the rotating flux path. In a practical machine, the saturation and cross saturation together drift the MTPA trajectory to a higher angle than $45°$ depending on the level of saturation. The impact of saturation is further discussed in detail in section 3.7.

2.5.2 The power factor of SynRM

SynRM generally has poor pf. Thus, it requires greater attention in the study of SynRM, which was even acknowledged by Kostko more than a century ago [5]. The way forward, to optimise the pf, is increasing its saliency ratio. The power factor of the machine simply can be obtained from the phasor diagram as given in Eq. (2.32):

$$pf = \cos(\varphi) \tag{2.32}$$

From the phasor diagram, it can be simplified as given in Eq. (2.33) by neglecting the stator resistance. Unlike torque, the power factor is calculated using L_d and L_q that includes the leakage inductance.

$$\cos(\varphi) = \frac{v_q \sin(\theta) - v_d \cos(\theta)}{\sqrt{v_d^2 + v_q^2}} \tag{2.33}$$

By substituting (2.20) and (2.21), and further simplification, the pf equation can be expressed as (2.34) and simplified as Eq. (2.35). The power factor is plotted against the current angle in Figure 2-12. As can be seen, the maximum pf is drifted from equivalent torque locus due to the leakage inductance. For a unity saliency ratio, the power factor is zero, as noted in the figure. Then the pf increases with the saliency ratio.

$$\cos(\varphi) = \frac{(L_d - L_q)\sin\theta\cos\theta}{\sqrt{(L_d\cos\theta)^2 + (L_q\sin\theta)^2}} \tag{2.34}$$

$$\cos(\varphi) = \frac{(L_d - L_q)}{L_q}\sqrt{\frac{\sin(2\theta)}{2(\tan\theta + \xi^2\cot\theta)}} \tag{2.35}$$

$$\cos(\varphi) = \frac{\left(\frac{L_d}{L_q} - 1\right)}{\sqrt{\left(\frac{L_d}{L_q}\right)^2 (\sin\theta)^{-2} + (\cos\theta)^{-2}}} \tag{2.36}$$

In theory, the saliency of above 9 is required to achieve pf of 0.8 at the current angle of around 75° and 19 for pf of 0.9 at around 78°. Almost above 10 or more saliency ratio is needed to lift the pf from 0.8 to 0.9 that explains the difficulty of achieving a reasonably high saliency ratio in this machine.

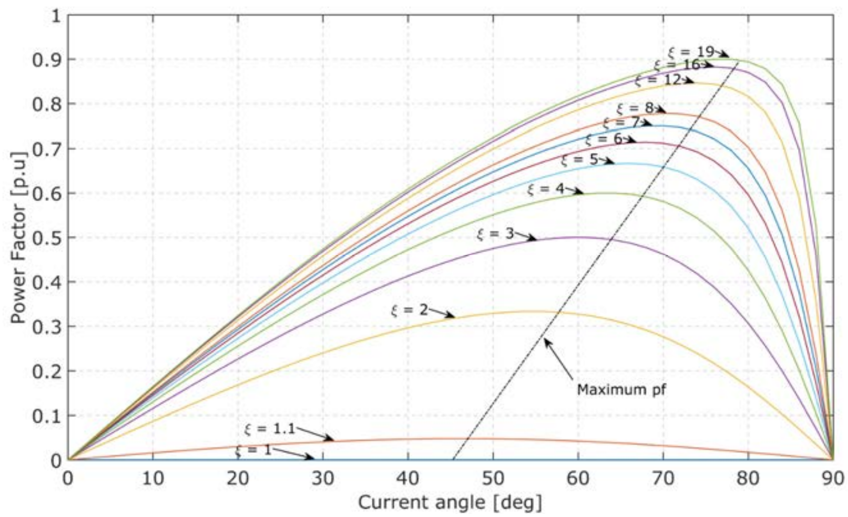

Figure 2-12: Power factor of SynRM with changing saliency.

An increased pf will help to understand the optimum operating point of SynRM. The maximum power factor can be obtained by taking a derivative of Eq. (2.35):

$$\frac{d\cos(\varphi)}{d\theta} = \frac{d\left(\frac{\left(L_d - L_q\right)}{L_q}\sqrt{\frac{\sin(2\theta)}{2\left(\tan\theta + \xi^2\cot\theta\right)}}\right)}{d\theta} = 0 \qquad (2.37)$$

It will yield the condition for maxima at:

$$\sin^2\theta = \xi\left(1 - \sin^2\theta\right) \qquad (2.38)$$

Maximum power factor is obtained for:

$$\tan\theta = \sqrt{\frac{L_d}{L_q}} \qquad (2.39)$$

By substituting Eq. (2.39) into (2.35), the maximum power factor can be obtained as in Eq. (2.40) and using the leakage inductance as in Eq. (2.41).

$$Cos(\varphi)_{\max} = \frac{\xi - 1}{\xi + 1} \tag{2.40}$$

$$Cos(\varphi)_{\max} = \frac{L_d - L_q}{L_d + L_q} = \frac{L_{md} - L_{mq}}{L_{md} + L_{mq} + 2L_l} \tag{2.41}$$

The maximum pf of SynRM is plotted against the saliency ratio in Figure 2-13. The power factor analysis matches the above analysis where it requires saliency ratio of 9 to obtain 0.8 pf and 19 to obtain pf of 0.9 for a maximum saliency ratio operation. Moreover, it requires infinity saliency ratio for a unity power factor. In theory, a power factor of 0.9 seems possible. However, in reality, such a high-power factor for a small power SynRM is impossible without affecting other machine performance parameters. The only way to achieve high power factor in this machine is by going hybrid, which is discussed in section 5.

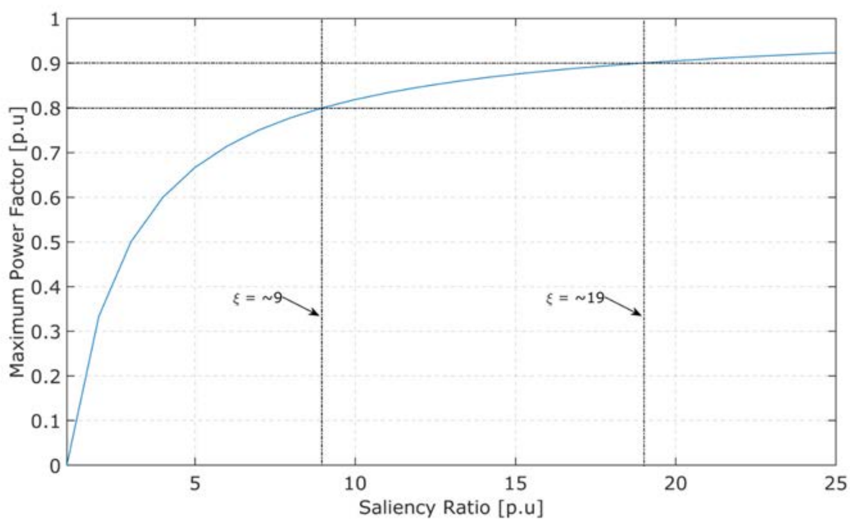

Figure 2-13: Maximum factor with saliency ratio

Figure 2-14 shows the DQ current and voltage changes with respect to the current angle in a practical SynRM. The maximum power factor trajectory is marked by a blue line. As can be seen from the figure, the current controller for SynRM is much easier compared to a voltage controller. The voltage changes are non-linear and change with designs, but the current changes are not affected by design types. Further, the maximum pf is obtained for higher D current, as shown in Figure 2-14.

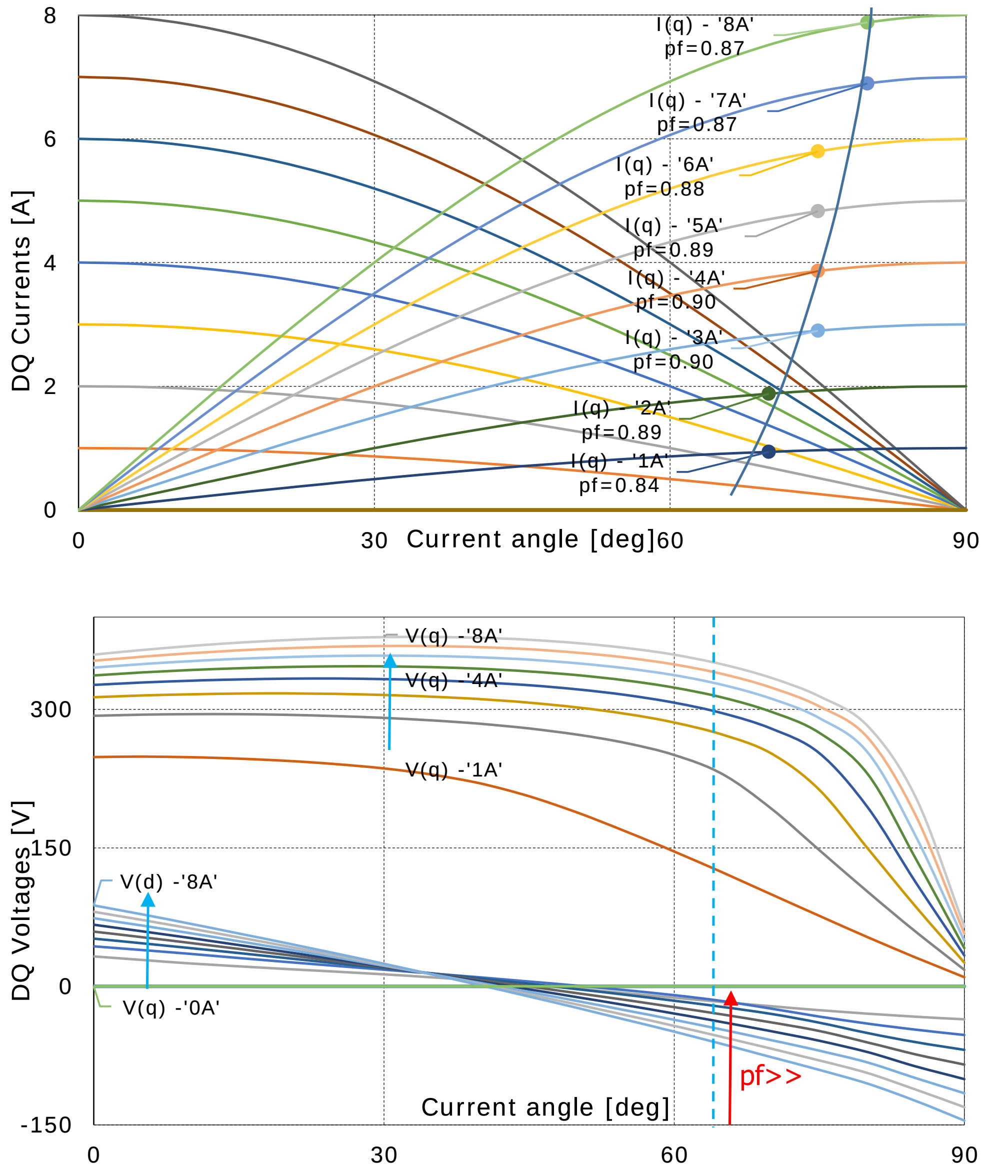

Figure 2-14: DQ current and voltage characteristic with respect to the current angle in a SynRM

The control of SynRM should be performed in such a way that increases the current angle to enhance the pf by controlling the D axis current. The analytical study has shown that SynRM's power factor can be improved by different means such as improving the saliency ratio above 9 and controlling the machine at a specific operating region. The results are further investigated with FEM, and experimental results are presented in the subsequent chapters.

2.5.3 Power and Efficiency

The instantaneous input power of SynRM into the terminal can be defined by (2.43) like any other conventional electrical machine.

$$P_{in} = \frac{3}{2}\left(v_d i_d + v_q i_q\right) \tag{2.42}$$

By substituting Eq. (2.20), (2.21) and (2.22) into (2.43) will yield:

$$P_{in} = \frac{3}{2}V_s^2 \frac{\left[R_s + \left(X_d - X\right)\frac{\sin 2\delta}{2}\right]}{R_s^2 + X_d X_q} \tag{2.43}$$

R_s is relatively small compared with $X_d$and X_q therefore, the power equation can be further simplified to Eq. (2.44). However, it should be noted that when $R_s = 0$ the electrical power equals the mechanical power out of the machine which is in Eq.

$$P_{in} = \frac{3}{2}V_s^2 \frac{\left(X_d - X\right)}{X_d X_q}\frac{\sin 2\delta}{2} \tag{2.44}$$

$$P_{mch} = \frac{2}{p}\omega T \tag{2.45}$$

The output power can be obtained as Eq. (2.46).

$$P_{out} = \frac{3}{2} V_s \, I \ \cos(\varphi) \tag{2.46}$$

At maximum pf condition, the output power will be:

$$P_{in(\max)} = \frac{3}{2} V_s I_s \frac{(L_d - L_q)}{(L_d + L_q)} \tag{2.47}$$

The efficiency of the machine can be defined by Eq. (2.48). Alternatively, it can be given in more details as in Eq. (2.49)

$$\eta = \frac{P_{out}}{P_{in}} \times 100 \quad (\%) \tag{2.48}$$

$$\eta = \frac{P_{out}}{P_{out} + W_{Tlosses}} \times 100 \ (\%) \tag{2.49}$$

Where, $W_{Tlosses}$ is a combination of friction losses, windage losses, rotational losses, eddy current losses and leakage losses. The above analogy is implemented in FEM tool for simulation, as explained in section 3.4 and used for experimental verification in chapter 6.

2.5.4 Torque ripples

The SynRM is well known for its high torque harmonics due to its hybrid rotor structure where the air-gap flux is distorted via a series of transversally laminated flux guides. Depending on the dimensions of flux guides and its end profiles, the torque ripples can almost be equal to the average torque in certain designs which may severely impact the motor application. Therefore, the smoothness of the torque is inevitable in these types of machines. The causes of ripples can be attributed to various reasons. Firstly, the quality of manufacturing, especially, smooth finishing of the surface is vital for any electrical machines. The modern machining, wire cutting technology and tools should ensure the final product has good completion in order to have smooth torque characteristics. Secondly, two types of excitations are in use for conventional AC machines, either sinusoidal or trapezoidal excitation. Both excitations have their advantages and disadvantages. The conventional AC machines predominantly utilise sinusoidal excitation.

SynRM and permanent magnet synchronous machine drive's current excitation and back EMF are designed to be sinusoidal for optimised torque harmonics [126]. It requires sinusoidally distributed stator winding similar to any other AC conventional machines, as shown in Figure 2-15 where phase A current and the induced voltage is plotted as a function of time. The sinusoidal excitation is generated by current controlled inverters that need an additional system to monitor the rotor angular position using high-resolution sensors continuously. Any design issues, rotor position feedback issue or other causes can lead the supply current or back EMF to diverge from the sinusoidal waveform, thus resulting in high torque ripples. The location, dimensions, tangential and radial ribs, and profile of flux barrier(s) are the most vital part in optimising the torque harmonics.

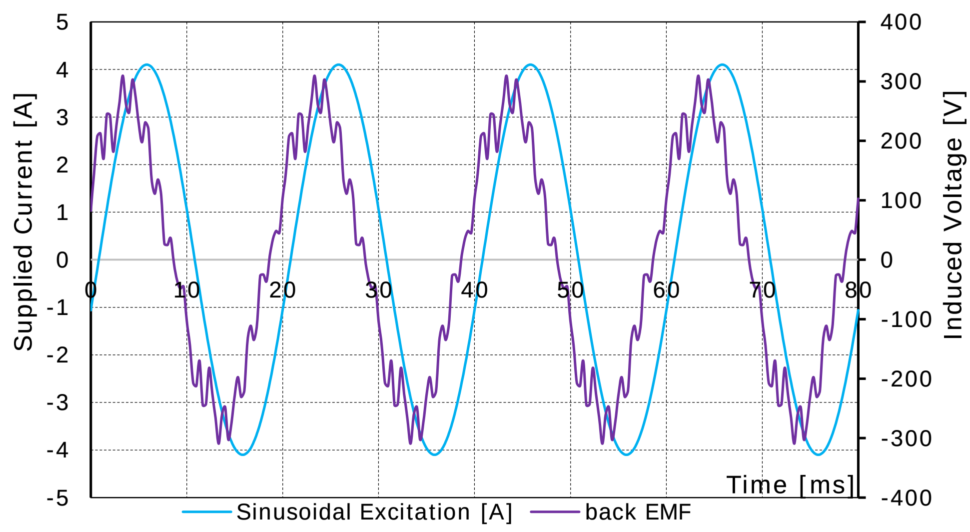

Figure 2-15: Sinusoidal excitation of phase A and induced voltage on the stator winding of a SynRM

Given that the reluctance torque is generated by transversally laminated anisotropy structure characterised with flux guides to couple itself to rotating magnetic field, optimisation of the reluctance is inevitable in this type of motors to smooth the torque production. The other factors such as dealing with higher-order torque harmonics and controller designs that change the excitation in order to adjust supply for non-ideal characteristics are also worth considering in torque smoothness [97, 99, 126, 189].

To start with, it is essential to define the torque-harmonics (or torque-pulsations) for further understanding of the minimisation techniques. When standard conditions of the motor or its controller drift, it creates the prospect to upswing unwanted torque-pulsations in the system. In SynRM it is the combination of cogging torque and torque ripples. The variation of reluctance in between stator and rotor due to angular variation causes the cogging torque. The cogging torque is independent of supply source or excitation methods instead, it is caused by the geometry of the motor structure. The number of stator slots increases the frequency of the cogging torque but reduces the magnitude. Moreover, the air-gap winding (no teeth) eliminates the cogging torque. On the other hand, the torque ripples is instigated by the interaction between stator mmf and rotor magnetic characteristics (reluctance). Therefore, an optimised sinusoidal mmf to SynRM is the basis to reduce torque ripples. However, it does not just stop with mmf, it is also vital to design the rotor magnetic reluctance path.

The analysis of cogging torque can be performed using magnetic energy model. However, the same analogy cannot be used for torque ripples analysis due to the change of the magnetic flux path and core's non-linear permeability [99]. In basic terms, the torque ripples can be defined mathematically as given in Eq. (2.50). Generally, it is either expressed as per unit value or percentage as given in equation (2.51). It can also be expressed in Nm (peak to peak) depends on the situations. However, the cause of ripples goes beyond the simple definition. Historically, the torque of the SynRM machine was derived in two methods. One was using the electromagnetic co-energy method. It is the derivation of co-energy by mechanical angle gives developed torque Eq. (2.52) and (2.53).

$$T_{ripple} = \frac{T_{\max} - T_{\min}}{T_{avg}} \tag{2.50}$$

$$T_{ripple} = \frac{\Delta T_{pp}}{T_{avg}} \times 100 \tag{2.51}$$

$$T = \left.\frac{\partial w}{\partial \vartheta_i^m}\right|_{i-const} \tag{2.52}$$

$$T = kp\lambda_{dq} i_{dq} - \frac{1}{2} i_{dq} \frac{\partial \lambda_{dq}}{\partial \vartheta_i^m} \tag{2.53}$$

The ripples components can be further expressed as in the Eq. (2.54), and substituting it into Eq. (2.27) will yield complete SynRM torque equation (2.55). However, in this case, the saturation, slotting, and cross-coupling effects aren't ignored.

$$T_{ripples} = \frac{\partial w'}{\partial \vartheta_i^m} = \frac{1}{2}\left(i_d \frac{\partial \lambda_d}{\partial \vartheta_i} + i_q \frac{\partial \lambda_q}{\partial \vartheta_i} \right) \tag{2.54}$$

$$T_{SynRM} = \frac{3}{2}\frac{p}{2}\left(\lambda_d i_q - \lambda_q i_d + \frac{1}{2}\left(i_q \frac{\partial \lambda_q}{\partial \vartheta} \omega + i_d \frac{\partial \lambda_d}{\partial \vartheta} \right) \right) \tag{2.55}$$

Even though there is a contradiction between some of the literature in evaluating ripples and cogging torque from co-energy, most of them agree with the work and validates the analytical derivation. Reference [190] recommends against the use of the co-energy method to analyse the torque ripples. It justifies that it is ineffective due to the non-linearity of permeability and high saturation in the core. In this case, the first component is the average torque, whereas the second term in (2.55) is the combination of torque ripples and cogging torque, the pulsating torque component. The second term in (2.55) attributed to the number of stator slots resulting in torque pulsation. On the other hand, the torque pulsation is expressed as in Eq. (2.56) by [87].

$$T_{pulsation} = \left(\Delta L_d + \Delta L_q\right) i_d i_q \cos(pq\vartheta) - \Delta L_{dq}\left(i_d^2 - i_q^2\right)\sin(pq\vartheta) \tag{2.56}$$

The first term in Eq. (2.56), dominated by $(\Delta L_d + \Delta L_d)$, is only present on load condition where $i_d \neq 0$ termed as torque ripples. The second term is the cogging torque, also present at the no-load condition. It is generated due to the cross term ΔL_{dq} also called magnetic interaction of D & Q axis. On the other hand, the electromagnetic torque can be derived as given in Eq. (2.54) where variation in electromagnetic co-energy in the direction of rotation is considered. The rotor barrier slots and stator slots effect create ripples in air-gap flux linkage resulting in cross inductance ΔL_{dq} as given in second torque term in Eq. (2.56). Thus, it can be safely assumed, the variation in magnetic reluctance path, due to the slotting effect, is one of the primary reasons for the torque ripples.

On the other hand, a group of researchers led by Nicola Bianchi primarily focus on evaluating torque as a function of stator electric loading and rotor magnetic potential $U_{s(\vartheta)}$ or it is also called integration of Lorentz's force [103, 144, 168, 169]. The air-gap magnetic flux density is defined as a function of rotor magnetic potential yielded by stator electric loading (2.58). The air-gap flux density distribution as a function of stator magnetic potential is given in Eq. (2.58) The instantaneous torque can be defined as the integration of stator electric loading and rotor magnetic potential Eq. (2.59) which can then be derived to Eq. (2.60). The second term in equation (2.60) is the torque pulsation caused by angular variation of the rotor. It is an effective way to determine the torque ripples. However, while defining the ripples, substantial assumptions are made to linearize the model. One of them is neglecting the slotting effects, which is one of the main causes of cogging torque. In this method, only higher-order harmonics that cause high torque ripples are considered.

$$U_{s(\vartheta s)} = \int K_s\left(\vartheta_s\right)\frac{D}{2}d\vartheta_s \tag{2.57}$$

$$B_{g(\vartheta)} = \mu_0 \frac{-U_{s(\vartheta_r)} + U_{r(\vartheta_r)}}{l_g} \tag{2.58}$$

$$T_{(\vartheta)} = K_r \int_0^{2\pi} K_s\left(\vartheta_r, \vartheta_s\right) U_r\left(\vartheta_r, \vartheta_m\right) d\vartheta_r \tag{2.59}$$

$$T_{(\vartheta)} = T_m + \Delta T_m(\vartheta_m) \tag{2.60}$$

On the other hand, the cogging torque is also directly derived using magnetic co-energy in the rotor core, which is given in equation (2.61). It can be noticed from the equation that the magnitude of the cogging torque is directly proportional to the stator teeth magnetic flux density B along the periphery of the rotor. The cogging torque is typically calculated using FEM at 0 current and very low speed in order to capture the magnetic flux against the angular variation. High cogging torque is primarily caused by the poor stator winding distribution [105, 191]. The torque ripples and cogging torque can be minimised. However, it comes with the drawback of compromising the average torque [88, 93, 106, 114, 170-172].

$$T_{cogg} = \frac{\partial\left(\frac{1}{2\mu}\left(\int_v B^2 dv\right)\right)}{\partial \vartheta_{(r)}} \tag{2.61}$$

This section analyses and discusses the traditional and modern techniques that have been used to minimise torque ripples and cogging torque. Numerous methods have been suggested in the past to minimise torque ripples for conventional electrical machines such as induction motor, most widely used technique is skewing. However, SynRM does not show much improvement when skewing is applied and discussed in details in the subsequent section. Therefore, a quest for an alternative technique is required to improve the machine's performance, especially for high-speed applications. Various techniques have been suggested for minimising SynRM's torque ripple effects such as skewing, fractional winding stator, asymmetric flux barriers, eccentric rotor design, step skewing, a high number of phases (e.g. five phases SynRM) and the optimum number of barriers. However, some techniques are not cost-effective such as step skewing, five-phase SynRM due to the manufacturing complication. This study focuses on the rotor and discusses the possibilities of torque ripples minimisation by improving rotor dimensions.

Skewing

Skewing is a technique that maintains a slight angle difference between rotor slots and stator slots transversally throughout the length not only to minimise the ripples effects but also to reduce cogging *i.e.* magnetic locking between stator teeth and rotor slots. It minimises the change in reluctance seen by the rotor flux path. Thus, the cogging torque is also minimised if skewing is employed. This technique is better suited for the transversally laminated machine, while it is difficult to make an axially laminated rotor with skew. It reduces the average torque by several percentages as the flux linkage is reduced by skewed rotor [81].

Alternatively, the stator can be skewed in the case of an axially laminated machine, but retraction of stator winding will be a challenge. This method has been successful in the case of other conventional machines such as IM and extensively implemented. References [93, 126, 148, 189] suggest that ripples can be optimised by skewing while references [173, 190] concludes that it is not feasible for SynRM. It is claimed that skewing may change the D & Q torque contribution axially. The step skewing is suggested for PM machines which is an alternative to skewing that split the rotor into a few different steps [168, 173]. In general, a well-optimised skewing reduces the reluctance experienced by rotor and high-order harmonics with little impact on average torque as well as the cogging torque.

Step skewing (also called discrete rotor skewing) is an alternative method which can reduce manufacturing cost while providing similar results [97]. Regardless of what method is employed, it is vital to design the step angle in order to achieve an optimum result as wrong skew angle may lead to high ripples and a significant reduction in average torque. Skewing not only reduce the average torque but also reduce efficiency and increase manufacturing complexity and cost. The continuous skewing is not suitable for PM assisted machine, instead step skewing can help where skewing is needed.

Asymmetrical Flux Barriers

The asymmetrical rotor design is a methodology used by researchers to modify the flux density in the air-gap by designing either irregular flux barriers or create dis-oriented barriers in each pole. It has been argued that the proper design of asymmetrical barriers can result in significant improvement in torque ripples [91, 144, 173, 192]. Asymmetrical barrier method is proposed in a few different configurations such as conventional asymmetry of barriers in each pole or individual laminations for each pole and stacked them in asymmetry quite similar to step skewing [97]. It is claimed that the ripple torque can be nullified without affecting the average torque of the machine. Though this method reports, ripples can be minimised in SynRM but failed to further influence due to the complexity in manufacturing. Further, the same design can't be simply adopted for all sizes and requires individual design and testing.

Number of Flux Barriers

The ripples reduction in a symmetrical rotor with a smaller number of barriers is challenging. Hence, the optimisation process would not significantly reduce ripples in a SynRM with fewer barriers [81]. Instead, the nature of the rotor structure with fewer barriers induces high ripples when the rotor revolves through the stator perimeter due to the asymmetrical flux path between stator and rotor. In order to tackle the issue, Vagati [81] proposed to have a certain number of rotor slots to eliminate high order harmonics in the torque. This study, coupled with FEM and experimental verification, reveals that an optimum number of barriers can lead to significantly reduced ripples in SynRM [104]. It is further discussed in section 4.8.

Segmented Rotors

The primary reason for torque ripples is the slotting effect not only in stator but also by the rotor slots. It creates air-gap flux harmony with rotation. The torque is directly proportional to the air-gap flux linkage, resulting in torque ripples. In order to minimise the air-gap flux linkage harmonics caused by rotor and stator slots, the researchers investigated the split pole rotor technique, also known as the segmented rotor [97, 98, 169].

This thesis focuses on minimising the ripples by optimising rotor parameters in order to find a solution that practically feasible and cost-effective for manufacturing. The skewing method is not discussed in this thesis as it is not a preferred practice for PM assisted design. Even though there are numerous ways to analyse the ripple effect, it is relatively impossible to evaluate or precisely estimate the torque ripples using mathematical analysis due to the non-linear magnetic circuit and cross saturation effects. Thus, the finite element method (FEM) should be utilised in order to simulate, analyse, verify, correct, and justify ripples effect. However, there are a number of factors to be considered to optimise the design. These will be discussed in section 4.8

2.6 Impact of Saturation on SynRM

Magnetic saturation in an electrical machine is a common phenomenon, and SynRM rotor is not an exception. The very nature of the SynRM with flux barriers, steel segments, tangential ribs and radial webs make it more vulnerable to saturation. The saturation of the rotor iron, especially the ribs and webs, are the limiting factors of this motor. As the current increases, the magnetic field in the rotor segments increases. At lower currents, the rate of change of the magnetic field is proportional to the current, but the rotor core eventually gets saturated with the field. The point where the saturation begins is called the working point, as shown in Figure 2-16. Beyond this point, it is harder to increase the strength of the field, so it draws more currents to increase the field. The machine shall be designed to operate below the saturation point. If the machine is pushed into the saturation region, as shown in Figure 2-16, it will draw larger magnetising current consequently higher i^2r. It will not only result in efficiency drop but also results in heating issues causing mechanical damage to the machine.

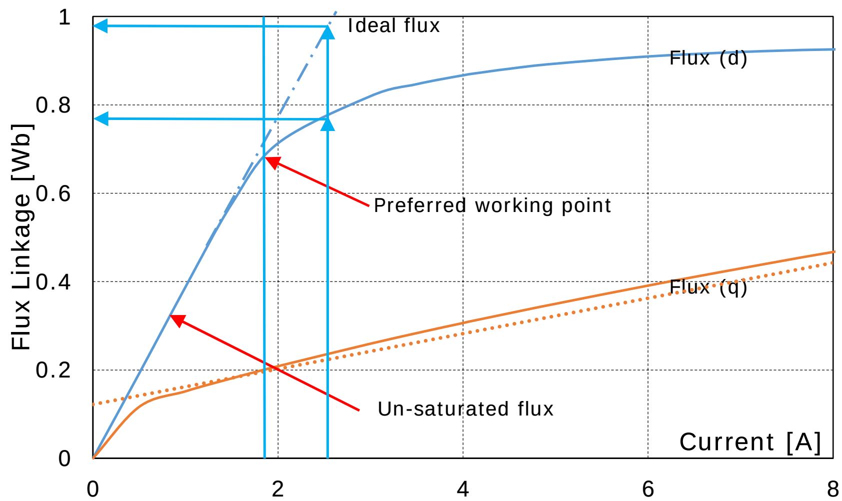

Figure 2-16: Field saturation in a SynRM obtained from a FEM simulation

In an electrical machine, the voltage, frequency, and flux are interrelated. If anyone of these properties changes, the other two will be affected. It should be noted that FEM results yield a practical outcome, whereas an analytical model ignores the slotting effects, saturation, and cross-couplings. Thus, the analytical finding will not be similar to the FEM results, as shown in Figure 2-16. The saturation in SynRM helps to saturate the ribs and webs, thus the machine can become an ideal SynRM. As discussed earlier, an ideal SynRM should not have rips and webs as they become a viable flux path in the Q axis. Figure 2-17(a & b) shows a realistic and ideal SynRM with and without tangential ribs and radial webs, respectively. If only the ribs and webs are saturated while the rotor core segments remain within a working point, the ribs and webs become high reluctance path. Thus, a practical rotor becomes an ideal rotor, as shown in Figure 2-17 (b).

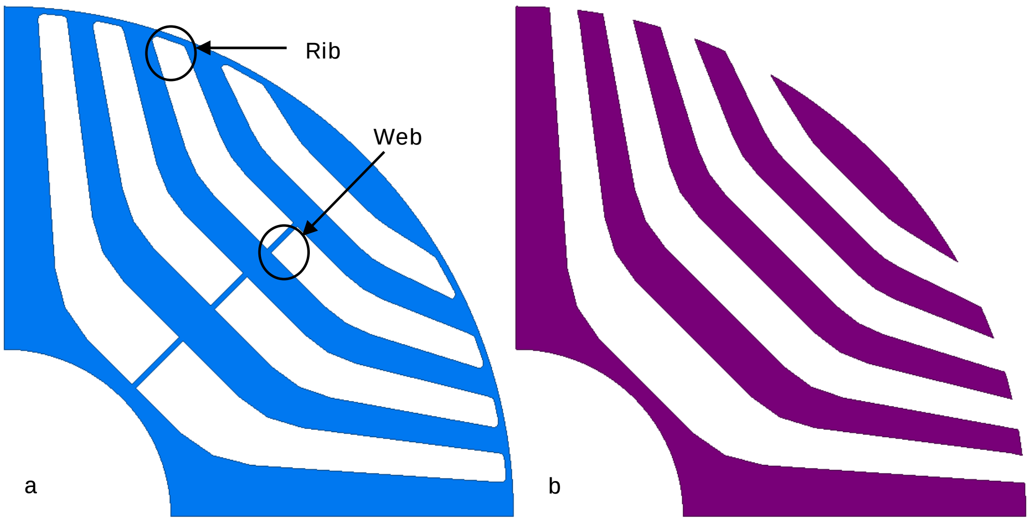

Figure 2-17: (a) Realistic SynRM with barrier rips and webs (b) Ideal SynRM without ribs and web

2.6.1 Cross-saturation in SynRM

If saturation is caused by inter axis parameters in DQ frame, it is called cross-saturation. It is primarily due to the magnetic steel shared by DQ magnetic axes such as ribs and webs. The cross-saturation effect is vital in sensor-less control of SynRM [193]. If magnetically linear segments are considered, the DQ flux can be given as in Eq. (2.62). However, if the cross-saturation is considered, D axis flux is influenced by Q axis current and vice versa. Therefore, the corrected DQ flux for cross-saturation is as in Eq. (2.63)

$$\begin{aligned} \lambda_{md} &= L_{md} i_{md} \\ \lambda_{mq} &= L_{mq} i_{mq} \end{aligned} \tag{2.62}$$

$$\begin{aligned} \lambda_{md} &= \lambda_{md}(i_{md}, i_{mq}) \\ \lambda_{mq} &= \lambda_{mq}(i_{mq}, i_{md}) \end{aligned} \tag{2.63}$$

However, if the machine is assumed to be magnetically symmetrical, then $\lambda_{md} = 0$ for $i_{md} = 0$ regardless of i_{mq} and $\lambda_{mq} = 0$ for $i_{mq} = 0$ regardless of i_{md}. Thus, the fluxes can be derived, as shown in Eq. (2.64)

$$\begin{aligned} \lambda_{md} &= L_{md}(i_{md}, i_{mq}) i_{md} \\ \lambda_{mq} &= L_{mq}(i_{mq}, i_{md}) i_{mq} \end{aligned} \tag{2.64}$$

The cross-saturation must be minimised not only to improve the efficiency of the machine but also operate the machine in the MTPA and field-weakening region. The cross-saturation is relatively high in the field-weakening region due to the high current.

2.7 Importance of Webs and Ribs and optimisation

As shown in Figure 2-17, the ribs and webs are unavoidable in a TLA design. They are the sole mechanical connection between each steel segments. If the thickness is more than what is required for mechanical integrity, the ribs will become a low reluctance path along the Q axis and reduce the machine performance parameters. As we have seen in the above sections, the torque and power factor of SynRM is directly proportional to its saliency ratio. If the thickness is smaller, then it will be susceptible to low mechanical strength and can deform due to heat and cause mechanical damage to the machine.

It has been initially proposed by Vagati [80] and then further analysed for better machine performance [104]. The ultimate objective of the rib design is to saturate it within $\pm 10\ \%$ of working point. If the ribs are saturated below the recommended limit, they are undersized and may experience heat deformation at high speed. If they do not saturate in the $+10\ \%$region, it is oversized, and degrade the machine performance. It is one of the challenges in the SynRM design process to get the rib size as optimal as possible.

2.8 Application of variable speed drive for SynRM operation

A SynRM shall use variable speed drive so that it can be soft started, gradually loaded, speedup and controlled at any speed. The VSDs are devices with field-oriented control algorithm inbuilt. It controls SynRM vectorially using the pre-configured algorithm. The optimum performance of SynRM is achieved by controlling the current vector in the DQ plane. In a constant flux method, the VSD keeps Id constant for any speed below the rated speed to maintain constant flux. In the case of current angle control, the angle between rotor D axis and the current vector is controlled to yield the optimum machine performance at any steady-state condition. Thus, SynRM more often equipped with a current angle-controlled field-oriented controller. The DQ current relationship of this machine can be given as in Eq. (2.65). This is an ellipse in the DQ current space-oriented at (0 A, 0 A). As can be seen in the Figure 2-18, the machine induced voltage is directly proportional to the machine speed.

$$e^2 = \left(\omega L_q\right)^2 \left(i_q^2 + \left(\xi i_d\right)^2\right) \tag{2.65}$$

If the supply frequency is $f = \frac{\omega}{2\pi}$ the air-gap flux distribution of a balanced supply can be assumed to be constant and in synchronisation. In an ideal machine, the maximum torque is at $45°$ for the MTPA region. Figure 2-18 shows an ideal 7condition control region of a SynRM in DQ current space. The MTPA and field-weakening locus are indicated with respect to maximum current and voltage ellipses. The supplied current reaches its maximum value at nominal state, or in other words, the speed reaches its nominal value. At this condition, the controller switches from MTPA to field-weakening as shown by the locus (Figure 2-18). As can be seen, MTPA is the best control technique for constant torque regions, due to its linearity with torque.

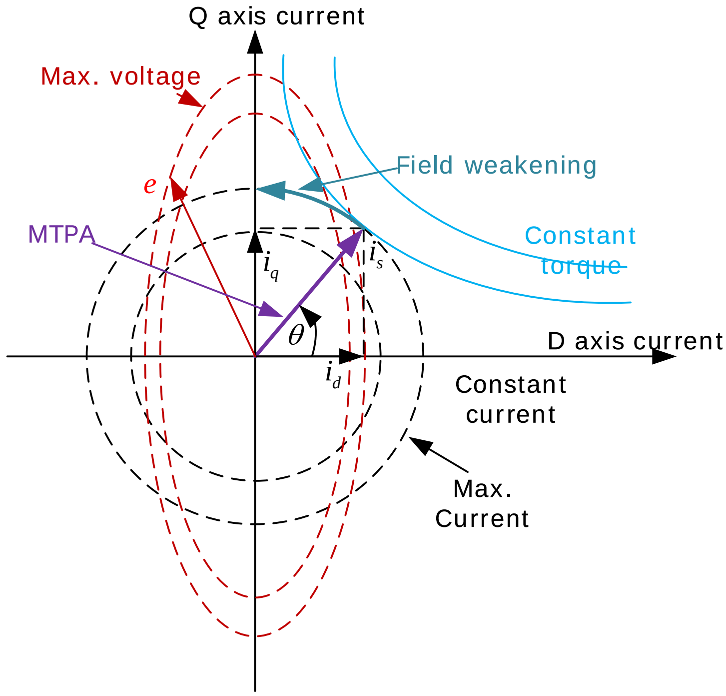

Figure 2-18: DQ current plane of a SynRM for field-oriented control

The torque can be maintained constant throughout this region, as shown in Figure 2-19. When the speed increases beyond rated value or base speed, the torque-producing ability of the machine declines as the field in the air-gap is weakened to increase the speed. Thus, the torque reduces with speed in this region to its minimum. In order to achieve high speed, the torque should be compromised. However, the maximum torque at each field-weakening speed point shall be determined to yield the maximum torque, as shown in Figure 2-18 and Figure 2-19, which is further discussed in detail in section 5.11. The value of minimum torque at high speed is dependent on the machine's load torque curve. The field-weakening is achieved by minimising magnetising current, in the case of SynRM, it is i_d. The drawback of this method is, especially in PMSynRM, the PM can get demagnetised permanently. But high-grade rare-earth PMs such as neodymium magnets can withstand significant magnetisation current i_d up to twice the rated speed. It is not hard to understand the challenges involved in field-weakening control. Machine's maximum speed is reached at i_d equal to 0 A, or at current angle $90°$.

From Figure 2-18, it can be seen that the current angle shall be increased to compensate for the air-gap flux shift caused by saturation and other losses. The increase in the current angle reduces i_d and hence, D axis saturation is reduced. This will increase i_q resulting in higher torque without saturating the machine. The combination of winding and iron losses, saturation and cross saturation increase the optimum current angle to a higher angle for MTPA operation. Because of the core loss current (refer to Figure 2-7 and Figure 2-9), the resultant current is moved towards D axis [194]. Thus, for optimum operation, the current angle should be increased to compensate for saturation, cross saturation, and core loss. At rated condition, the induced voltage goes to maximum, until the machine is under constant flux condition or constant torque region. The invertor cannot produce a voltage above the maximum available and have, which is called field-weakening or flux weakening region. The machine can be operated in two regions, constant torque and constant power region using the same inverter, as shown for an ideal machine in Figure 2-19, where ω_0 is reference speed. The control and operation of SynRM in the field-weakening region are further discussed in section 5.11 with simulation results for SynRM and PMSynRM.

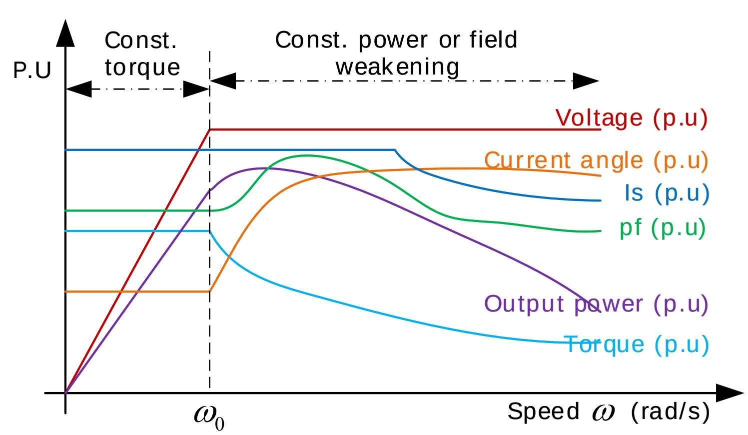

Figure 2-19: MTPA and field-weakening control regions with respect to machine speed

2.9 Effect of Magnetic Steel Materials on Machine Performance

It is a standard procedure to use high permeability magnetic steel for a reluctance machine to improve the flux path in the D axis. In a TLA design, the magnetic anisotropy in the D axis should carry lower reluctance or high permeance in order to improve the saliency ratio. A composite of electromagnetic steel material is suggested in the literature for SynRM [195]. A ferromagnetic and non-ferromagnetic material composed together to produce an axially laminated SynRM. The researchers almost followed the automotive industries techniques to produce a disk-type rotor. Although the innovative approach could produce flexible machine parts, it meets only 87 % of its predictable performance.

The modern SynRM manufacturing uses medium-speed wire-cutting technology to achieve high precision. Unlike stamping, any electrical steel can be used for wire cutting regardless of its toughness. Small range SynRM typically employs 0.5 mm thickness laminations to overcome the eddy current and hysteresis losses. This study uses grain-oriented electrical steel of 0.50 mm (M400-50A) due to its unique magnetic properties and unique structure. It is a high silicon hot rolled feedstock. This type of steel re-constructed through crystallisation process to grow grain's length. The orientation of the grain structure provides considerable magnetic properties. Its enhanced grain structure makes it an excellent choice over traditional mild-steel for required grain-oriented anisotropy.

2.10 Conclusion

This chapter comprehensively discusses the analytical model of a SynRM. The two common types of rotor structures TLA and ALA are discussed with respect to their anisotropies. Machine operating principle is discussed in DQ frame, and the important of saliency ratio and its importance in defining machine parameter are demonstrated. A detailed and complete phasor diagram of SynRM is presented. The reluctance theory concept is investigated via means of examples to improve the saliency and methods to reduce D axis reluctance and increase Q axis reluctances are discussed in details and demonstrated.

The flux path in non-linear SynRM magnetic circuit is graphically presented, and methods to improve saliency is also presented. The non-linear magnetic circuit is simplified into the equivalent circuit, and machine characteristics are developed. The 3-phase to DQ frame conversion is prepared for SynRM, and the vital machine parameters torque, power factor, torque ripples and efficiency are analytically defined. The parameters are theoretically analysed and graphically presented. The differences between theoretical results and a real-time performance are investigated and measures to minimise the saturation also discussed. The impact of saturation and cross-saturation on machine performance are demonstrated via analytical model and simulation results.

Torque ripples of the SynRM have been defined, and methods to minimise are presented. The control methods and machine behaviour in each control region are demonstrated through various analytical models. Moreover, the material used for reluctance machines is briefly discussed. Finally, the material for SynRM is investigated with the required material properties.

3 FINITE ELEMENT ANALYSIS AND OPTIMISATION

3.1 Introduction

Analytical investigation on a SynRM provides an intuitive analysis into the machine parameters, operating conditions, and behaviour of the machine. The mathematical relationships are developed by making assumptions such as the stator slotting effects and saturation effects are ignored in order to derive torque equation. However, a real SynRM is more than a simpler structure. The rotor with multi-barriers, ribs and webs combine a highly non-linear structure. The first step in machine design is conceptual studies, where the machine specifications are defined. The analytical study assists in understanding the preliminary machine dimensions. The finite element method (FEM) should be utilised to simulate the machine to understand the machine performance in details due to its non-linear magnetic circuit before preparing prototype.

The parameterisation is a numerical process which changes the input parameters in a predefined step manner (parametric equation) to understand the machine's characteristics throughout the length of the input change. It is not an optimisation, preferably a process that can be used to understand the specific input domain to see where the best characteristics of the machine lie. The parametrisation can have multi inputs but the higher the number of inputs, the more cumbersome the computation process and combination of repetition. The input could be simple as a machine dimension or function. On the other hand, the optimisation is an automatic process that uses a specific algorithm to determine the cost function for a defined set of input domains.

The optimum design is determined based on the cost function in an optimisation. The optimisation can have multiple inputs and multiple targets. A cost function determines the quality of the target function. Ansys™ electronic desktop is used for FEM simulation in the present investigation. It does not have in-built tools to analyse SynRM like it has for other machines. A highly advanced, precise, and state of the art macro has been developed along with machine design toolkit to analyse SynRM/PMSynRM results. IronPython scripts also developed to verify the macro's outcome.

3.2 FEM application to SynRM Problem

There are numerous sophisticated FEM programs available. Some of them are coupled with mechanical and thermal analysis programs [196-198]. FEM is essentially a numerical method for solving various engineering problems in a software environment. It is somewhat different to obtain precise results from an analytical solution for irregular geometries like SynRM. The electrical machine design requires electromagnetic FEM modeller that uses Maxwell equations efficiently. Due to its non-linearity, electromagnetic problems are different or near impossible to solve analytically. The FEM produces a series of discrete mathematical structures either tetrahedral, hexahedra or prisms and generates a sequence of finite element spaces, as shown in Figure 3-1, called meshing and it is the first step in FEM analysis.

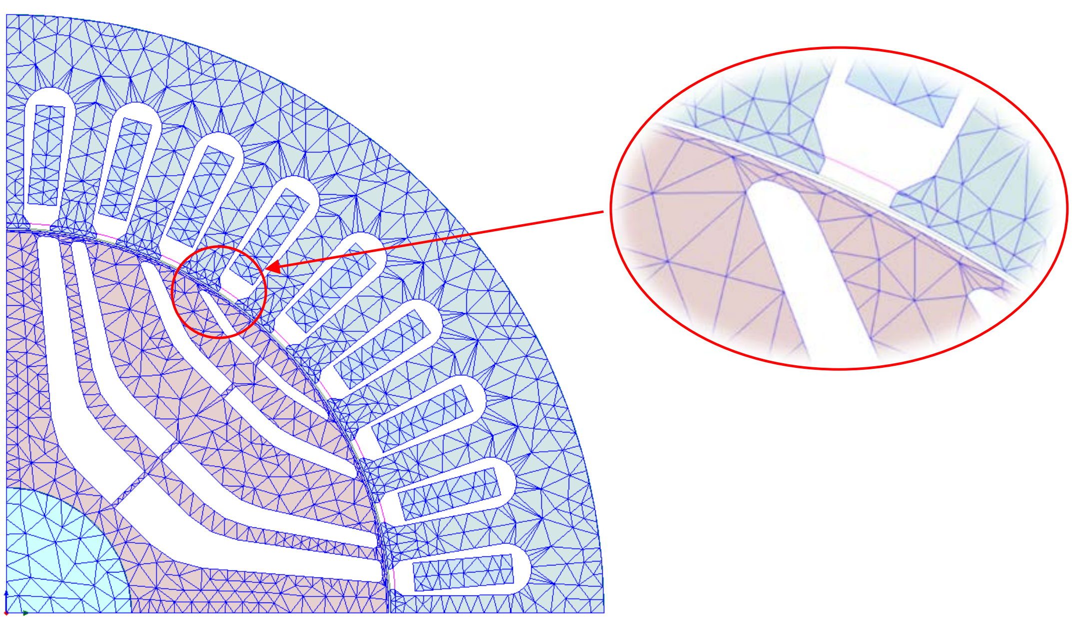

Figure 3-1: Technique to produce the best mesh on an electrical machine

FEM programs (in this case Ansys) have meshing inbuilt into them by default. However, the effectiveness of meshing depends on the user's skill. The fine meshing will produce precise results, but it will take long computational time. Larger mesh length will reduce the mesh number in the structure, but it will compromise the accuracy of the results. Thus, the best practice is forming high-resolution mesh in critical areas, as shown in Figure 3-1. The fine mesh is generated around the air-gap, edges of stator teeth, ribs and webs and the other sections of the stator and rotor core are left with standard meshing. The enlarged section in Figure 3-1 shows the meshes around the ribs and the air-gap. Such a fine mesh can be created around the critical areas by forcefully having a non-model line around the critical area. The enlarged section shows multiple lines passing through air-gap and stator teeth.

Historically, FEM simulations have been performed on a symmetrical fraction rather than on the complete model. A quarter symmetry fraction is used in simulating as shown in the above figure. The symmetrical fraction method was introduced to overcome the challenge of slow computation. However, modern computers are well equipped with the required memory and multi CPUs of maximum 256 logical cores. Therefore, the simulation of the complete model is not an issue anymore. Furthermore, FEM can be simulated in 3D which need significantly high computing power compared with equivalent 2D simulations. Best simulation practice is to perform the preliminary simulation on optimised mesh and symmetrical fraction model to minimise the simulation time. Once the design is agreed upon for the final analysis, a complete model with high-quality mesh can be used for final results. Surface approximation meshing should be employed along with length-based meshing as SynRM has curved surfaces.

3.3 Basis of Design

This study utilises a real-world problem using the same dimensions of a real machine. The machine parameters including stator winding details, coil resistance, slot dimensions, core materials, and air-gap length are carefully replicated into the software model for accurate results. Figure 3-1 shows a factional design where the machine slots are imitated similar to the original machine. The present research is focussed on improving the machine performance of a small range of SynRM. Therefore, an ABB IM stator is chosen to be the experimental machine with little modification. The machine nameplate ratings and dimensions are listed in Table 3-1.

Table 3-1: Base Design Dimensions and Name plate details

Base Design Machine Name Plate Details and Dimension	
Power [W]	1100
Torque [Nm]	7
Power factor [p.u]	0.72
Efficiency [%]	81.40
Rated Voltage [VAC]	380
Full load current [A]	2.9
Frequency [Hz]	50
Angular speed [rpm]	1500
Network voltage [VAC]	400
Winding resistance [Ω]	6.6
Stack length [mm]	66
Stator inner radius [mm]	46
Shaft radius [mm]	15

This investigation emphasis only one stator design due to the number of experiments performed based on the above-listed model. The stator of the base design is shown in Figure 3-2.

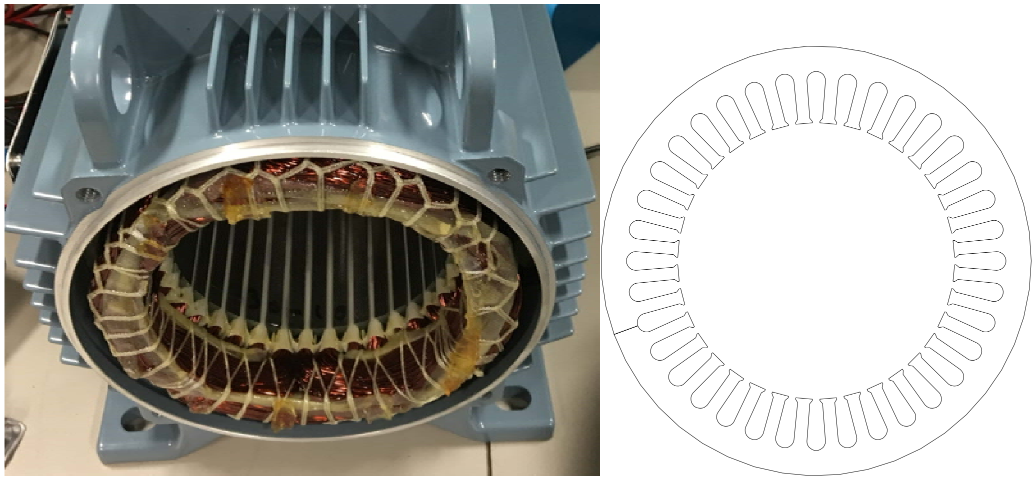

Figure 3-2: Stator of the base design and its detail slot view in FEM tool

The stator is selected with 36 slots and half coil distributed winding. The stator slots are of the parallel type with the industry standard. The ampere per turns pre-defined from the stator configuration. However, the ampere per turn parameter used in the simulation is obtained from real stator parameters. The slot dimensions are depicted exactly the same as the practical stator for precise results as shown in the figure.

3.4 Modelling Average Solution in FEM

In Ansys electronics desktop, SynRM parameters are required to be scripted into the FEM tool in order to evaluate average solutions. This section outlines the methods used for evaluating the average solution using scripts. In FEM, the average solutions are calculated per each electric period. The stator phase current is computed as in Eq. (3.1) where T is the electrical period and $i(t)$ is input current

$$I_{phase\_rms} = \sqrt{\frac{1}{T}\int_0^T i^2(t)\,dt} \tag{3.1}$$

The stator supply phase voltage is computed as in Eq. (3.2)

$$V_{phase\_rms} = \sqrt{\frac{1}{T}\int_0^T v^2\left(t\right)dt} \tag{3.2}$$

The input voltage $v(t)$ is known from Eq.(2.10) and (2.11). The leakage inductance and stator DC resistance are measured values.

The instantaneous torque, in the case of Ansys Electronics Desktop, is calculated by FEM tool. In order to find average torque over an electrical period, the instantaneous torque is integrated as given in Eq. (3.3) where $\tau(t)$ is instantaneous torque.

$$T = \frac{1}{T}\int_0^T \tau(t)dt \tag{3.3}$$

The power factor is not generally evaluated by FEM, but calculated using apparent and active powers as given in Eq. (3.4)

$$\begin{aligned} &S = VI \\ &\cos(\varphi) = \frac{P}{S} = \frac{P}{VI} \end{aligned} \tag{3.4}$$

The input power of the motor is calculated using instantaneous voltage and current values as given in Eq. (3.5)

$$\begin{aligned} &P_{in} = \frac{1}{T}\int_0^T p(t)dt \\ &P_{in} = \frac{1}{T}\int_0^T v(t).i(t)dt \end{aligned} \tag{3.5}$$

The output power is evaluated using the average torque at simulated speed as given in Eq. (3.6)

$$P_{out} = \frac{1}{T}\int_0^T \tau(t)\omega(t)dt = T\omega \tag{3.6}$$

The efficiency is typically evaluated using Eq.(3.7). However, because the shaft power is less sensitive to electrical period, it is evaluated using the machine's shaft power as in Eq. (3.8)

$$\eta = \frac{P_{out}}{P_{in}} \times 100\% \tag{3.7}$$

$$\eta = \frac{P_{shaft}}{P_{shaft} + P_{tot\_loss}} \times 100\% \tag{3.8}$$

3.5 Flux Guides

Although SynRMs employed ALA or segmented anisotropy rotors, modern machines have hybrid type flux barriers. There are many types of barriers used. The shape of barriers also depends on the FEM program's ability to draw and make primitive designs. Some FEM programs already have a user-defined library where barriers can be formed by simply changing the dimensions and can be directly used for either parameterisation or optimisation. On the other hand, some FEM programs require developing new user designed models but with a lot of limitations in modelling. The reason for most of the different types of barrier shape is mainly hidden behind the limitation and ability of the FEM program.

Figure 3-3 shows some of the common types of flux barriers used in the recent literature where (a) is WEE type barriers used [54], (b) is the circular type that are very rarely used, (c) the arc type hyperbolic barriers, and (d) hyperbolic barriers are very commonly used by researchers and industry. The latter one suits for PMSynRM due to the flat barrier section along Q axis where rectangle PMs can be fit it without additional mechanical arrangements.

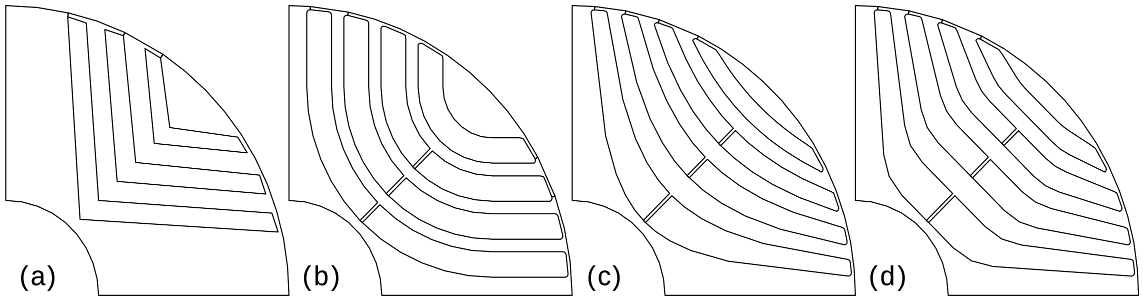

Figure 3-3: Types of modern hybrid barriers

The question is, which is the best shape of the barrier? In order to answer the question, a special simulation is performed on a barrier-less rotor that has the same reluctance in both axes. Its flux path is produced using FEM and shown in Figure 3-4. The flux lines closer to the air-gap is straighter and denser. Figure 3-4 (a) and (b) are the same simulation but (b) with a high number of flux lines to distinguish the flux density closer to the air-gap and the shaft. The shaft is of non-magnetic material. As can be seen, the flux density is higher along the air-gap and lower closer to the shaft. These two observations are the key factors in deciding the barrier shape.

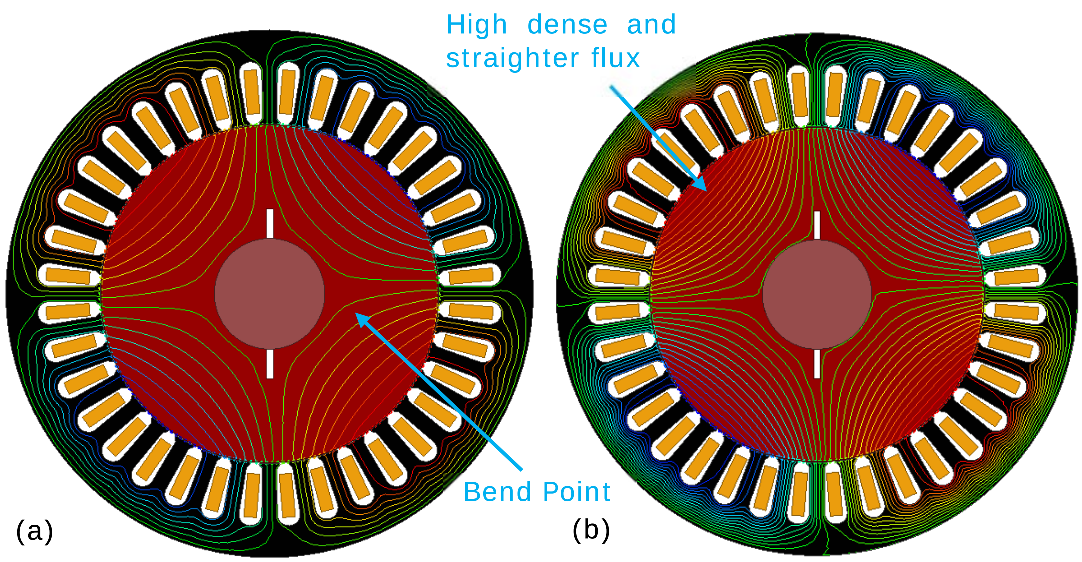

Figure 3-4: Flux path on a flat rotor without barriers to understanding the phenomenon of anisotropy

The above findings yield the vital concept to design the flux barriers. It shows that the barrier closer to the shaft should be thicker in order to improve the flux density, and the barrier closer to the air-gap should be thinner in order to accommodate more flux in around that area. At the same time, the barrier closer to the air-gap should be straighter, and the barrier closer to the shaft should follow the shape of the flux lines. It can be concluded that a single flux barrier alone is not enough to achieve high field intensity along the D axis. Thus, multiple-barrier structures will enhance the saliency ratio. From the findings, the barrier shape illustrated in Figure 3-3(d) is the first optimal shape.

Now, another question arises about the number of barriers. As can be seen in Figure 3-4, the flux spreads from the edge of the shaft (non-magnetic) to the circumference of the rotor. Therefore, in order to intensify the flux density, the barriers shall be used in the same shape as the flux lines. At the same time, a higher number of barriers will draw the rotor into saturation. There is a norm for selecting the number of barriers as given in Eq. (3.9) [166, 199].

$$n_s = n_r \pm 4 \tag{3.9}$$

Where n_s is even number of stator slots per pair of poles and n_r number of equivalent slots per pair of poles. This analogy is used primarily to design a SynRM rotor with low torque ripples. However, this is dependent on the very design that Vagati proposed [81]. The tolerance ± 4 is quite high for a small range of SynRM. The suggestion by Vagati can be used to understand, but the final number shall be determined using either parameterisation or optimisation.

3.5.1 Barrier Design

In order to implement the above analogy in the simulation model, an automated design is needed. Ansys Electronic Desktop® has a machine design package called RMXprt®. It supports most of the electrical machines but does not support SynRM simulation. Therefore, scripts using IronPython have been developed to analyse the post-simulation results. Electronic Desktop® a has user-defined library for SynRM, but it required customisation to develop the unique primitive design. Thus, the barrier presented in Figure 3-3(d) slightly modified with added parameters so that it can be used for automated optimisation and parameterisation that can yield optimum design. The modification closely follows Pellegrino's dimensioning topology [200] to generate two types of the similar barrier one without the radial web and other with the radial web so that it can be used for SynRM as well as PMSynRM.

The significance of the new type of barrier is, end barrier width and barrier fin angle (φ_i^m) can be automated with greater freedom in changing dimensions during parameterisation and optimisation processes. The customised hyperbolic barrier without radial web is shown in Figure 3-5. The customised barrier with the radial web is shown in Figure 3-6, which is specially designed for PMSynRM. The end barrier design followed precisely the same as the library function. However, one end of the barrier edge made changeable, as shown in Figure 3-7. The new barrier shapes allow the user to design and automatically change the required barrier shape through dimension parameters. The new design allows the user to change barrier end leg angle so that it can be included for torque ripple investigation.

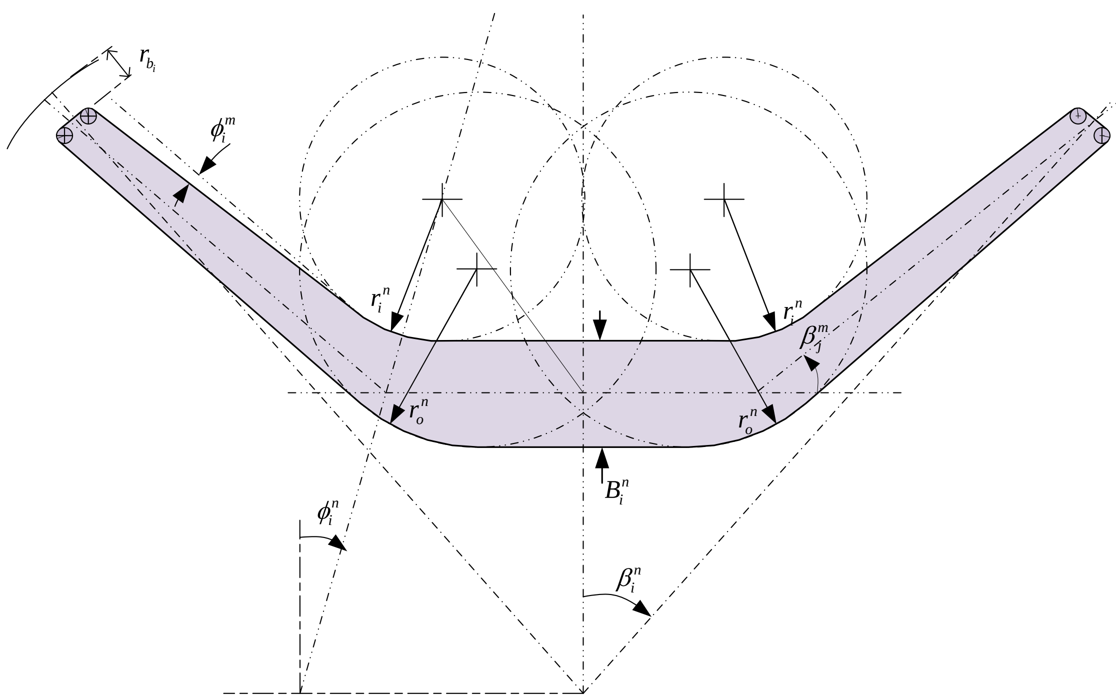

Figure 3-5: Customised hyperbolic barrier without radial web

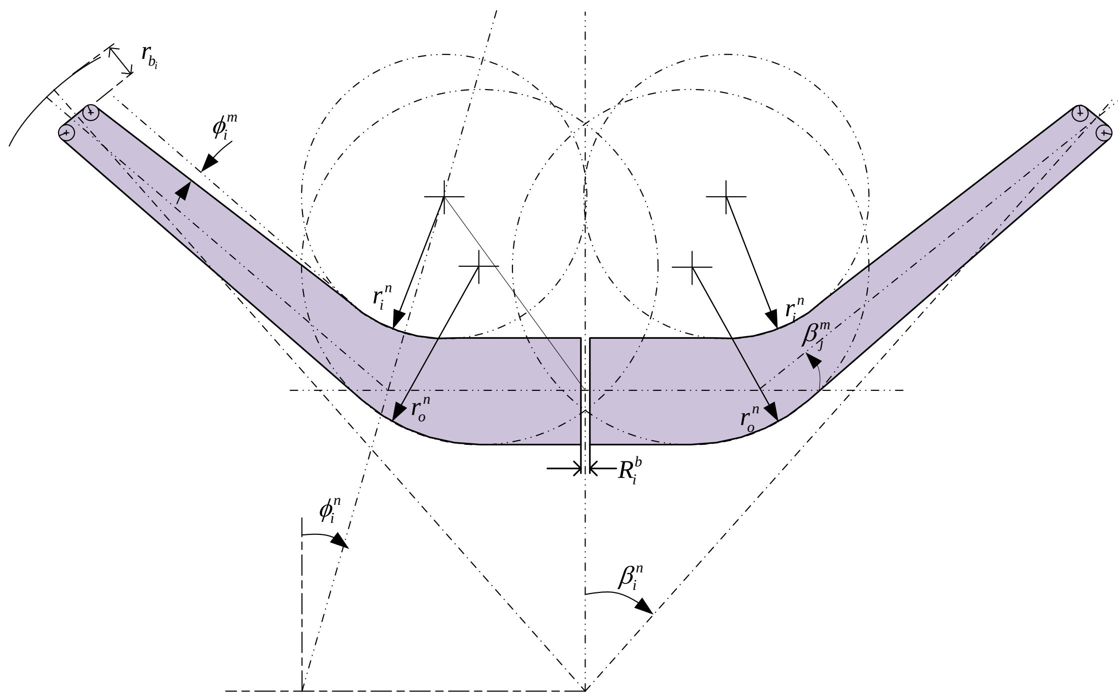

Figure 3-6: Customised hyperbolic barrier with radial web

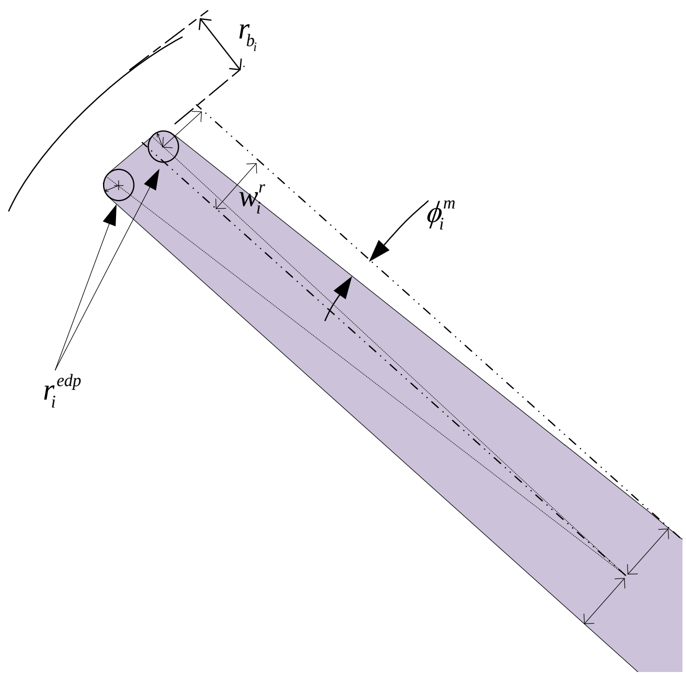

Figure 3-7: End barrier design topology for hyperbolic barrier

The optimum barrier shape for high saliency is shown in Figure 3-5 and Figure 3-6. From the analysis, it is simple to devise a strategy to place the barriers in the flux space. The important observations from the flux space shown in Figure 3-4 are listed below:

- Flux density is high towards the air-gap, and it gradually decreases towards the shaft
- Flux closer to the air-gap is lot straighter
- Flux closer to the shaft follows Obtuse angle curvature
- Flux lines are symmetrical along Q axis
- The bend point in the flux gradually moves towards Q axis as it goes away from the shaft
- If the non-magnetic shaft is used, the flux lines bend when it passes the shaft

The above observations are the key points in designing the barrier shape. Based on the observations, the design strategy is as follows:

- In order to increase the field density along the D axis, the insulation ratio should be optimised. If a wider barrier is placed closer to the shaft, it will optimise the field intensity
- Insulation ratio should be minimised closer to the air-gap to avoid saturation as well as improve the flux path
- The insulation ratio should be gradually reduced towards the air-gap ($B_1^n > B_2^n > B_3^n$) and ($Y_1^n > Y_2^n$)
- The barrier bend should follow flux line bend

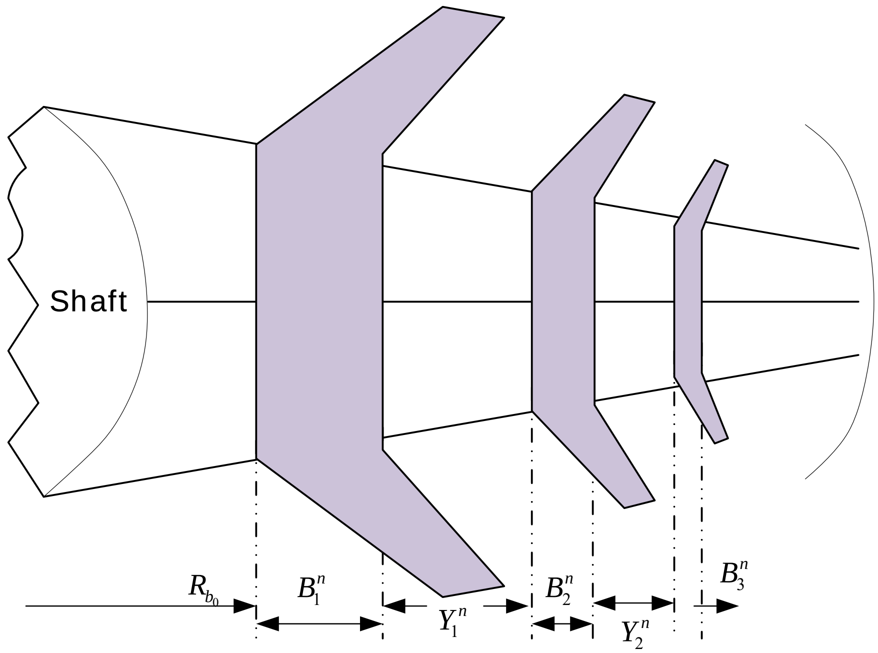

Figure 3-8: SynRM rotor design topology

Based on the above observations, the SynRM rotor should follow either one of the rotor shapes in Figure 3-9, which will be further verified by using the FEM primitive design technique in section 3.6.1.

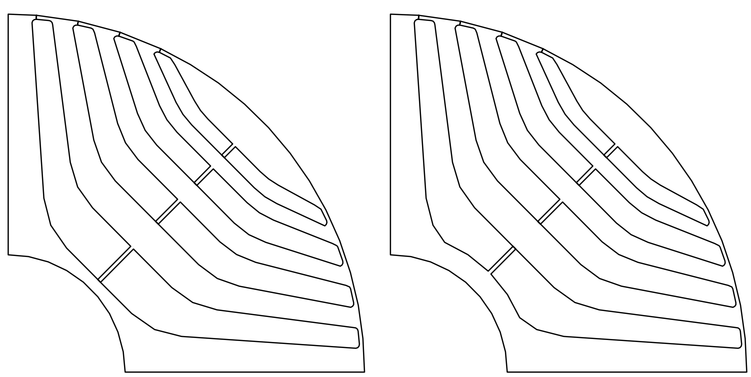

Figure 3-9: Optimum rotor shapes for SynRM

3.5.2 Parameterisation techniques

The parameterisation is a process of refinement method for sweeping analysis. The benefits of this process are, it significantly reduces the simulation time, stores each design mesh thus, re-meshing is instantaneous. The refinement process can be achieved in adaptive manner using the stored mesh data. Single or multiple design variables can be defined. Each variable is specified with discrete values within a domain. This procedure allows the designer to understand the behaviour of the output of each input better. In machine design, the results of the parameterisation can be compared to determine how a specific input changes the machine performance. The advantage is it reduces the time and effort to find an optimum value of a parameter for optimum design as well as the raw results can be directly fed into an optimisation study. The optimiser will understand the characteristic of the design even before the optimisation process begins using the parametrisation results, which will reduce the simulation time. The drawback is that it does not evaluate the optimum design. In order to find optimum design, the optimisation shall be used.

3.5.3 Optimisation

The optimisation is a mathematical tool to identify the maximum or minimum of a real function by selecting the input(s) or variable(s). An optimisation is associated with a function called cost function. The best element is selected based on the cost function. The inputs are defined in discrete function within a range and for some optimisation algorithms, focal range can also be defined.

The optimisation of the electrical machines is an essential process in machine design. There are several optimisation algorithms available. However, an algorithm for SynRM optimisation is essential to reduce expensive computations and reduce design time. Recent studies of machine design focus on FEM techniques coupled with optimisation algorithms [96, 110, 200-202]. Recent studies on optimisation report few specific algorithms for SynRM optimisations such as the use of genetic algorithms (GA), Deferential Evaluations (DE), DE and simulated annealing (SA) [200, 201, 203]. However, other studies focus on static FEM solutions to design and optimise SynRM.

A rotor of SynRM can have several variations to flux barriers, rib sizes/locations, and insulation ratio. Therefore, the researchers have used FEM tools for analyses of SynRM. The modern FEM tools are generally equipped with optimisation algorithms for post-processing. A higher number of variables in optimisation increases the need for computation power as well as the processing time. The optimisation of SynRM requires an algorithm to optimise multi-variables with fast optimisation attribute as well as fine-tuning for multiple variables. This study exploits a computationally efficient optimisation algorithm in conjunction with FEM tool in order to optimise the predefined surrogate model.

The optimisation algorithm uses response surface technique to determine the next solution, which is explained in the subsequent section. An existing algorithm which was designed to optimise PM Synchronous machine is scripted to suit SynRM with gradient calculation and sequential non-linear programming. The Sequential non-linear program is selected over other techniques for this investigation due to its fast and multivariable processing and fine-tuning abilities. Another option is the utilisation of artificial intelligence techniques that can significantly reduce manual interaction and cost involved in machine design.

However, the application of artificial intelligence with FEM tools on SynRM design optimisation is not encouraged because of the long process duration, and multiple selection scenarios involved in the design process [200]. In this thesis, the optimisation used for three objective functions, *i.e.* torque, power factor and torque ripple to ultimately improve the efficiency without compromising any of the other machine parameters. The high torque density is fundamental in any rotating machine design. However, the torque is not the only parameter that requires utmost attention for a motor application. On the other hand, the parameters such as pf and torque ripples are also vital in machine design. Most of the literature focus on optimisation of either torque or power factor optimisation. Only hands full of studies have been published on multi-objective optimisation algorithms [203-205]. The optimisation of three parameters requires a compromising approach during the selection of input variable domains.

The preparation of a suitable model for optimisation is the most crucial step in an automatic optimisation process. The rotors in the study are modelled using highly-advanced vector coordinate system and primitive design technology that can significantly reduce the number of variables used in optimisation. An existing model is scripted using IronPython to include more variations. The optimisation variables are then formulated using logical relationships with regard to the cyclic coordinates system. This procedure offers freedom in selecting inputs and modelling any barriers and barrier end fillet profiles.

3.6 Synchronous Reluctance Machines

3.6.1 Analysis I – Barrier Shape

This section analyses the machine performance for three types of barriers. The Wee type of barrier design is not further analysed due to its inflexibility in developing the primitive design and using it for optimisation. The three model's circular (CIR), hyperbolic arc (HY-I) and hyperbolic non-arc (HY-II), as shown in Figure 3-10, respectively. The designs are equipped with unsaturation rings to minimise the saturation on the segments. All other parameters such as ribs, webs, insulation ratio, and the number of barriers and location of barriers kept identical for all three designs. However, some aspect of the designs is difficult to control, such as the barrier end locations, Q axis insulation ratio, and length to thickness ratio. Because of this reason, there are differences within the designs.

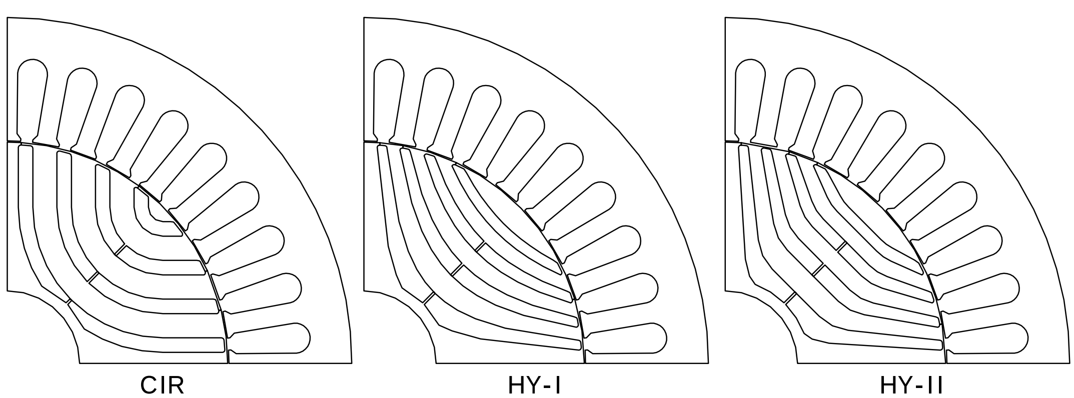

Figure 3-10: Analysis I - Barrier shape analysis

All three designs are simulated in the same way, and the results are given in Table 3-2. HY-II produces better performance compared with the other two designs due to its geometry as studied earlier. However, the HY-I is not far behind. The torque ripples need optimisation to minimise, and although it is included in the table it is not considered as a deciding factor. HY-II produces 0.08 %, 1.22 %, 0.46 % and 5.5 % more torque, power factor efficiency and saliency ratio over HY-I respectively and 4.04 %, 5.10 %, 1.03 % and 17.51 % more torque, power factor, efficiency, and saliency ratio over CIR. Therefore, further investigations focus primarily on HY-II type of barrier design. However, the CIR type is included in the torque ripple studies for further investigation.

Table 3-2: Simulation results of the three design

Parameters	**CIR**	**HY-I**	**HY-II**
Torque [Nm]	7.323	7.625	7.631
Power Factor [p.u.]	0.781	0.813	0.823
Efficiency [%]	84.961	85.458	85.850
Torque Ripple [Nm]	4.700	3.639	2.560
Saliency	7.439	8.572	9.021

The geometry optimisation is vital for SynRM design. The slightly oversized or undersized design may produce rather poor machine parameters. It will be further discussed in the optimisation section. Many geometries require comprehensive analysis in order to understand the impact of each machine performance parameters. This study focusses on every rotor parameter one by one. The simulation is performed on the same system except for the rotor, which is changed in each analysis.

The following analyses primarily focuses on three machine parameters including torque, power factor and saliency ratio. In some cases, the efficiency and torque ripples are also recorded. In each study, the impact of changes in dimensions is explicitly analysed with possible variations. A four-barrier hyperbolic design is chosen for the entire analysis so that consistency can be maintained for comparison between each analysis.

3.6.2 Analysis II - Impact of barrier location on machine performance

This study focuses on the barrier location on a four-barrier design. The location of barriers is systematically moved in each variation. Four variations (AN-II01, AN-II02, AN-II03 and AN-II04) are studied, as shown in Figure 3-11. The insulation ratio of all four designs is kept constant while the barriers are moved. The design AN-II01 has all four barriers placed as close as possible to each other to make room in the circumference, while the design AN-II04 has all four barriers moved away to produce a distributed design. The segments along the circumference are narrowed down in the design AN-II04 as can be seen in the figure. The location of the first barrier (from the shaft) is maintained the same in all designs as it is separately studied in subsequent sections. The length of the barrier and segment thickness is varied in each design.

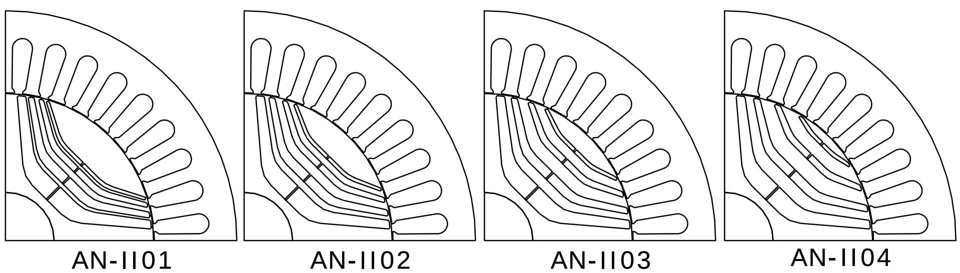

Figure 3-11: Analysis II – Four designs that are used for barrier location study

Table 3-3 shows the simulation results. The torques of all four designs are gradually increased with the location of barriers moving away from the shaft, as shown in Figure 3-12. The power factor gradually increases similar to torque, but it slightly dropped in case of AN-II03. The saliency ratio also exhibits similar characteristics as in Figure 3-13. The design AN-II03 shows relatively good performance compared with the other three designs due to the barrier dimensions and location. The end segment closer to the circumference is vital for the difference in performance between the four designs. An excellent end segment can lead to high performance as it is the critical flux path in the D axis, as shown in Figure 3-4. The designs AN-II03 and AN-II04 slightly differ in performance due to the difference in end segments.

An oversized or undersized end segment can result in poor performance as in the case of design AN-II01. The saturation in AN-II01 is relatively high compared with AN-II03 due to the tiny segments between barriers, and its end segment is wide open. Hence Q axis flux path is improved that reduces the saliency ratio. Therefore, as already discussed in section 4.4, the end segment shall be optimised.

Table 3-3: Analysis II – Simulation results of the barrier location study

	AN-II01	**AN-II02**	**AN-II03**	**AN-II04**
Torque [Nm]	7.414	7.875	8.123	8.132
Power Factor [p.u]	0.787	0.805	0.814	0.813
Efficiency [%]	84.482	85.264	85.665	85.714
Torque Ripple [Nm]	5.369	2.559	2.146	2.503
Saliency	8.183	8.68	9.025	9.003

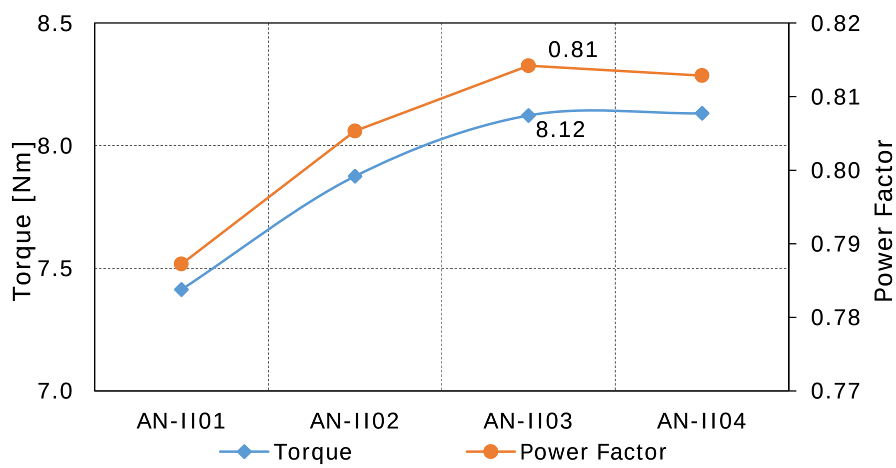

Figure 3-12: Analysis II - Torque and power factor of all four design

The saliency ratio is plotted, along with torque ripples in Figure 3-13. The saliency ratio is evaluated at the steady-state condition and represents saturated saliency ratio. The torque ripples are evaluated for comparison purpose only. A detailed investigation is required to understand the ripple effect with varying design parameters which is studied and reported in section 4.6. However, it must be noted that the rotor model discussed in 3.5.1 can minimise the ripples. As can be seen, the saliency ratio is the highest and the torque ripples is the lowest for AN-II03.

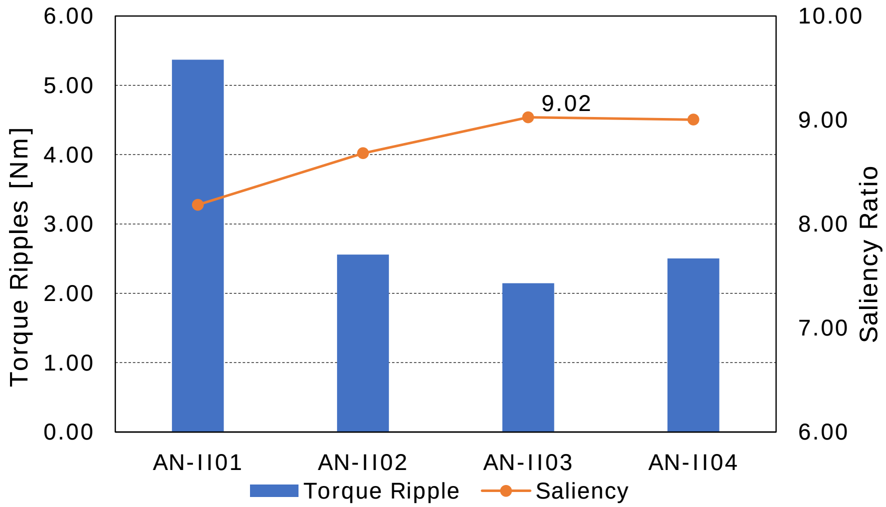

Figure 3-13: Torque ripples and saliency ratio of the barrier location study

The power factor and saliency ratio is increased with each barrier moving away from shaft up to design AN-II03, it starts to decline for design AN-II04 as can be seen in the graphs (Figure 3-12 and Figure 3-13) and table (Table 3-3). However, in the case of torque, it keeps increasing with the barrier location. Because the torque is developed by magnetic inductance whereas terminal inductances determine saliency ratio and power factor. The investigation concludes that merely having the same number of barriers will not yield the best performance. The study revealed the importance of placing barriers as described in the initial investigation. The designs with barriers are too close to the shaft or closer to each other does not yield the best performance. The saliency ratios of all four designs show the importance of having a barrier shape, as discussed in 3.5.1. The design AN-II03 is very similar to the optimum rotor that discussed in the section which produced not only high saliency ratio but overall improved performance.

3.6.3 D & Q axes insulation ratio

Insulation ratio is another parameter used in SynRM design and analysis to differentiate geometries. The insulation ratio has been defined in many ways by various researchers. This study follows a common definition that is easy to understand and used by many literature [80, 194]. The rotor is parameterised for insulation definition and shown in Figure 3-14 where the barrier (air) thicknesses and iron segments are indicated. The insulation ratio is defined in Eq. (3.11). When the ratio becomes 0, the design becomes a barrier-less structure, and when it became 1, the rotor will have half space of insulation and half space of iron.

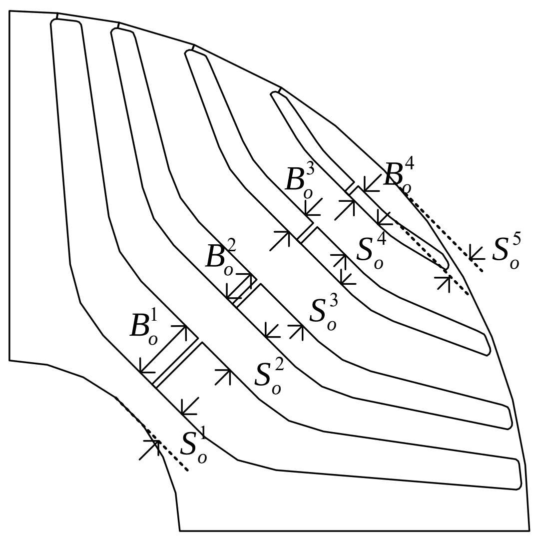

Figure 3-14: Definition of insulation ratio

$$\begin{aligned} R_{insul} &= B_o^1 + B_o^2 + B_o^3 + B_o^4 \\ R_{iron} &= S_o^1 + S_o^2 + S_o^3 + S_o^4 + S_o^5 \end{aligned} \tag{3.10}$$

$$Insulation\ ratio = \frac{R_{insul}}{R_{iron}} \tag{3.11}$$

The insulation ratio cannot be infinity, then the rotor becomes air. It can take any value between infinity and 0. However, the increase in insulation ratio will enhance the saturation in the iron segments resulting in poor machine performances. Therefore, the design of insulation ratio is a critical process. This study analyses five designs with various insulation ratios, as shown in Figure 3-15, and in ascending order of insulation ratio for comparison purpose. Five designs are selected for further analysis with close to optimum design so that high machine performance can be achieved. The locations of the barriers are not changed, but the barrier widths are varied in such a way the ratios between each adjacent barriers are the same. By doing this, the rotor shape in each design is maintained the same except the insulation ratio. Insulation ratios are changed from 0.58 to 0.95. The study results are given in Table 3-4.

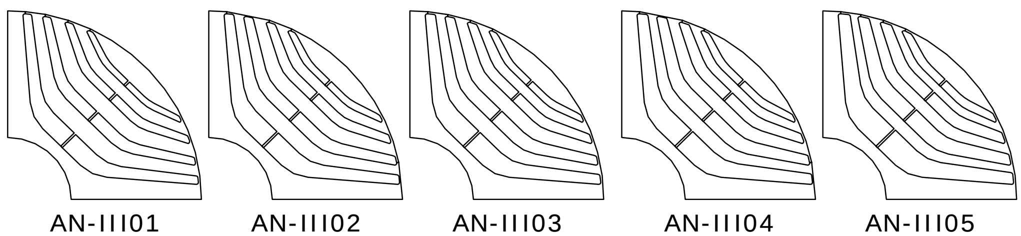

Figure 3-15: Analysis III - Designs for insulation ratio investigation

The torques and power factors are plotted as a function of insulation ratio in Figure 3-16. Maximum torque and power factor lie within the selected insulation ratio. As can be seen in the figure, the torque increases with insulation ratio and reaches the maximum for insulation ratio between 0.65 and 0.8. Whereas, the power factor keeps increasing because it is not susceptible to saturation as torque does as mentioned earlier. Similarly, the maximum efficiency also obtained for the same insulation ratio, is shown in Figure 3-17. The power factor and saliency ratio gradually increases with insulation ratio.

Table 3-4: Analysis III - Insulation ratio investigation results

Parameter	**AN-III01**	**AN-III02**	**AN-III03**	**AN-III04**	**AN-III05**
Insulation ratio	0.58	0.68	0.73	0.81	0.95
Torque [Nm]	8.225	8.271	8.267	8.260	8.182
Power Factor [p.u]	0.812	0.821	0.825	0.827	0.834
Efficiency [%]	85.523	85.584	85.893	85.880	85.482
Torque Ripple [Nm]	2.377	2.275	2.271	2.017	2.289
Saliency	8.48	8.75	9.07	9.24	9.21

Four barriers and high insulation ratio improve saliency ratio, which is directly correlated to the D and Q axes inductances. L_d is not significantly affected by the insulation ratio as the supplied current impacts it. Nonetheless, L_q is significantly reduced due to the high insulation present in its path. It has resulted in increasing saliency ratio for increasing insulation ratio. On the other hand, the efficiency and torque are affected by the rise in saturation, as shown in Figure 3-17.

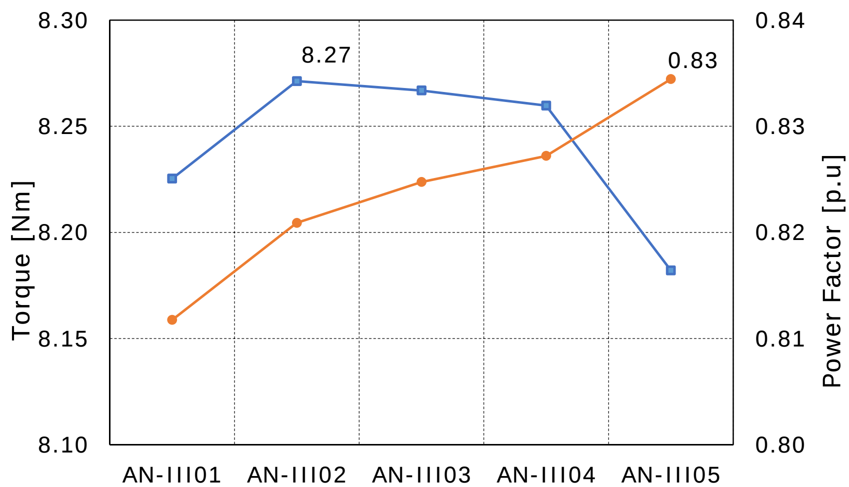

Figure 3-16: Analysis III - Torque and power factor as a function of insulation ratio

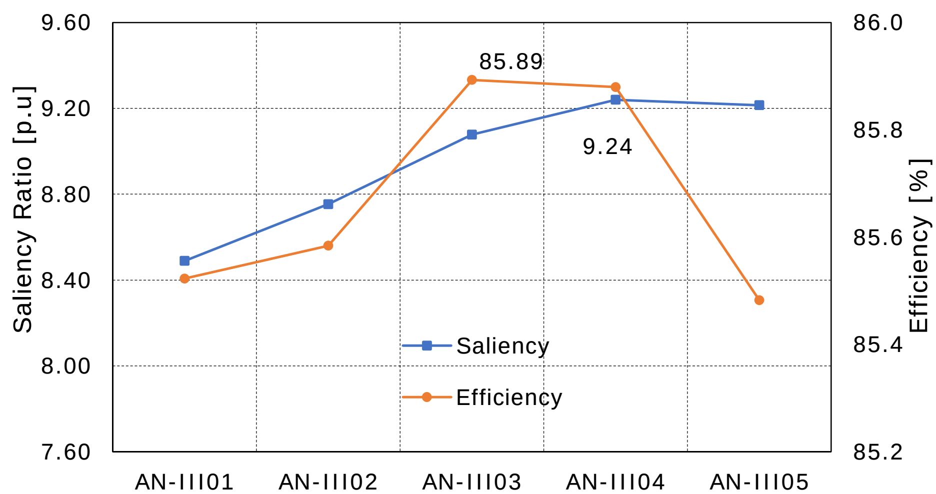

Figure 3-17: Analysis III - Saliency ratio and efficiency as a function of insulation ratio

The insulation ratio beyond 0.8 may increase saturation and may reduce the machine efficiency depending on other machine dimensions. This tool can be used to understand the geometry and performance even before FEM simulation. It can be used for fine-tuning the design during FEM analysis. This study is not conducted on an optimised design, but rather to understand the characteristic of the insulation ratio. Insulation ratio is studied in detail in an optimised design in sections 4.6 and 4.7.

3.6.4 First barrier location

The placement of the first barrier is essential to understand the placement of all barriers. The first barrier location significantly influences machine performance, especially the torque density of the machine is depended on the location of the barriers [104, 151]. Thus, a detailed investigation is carried out to understand the location of the first barrier in this section. Two cases are investigated in this study. In the first case (case I) only the first barrier is changed while all other parameters and dimension of the rotor maintained unchanged. In the second case (case II), all four barriers are changed, but the insulation ratio and other parameters remain the same.

Case – I (First Barrier Location Varied)

A single barrier design could have been employed to understand the issue, but it will not yield practical results. Hence a practical design is considered for this investigation. Figure 3-18 shows the changes in first barrier location closer to the shaft and move further from the shaft for the four designs. The designs also developed with unsaturation ring to minimise the saturation effect (only needed for AN-IVCI01) where the first barrier is closer to the shaft. The other three barriers are kept at the same locations with all other dimensions such as insulation ratio.

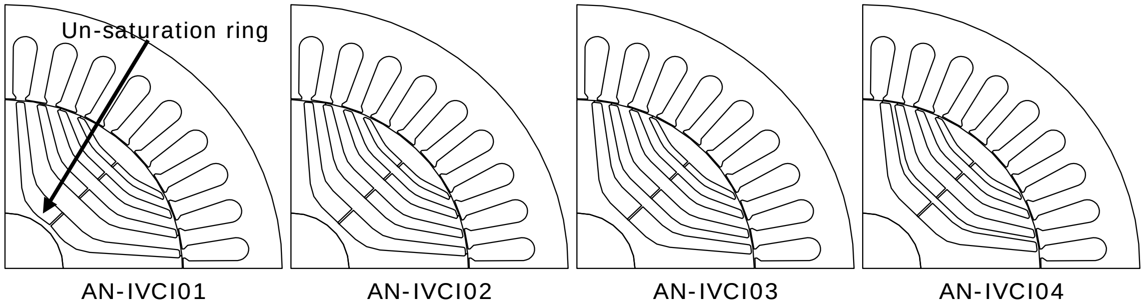

Figure 3-18: Analysis IV - Case I: Investigation on first barrier location

The designs are simulated using parameterisation, and the results are plotted in Figure 3-19 as a function of distance from the centre. The results show the maximum torque and power is obtained at some optimum location closer to the shaft. The first case, AN-IVCI01 has high saturation due to a rather tiny segment between the barrier and non-magnetic shaft. AN-IVCI02 shows improved performance, but the freedom of moving the first barrier is limited in this design. For further away designs (AN-IVCI03 and AN-IVCI04), the machine performance drops significantly. It has been already identified and reported in [165, 206, 207].

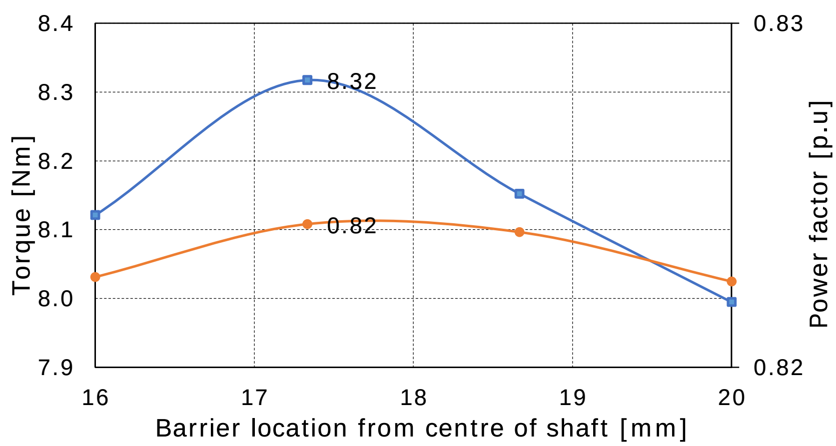

Figure 3-19: Analysis IV - Case I: Torque and power factor changes with respect to the first barrier location

Case – II (Barrier Location)

This study moves all the four barriers in a systematically arranged manner, as shown in Figure 3-20. AN-IVCII01 has all four barriers placed as close as possible to the shaft, and the location of barriers moved away from the centre.

Although there is no consistency between each design in this study, the primary goal is to analyse and see the machine performance for multiple designs with various first barrier location. All designs follow the same topology to maximise the performance expect barrier locations, and other parameters remain same.

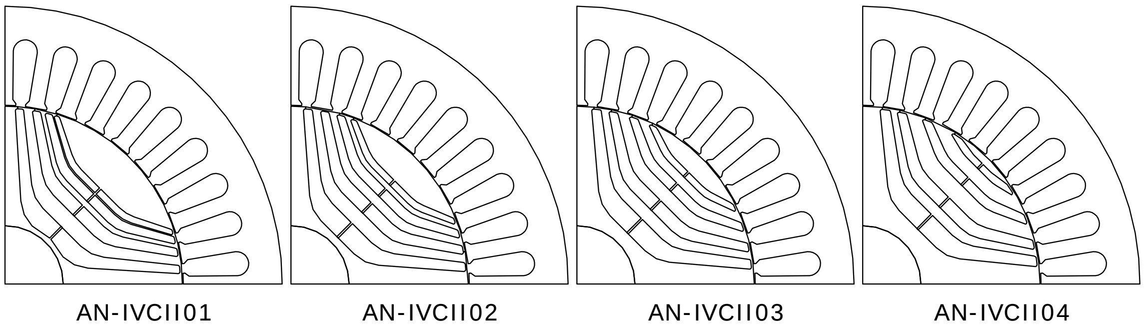

Figure 3-20: Analysis IV - Case II: Barrier location study

The study results are quite similar to the case I, which reiterates the high torque density of a design lies when the first barrier is closer to the shaft but outside the saturation area. The design AN-IVCII01 is a hypothetical one to give high freedom of movement for the first barrier during parameterisation. However, the results show that the design can be improved with thicker unsaturation ring for high torque density which is discussed in the optimisation section 4.3.1. On the other hand, the power factor is highest for AN-IVCII03. As mentioned in section 3.6.2, the end segment should have an optimum size, otherwise, it increases Q axis flux path resulting in poor saliency ratio. The study reveals the importance of the end segment, which will be further studied in optimisation section 4.3.

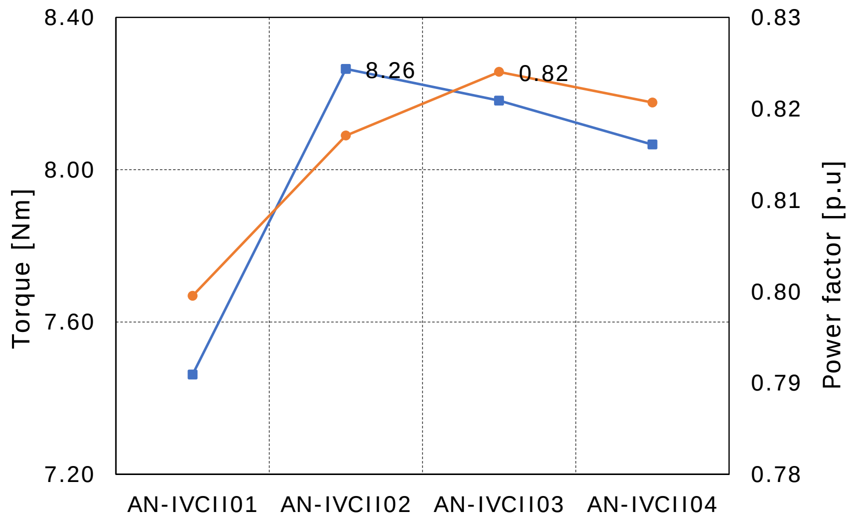

Figure 3-21: Analysis IV - Case II: Torque and power factor of Case II

3.6.5 Number of barriers

The above studies focused on barrier shape, location, and insulation ratio. However, a combined analysis is essential to improve the overall performance of the machine. The following study, although analyses number of barriers, focuses on a broader scale to analyse overall rotor dimensions with the number of barriers, critical elements in SynRM. As discussed, more number of barriers should increase the saliency ratio and hence, performance. However, due to the saturation, increasing number of barriers above specific value can cause serious saturation on the rotor core, resulting in poor performance.

Discrete barrier models (number of barriers above 10) have been studied in the past [208], but it compromised efficiency. The analogy in section 2.3 shows that splitting the rotor magnetic core into multiple segments is vital as Kostko suggested for increasing saliency as well as performance. Thus, a balance must be maintained between in splitting segments to avoid saturation while enhancing performance. Vagati [80] suggested a solution to start the design with predefined numbers based on the stator slot number as in Eq. (3.9). The suggestion focusses on rather avoiding high order torque harmonics. Nonetheless, the numbers suggested is rather broad for a small machine and require critical analysis to conclude the final number based on the size.

The investigation of the number of barriers requires multiple studies to understand. Therefore, this study is divided into six cases with the number of barriers varied from low as 2 to high as 7, but the insulation ratio is not altered (kept at optimum 0.73) in order to keep the consistency between the designs. An algorithm is developed to assign the right ratio of barrier thickness across the designs in order to keep the consistency. The algorithm is based on optimum design strategy found from numerous optimised designs. Unlike the above studies, this is a critical analysis for the number of barriers in several locations. For all the cases, the barrier thicknesses are assigned in the following manner. If the first barrier's thickness is x mm, then the second barrier's thickness is $\frac{2x}{3}\ mm$ and so forth, as shown in Figure 3-22, as an example for a four barrier design. The strategy is applied in the assignment of barrier thickness for multi-barrier cases to keep the insulation ratio constant.

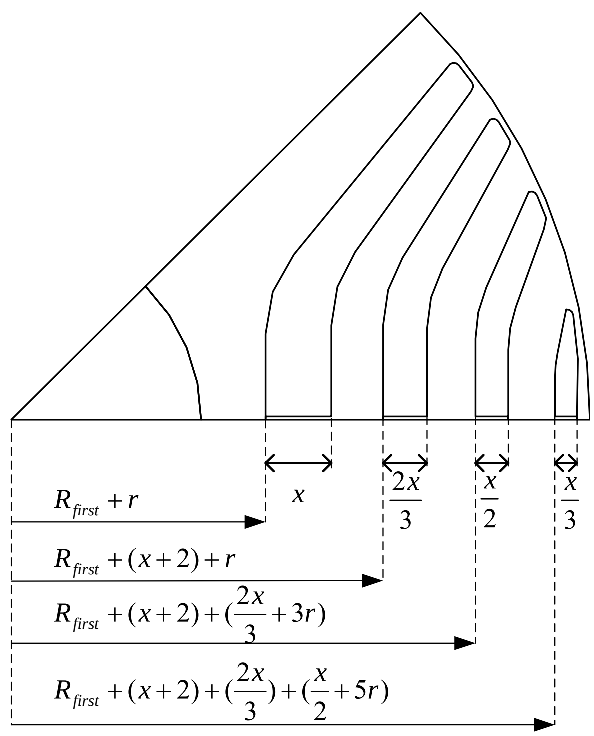

Figure 3-22: Barrier thickness assignment for a multi-barrier design

The investigation is conducted for the number of barrier study for six cases (case I to VI). Each case analyses each number of barriers by placing them at various location to determine the best combination.

Case I: two barriers

In this case, two barriers are investigated using the above-mentioned strategy. The location of the barriers is changed along with the rotor space over six designs, as shown in Figure 3-23. The simulation results are plotted in Figure 3-24 and Figure 3-25. AN-VCI05 has maximum torque and maximum power factor, and hence the saliency (Figure 3-25). The design AN-VCI06 has tiny end segment and susceptible to saturation which resulted in lower torque density and power factor than AN-VCI05.

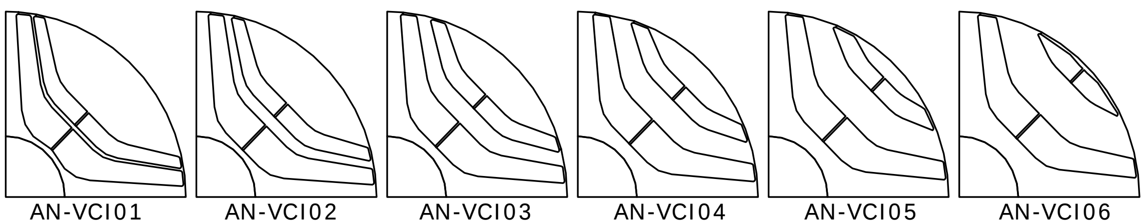

Figure 3-23: Analysis V - Case I: two barriers studied for varying location

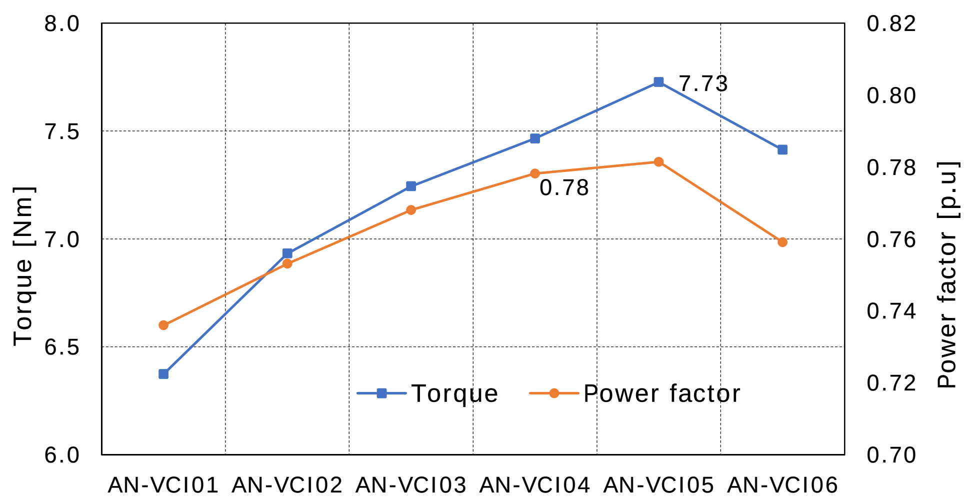

Figure 3-24: Analysis V - Case I: Torque and power factor with respect to design

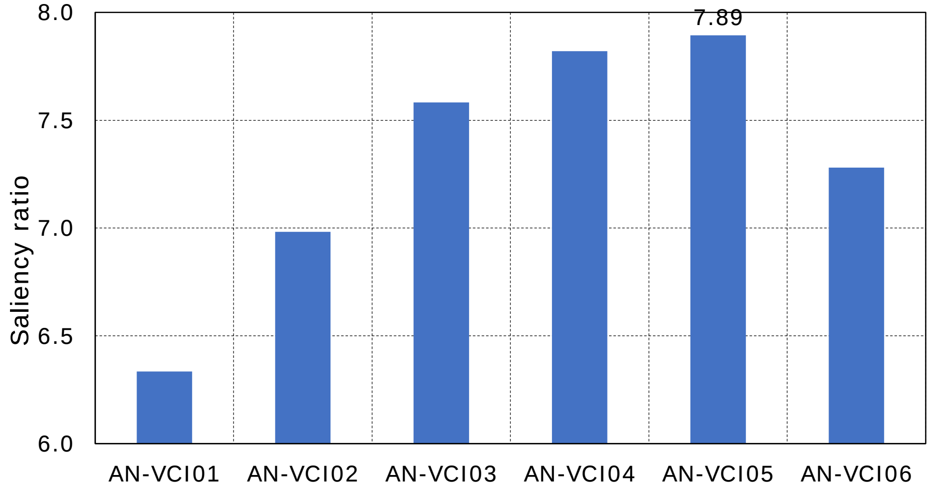

Figure 3-25: Analysis V - Case I: Saliency ratio with respect to design

Case II: Three barriers

Three barriers are systematically arranged as per the above strategy and shown in Figure 3-26. In this simulation, the design AN-VCII04 is close to the optimum design compared with the other four designs. The torque and power factor are plotted in Figure 3-27, where the torque and power factor gradually increases to 8.01 Nm and 0.81 before dropping for the design. The saliency ratios are shown in Figure 3-28. The maximum saliency ratio increased by almost 9.5 % compared with the case I (two barriers).

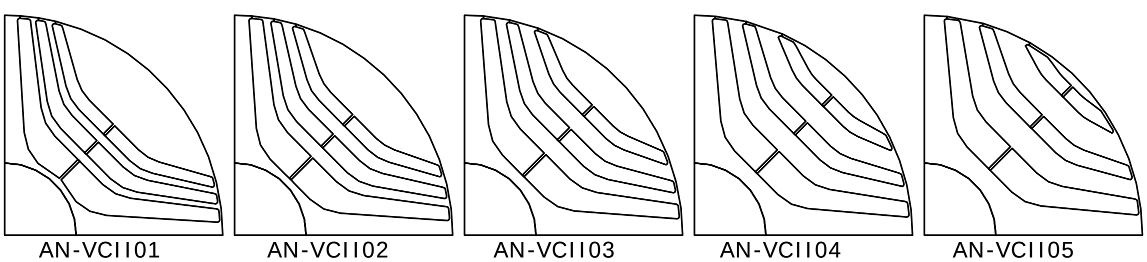

Figure 3-26: Analysis V - Case II: three barriers studied for varying location

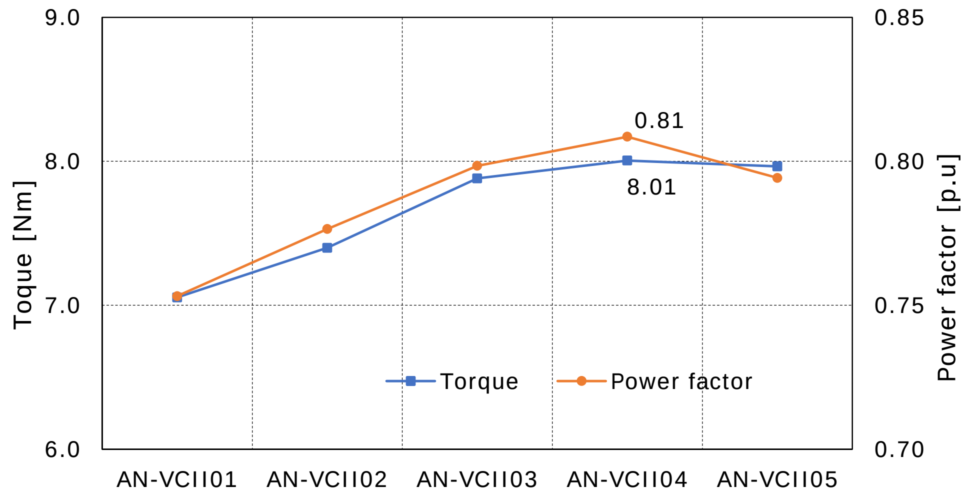

Figure 3-27: Analysis V - Case II: Torque and power factor with respect to design

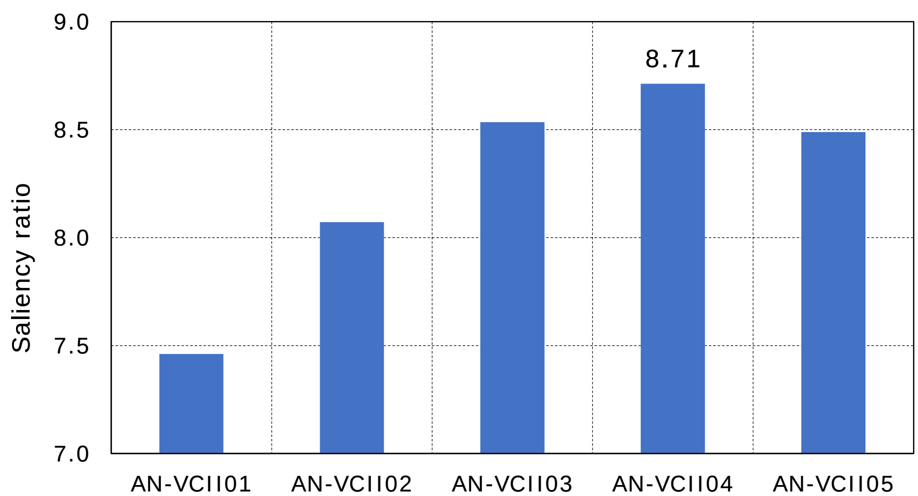

Figure 3-28: Analysis V - Case II: Saliency ratio with respect to design

Case III: Four Barriers

Similarly, four-barrier designs are simulated five different designs, as shown in Figure 3-29. Design AN-VCIII04 is closer to optimum design. The simulation results of torque and power factor are shown in Figure 3-30 and the saliency ratio in Figure 3-31.

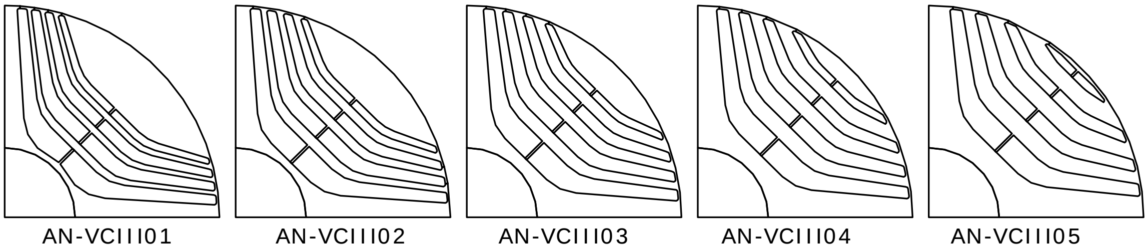

Figure 3-29: Analysis V - Case III: four barriers studied for varying location

The design AN-VCIII04 was expected to have high torque (as it follows the pattern discussed in section 3.5.1), but the design AN-VCIII03 exhibits high torque than other designs while AN-VCIII04 has maximum power factor. The design AN-VCIII03 and AN-VCIII04 have nearly equally distributed barriers where design AN-VCIII03's first barrier is closer to the shaft. Therefore, high torque density is obtained by design AN-VCIII03 while high power factor is obtained by design AN-VCIII04. As mentioned earlier, the torque is not impacted by leakage inductance, whereas power factor does.

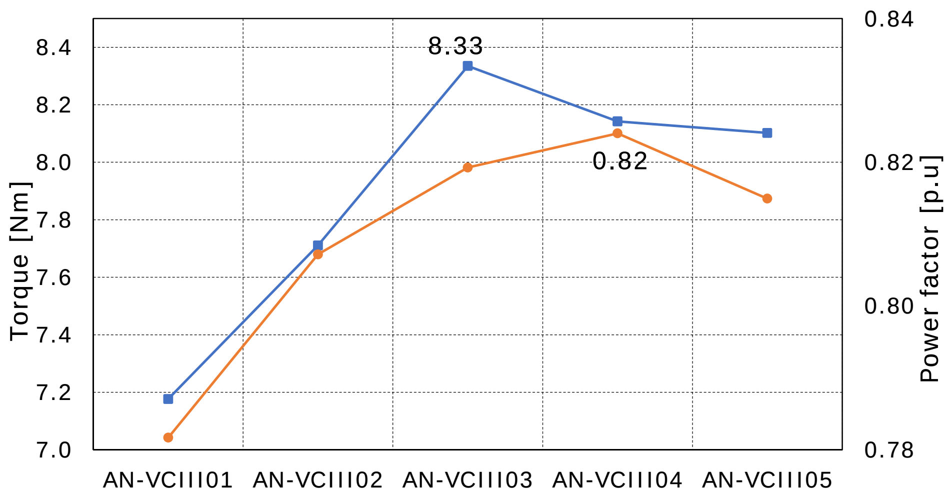

Figure 3-30: Analysis V - Case III: Torque and power factor with respect to design

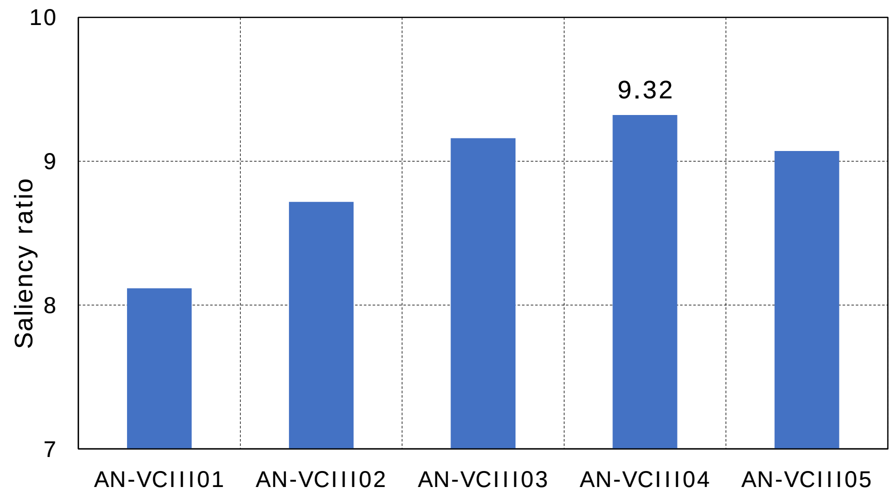

Figure 3-31: Analysis V - Case III: Saliency ratio with respect to design

The maximum saliency ratio of this design is increased by 6.7 % with respect to case II and 14.3 % compared with case I. It shows each barrier increases saliency ratio by an average of 7 %.

Case IV: Five barriers

Five barrier designs are investigated using the same strategy. The investigated six designs are shown in Figure 3-32. The results are plotted in Figure 3-33 and in Figure 3-34. The designs AN-VCV04 and 05 are closer to the optimum pattern among the six designs, with AN-VCIV05 resulting in maximum torque and power factor. It must be noted that the power factor has not much changed from case III with an increasing number of barriers. The torque dropped slightly compared with case III.

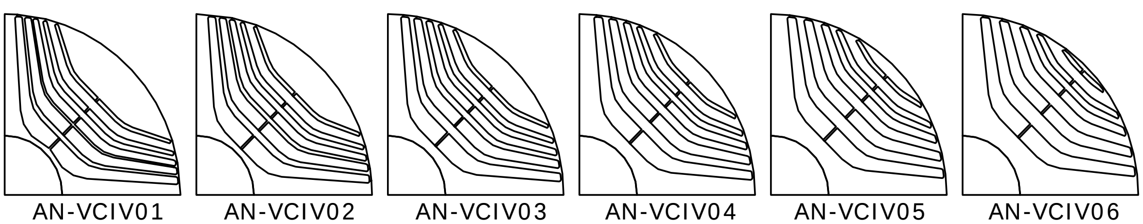

Figure 3-32: Analysis V - Case IV: five barriers studied for varying location

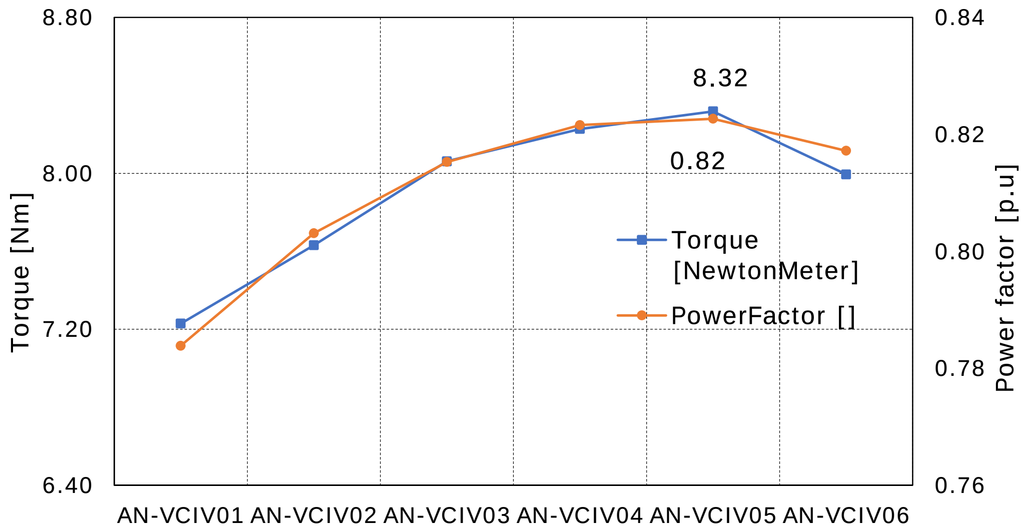

Figure 3-33: Analysis V - Case IV: Torque and power factor with respect to design

On the other hand, the saliency ratio, even though increased compared with case III, but has not seen the same increases that have been between the cases I, II and III. It clearly shows that increasing the number of barriers with the same insulation ratio will increase saturation. However, it could be different for other insulation ratios.

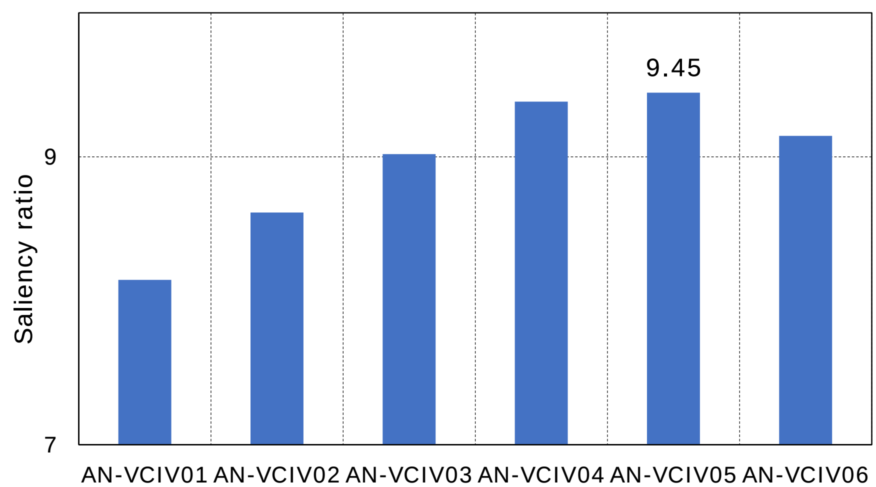

Figure 3-34: Analysis V - Case IV: Saliency ratio with respect to design

Case V: Six barriers

In this study, six barrier designs are studied, as shown in Figure 3-35. Unlike other studies, the barriers are organised, such as the end segment (further studied in detail in section 4.8.3) is not narrowed. Hence, the saturation impact is minimised for a large number of barrier designs. The simulation results torque and power factor, are plotted in Figure 3-36, and the saliency ratio is plotted in Figure 3-37. The torque increases gradually for moving barriers while power reached a maximum for AN-VCV04 and slightly dropped for the last design and same is true for saliency ratio.

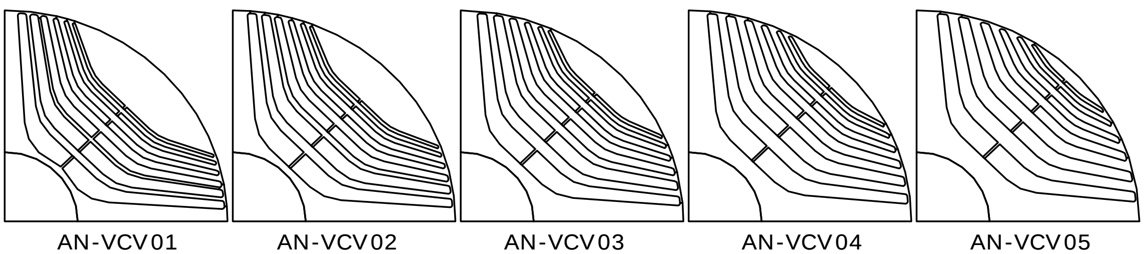

Figure 3-35: Analysis V - Case V: six barriers studied for varying location

Although the torque is improved slightly compared with case IV, the power factor remains the same due to the increase in the number of barriers. The saliency ratio is also slightly increased in this case by 1 % compared with case IV.

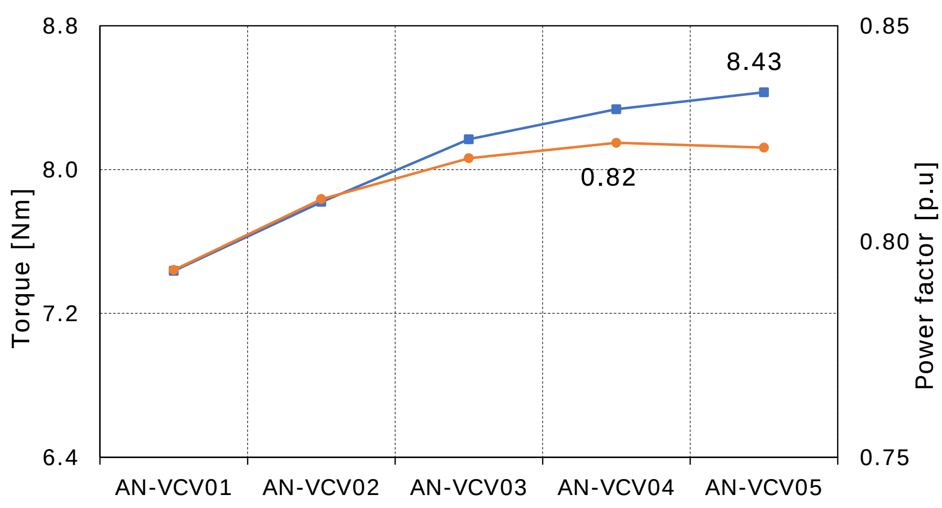

Figure 3-36: Analysis V - Case V: Torque and power factor with respect to design

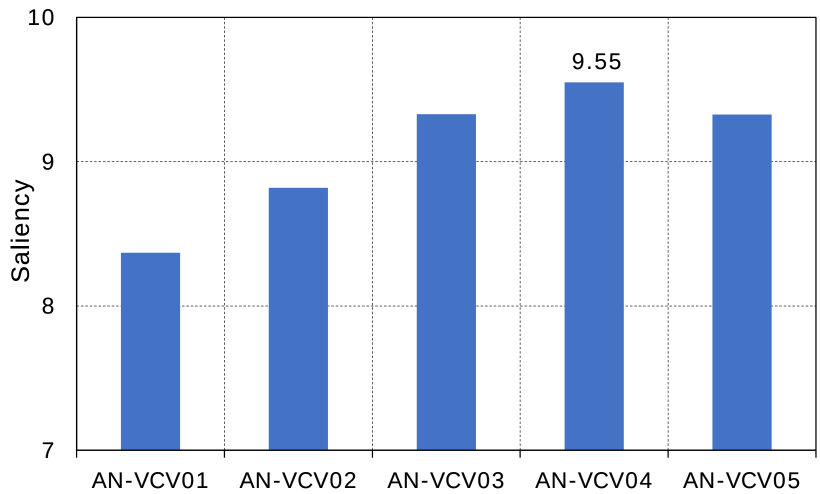

Figure 3-37: Analysis V - Case V: Saliency ratio with respect to design

Case VI: Seven barriers

In this study, seven barrier designs are investigated. It becomes almost a distributed anisotropy design due to the high number of barriers. Similar to case V, this study also focusses on barrier arrangement to have a higher number of barriers towards the circumference, as shown in Figure 3-38. The simulation results of torque and power factor are plotted in Figure 3-39 and saliency ratio is plotted in Figure 3-40. The design AN-VCV04 produces a maximum torque of 8.46 Nm, but its power factor is similar to previous cases. The saliency ratio is also slightly increased by 0.4 %.

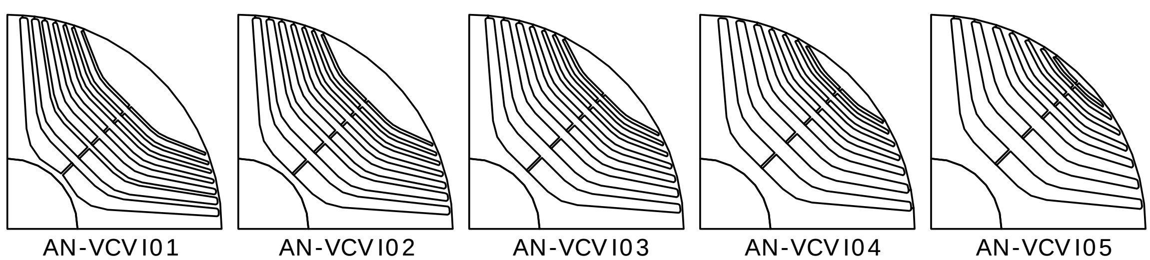

Figure 3-38: Analysis V - Case VI: seven barriers studied for varying location

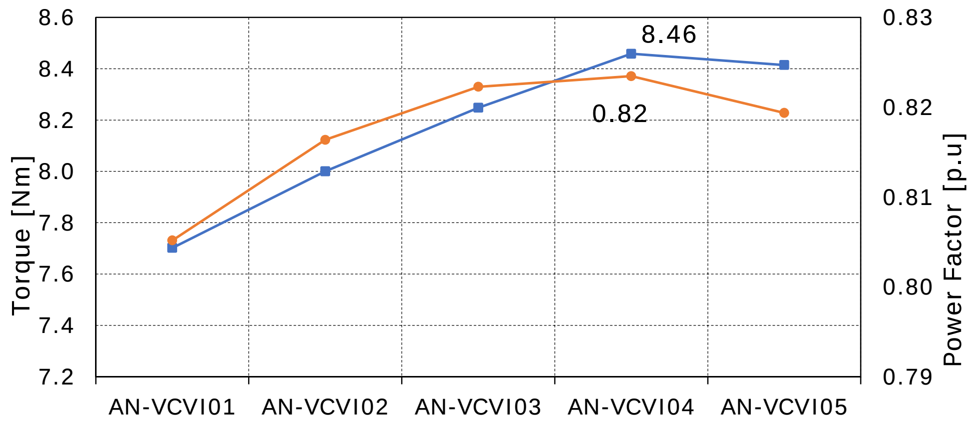

Figure 3-39: Analysis V - Case VI: Torque and power factor with respect to design

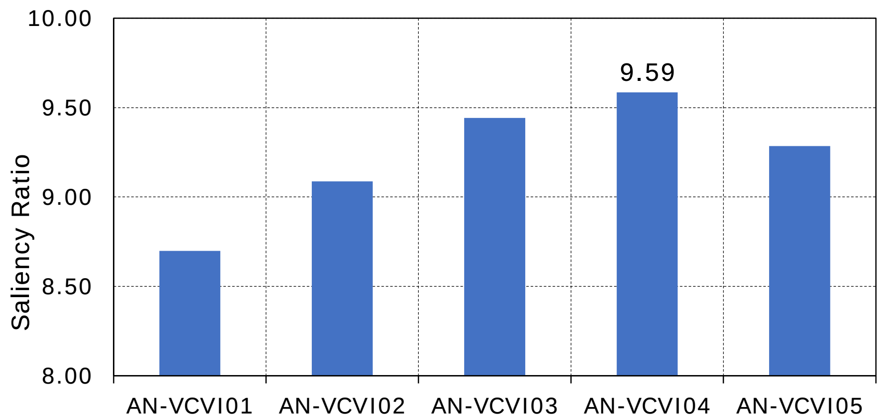

Figure 3-40: Analysis V - Case VI: Saliency ratio with respect to design

Although the saliency ratio has increased slightly (0.4 %) compared with case V, further increase in saliency is an immense challenge. The insulation ratio is constant, the number of barriers is the same for each case. The saliency ratio and performance are still different between those designs in each case. The only change is the location of the barriers. It shows the importance of the barrier location. Although high torque density is possible with a high number of barriers but rather with proper placement of barriers. The increase in the number of barriers, alone without proper arrangement, will not improve the machine performance.

This study reveals the importance of the number of barriers, placement of barriers, and insulation ratio. The optimisation of all three parameters is essential for a SynRM design. Although the saliency ratio is the critical component in SynRM, it is alone will not yield the best performance as the dominant parameter. The saliency ratio optimisation, coupled with other parameters is essential to design the best machine. On the other hand, the best design in each case had the same power factor, and torque is slightly increased for the higher number of barriers as given in Table 3-5.

Table 3-5: Overall results of maximum torque, power factor and saliency

Number of Barriers	Max torque [Nm]	Max power factor [p.u]	Max efficiency [%]
2	7.72	0.78	85.07
3	8.00	0.80	85.62
4	8.33	0.82	85.66
5	8.32	0.82	85.68
6	8.43	0.82	85.67
7	8.45	0.82	85.8

From Table 3-5, it can be concluded that the higher the number of barriers, the better the machine performance. However, the statement is valid in term of theoretical analysis. In terms of practical aspects, many other parameters need to be looked into before deciding the number of barriers. The most crucial factor is the machine's mechanical integrity. If the number of barriers is increased, the mechanical strength of each segment can be weaker, and ribs and webs will not have enough strength to hold the structure. The structure is susceptible to deformation due to a slight increase in temperature during high-speed applications.

3.6.6 Impact of Ribs and Webs

Tangential ribs and radial webs are there in order to hold the transversally aligned segments together in a TLA structure (as shown in Figure 2-17). They are essential elements of the TLA rotor. The design of the ribs and webs are significantly important as it can reduce machine performance if it is not correctly sized. As already discussed, they act as a flux carrier in the Q axis path, thus adds to the Q axis flux. However, their existence is essential. The impact can be minimised by adequately designing them so as they are saturated at low currents.

In some cases, the radial webs are not required if the tangential ribs are strong enough. Hence, a study of the structure with and without webs are essential. In this section, two types of rotors are analysed one with ribs and webs, and the other with ribs only while the webs are removed from the rotor structure. When webs are removed, an adequate mechanical strength may be required via other means to the entire rotor for high-speed application. It can be achieved by re-sizing the ribs.

Case I: SynRM rotor with ribs and webs

In this section, the SynRM rotor with both ribs and webs are investigated and optimised. The study is conducted with two cases, first with the rib and web sized equally in each design. In the second case, the rib and web sizes are not kept equal somewhat increased in a step manner.

Case I(a): Rib and Web sizes are equal

In this case, the rib and web sizes are equal throughout the study. The rib and web thicknesses are varied from 0.2 mm to 2 mm. As 0 mm thickness is not practically feasible, the smallest size selected is 0.2 (although practically it is not strong enough) and then it is equally distributed for the five analyses, as shown in Figure 3-41. All other parameters are maintained constant except the rib/web size. The results of torque and power factor are plotted as a function of rib thickness in Figure 3-42.

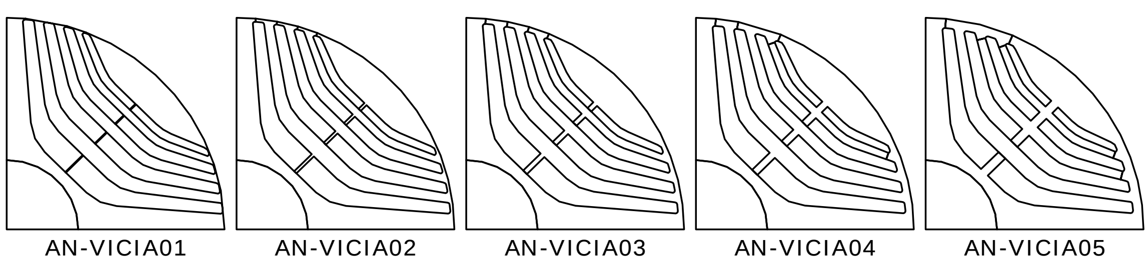

Figure 3-41: Analysis VI - Case I(a) rib and web sizes are equal in each design

Figure 3-42 shows the torque and power factor with respect to barrier ribs and web width. Where the highlighted area marks the rib size that is not suitable for practical applications. The rotor segments need enough strength to hold the transversally aligned segments even for a small range SynRM small as 0.5 kW. Therefore, the highlighted area can be ignored for this investigation. However, it is apparent that the increase in rib size linearly reduces machine performance. A SynRM machine of 1.00 kW need at least 0.50 mm to withstand high-speed applications. It is evaluated and discussed in section 6. The increase in size from 0.50 mm to 1.00 mm reduces the torque by almost 10 % and power factor by 7.30 % while from 0.50 mm to 2.00 mm reduces the torque by 31.60 % and power factor by 23.20 %, respectively.

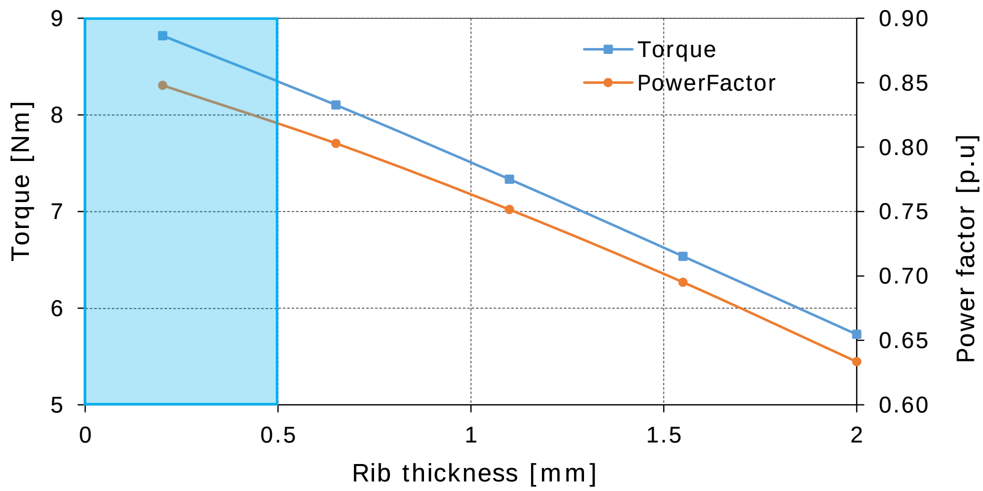

Figure 3-42: Analysis VI - Case I(a) torque and power factor as a function of rib thickness

As discussed earlier, the saturation of the ribs and webs are critical in achieving high performance. The reason for the reduction in torque and power factor is that the ribs are not saturated enough in the large size designs. The saturation of selected three models is shown in Figure 3-43. The smaller the ribs size, the quicker the saturation occurs and does not allow any more flux to pass through. On the other hand, the bigger ribs, as in the figure, take longer to saturate (depending on the current level). On the other hand, due to the small ribs size, the segments can be saturated, as shown in Figure 3-43 (0.20 mm).

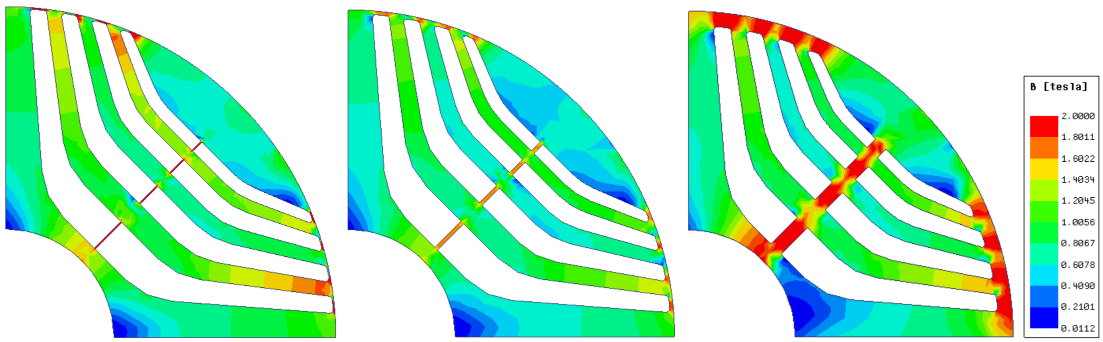

Figure 3-43: Analysis VI - Case I(a) saturation of the selected three models from left to right model 0.2 mm, 0.56 mm and 2.00 mm, respectively

Case I(b): Variable Ribs and Webs

In this study, the rib and web sizes are varied independently using two variables in the parameterisation process using the same model in case I(a). The rib and web thickness are varied from 0.2 mm to 2 mm. The results are plotted in Figure 3-44 and Figure 3-45.

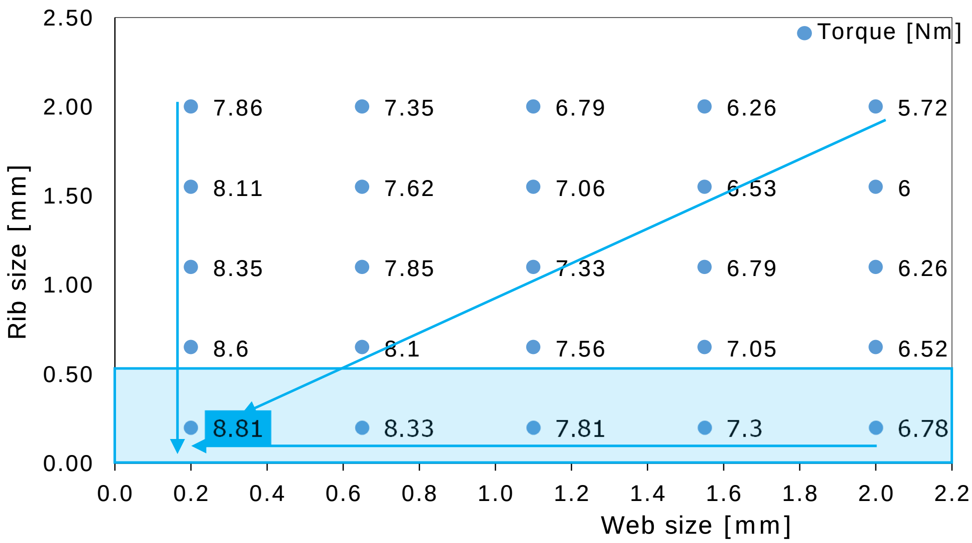

Figure 3-44: Analysis VI - Case I(b) torque as a function of rib and web thicknesses

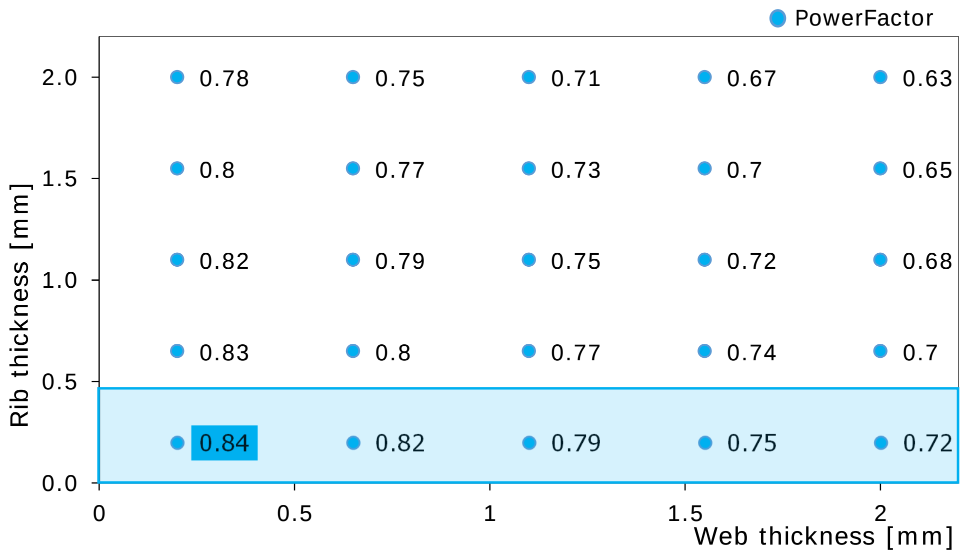

Figure 3-45: Analysis VI - Case I(b) power factor as a function of rib and web thicknesses

The web size is less than 0.5, mm can be tolerated to a certain extent, but rib thickness less than 0.5 mm is not practically strong enough to provide required mechanical strength. The maximum feasible torque and power factor are attained in this case for a combination of the same rib size and web size. The results are quite similar to the case I(a). Therefore, the highlighted area, in the simulation results, should not be considered though the maximum torque is obtained for the smallest rib and web combination. On the other hand, smaller size web can deform due to change in temperature and acting radial forces towards the circumference during high-speed application. Hence, serious deformation of the rotor can make contact with stator inner surface and damage the machine. Thus, ribs and webs are to be designed so that the mechanical integrity is not compromised.

Case II: SynRM with only ribs (no radial webs)

Generally, a SynRM is designed with webs to provide the necessary mechanical strength. However, if the SynRM is used as PMSynRM, then the web will obstruct the PMs. Hence, the SynRM should be designed without webs. Although, some researcher use dual webs on both sides of the PMs [209, 210] and other researchers use webs in the middle with PMs on either side [108, 211, 212].

However, for special high-performance machines, the web is eliminated with thicker rib size [111, 183, 213]. SynRM with no webs is studied in this section. Five different designs are simulated for rib size varying between 0.20 mm and 2.00 mm, shown in Figure 3-46. The model used for the case I(a) and I(b) is also used here to maintain the consistency between the three cases. The simulation results, torque, and power factor are shown in Figure 3-47.

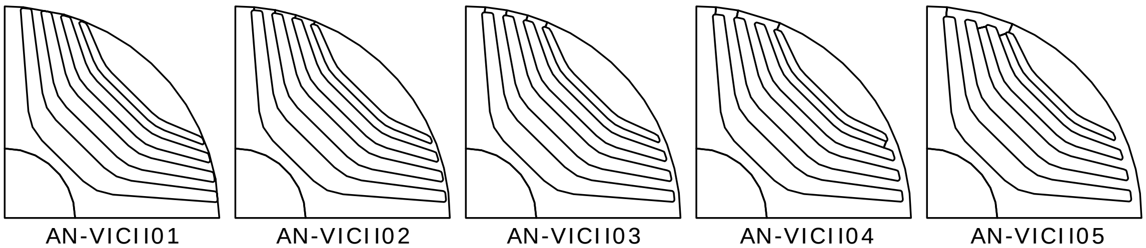

Figure 3-46: Analysis VI - Case II SynRM with only ribs

The results show that the torque and power factor of the design AN-VICII01 gained 4 % and 2.90 %, respectively compared with its equivalent design with webs (AN-VICIA01). Similarly, AN-VICII02 gained 8.00% and 5.80 % torque and power factor over AN-VICIA02. This study has revealed that SynRM that used for PMSynRM without any webs, can have naturally higher performance if the ribs are optimised even before PMs are inserted. Based on the above findings, this study recommends mechanical analysis in order to finalise the rib size as it is based on the mechanical integrity requirement.

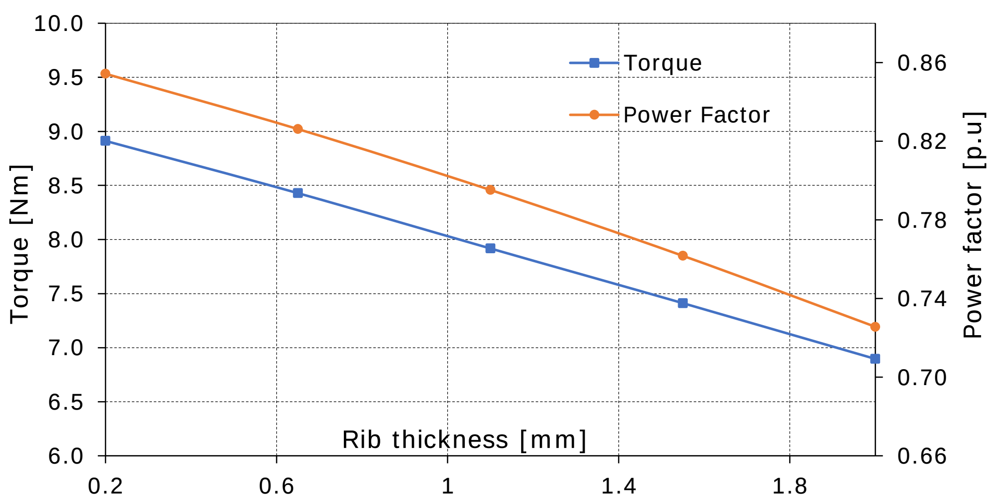

Figure 3-47: Analysis VI - Case II torque and power factor of rib only designs

3.6.7 Air-gap Length and Flux Density

It is well known that large air-gap will result in poor machine performance. As discussed in section 2.1, the large air-gap length will increase the reluctance of both the D and Q axis. Furthermore, D axis current i_d defines the magnetic loading in the case of SynRM, which is dependent on the air-gap length. A large i_d will increase the angle between the current and voltage for the same supplied source as can be seen in Figure 3-48, resulting in reduced power factor. However, it is not always the case due to the cross-saturation for smaller air-gap lengths which will be discussed in the following. Thus, the air-gap length is one of the critical design parameters in any rotating machine.

The air-gap length is generally larger than manufacturing tolerance which is significantly high in traditional machines. However, the latest and sophisticated lamination technologies, such as medium speed wire cutting, can make laminations with the accuracy of $\pm 0.01\,mm$. It allows the designers to cut down the air-gap length significantly. On the other hand, the rotor and stator cores may expand, resulting in core deformation at high speed and overload applications, thus requiring critical analysis for air-gap length.

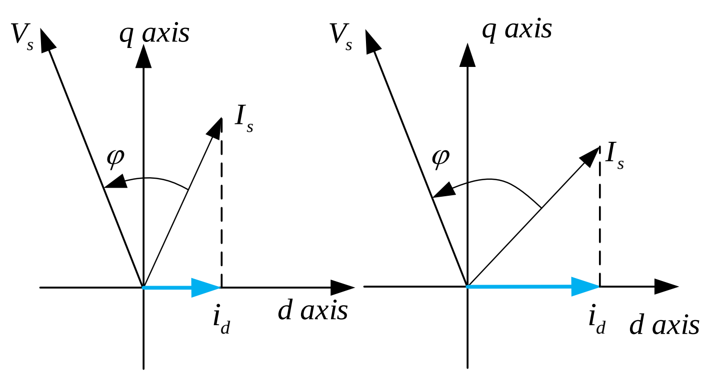

Figure 3-48: Phasor diagram of SynRM with two different D axis currents

In general, advanced small range modern machines can have air-gap length of between $0.25 - 0.50\,mm$, and some may have even higher. In this study, the significance of air-gap length is simulated using parameterisation tools. Air-gap length is altered by changing the rotor diameter between 90.2 mm (air-gap length is 0.9 mm) and 91.8 mm (air-gap length is 0.1 mm) (stator inner diameter 92.00 mm). The stator structure is not altered. The input and output power of the study is shown in Figure 3-49.

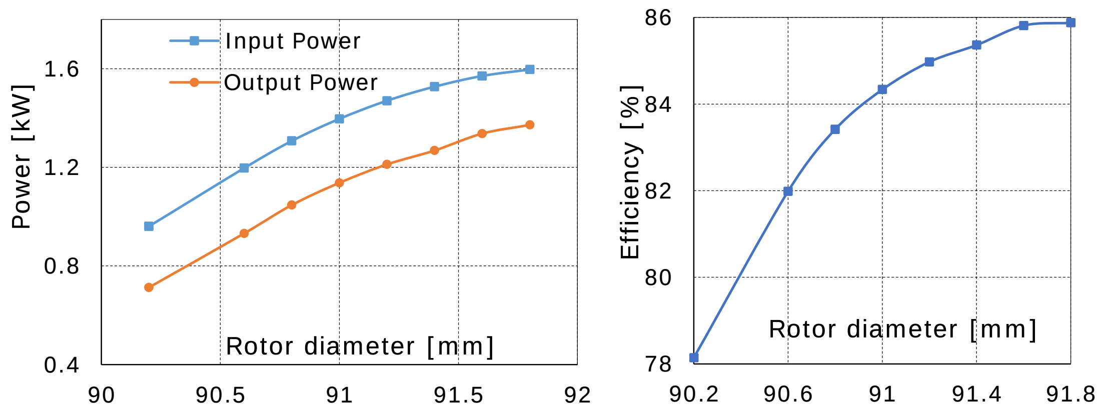

Figure 3-49: Analysis VII – Power (left) and efficiency (right) as a function of air-gap length

Both powers experience similar changes due to changes in the air-gap length. Nevertheless, the difference in input power of design with 0.9 mm and 0.1 mm is significantly high 39 % and the output power shows similar changes. The efficiency is shown in the same figure for the changes in air-gap length. The efficiency dropped almost 9 % for the difference in 0.9mm to 0.1 mm gap length. The changes in the efficiency with respect to air-gap length, validate the importance of having a smaller air-gap length, minimised as low as practically possible.

The torque and power factor of the simulation are plotted in Figure 3-50. The torque increases linearly with air-gap length while the power factor increases up to 0.4 mm and starts to drop in a non-linear manner for further increase in air-gap length. The changes in power factor are not much significant with other parameters. The saliency ratio is only dependent on DQ inductances. Both L_d and L_q are driven by resultant flux linkage, which is shown in Figure 3-51 along with DQ inductances. The changes in D and Q axes flux linkage and inductances against gap length is the reason for the drop-in power factor for smaller air-gap lengths.

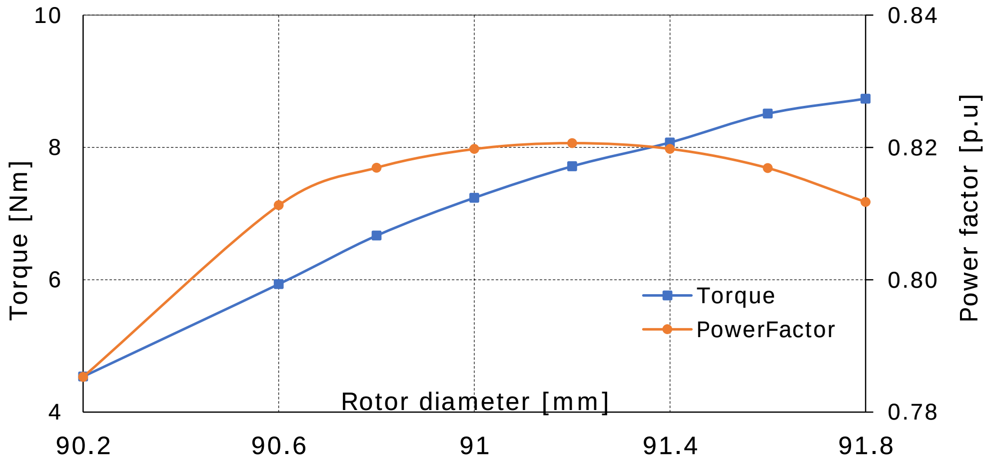

Figure 3-50: Analysis VII - Torque and power factor as a function of air-gap length

The D axis flux linkage has a rather rapid increase for a large air-gap length and lower rate of change for the rest of the gap length. While the Q axis flux linkage increases gradually for large gap length and rapidly increases for lower ones that make the DQ inductance to follow the same. It is replicated in the DQ voltages as well as flux linkages are shown in Figure 3-51. DQ frame voltages are obtained from the derivation of the flux linkage with respect to the time. As anticipated, the magnitude of both v_d and v_q are reduced for small gap lengths because the rate of change of flux linkage is less at small gap lengths. The DQ magnetising inductances are given in Figure 3-52.

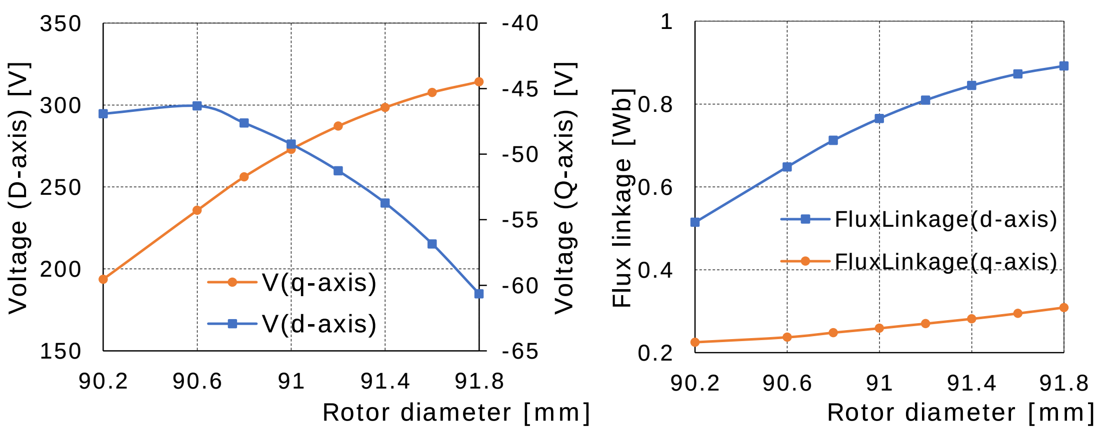

Figure 3-51: Analysis VII - DQ flux linkages and Inductances as a function of air-gap length

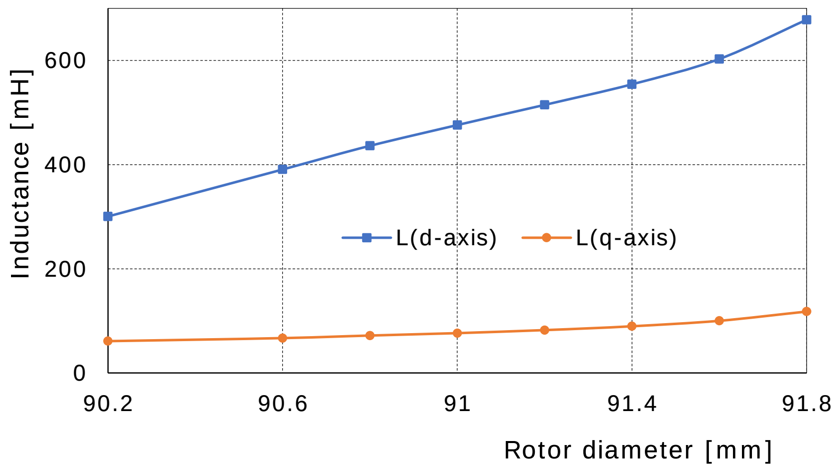

Figure 3-52: Analysis VII - DQ voltages and torque ripples as a function of air-gap length

The air-gap length has a significant impact on the D axis inductance and flux linkage compared with Q axis counterparts. Because the D axis flux directly crosses the air-gap to reach rotor whereas the Q axis flux crosses air-gap, ribs and then barrier where the barrier insulation length is much higher. The study reveals that a smaller air-gap length does not guarantee machine performance.

3.6.8 Impact of Non-Magnetic and Magnetic Shaft

PM machines use a non-magnetic shaft to achieve high machine performance, applications that use anti-friction bearing. However, it is a question in the case of SynRM whether to use non-magnetic or magnetic steel for SynRM. Few studies are published on this topic regarding the material for the shaft. As SynRM performance is dependent on increasing the saliency to segregate the magnetic axes. It is essential to understand the field intensity along with the rotor and shaft space. Figure 3-53 shows the field intensity around a SynRM space. The intensity of the field is very high closer to the circumference and quite low along the shaft and almost zero within the shaft. Three different shaft materials are considered to verify the above statement. The flux lines diagram of all three designs is shown in Figure 3-54.

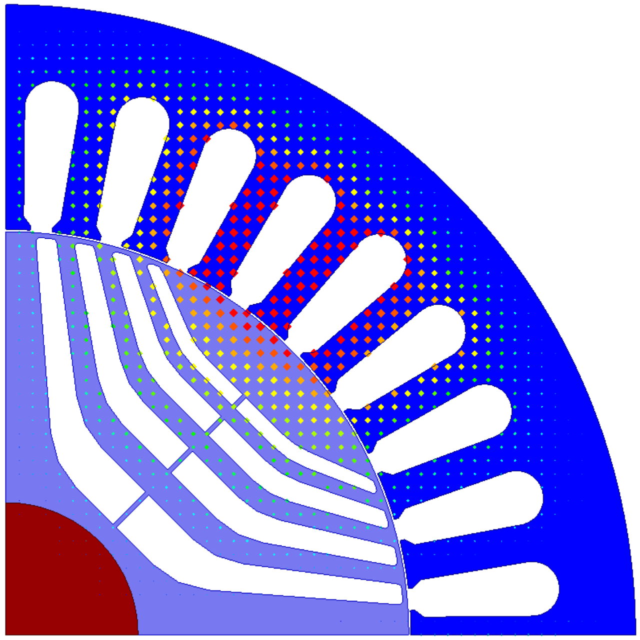

Figure 3-53: Analysis VIII - flux density vector diagram

Although some flux lines pass through the shaft on a magnetic steel shaft, the flux linkage through the air-gap is not affected, as shown in Figure 3-55. A magnetic shaft, in theory, should improve the Q axis flux path. However, in this case, the DQ inductances are not significantly impacted due to low flux intensity around the shaft area. All three models have exactly similar D and Q flux linkages. The only publication that analysed shaft in detail also reported similar results [214].

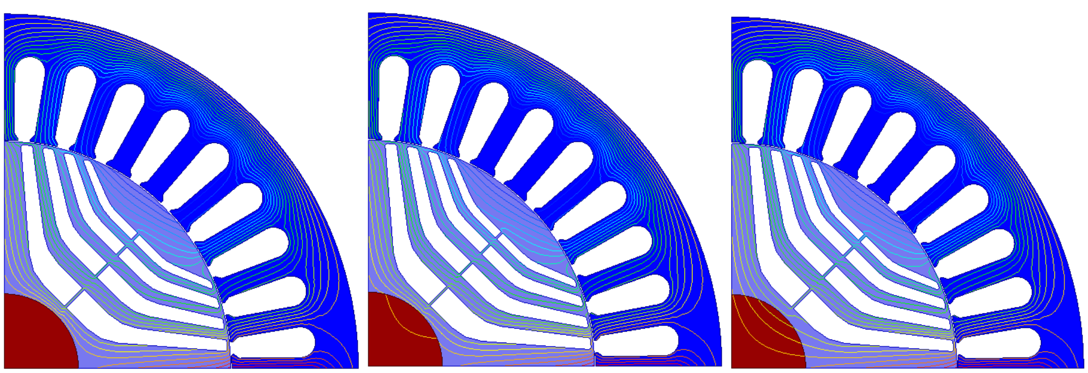

Figure 3-54: Analysis VIII - three different shaft materials are simulated using the same rotor those are Non-magnet shaft on the left, regular steel (1010) shaft on the centre and magnetic steel shaft (M400-50A) on the right

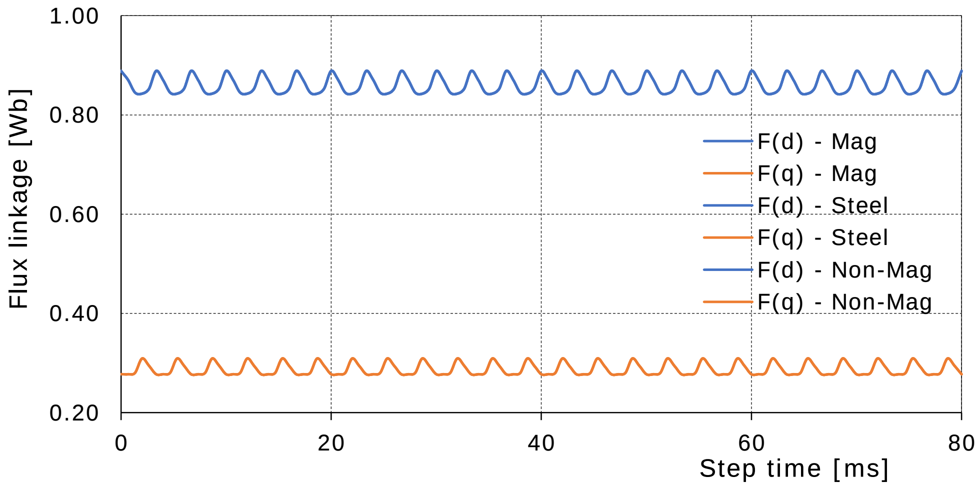

Figure 3-55: Analysis VIII - flux linkages for three different shaft materials

As can be seen, D and Q axes flux linkages of all three designs are equal and not affected by shaft material. Thus, the shaft material does not play any critical role in the case of SynRM as it does for PM machines.

3.7 Impact of Saturation

Analytical investigation of saturation in a highly complicated non-linear magnetic circuit such as SynRM as discussed in section 2.6. FEM tool must be utilised to understand the total effect of saturation. This section investigates the saturation effects in-depth. The rotor and stator slotting effect, end coil resistance, end coil inductance, leakage flux and inductance, coil and lamination insulation are all included in this study to cover the complete practical model. In addition, the practical losses of the machine have been obtained by experimental results and are also fed into the FEM tool for precise results. The study is conducted on the same design from section 0 case I(a). The simulated results are plotted in a 3D graph for intuitive analysis. The torque as a function of current and rib thickness is plotted in Figure 3-56.

As reported in [104] and the above studies, the impact of saturation on the torque is minimal compared with other parameters. However, Figure 3-56 compares torque of smaller and thicker ribs for varying currents where thicker ribs are not saturated enough to stop flux passing through them. It has resulted in a drop-in torque. It is worth noting that for lower currents up to almost 2 A, the machine does not develop the torque regardless of rib size, as it is used for magnetising the core. Regardless of the rib size, the characteristic of torque for change in current is not impacted. The torque is dependent on the magnetising inductance, is quite linear with increasing current as it increases the magnetising inductance. It is not the case for power factor and efficiency. The power factor depends on terminal inductance and does not increase further as increasing currents are wasted in saturating the core.

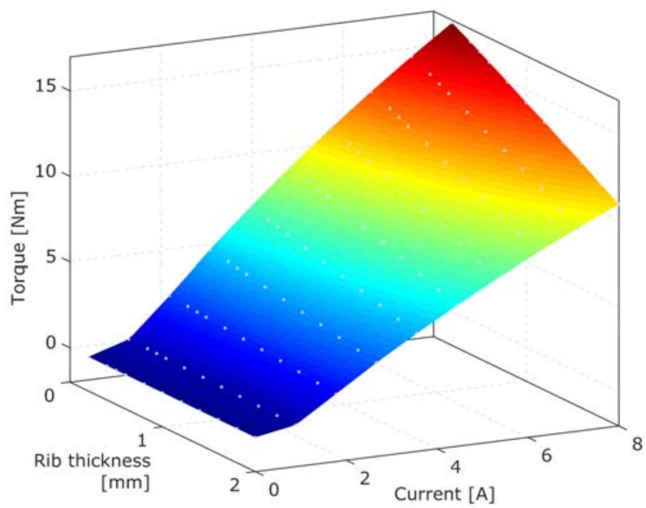

Figure 3-56: Analysis IX - Torque as a function of rib size and supplied current

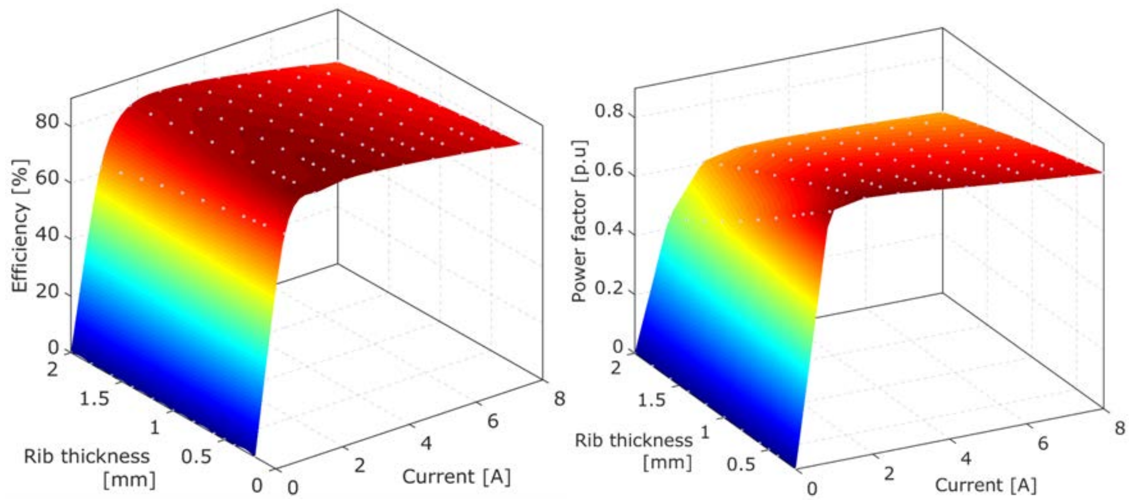

Figure 3-57: Analysis IX - Efficiency and power factor as a function of rib size and current

The efficiency and power factor experience high saturation, as shown in Figure 3-57. When the current goes above rated value, the ribs are fully saturated. The higher currents not only saturate the ribs but also saturate rotor core, especially the tiny segments resulting in reduced efficiency. Smaller size ribs improve the machine performance such as torque and power factor significantly as shown in the figures. However, it does not significantly change the efficiency. The saturation of DQ flux linkages is plotted in Figure 3-58. D axis flux linkages are shown in dots to distinguish it from Q axis flux in the figure. As can be seen, F_d is higher for smaller rib designs with current increases whereas, F_q experience the opposite effect.

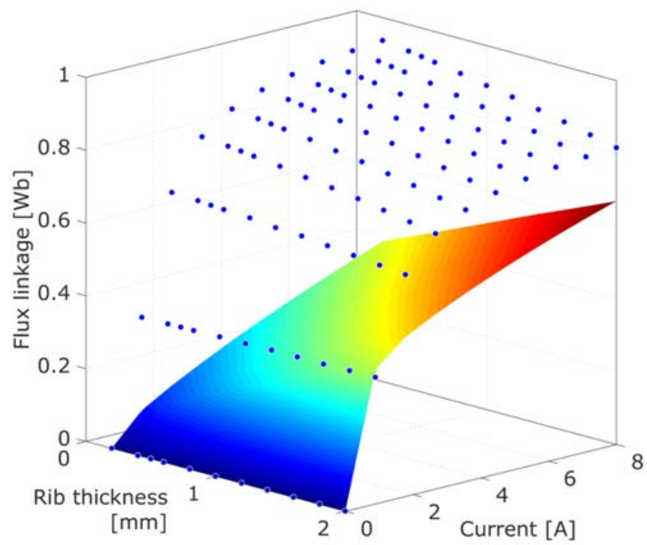

Figure 3-58: Analysis IX - DQ flux linkage as a function of rib size and current

3.8 Core Losses

The core loss in an electrical machine accounts for a significant percentage of total losses. The loss is vital to understand the performance and efficiency of the machine. In some machines, the core loss is nearly 15 % to 20 %, and it can be even higher in PM synchronous machines. In general, the magnetic steel manufacturers provide an estimated core loss data that can be fed into FEM tool's material library (if not already included) to model core loss for a particular design. However, the non-linear magnetic model in SynRM and PM machines makes it harder to model the core losses as conventional curve fitting cannot be implemented in these machines.

The core loss in the electrical machines is given by Eq. (3.12) [215].

$$P_c = P_h + P_e + P_a \tag{3.12}$$

Where P_h is hysteresis loss, P_e is eddy current loss and P_a is called excess loss. The loss can be further broken down as Eq. (3.13)

$$P_c = k_h f B^n + k_e f^2 B^2 + k_a (fB)^{\frac{3}{2}} \tag{3.13}$$

Where f is the frequency of applied magnetic field, k_h , k_e and k_a are lamination thickness dependent coefficients.

In order to model the core loss, it is essential to review the fundamental electromagnetic theory, also known as Maxell's equations in Eq. (3.14). The eddy current constant k_e can be obtained from Maxwell's equations as in Eq. (3.15) where $2L$ is steel lamination thickness.

$$\begin{aligned} \nabla \times \vec{E} &= -\frac{\partial \vec{B}}{\partial t} \\ \nabla \times \vec{H} &= \vec{J} + \varepsilon \frac{\partial \vec{E}}{\partial t} \\ \vec{J} &= \sigma \vec{E} \end{aligned} \tag{3.14}$$

$$k_e = \frac{(2L\pi)^2 \sigma}{6} \tag{3.15}$$

Like k_e, other coefficients can also be broken down to show the correlation with lamination thickness, but it is not the scope of the present study. The Eq. (3.13) shows that the core loss can be minimised by merely using laminations. In order to achieve low core loss, 0.50 mm lamination is used in present study. The stator and rotor core losses are modelled into the equivalent circuit, shown in Figure 2-6 and accounted in the torque Eq. (2.27). The total core loss of a DQ frame can be typically defined as given in Eq. (3.16)

$$P_{coreloss} = \omega^2 \left(\frac{\lambda_{md}^2}{R_{cr\_q}} + \frac{\lambda_{mq}^2}{R_{cr\_d}} \right) \tag{3.16}$$

And the core loss current can be defined as in Eq. (3.17)

$$i_{cdq} = \omega\left(\frac{\lambda_{mdq}}{R_{cdq}}\right) \tag{3.17}$$

Therefore, the core loss not only stator and core iron volume dependent, but also current dependant. It reduces output power as well as increases the terminal current angle. The time-harmonic technique is utilised to model the core loss of SynRM in FEM tool for faster results. As the magnetic circuit of the machine is not linear, the curve-fitting method is typically utilised to determine the core loss constants in FEM tool.

The following study to investigate the core loss is also conducted on the same design from section 0 case I(a). The study results are plotted in 3D using a curve fitting technique and a nearest neighbouring tool to clearly understand the changes with respect to rib thickness, as shown in Figure 3-59. Although the changes in rib and web thickness are minimal in terms of the core volume, the results show a slight difference in core loss with change in rib and web size. Thicker ribs add more to the volume, which leads to added core loss in comparison with smaller ribs. The core loss increases with current as per Eq. (3.17) which is validated with the simulation results. It is one of the reasons for poor efficiency for increasing current that was discussed in section 3.7.

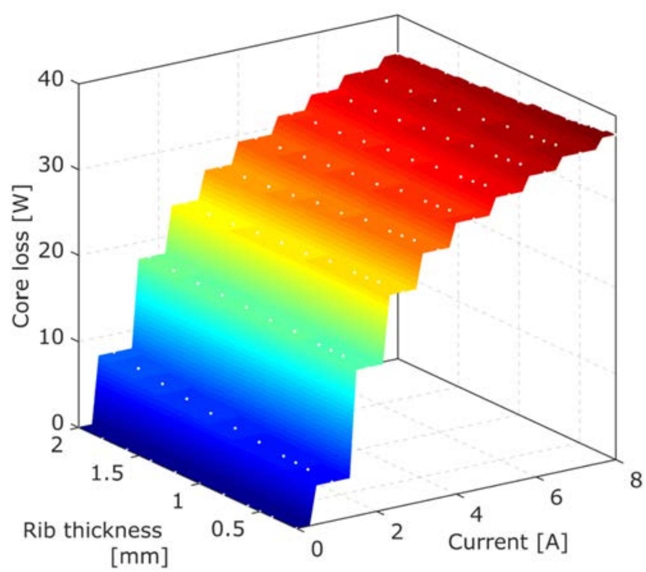

Figure 3-59: Analysis X - Core loss as a function of rib thickness and current

3.9 Impact of Cut-Off Design on Machine Performance

Historically, SynRM with grooves is well known, which are placed at the circumference parallel to other barriers. Some earlier SynRMs had very long depth notches. The grooves and notches are placed to naturally improve saliency ratio as researchers were trying to optimise SynRM with line start cages in the earlier rotors. Later in the history of SynRM, the grooves were found to be a primary reason for high torque ripples. They are removed from modern SynRM, and little is reported on the topic [216-220]. In this study, the groves are chosen relatively similar to the barrier shape to follow the same design topology, as shown in Figure 3-60 instead of notch shape. The reason is that notch shape introduces a shape edge on the reluctance path. The study conducted over 12 designs with grove's length varied from 5 mm to as low as 0.15 mm. The samples of five designs are shown in Figure 3-60.

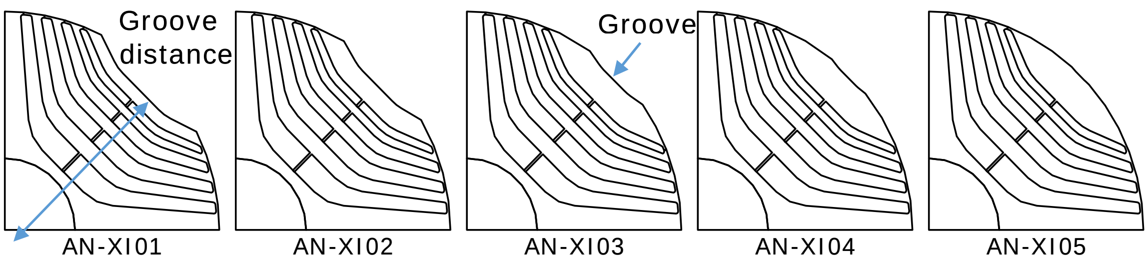

Figure 3-60: Analysis XI - SynRM with grooves, samples of 5 designs are shown out of the 12 simulated (groove depth from left: 5 mm, 3 mm, 2 mm, 1 mm and 0.15 mm)

The saliency ratio and torque of the simulation are plotted as a function of groove distance from the centre in Figure 3-61. The study confirms that the grooves can enhance the saliency ratio close to 10. The saliency ratio to the groove depth is almost linear and proportional. The design with high groove depth exhibits a 31 % increase in saliency ratio compared with the design that has no grove. It was already proven that the groove could enhance saliency and performances, the challenge in this type of design was the torque ripples.

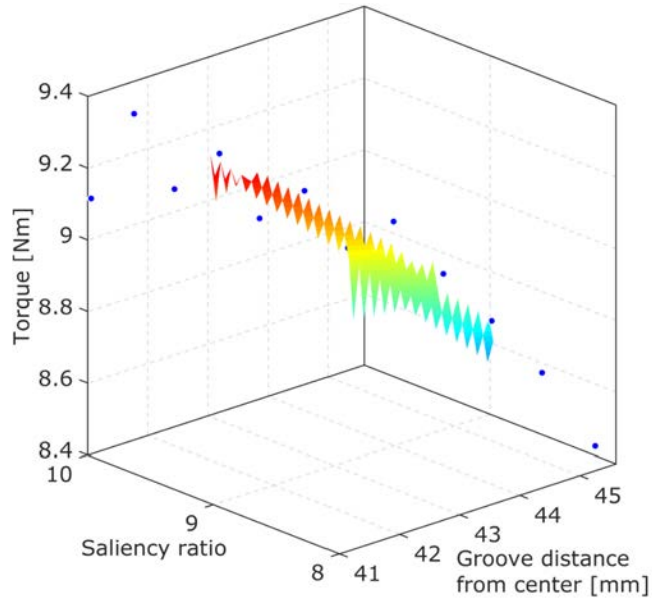

Figure 3-61: Analysis XI - saliency and torque as a function of the groove distance from the centre

The torque and torque ripples are plotted against the groove's distance from the centre of the rotor in Figure 3-62. The study found that for higher groove depth, the torque ripples are reduced while designs with mid-groove depth (between 3 mm to 1 mm) show high torque ripples. The study also reveals high groove depth significantly increased torque. The design with 5 mm groove produced 9.4 % more torque in comparison with a design without groove while torque ripples are also reduced by 4.58 %. The power factor followed a similar pattern as torque for the increase in depth of groove, as shown in Figure 3-63.

Note: the groove distance is defined by the length between the centre of the rotor and inner surface of the groove.

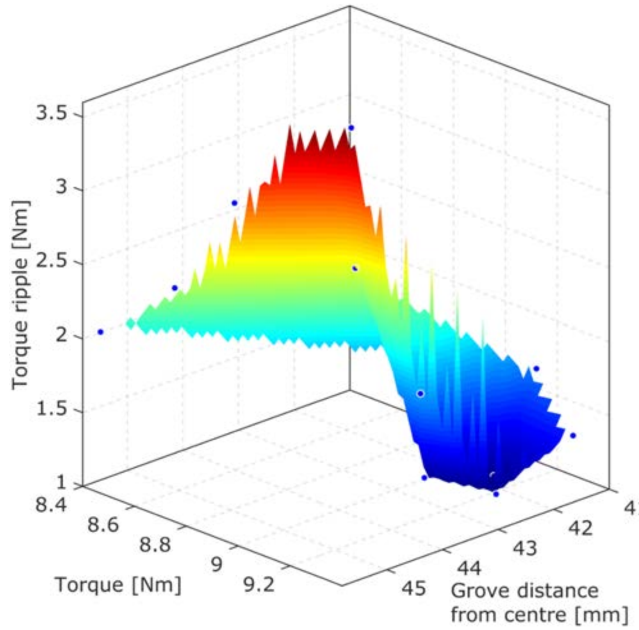

Figure 3-62: Analysis XI - torque and torque ripple as a function of the grove distance from the centre

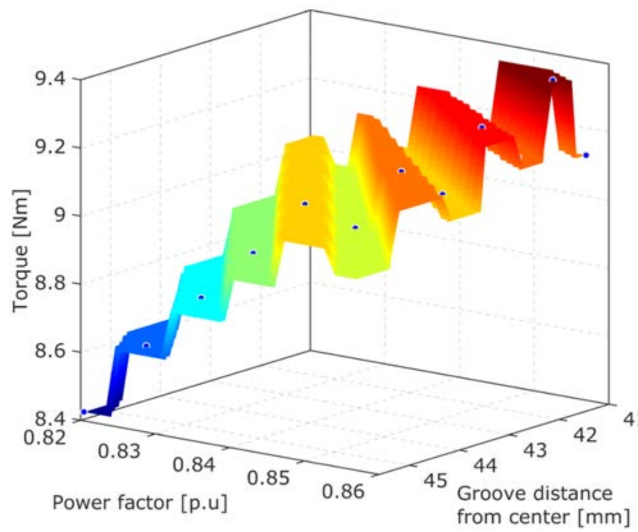

Figure 3-63: Analysis XI - torque and power factor as a function of the grove distance from the centre

This study confirms that with a proper optimisation process, a SynRM can be designed with low torque ripples and high performance compared with an equivalent machine without the groove.

3.10 Current angle

The changes in current angle change the load and torque angles, as already discussed in section 2.4.1 (Eq.(2.18)). It acts as an excellent element in SynRM control. This section studies the machine performance due to the changes in the current angle. The same design, used above, with 0.5mm ribs and webs, is used for this study without grooves. The study is conducted by applying current source at the rated condition, and the current angle changed from $0°$ to $180°$. As already discussed earlier in section 2.4.1, the current angle is responsible for torque development in SynRM. At current angle equivalent to $0°$ Q axis current i_q is at 0 A (refer to Eq. (2.30)). The torque will not be developed at this condition. When the current angle is gradually increased i_q increases to increase the torque (as shown in Figure 3-64).

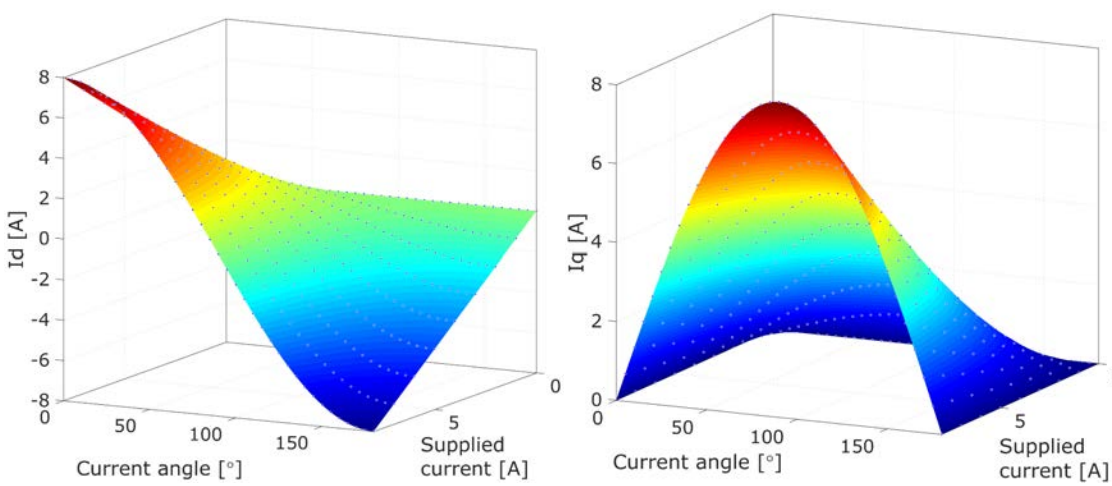

Figure 3-64: Analysis XII - DQ current changes with respect to the current and current angle

Figure 3-64 shows D and Q currents with respect to supplied current and current angle. The unique characteristic is an excellent choice in controlling the machine. D axis current i_d changes from positive to negative for the changes in the current angle as it is the cosine function of the current angle. Whereas the i_q is the sine function that follows sinusoidal changes for $180°$ changes, both aligned with the phasor diagram of SynRM. On the other hand, the changes in the current angle change the power factor as already discussed in 2.5.2. The saturation and cross-saturation drift the maximum power angle away from its theoretical value of $45°$ as shown in Figure 3-65. Unlike PM machines whose motoring cycle is $45°$, SynRM's motoring cycle is $90°$ as we have already seen. The figure shows motoring and generating cycle throughout the $180°$.

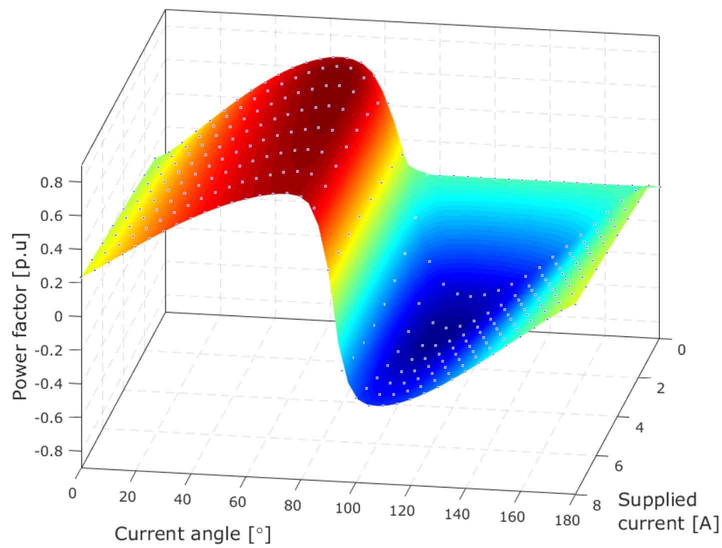

Figure 3-65: Analysis XII - power factor as a function of the current and current angle

The current angle of maximum power factor changes with current but only slight change and within $73°$ to $78°$. The maximum power factor of 0.86 $p.u$ is obtained for 3 A (peak-peak) case which is below the machine's rated current at the current angle of $75°$. As it is already seen in theoretical analysis, the maximum power factor drifts away from its theoretical value of $45°$ (shown in Figure 2-12). However, it is even shifting more from the theoretical values in a practical case. The maximum power factor experiences high saturation as it was already discussed in section 2.5.2.

Similarly, the torque of SynRM shows the same characteristics as in Figure 3-66. The maximum torque of simulated case drifting away from its practical prediction (shown in Figure 2-10). Unlike power factor, the maximum torque does not experience significant saturation effect thus, it increases with current. The maximum torque is obtained at $65°$ regardless of the supplied current. It must be noted that the maximum torque angle does not change with increasing current, which makes this machine for torque control.

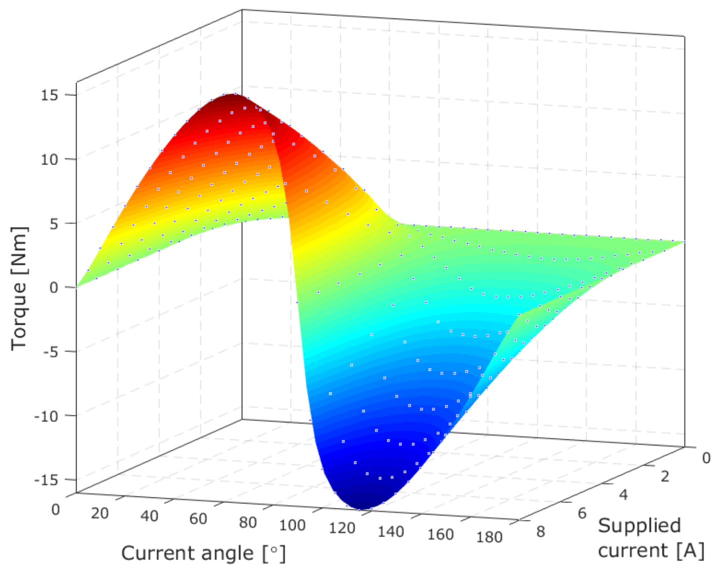

Figure 3-66: Analysis XII - torque as a function of the current and current angle

Therefore, the current controller is one of the best options for SynRM due to its unique characteristics with torque.

3.11 Barrier end profile

One of the often-ignored features in SynRM design is its end barrier profile. The design of the barrier end profile is very challenging and the only way to analyse it is using FEM. Though it is tiny and ignorable in terms of the core, its impact during optimising barrier shape for low torque ripples is substantial. Few studies have been published on this topic [165, 200, 221]. Figure 3-67 shows the changes in barrier profile for changes in barrier end radius. A sample of 0 mm radius end profile to 0.75 mm end profile is shown in Figure 3-67. However, the radius of each barrier for the same design is kept the same. As can be seen, the barrier radius has a limit which is primarily limited by the end barrier thickness to suit the design. Thus, the end profile radius of a design is determined by the thickness of the smallest barrier, typically the last barrier in the design.

Six different designs are simulated by varying the radius in this investigation for an optimised design. The torque ripples and saliency ratio of each design is plotted in Figure 3-68 as a function of the end barrier radius. The torque ripple is reduced by 48 % by merely changing the end barrier radius from 0.00 mm to 0.75 in a design. This novel approach will be further discussed in the subsequent section 4.6 for practical applications. On the other hand, the saliency ratio is dropped by 3.4 % for the same change in the radius that resulted in a drop in performance, as shown in Figure 3-69. The torque and power factors are reduced by 1% for the same change in the end barrier radius.

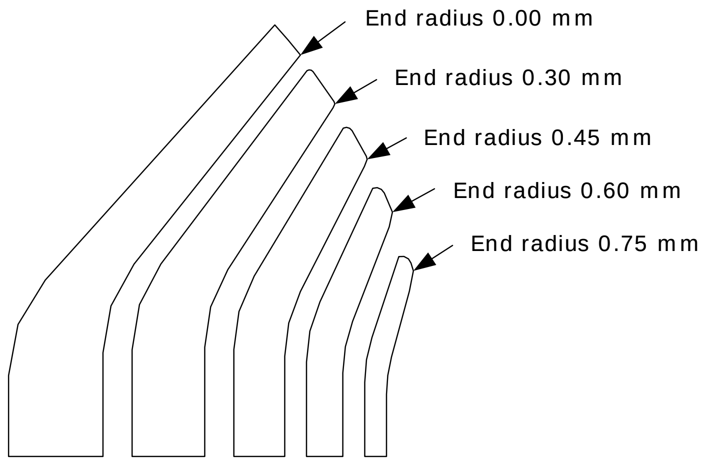

Figure 3-67: Flux barrier end radius of five barriers that are simulated for this study

The smooth end barrier profile can help to reduce the torque ripples. It has a drawback as it impacts the machine performance. However, the drawback can be tolerated as it always in the range of 1 % regardless of the machine size.

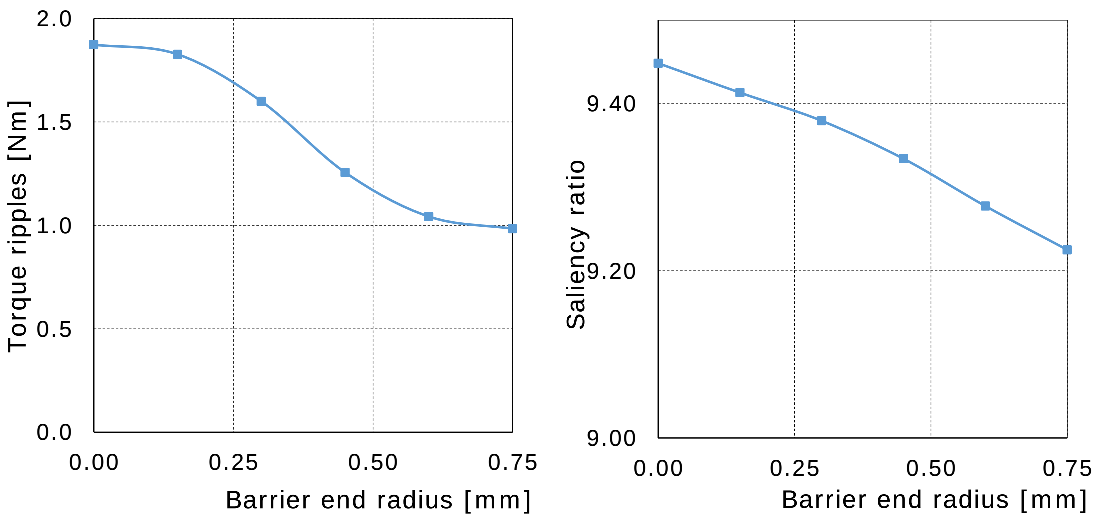

Figure 3-68: Analysis XIII - Torque ripples and saliency ratio changes as a function of barrier end radius

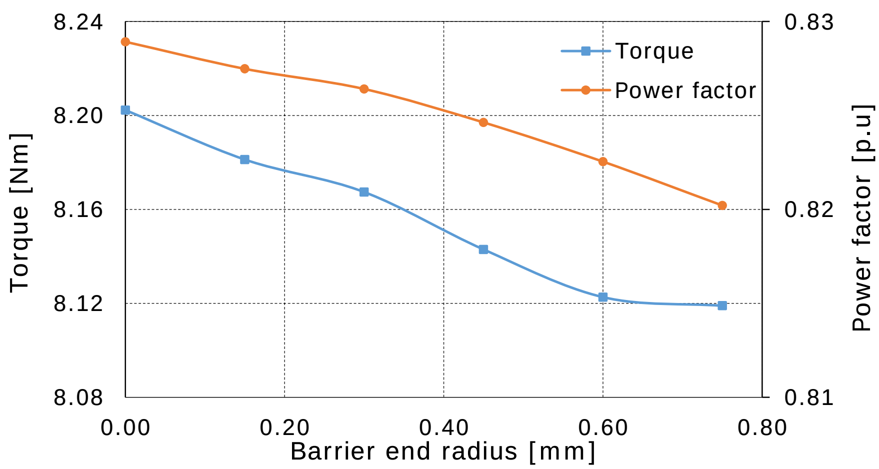

Figure 3-69: Analysis XIII - Torque and power factor as a function of barrier end radius

3.12 Conclusion

This section investigates the machine in a simulation environment using an advanced FEM tool. Design meshing is one of the most critical items in the modelling and simulation of SynRM. It makes sure the results are accurate. An advanced technique, especially for rotating machines, is introduced in this section to improve the meshing (in section 3.2) only around the critical area such as air-gap and stator slots. This section also modelled the base SynRM in FEM.

The average solutions of SynRM such as torque, power factor, efficiency, core-loss DQ currents, DQ flux linkage and DQ voltages are not in-built in Ansys Electronic Desktop. The average solutions have been developed in this section via output parameters based on the analytical models developed in section 2. The machine performances are determined using the developed average solutions. Researchers have used various shapes of flux guides for SynRM. This study finds an optimum barrier shape that can yield the best performance. And using the barrier shape and further simulations, it also develops a multi-barrier design for high performance.

SynRM rotor dimensions such as barrier location and number of barriers are investigated by utilising parameterisation method to define the optimum rotor. The tangential ribs and radial webs are investigated as never before using primitive barrier design techniques, and an optimum rib and web sizes are defined for small range machines. The study further investigates the saturation and cross-saturation effects on the machine special on flux linkage. An alternative solution is proposed to avoid unnecessary saturation and cross-saturation. Core-loss of a SynRM is has been defined methods are proposed to model in the simulation environment. A cut-off design has also been revisited with advanced FEM simulation and solution to improve the machine performance is proposed.

4 OPTIMISATION OF MACHINE PERFORMANCE PARAMETERS

4.1 Introduction

Analytical method lays a platform to define the necessary specification of SynRM. Due to the highly complicated non-linear magnetic circuit in a SynRM, it is not easy to model it by an analytical formula. Although the literature on the SynRM derives equations, they are based on many assumptions thus, the outcome is not always nearly as a practical rotor. Notably, in the case of SynRM, the dimensions should be highly precise to obtain a machine with not only better torque and power factor but also with acceptable torque ripples.

On the other hand, the FEM is a great tool to model the SynRM non-linear magnetic circuit. In FEM, all the practical elements that cannot even be considered in an analytical method such as end coil inductance and end wire resistance, eddy current effect and core losses can be included to its precise core. If the machine is properly modelled, the results are almost as accurate as a prototype. However, the question is, can it be adequately modelled at first attempt. Based on the above studies, there are numerous factors that should be looked into to model an optimum SynRM that is close to a real one. It requires highly precise detail to start the design process, which is very challenging to find from a rational design.

Hence, the solution to yield an optimum machine, FEM should be coupled with either parameterisation techniques or optimisation technique. Although parameterisation can predict the domain that the solution lies, optimisation can precisely find the answer if it is correctly handled. In the modern machine design practice, it is a common practice to couple FEM with optimisation to achieve the best solution. Otherwise, it will only be a trial and error process. In this section, the same primitive design discussed in section 3.3 is used as a sample for single-objective optimisation (SOO) and multi-objective optimisation (MOO) to reveal the significance of each optimisation.

This study exploits a computationally efficient optimisation algorithm in conjunction with FEM tool in order to optimise the predefined surrogate model. The optimisation algorithm uses response surface technique to determine the next solution, which is explained in the subsequent section. An existing algorithm which was designed to optimise PM Synchronous machine is used. The Sequential non-linear program is selected for the initial optimisations due to its fast and multivariable processing capabilities. Also, its outcome is relatively accurate, so fine-tuning is not needed. Another option is the utilisation of artificial intelligence techniques that can significantly reduce manual interaction and cost involved in machine design. However, the application of artificial intelligence with FEM tools on SynRM design optimisation is not encouraged because of the long process duration, and multiple selection scenarios involved in the design process [200].

4.2 Optimisation Algorithm

Electrical machine design optimisation is a step by step procedure. All algorithms necessitate the nominal problem to be closer to the optimal solution. Therefore, it is significant to specify a domain that is close enough to the optimal solution. As it involves a sequence of steps, the optimiser should be a sequential one to determine the next step for the lower cost function. After careful considerations, sequential non-linear programming (SNLP) is selected for this investigation over others because it handles the problem in more depth as well as it supports large scale design optimisation. SNLP is similar to sequential quadratic programming equally sequential and moves step by step toward a solution. However, in SNLP, the reference surface is in higher order that permits a higher number of variables (optimisation inputs).

The SynRM problem requires optimiser to handle continues variables (variable range is continuous) in sequential space. SNLP and Quasi-Newton (QN) optimisers assume that the noise is insignificant. From FEM approximation and determination of cost function, it makes a decent approximation of the cost function with regards to input variables which permits SNLP to determine the location of improvement points for the next iteration. General cost approximation of SNLP is more precise over other algorithms, which makes SNLP to reach a solution faster than others.

SNLP creates a response surface (RS) using Tayler series from previous FEM simulations to determine the direction of the next iteration. RS acts as a substitute for simulation results and reduces the number of iterations during optimisation. As a result, it improves convergence and RS approximation. The goal is to achieve a response model that is accurate enough on a broader scale hence, the search steps are properly led by the surrogate model even for higher steps. Besides, the RS technique in SNLP proves to have noise suppression properties. The SNLP algorithm handles sequential discrete inputs well (8-12).

For this reason, the external calculation (optimisation) can be detached to FEM analysis. The objective function of SNLP $f(x)$ is given by its local non-linear gradient for continuous and discrete variables (Eq. (4.1)), where $g(x)$ and $h(x)$ are constraint functions by their local affine approximation (Eq. (4.2) and (4.3)). The algorithm defines a multi-objective optimisation with three objectives *i.e.* $f(x)$, $g(x)$ and $h(x)$. A single-objective optimisation will only have one objective.

$$f(x) \triangleq f\left(x^k\right) + \Delta f\left(x^k\right)\left(x - x^k\right) + \frac{1}{2}\left(x - x^k\right)^T Hf\left(x^k\right)\left(x - x^k\right) \tag{4.1}$$

$$g(x) \triangleq g\left(x^k\right) + \Delta g\left(x^k\right)\left(x - x^k\right) \tag{4.2}$$

$$h(x) \triangleq h\left(x^k\right) + \Delta h\left(x^k\right)\left(x - x^k\right) \tag{4.3}$$

Whereas, QN works on the basis of finding minima or maxima of a cost function which relates to variables in the model to overall simulation goal. The cost function relates the variables to field quantities. However, QN is a gradient method, with two fundamental problems. The first is a possible local minimum; once the optimiser positioned the minimum point, it will not look further. The next drawback is, QN has high numerical-noise, which is not preferred in gradient techniques. In order to use QN effectively, the cost function should be modelled with smooth characteristics, and the starting point should be selected near to the optimal point as far as possible. It makes QN an excellent fine-tuning tool than an overall optimise tool.

In addition, a parametric approach can be coupled with optimiser in order to better prepare for the optimisation process using the same inputs. Hence the focus minimum and maximum points of each variable can be determined even before the optimisation process. The parametric study results can automatically be used as input into a rather sophisticated optimisation analysis tool. As a result, the process time can significantly be reduced. The optimisation tool will then obtain local minima (lowest cost), contour details of the parametric study, and continue optimisation from the lowest cost design. Figure 4-1 shows an example of the contour of the cost function $f(x)$ in large-scale optimisation. If the focus range of each input is fed into sequential mixed non-linear programming optimiser, it can narrow down the domain of the problem and redevelop the solutions.

Nevertheless, there is a drawback associated with it, as discussed with results in a later chapter. The numerical noise in SNLP is considerably low, as displayed in the figure. The SNLP optimisation is decided based on local minima to obtain better optimisation parameters. The SynRM average performance (mentioned in section 3.4) parameters are typically not inbuilt in the FEM tool. Thus, it is scripted using IronPython language and used as performance computing tool on the optimisation results.

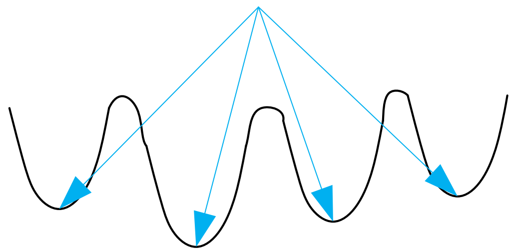

Figure 4-1: Typical Contour of the cost function $f(x)$

4.3 Optimisation Topology of a four-barrier model

A rotor of SynRM can have several distinctions in regards to rotor dimensions such as rib sizes, the location of the barrier, insulation ratio and barrier end profile. The researchers have taken FEM tool for analyses and optimisation of SynRM. The modern FEM tools are generally equipped with optimiser and optimisation algorithms for post-processing while a customised algorithm can also be coupled with FEM tool, such as MATLAB based algorithm can be coupled into a FEM program for optimisation processing.

The optimisation process includes input variable(s) and target(s). The number of inputs and targets are generally limited by the algorithm. Some algorithm is designed to work with multiple inputs and target such as sequential mixed integer non-linear programming. Generally, the outcome of this type of algorithm needs fine-tuning. On the other hand, some algorithm such as Quasi-Newton's method can only take a minimal number of inputs variables (single variable provides the precise solution), but the outcome is accurate.

Moreover, the higher number of variables in the optimisation process increases the need for computation power as well as design time. Besides, the design shall also be modelled in such a way that it can be used for optimisation.

In general, a primitive design is preferred so that the dimensions can be altered during automated optimisation and parameterisation processes.

A high torque density is fundamental in any rotating machine design. However, the torque is not the only parameter of importance and other parameters, such as power factor and torque ripples are also crucial in machine design. Although, a vast amount of research has been published on SynRM, most of the research papers on optimisation focus on torque optimisation. However, few studies have been published on the optimisation of SynRM using multi-objective optimisation algorithms [92, 96, 201, 203]. The above mentioned three parameters require a compromising approach during the selection of each variable domain. This section analyses the limitation on each parameter and the influences of design variables to each parameter.

Torque density of SynRM motor depends on various design factors such as the number of flux barriers and insulation ratio as discussed in section 3. The ribs and webs, to some extent, help in reducing the torque ripples by the introduction of iron in the Q axis. However, it increases the flux in Q - axis, with negative impacts on D & Q inductances. A SynRM torque is proportional to the inductance differences. Therefore, the machine torque is reduced, which is not negligible. Thus, it is essential to make the ribs size as minimum as mechanically possible. Thus, the optimisation of torque, power factor and torque ripples is a great challenge in this type of machines.

4.3.1 Optimisation topology

Generally, the optimisation process takes longer time depending on the number of variables, meshing size and optimisation arrangement. Thus, the ultimate goal of any optimisation design is minimising the time and automating the design so that the solution is reached within reasonable duration as well as without any interaction or re–fine-tuning. The topology developed is designed in such a way that it achieves both expectations of an optimisation. The arrangement is also designed to be used for single and multi-objective problems so that the optimisation results can be compared.

This study focuses on four barrier–design to keep the consistency throughout as well as it is the optimum number selected for the prototypes of the machine. However, the topology can also be applied to any number of barriers–design by eliminating one barrier out from the design shown in Figure 4-2. It shows a parameterised half pole of a four-pole rotor with optimisation variables.

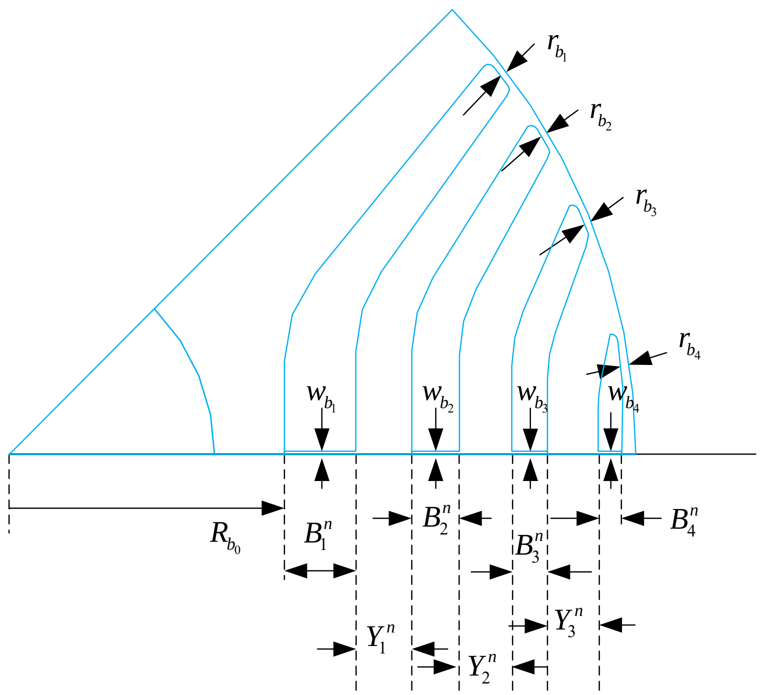

Figure 4-2: Optimisation topology with input variables of a four–barrier rotor

In order to enhance the optimisation process and minimise the optimisation time, the variables should be minimised as much as possible. Although there may be numerous ways to prepare and interconnect the variables, this study follows the following topology. The topology has been modelled based on numerous optimisation post-processing. The equations (4.4) – (4.7) relates the lengths between each barrier to the centre, where R_{first} is known from section 3.6.4 and x is constant. The topology can be changed by altering either or both of the two constants. By doing this, the optimisation inputs, corresponding to the location of barriers, are minimised from four variables to a single variable which is r. The first barrier location R_{first} is already known from the study conducted in section 3.6.4 for first barrier location.

All barriers are designed with webs while the ribs size is used to its mechanical minimum. The ribs and webs are associated as in Eq. (4.8) as it is already discussed in section 3.6.6. As the impact of ribs and webs is already known, it is selected as constant. Thus, the optimiser's complexity is minimised and consistency is maintained between SOO and MOO analyses. In order to give more freedom to vary the design, each barrier thickness is assigned with individual variables (B_1^n, B_2^n, B_3^n and B_4^n), as shown in Figure 4-2. The impact of barrier leg angle and its radius is already known. Thus, they have been selected constants for the optimisation process.

$$R_{b_0} = R_{first} + r \tag{4.4}$$

$$R_{b_1} = R_{first} + (x+2) + \frac{2}{3}r \tag{4.5}$$

$$R_{b_2} = R_{first} + (x+2) + (\frac{2x}{3} + 2) + 2r \tag{4.6}$$

$$R_{b_3} = R_{first} + (x+2) + (\frac{2x}{3} + 2) + (\frac{x}{3} + 3) + \frac{5}{2}r \tag{4.7}$$

$$\begin{aligned} r_{b_1} = r_{b_2} = r_{b_3} = r_{b_4} = 0.50mm \\ w_{b_1} = w_{b_2} = w_{b_3} = w_{b_4} = 0.50mm \end{aligned} \tag{4.8}$$

Thus, the number of input variables is reduced to five. The SynRM rotor design can be changed from one design to another by altering a single or multivariable during optimisation. The input variable domain is defined in Eq. (4.9).

$$
\begin{aligned}
& r = \{r \in \mathbb{R} \mid 0 < r \leq 3.8\} \\
& B_1^n = \{B_1^n \in \mathbb{R} \mid 3 < B_1^n \leq 6\} \\
& B_2^n = \{B_2^n \in \mathbb{R} \mid 2 < B_2^n \leq 4\} \\
& B_3^n = \{B_3^n \in \mathbb{R} \mid 1.5 < B_3^n \leq 3\} \\
& B_4^n = \{B_4^n \in \mathbb{R} \mid 1 < B_4^n \leq 1.9\}
\end{aligned} \tag{4.9}
$$

The following three sections investigate single-objective optimisation (SOO) for torque, power factor and torque ripples. All design parameters are kept identical for the investigation except the objective function, which is changed to suit for each optimisation problem. Finally, all three objectives are optimised together using the same objective functions combined into the multi-objective study with equivalent weight.

4.4 SOO: Optimising for Maximum Torque

Single–objective optimisation on torque is examined using the above optimisation topology. SOO torque optimisation problem is defined as in (4.10):

$$
T > 8.5\ [Nm] \tag{4.10}
$$

The four optimised models are shown in Figure 4-3. The best and near best designs are arranged from left to right and named in numerical order. On the other hand, it is also essential to see how the other designs look. Thus, the four worst designs are shown in Figure 4-4 in descending order. Seemingly, the worst design is not the worst, as the optimiser is not looking for the worst. All four optimised designs are very similar in terms of dimensions with minor changes. Hence, it can be confirmed that the numerical noise did not play any part.

The critical design aspects to note from the results are:

- *All good designs follow the same pattern. Therefore, the best solution lies in the same variable domain*
- *Barrier thickness for maximum torque is rationally distributed over the rotor space*
- *The segment along the circumference is neither too small nor too big. On the other hand, an oversized segment along the circumference reduces the developed torque (from* Figure 4-4*)*
- *First barrier should not be too closer to the shaft, as it will reduce the torque.*

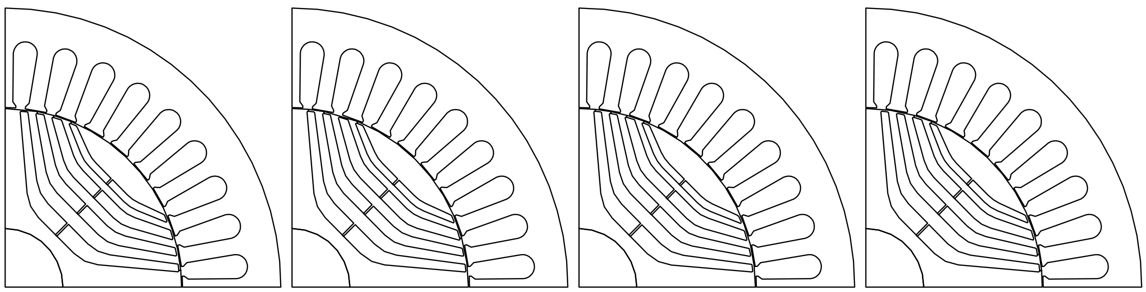

AN-XIVOI_B01 AN-XIVOI_B02 AN-XIVOI_B03 AN-XIVOI_B04

Figure 4-3: Analysis XIV – Optimised design of single-objective optimisation for torque: the finest four designs are given from left to right

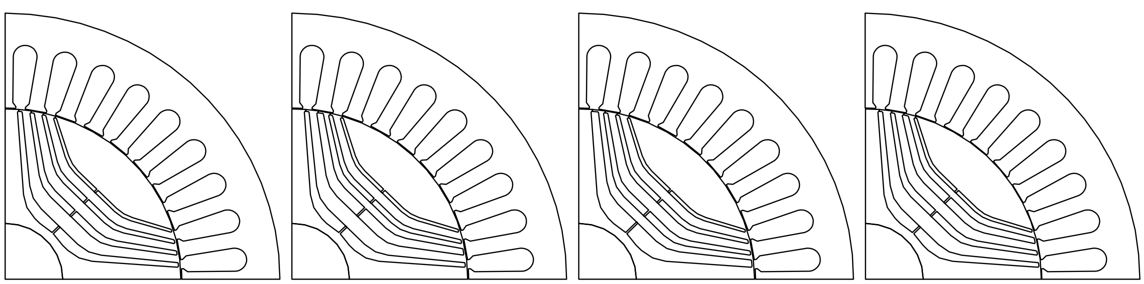

AN-XIVOI_W01 AN-XIVOI_W02 AN-XIVOI_W03 AN-XIVOI_W04

Figure 4-4: Analysis XIV – Single–objective optimisation for torque: the worst four designs are given from left to right

4.4.1 Overall performance of SOO for torque

The SOO for torque finds the solution with high torque, as shown in Figure 4-5. The optimised torque is almost 20 % higher than that of the base design selected for this study. The other parameters such as power factor and torque ripples, are not significantly impacted. The power factor of the optimised design is similar to the other designs and lies in the range of 0.82 $p.u$.

Note: The best designs and worst designs are marked as BSTX and WSTX (where X denote digits), respectively in the following graphs.

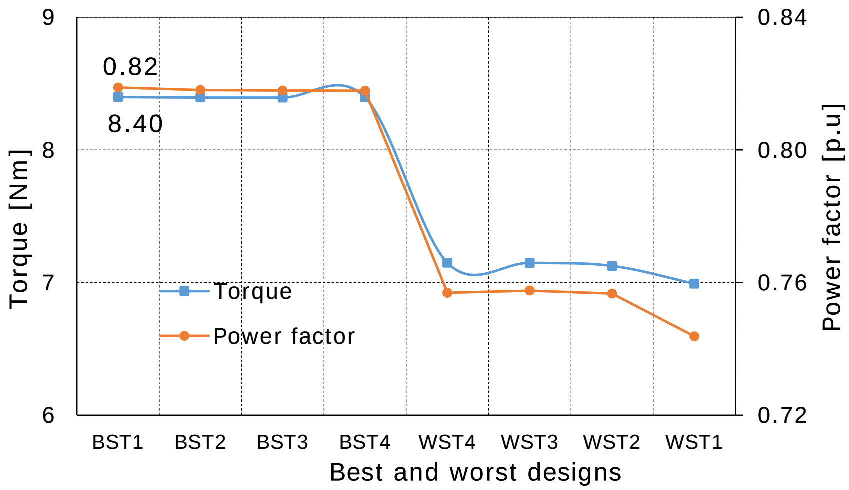

Figure 4-5: SOO for torque: torque and power factor as a function of best and worst designs

The torque ripples of the analyses are shown in Figure 4-6. Torque ripples of the optimised designs are in the lower range compared with the worst designs and follows the same range for all four designs. It is not in the acceptable range.

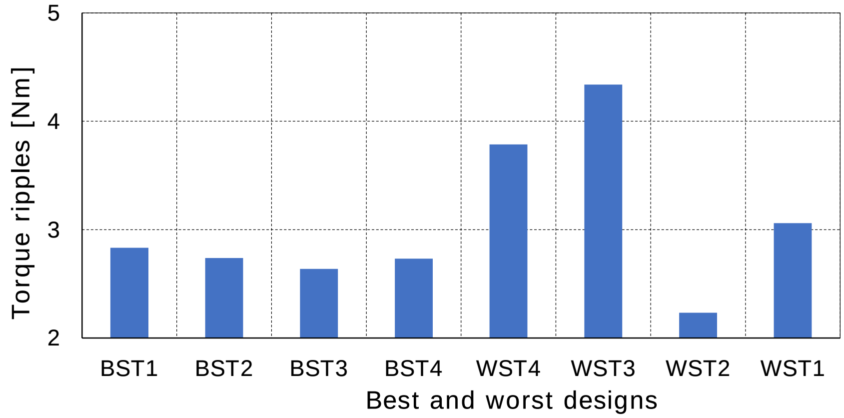

Figure 4-6: SOO for torque: torque ripple as a function of best and worst designs

Figure 4-7 shows linking between each design and insulation ratio. As anticipated, the insulation ratio of all four designs are quite similar and in the range of 0.40 for SOO for torque. The design with low torque density shows even smaller insulation ratio.

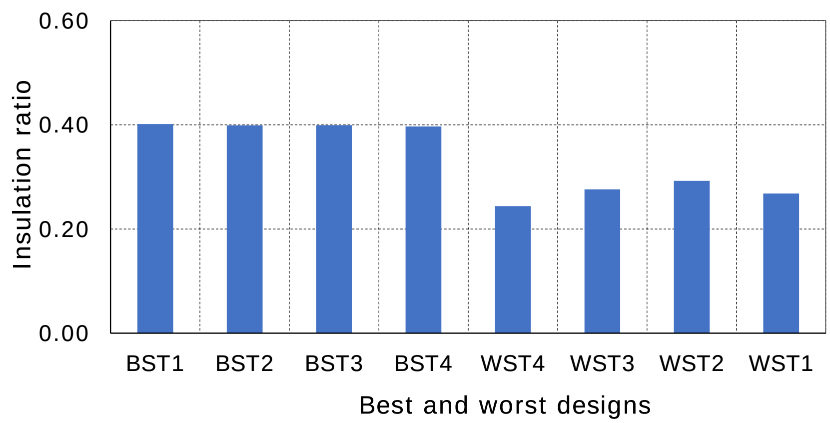

Figure 4-7: SOO for torque: insulation ratio as a function of best and worst designs

This SOO reveals an important design fact. SOO for torque indeed finds the solution with high torque density. However, the SOO for torque lacks to optimise other performance parameters along with torque.

4.5 SOO: Optimising for Power Factor

The SynRM machine generally has poor power factor. This study shows possible improvement in power factor by adopting the correct barrier dimensions and placing them at the optimum location without skewing.

The power factor is investigated on the same topology without any changes. The optimisation objective is defined as in (4.11).

$$pf > 0.85\ [p.u] \tag{4.11}$$

Figure 4-8 shows four designs, including the best to near best designs. As can be seen, all four designs are quite similar with small changes in dimensions except the best design. The designs are quite similar to the one obtained for optimal torque. The barriers are rather equally distributed, and the segment along the circumference is slightly smaller compared with the design for optimum torque designs, as shown in Figure 4-3. The first barrier location R_{b_0} is slightly higher than that of the one obtained for torque. On the other hand, the worst designs are shown in Figure 4-9, where the designs do not follow any patterns.

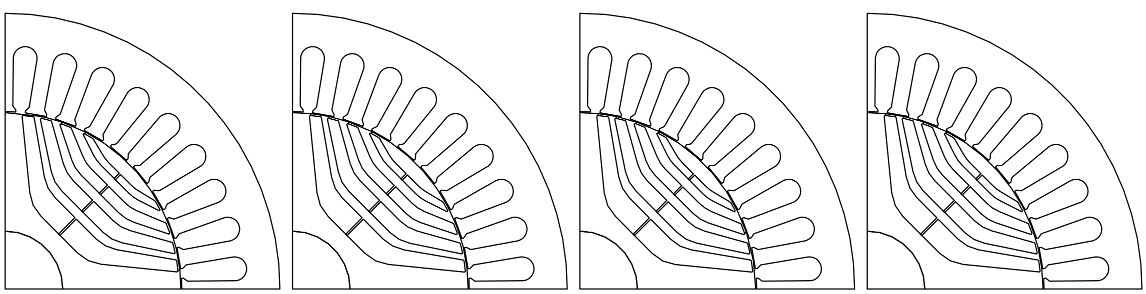

AN-XIVOII_B01 AN-XIVOII_B02 AN-XIVOII_B03 AN-XIVOII_B04

Figure 4-8: Analysis XIV – Optimised design of single–objective optimisation for power factor: the finest four designs are given from left to right

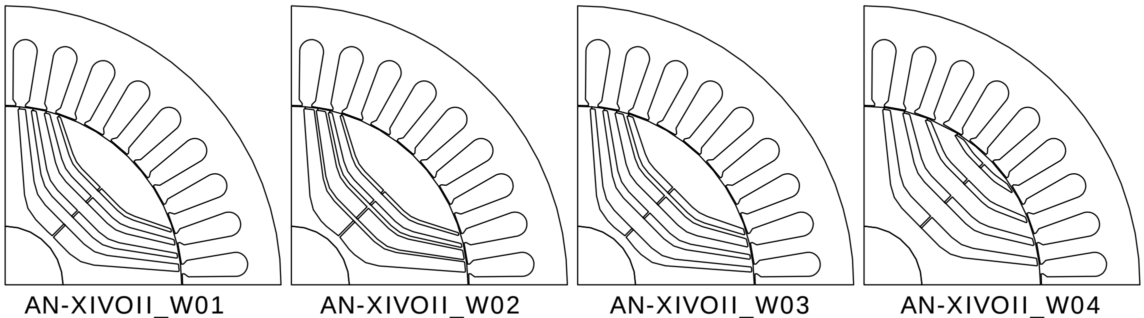

Figure 4-9: Analysis XIV – Single–objective optimisation for power factor: the worst four designs are given from left to right

The optimisation certainly enhances the power factor, as shown in Figure 4-10. However, an increase in power factor is not significant in comparison to the one obtained in the above study. On the other hand, the power factor is increased only by around 2 % compared to optimal torque. The torque and power factor are more or less the same between the four optimised designs, as shown in Figure 4-10.

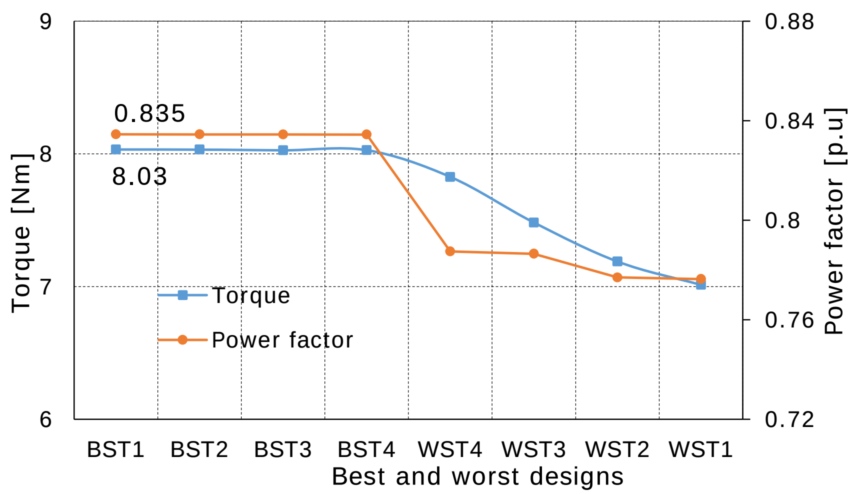

Figure 4-10: SOO for power factor: torque and power factor as a function of best and worst designs

Torque ripples of the optimised design (for power factor) are improved compared with the once for torque where the best design has seen a reduction of 33 % as shown in Figure 4-11. Overall, the ripples of this study are lower than that of the one for torque. Based on the investigation and previous simulations, it is quite safe to say the optimisation for power factor improves the ripples better than the optimisation for torque. However, set back of this method is, it reduces the torque by a substantial percentage.

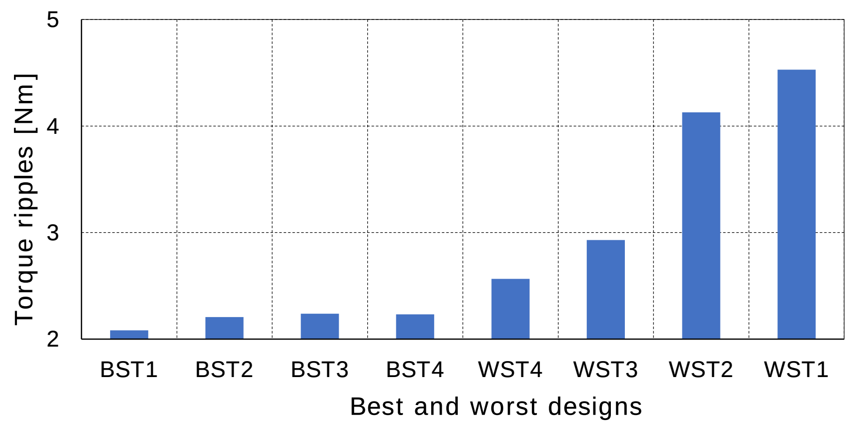

Figure 4-11: Torque ripples as a function of best and worst designs

The optimisation results show a slight increase of ripples for the other three optimised design compared to AN–XIVOII_B01, which is directly correlated to insulation ratio of the designs in Figure 4-12. Insulation ratio of SOO for torque as well as for power factor has insulation ratio between 0.4 and 0.5 should be noted as this is the same case for the next two optimisation which will be discussed further in the subsequent sections.

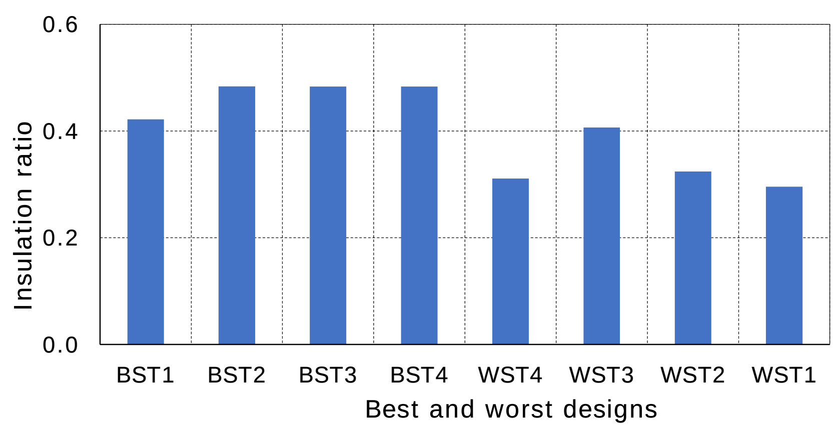

Figure 4-12: SOO for power factor: insulation ratio as a function of best and worst designs

4.6 SOO: Optimisation of Torque Ripples

SynRM has also have high torque ripples due to its polarised magnetic axes and asymmetric circumference. This section deals with single-objective optimisation of torque ripples, whereas detail study on this is discussed in section 4.8 with unique optimisation techniques. This section continues with the same SOO but for torque ripples.

SOO for torque ripple is investigated with the same topology without any changes. The optimisation objective is defined as in (4.12).

$$Torque\ ripple < 12\% \tag{4.12}$$

Similarly, the four best designs and worst designs are given in Figure 4-13 and Figure 4-14, respectively. As can be seen, the barrier thicknesses are reduced significantly compared with the above two investigations. Further, the barriers are placed away from the centre, and iron segments are quite bigger than the above two studies. On the other hand, inferior designs do not follow any pattern in this study. This optimisation substantially reduces machine performances for torque ripple as can be seen in Figure 4-15.

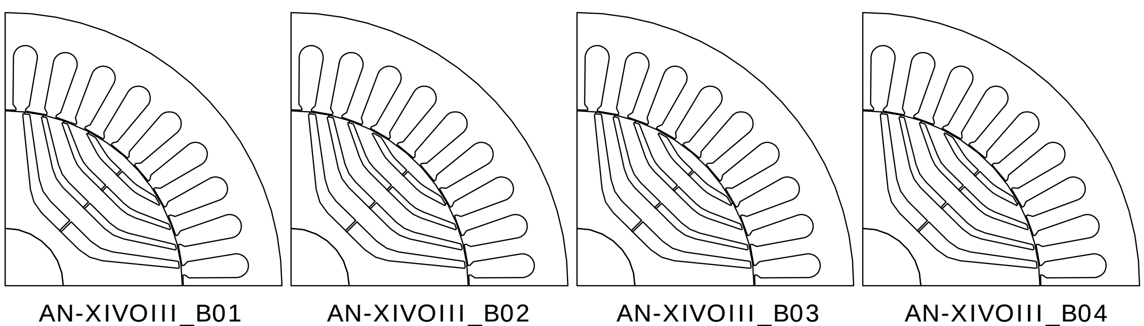

Figure 4-13: Analysis XIV – Optimised design of single–objective optimisation for torque ripples: the finest four fine designs are given from left to right

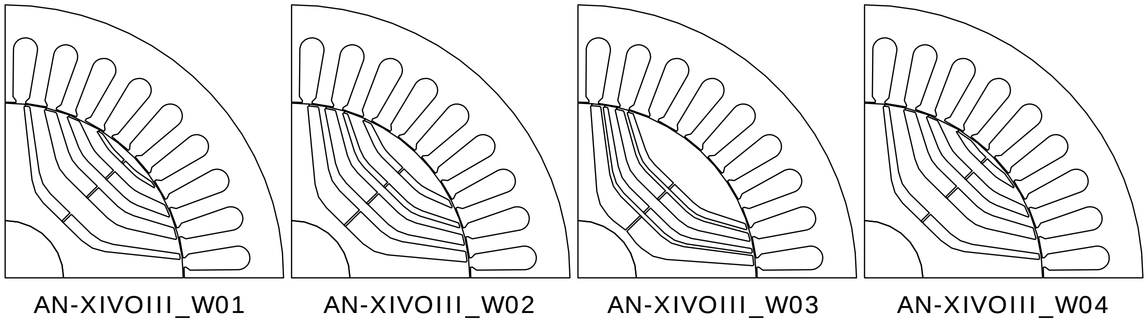

Figure 4-14: Analysis XIV – Single–objective optimisation for torque ripples: the worst four designs are given from left to right

The torque is almost reduced by 6 % compared with optimal torque and power factor is by 5.5 % compared with optimisation for power factor. However, the torque ripples are significantly reduced by 235 % and 147 % in comparison to the designs for torque and power factor, respectively. The optimised torque ripple is less than 10 % of the total torque which is well within the acceptable range for most of the applications.

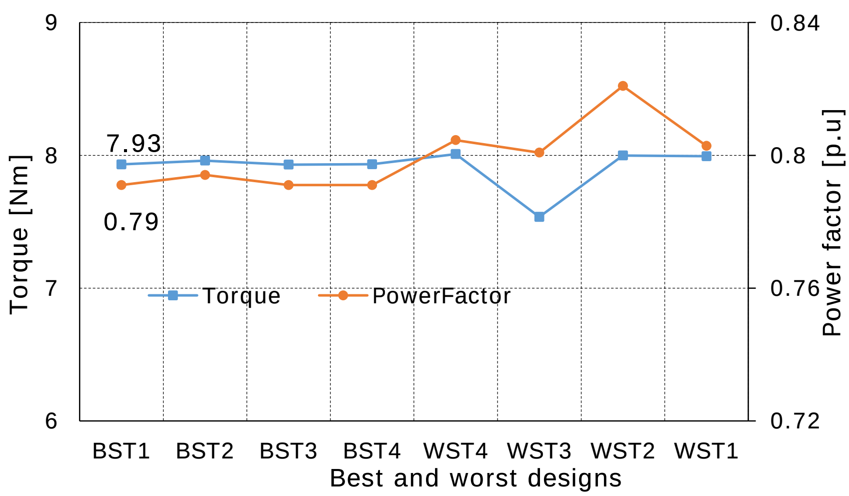

Figure 4-15: SOO for torque ripple: torque and power factor as a function of best and worst designs

The torque ripples are plotted in Figure 4-16. The four optimised designs show similar ripples below 10 % of the average torque. However, the poor designs attributed high ripples which are more than 50 % of average machine torque.

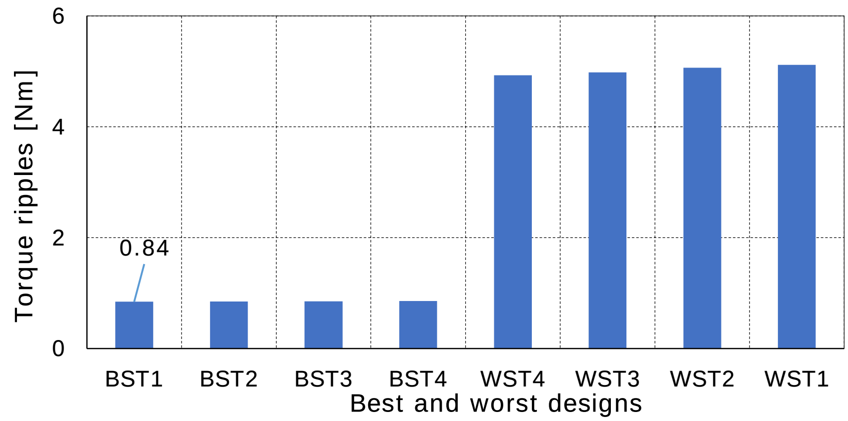

Figure 4-16: SOO for torque ripple: torque ripple as a function of best and worst designs

The insulation ratio is quite low as it can also be seen in designs (Figure 4-17). The design AN-XIVOIII_B01 has quite low insulation ratio compared with the other three optimised designs, and it does not follow any pattern. One key point to be noted that optimisation for torque ripple requires relatively low insulation ratio whereas the other two design requires slightly higher insulation ratio.

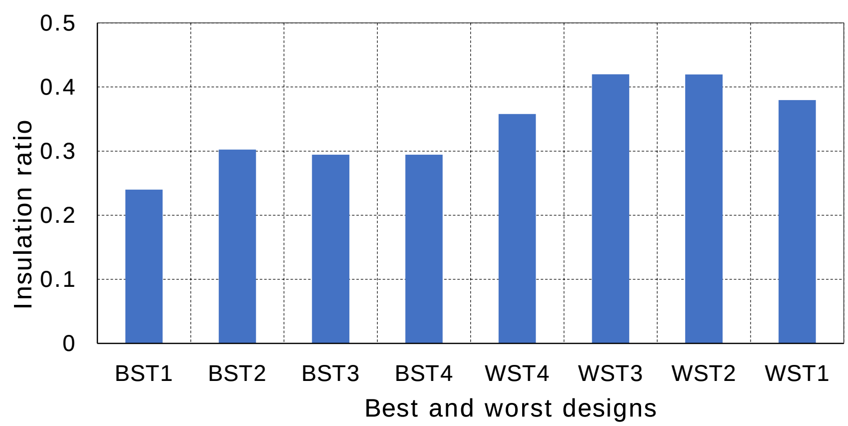

Figure 4-17: SOO for torque ripple: insulation ratio as a function of best and worst designs

This investigation obtains an expected torque ripple even without any other ripple minimisation methods such as skewing, segmental design, or the high number of phases.

Single–objective optimisation (SOO) is a useful tool if the problem has only a single target or problem's objectives are interconnected. However, in the problem such as SynRM, the objectives are independent. Applying single–objective optimisation, as shown earlier cannot optimise other objectives. The ripples are quite high when just optimised for either torque or power factor and vice versa. The three optimisations prove that a SynRM can be designed to have reasonably high torque density with relatively high–power factor and acceptable ripples by merely optimising the barrier shape. Thus, SynRM should use multi optimisation for a better outcome.

4.7 Multi-Objective Optimisation

Multi-objective optimisation (MOO) is utilised for the same problem as defined in (4.13). By defining the problem with the exact definition of SOO's, the consistency is maintained with added weight to the optimiser.

$$T > (8.5\ [Nm])\ \&\ pf > 0.85\ [p.u]\ \&\ Torque\ ripple < 12\% \qquad (4.13)$$

The optimisation results are, similarly, shown in Figure 4-18. As can be seen, the optimised design follows the design strategy in terms of barrier thickness and placements, as discussed in section 3.5.1. The thickness of all four barriers of design AN-XIVOIV_B01 is rationally distributed.

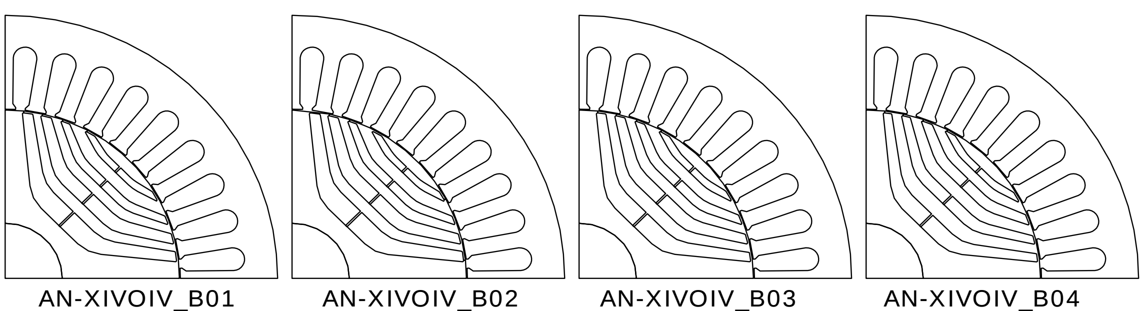

Figure 4-18: Analysis XIV – Optimised design of multi-objective optimisation: the finest four fine designs are given from left to right

The best designs from MOO shows insulation ratio between 0.4 and 0.6, as shown in Figure 4-19 and Figure 4-20. It is quite safe to assume that optimised designs have insulation ratio between 0.4 and 0.6, but vice versa is not always correct based on this investigation as well as the above SOO.

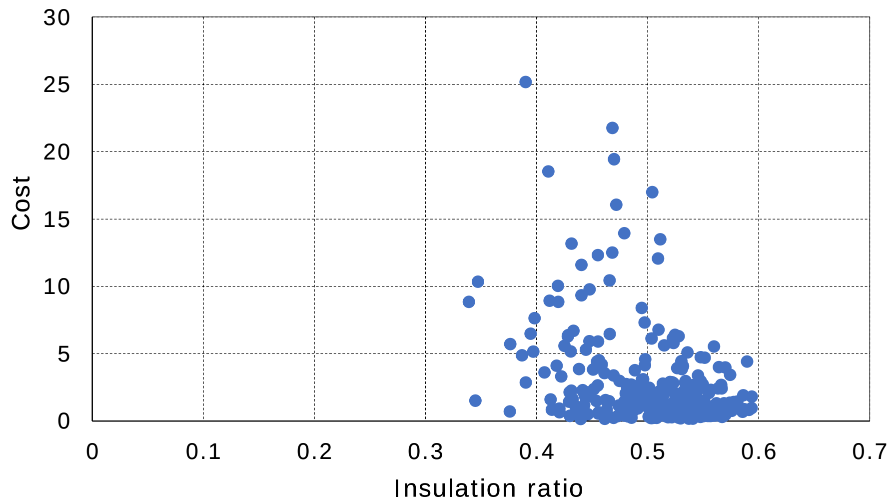

Figure 4-19: Analysis XIV – Multi-objective optimisation: cost function of optimisation as a function of insulation ratio (cost function is inversely proportional to performance)

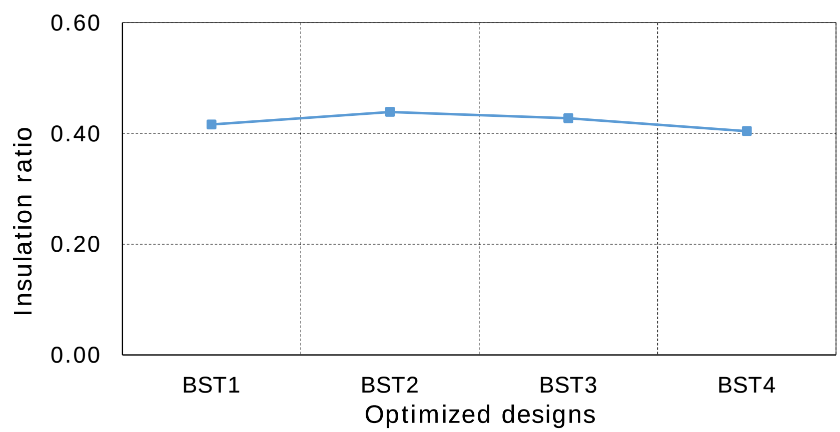

Figure 4-20: Analysis XIV –Multi-objective optimisation: insulation ratio with respect to optimised designs

The optimisation topology parameter r is plotted against the cost, as shown in Figure 4-21. The best designs for r lie between 3.00 mm and 3.25 mm. It suggests that for better machine performance, the barriers should have reasonably sized segments between each barrier. SynRM performance parameters, torque and power factor, are plotted in Figure 4-22 while torque ripples are plotted in Figure 4-23. The torque of MOO is slightly reduced by 1.4 % compared with SOO for torque. However, it is improved by 18 % compared to the base design given in Table 3-1. The power factor is slightly reduced by 0.5 % compared with SOO for power factor but still improved by 15.3 % compared with the base design. On the other hand, the torque ripples, shown in Figure 4-23, are slightly higher than that of the SOO for ripple by 20% but still within the acceptable range for most application.

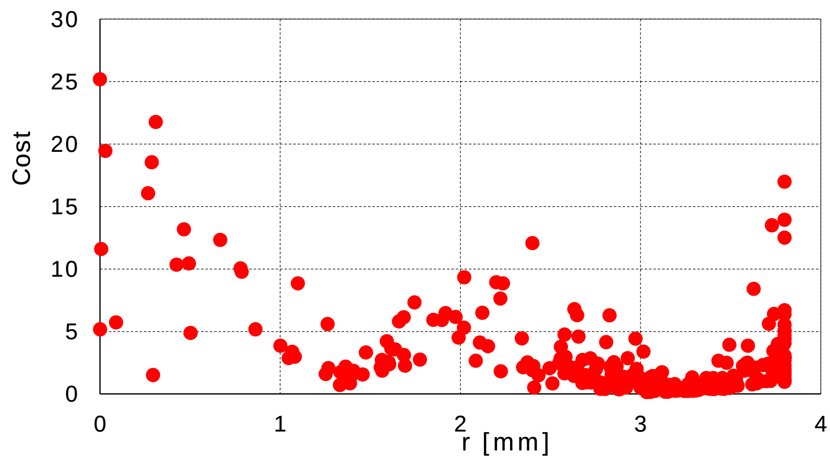

Figure 4-21: Analysis XIV – Multi-objective optimisation: cost function of optimisation as a function of the variable *r*

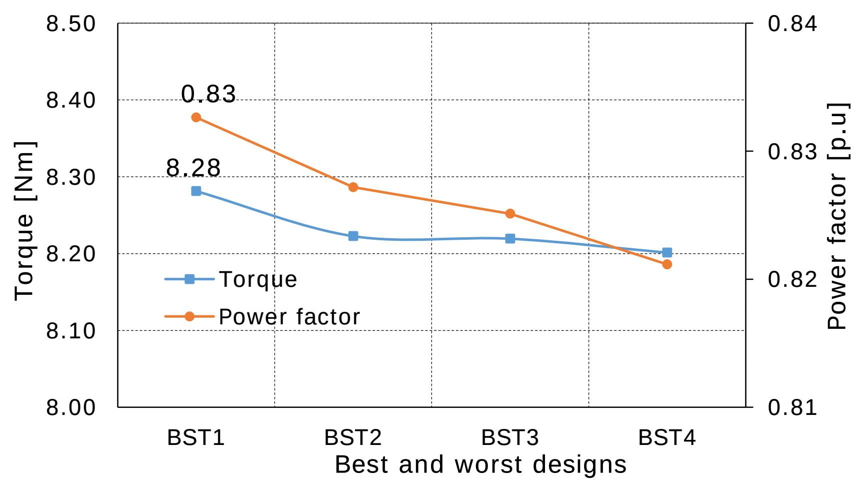

Figure 4-22: Analysis XIV –Multi-objective optimisation: torque and power factor with respect to optimised designs

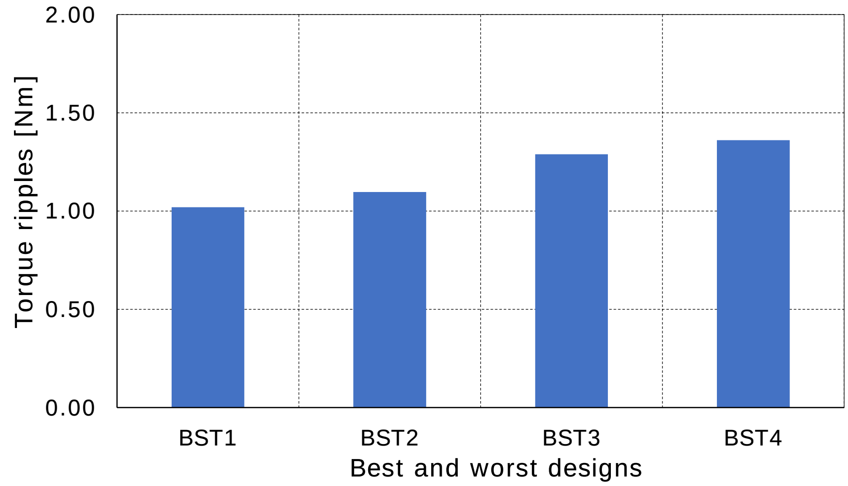

Figure 4-23: Analysis XIV –Multi-objective optimisation: torque ripple with respect to optimised designs

Multi-objectives, *i.e.* torque, torque ripples and power factor of the machine are optimised. This study investigates the application of single and multi-objective optimisation and its usefulness in SynRM optimisation. The optimisation of torque ripples is quite sensitive and need further analyses, simulation and optimisation which is discussed in the next section.

4.8 Optimisation for Torque Ripples

In this section, the torque ripples minimisation is studied using FEM and optimisation tools. The same optimised design from above studies is utilised for this analysis. As discussed in section 2.5.4, the rotor geometry should be optimised along with other factors in order to improve the ripples effect. The ultimate goal of this investigation to optimise the rotor barrier dimension to obtain a low torque ripple machine. As it is already discussed in Eq. (1.16) and Eq. (2.56), the primary cause of torque ripple is the DQ flux linkage fluctuations with respect to the rotor reference angel ϑ. The reason is that the cross flux from the stator to the rotor during the rotation is not smooth. As a result, the rotation experiences ripple effects, commonly known as torque ripples. However, it is not the only cause for torque ripples but there are other factors as already discussed in the section 2.5.4.

The investigation focuses primarily on rotor optimisation. One of the well-known methods to optimise SynRM for low ripples is selecting the number of barriers to match the stator slots as in Eq. (3.9) and aligning the barriers ends to stator slots, as discussed in [222]. Since then many methods are proposed such as fractional slot [128], optimising barrier shape [88, 223], segmented rotor pole lamination [97], rotor skewing [90, 172], and use of five-phase system [114, 183]. Each method has its pros and cons, such as a five-phase system need an entirely new design and drives system, which will be expensive for the industry. Further, a segmented rotor pole lamination can be expensive and reduce the machine's mechanical integrity.

In this study, a four-pole rotor with four barriers is selected since it can cover all stator slots. The investigation targets barrier slot pitch and the barrier position with respect to stator slots are vital for the ripple's minimisation. Therefore, the simulations carried out to determine the ripples effects of three different models where each barrier slot pitch is changed with respect to its stator slots. It is further verified using advanced optimisation techniques to determine the optimum position of barriers.

4.8.1 Barrier and Stator Slot Pitch Angle

A rotor with four barriers is selected for this analysis, as shown in Figure 4-24. The first section of the figure shows a linearised half pole rotor and barrier alignments of the three designs where the barriers are aligned in three possible scenarios. The SynRM, selected for this analysis, is not optimised one rather an arbitrary design for the purpose. The first scenario (a) is when the rotor barrier ends are aligned with stator slots (or slot pitch design - SP). In this case, the slot angle is defined as α_s^i. The second scenario (b) is when the barrier ends and slots are partially aligned (also called intermediate slot pitch - MSP). In this case, the slot angle can take any value in between $\alpha_s^1 < \alpha_s^i < \alpha_s^{imax}$. The final scenario (c) is when the barrier ends are aligned with the stator teeth, where the slot angle is aligned at its maximum α_s^{imax} (off slot pitch - OSP).

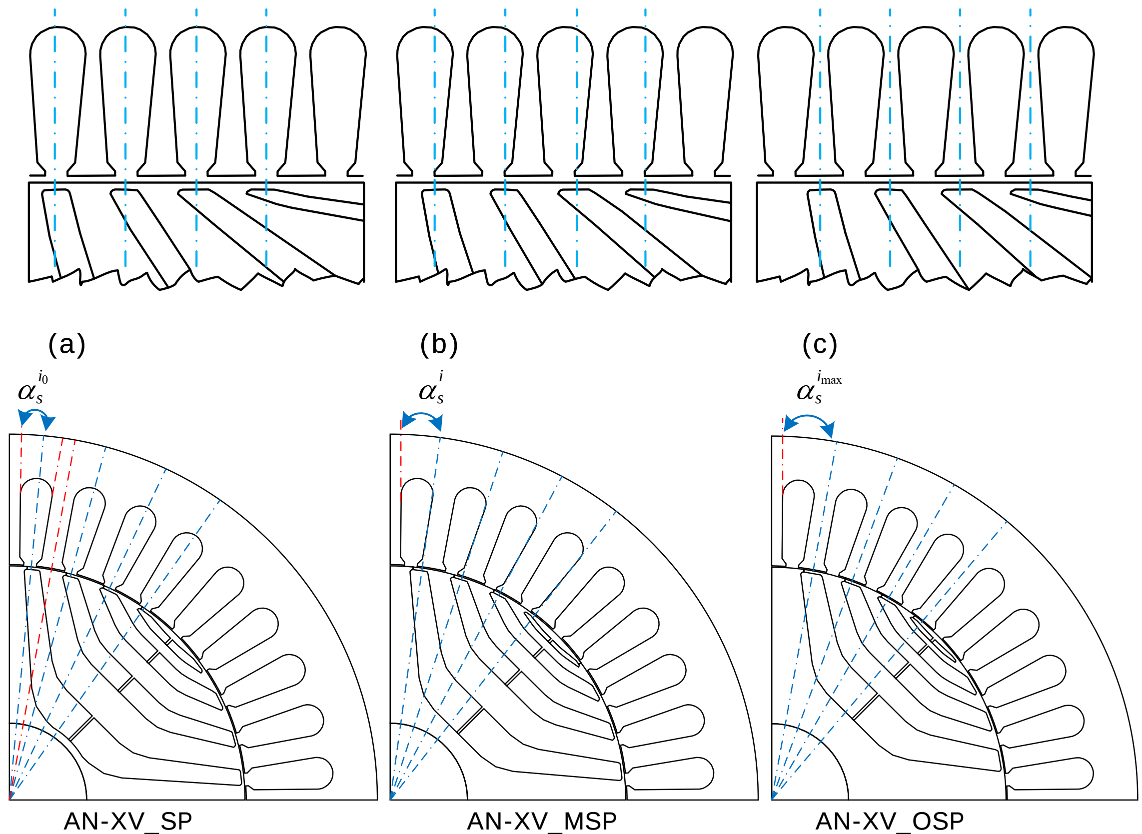

Figure 4-24: Analysis XV: (a) Each rotor barrier is aligned to the stator slot at slot angle(SP) α_s^{i0} (b) Each barrier at α_s^{i} with respect to the associated slot(MSP), (c) Each barrier at Maximum slot angle α_s^{imax} (OSP)

Though the barrier slot angle is investigated in this study, it is essential to note that the location of the barrier is naturally moved due to the placement of the barrier. Consequently, the shaft to barrier and barrier to barrier gap is altered. However, the air to steel ratio is not affected due to the barrier slot angle differences. In this FEM analysis, the stator slotting effects, end leakage inductance, coil inductance and resistance are included for precise results. The alignment of the rotor barriers to stator slots has been one of the few methods to minimise the torque ripples in SynRM. The instantaneous torque of the FEM simulation is plotted as a function of time in Figure 4-24 where the SP and MSP designs have higher ripples compared with an intermediate design.

The designs SP, MSP and OSP demonstrate torque ripples of 113 %, 62 % and 120 %, respectively, as shown in Figure 4-25 and Figure 4-26. As mentioned, the design used is only to investigate the three possibilities, hence the results are not optimum. The results show that neither slot pitch nor off slot pitch helps to improve the ripples effect, and the optimum topology lies for barriers in between stator slots. The slot pitch design recorded high average torque density of 8.38 Nm. It is due to the location of the first barrier. The further the barrier from the shaft, the lower the torque [91, 148]. It can be seen in the three designs that SP's first barrier is the closest to the shaft and OSP's first barrier is the furthest from the shaft. Therefore, SP has high, and OSP has the lowest torque of all three designs.

Whereas, the intermediate slot pitch design (MSP) shows better performance in comparison to the other two designs in terms of torque ripples, but its performance will always be within the other two low and high ends. Another intriguing effect worth noting is that pf of all three designs remain unchanged. The FEM simulation results show relatively high torque ripples for SP and OSP.

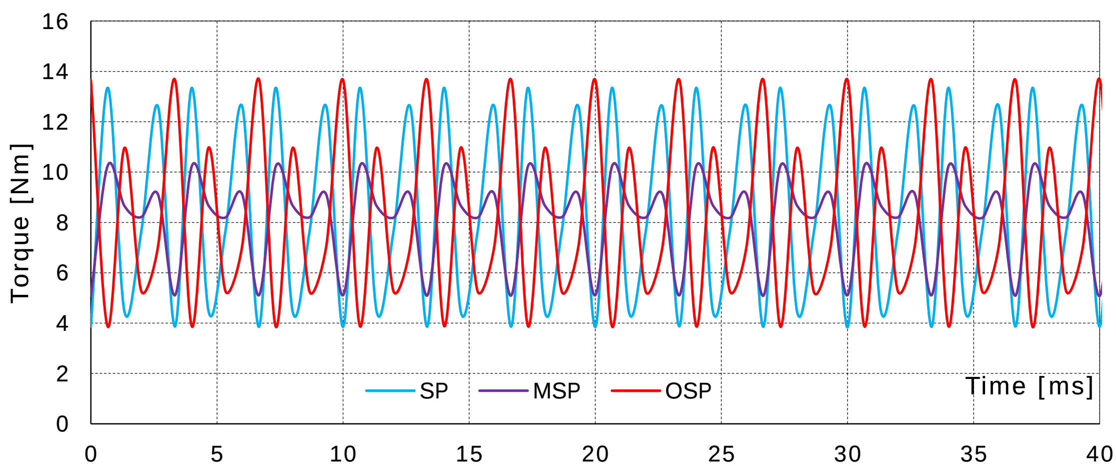

Figure 4-25: Analysis XV - Torque of the three designs as a function of time

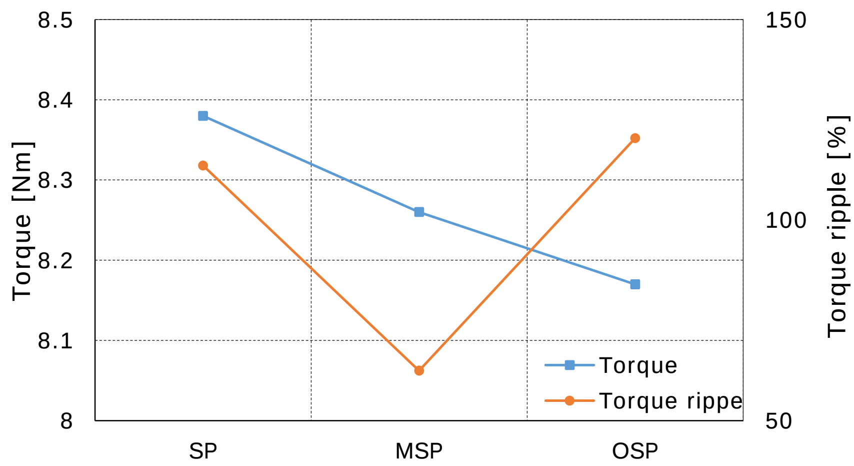

Figure 4-26: Average torque and torque ripple with respect to the three designs

Another study is performed to obtain torque pulsations at no-load equivalent of a PM machine’s cogging torque for the three SynRM’s. Although, there are no PMs in the rotor to produce the cogging torque, the machine experience torque fluctuations at no-load. A simulation is performed at really slow speed and no-load to understand the torque pulsations. The results are shown in Figure 4-27. A powerful simulation is carried out using the same 2D FEM on all three designs with precise fine time-steps. The number of FEM elements in the model is increased to have adequate mesh to determine the cogging torque. In order to simulate cogging torque, the load from models removed and simulated only for an electrical period. All other parameters of the three designs are kept unchanged.

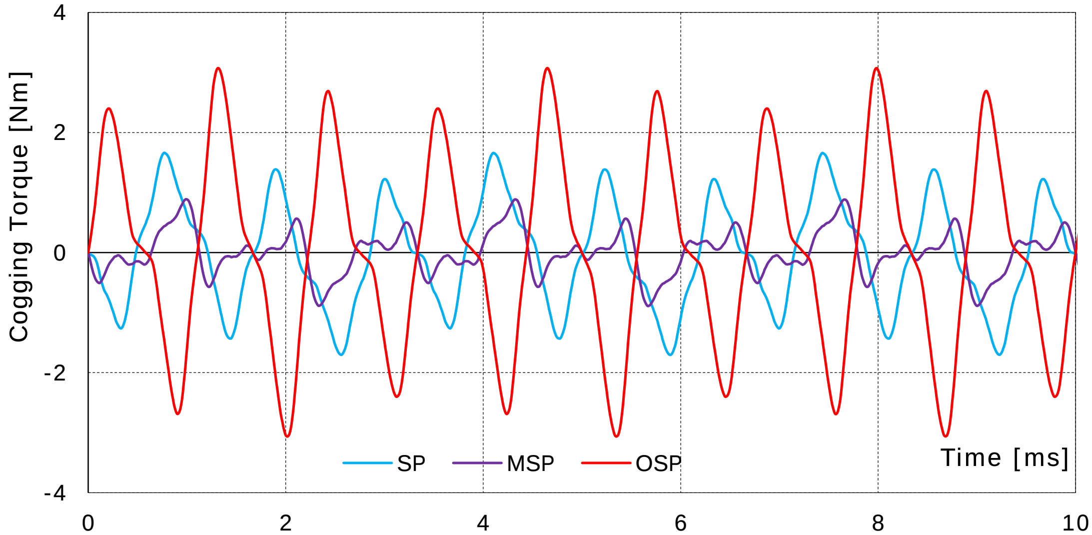

Figure 4-27: Analysis XV – Torque ripples of the three designs as a function of time

The torque pulsations of the three designs at low speed and no-load is exactly similar to the torque ripples obtained at rated condition. Similarly, design MSP shows lower ripples in this investigation. It validates the argument that by correctly placing barriers in such a way in between stator slots and teeth can significantly improve ripple effect.

4.8.2 Optimisation for Slot Pitch Angle

In this investigation, the same four barrier rotors are investigated with optimisation techniques specially designed for barrier slot angle variation. The shape of the barrier remains unchanged while changing the slot pitch angle. The optimisation of individual barrier shape or its other dimensions will not provide a systematic process. Minimisation of optimisation variables is impotent for effective time-saving. Therefore, all four barriers are selected as a group to perform this study. The change in one barrier angle may overlap into another and hence, result in crashing the optimisation process. Therefore, the projection angle of each barrier slots indirectly varied in such a way by changing each barrier distance to the shaft and the barrier thickness. The low and high limits of each barrier distances from the shaft and flux guide's thickness are defined. If they are not defined, then the optimiser will automatically overlap the barriers during optimisation.

Hence, it either results in false readings or end up crashing the entire process. For this torque ripples optimisation, a different approach is used from the previous optimisations. The optimisation variables are defined, as shown in Figure 4-28 where four space (R_{b_i}) and four barrier variables (B_i^n) are selected. Initial slot pitch angles (α_{er}^i) are selected arbitrarily. Therefore, the optimiser has a broader range to search for the best design, as shown in Figure 4-28. The optimisation process is not detailed here as it is out of the scope of this investigation

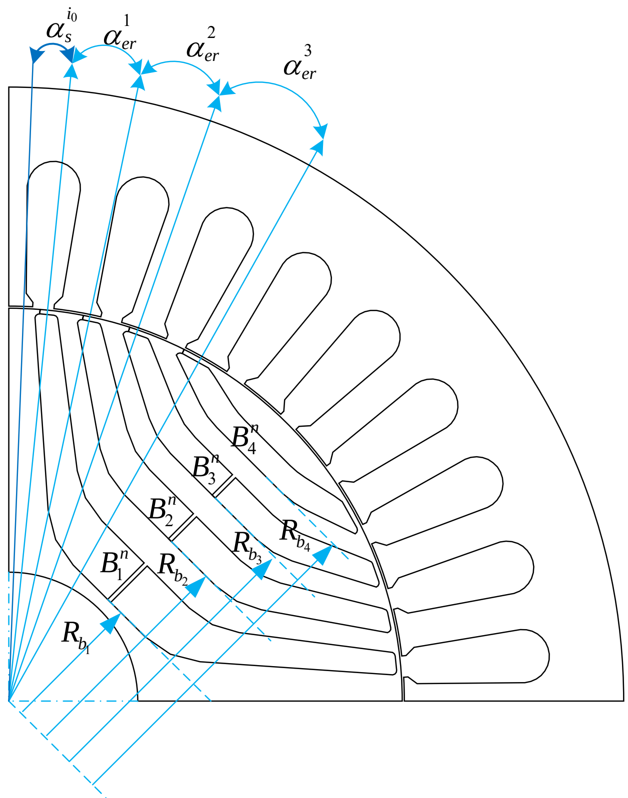

Figure 4-28: Analysis XV – Parameterised design with 4 hyperbolic barriers for optimisation

The optimiser finds numerous close designs with low ripples. The optimised four barrier design is shown in Figure 4-29. The design optimisation is found at the lower end of R_{b_2},R_{b_3}, R_{b_4} and high end of R_{b_1}. It is rather unconventional barrier arrangements for high torque density in above studies. However, in this study, high degrees of freedom have been granted in terms of barrier placements as well as movement to change the end angles. The torque pulsation of the optimised model (OPT-A) is shown in Figure 4-30. The improvement in ripples of OPT-A compared with SP, MSP and OSP is exceptional.

It is evident that slight movement and alignment of the barriers can minimise the torque ripples to an acceptable level without significant modification. However, the result is achieved with a slight drop in average torque of the machine by 2.6 % compared with the design from single-objective optimisation for torque (in section 4.4) and 2.02 % compared with design from multi-objective optimisation (in section 4.7). On the other hand, the torque ripples are minimised by 74.6% compared with the design from MOO. Moreover, the power factor is also slightly reduced by 1.2 % compared to the MOO design.

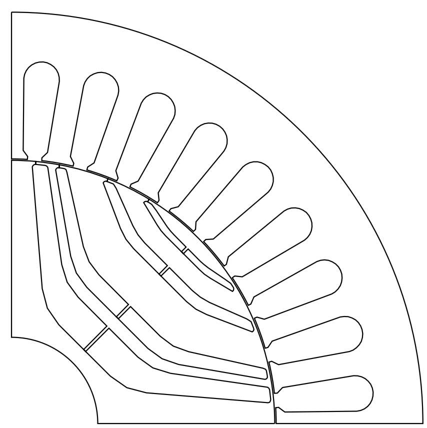

Figure 4-29: Analysis XV - Optimised SynRM with four hyperbolic barriers (OPT-A)

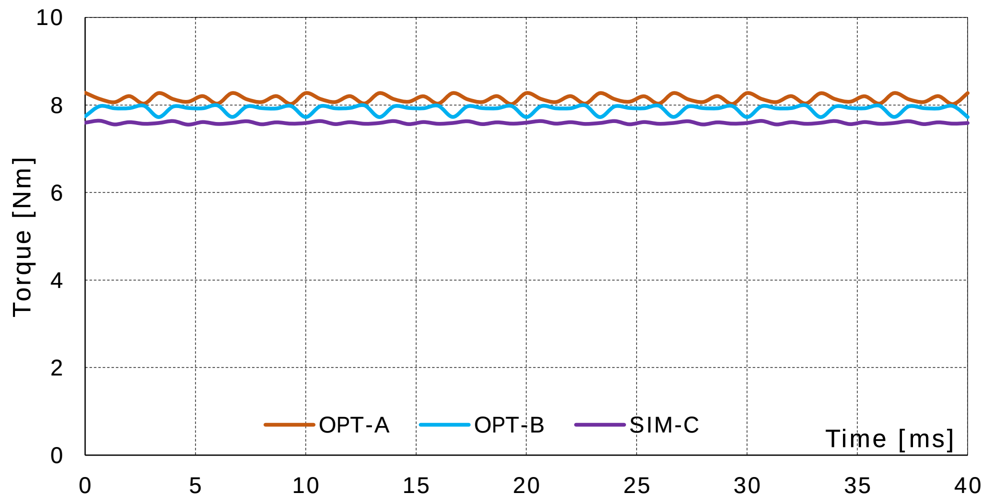

Figure 4-30: Analysis XV - Torques of three optimised designs (OPT-A, OPT-B and OPT-C) as a function of time

All the three barriers other than the first have moved towards the shaft (they are placed at the lower end of R_{b_2}, R_{b_3} and R_{b_4}). It is because, the optimiser tries to eliminate the barriers as they are causing ripples from the response surface results. To further study this problem, a three barrier-design (with the last barrier removed) is optimised by the same way by maintain all other parameters unchanged (OPT-B). The barrier shape discussed in section 3.3 primarily focused on the saliency ratio. In order to understand the influence of the barrier shape, hyperbolic arc (OPT-C) and circular (OPT-D) barrier designs are also simulated with exact design dimensions (but not optimised) and shown in Figure 4-31.

The optimised design is much similar to the one obtained in the above study (OPT-A) except it does not have the last barrier. The torque ripples of this design is reduced as given in Table 4-1, and the ripples are plotted along with OPT-A in Figure 4-30. As already seen, less-number of barriers mean lower saliency and poor performance which is shown in this investigation. On the other hand, the circular barrier design shows torque ripples of 1.1 % of its average torque. The machine performance of the circular barrier design is slightly lower compared with other designs, as shown in Table 4-1. The hyperbolic arc design shows quite high ripples compared with the other three designs, but still well within the acceptable range for most of the applications.

Table 4-1: Analysis XV - Machine performance of three optimised designs

Design	Torque [Nm]	Power Factor [p.u.]	Torque Pulsation [p.u]
OPT-A	8.14	0.81	0.032
OPT-B	7.90	0.79	0.031
OPT-C	7.59	0.79	0.011
OPT-D	8.25	0.82	0.103

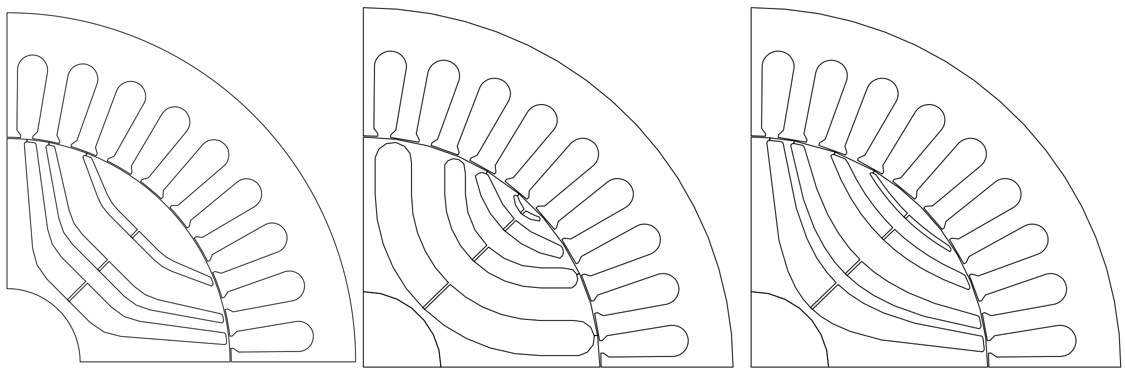

Figure 4-31: Analysis XV - Optimised SynRM with three hyperbolic barriers (OPT-B, OPT-C and OPT-D, respectively)

The results show two different number of barrier designs with very similar torque ripples. Although the barrier arrangement is unusual and non-conventional, the finding is quite interesting. The results prove that a special SynRM machine can be designed with high machine performance by proper optimisation techniques.

4.8.3 Impact of barrier end profile on torque ripples

The primary reason for high torque ripples in SynRM is that the circumference is magnetically not even. As the rotor rotates and barrier ends to pass through stator teeth, it causes magnetic asymmetry to the system. Although the tangential ribs provide considerable magnetic smoothness, the reluctance pulsation is quite high to cause torque pulsation. One way to minimise the torque pulsation is by increasing tangential rib size, but it will compromise the machine performance if oversized. Thus, the alternative way is to optimise the end profile. This study investigates torque ripples with respect to the end profile by changing barrier end radius, as shown in Figure 4-32 for the optimised design OPT-A. The torque ripples with respect to each design is plotted in Figure 4-33.

Figure 4-32: Analysis XV - Barrier end profile investigation

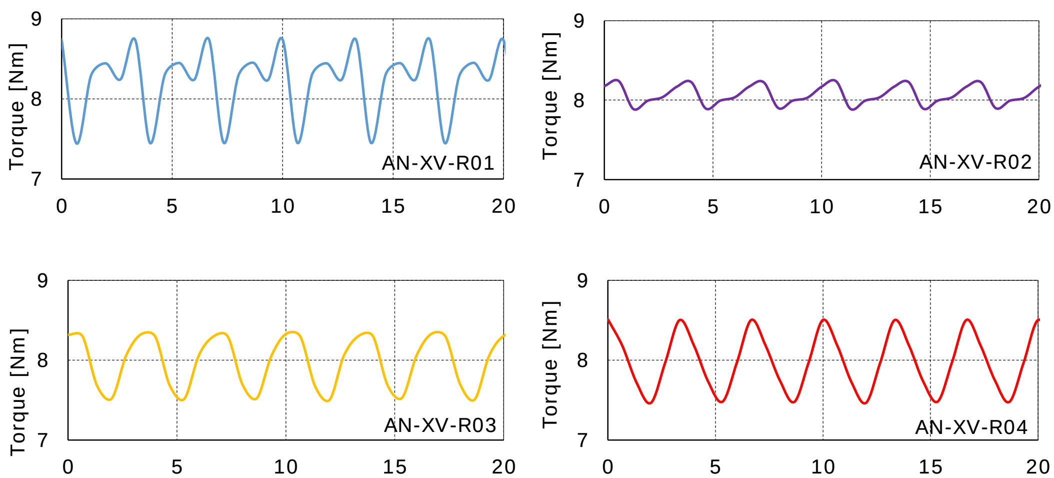

Figure 4-33: Analysis XV – Torque ripples of the four designs

The results reveal that there is an optimal end barrier radius for least ripples. The torque, power factor and torque ripples are plotted against the radius in Figure 4-34 where the changes in torque ripples have the lowest point. The minimum ripple is obtained at 0.5 mm for this design. As we have seen in section 3.11, the increase in the radius results in poor machine performance which is also proven in Figure 4-34 where torque and power factor has dropped higher radius. The results reveal that there is an optimal value for the end barrier radius. The drop-in machine performance is not significant though, a design guideline shall be used for final design in determining the radius.

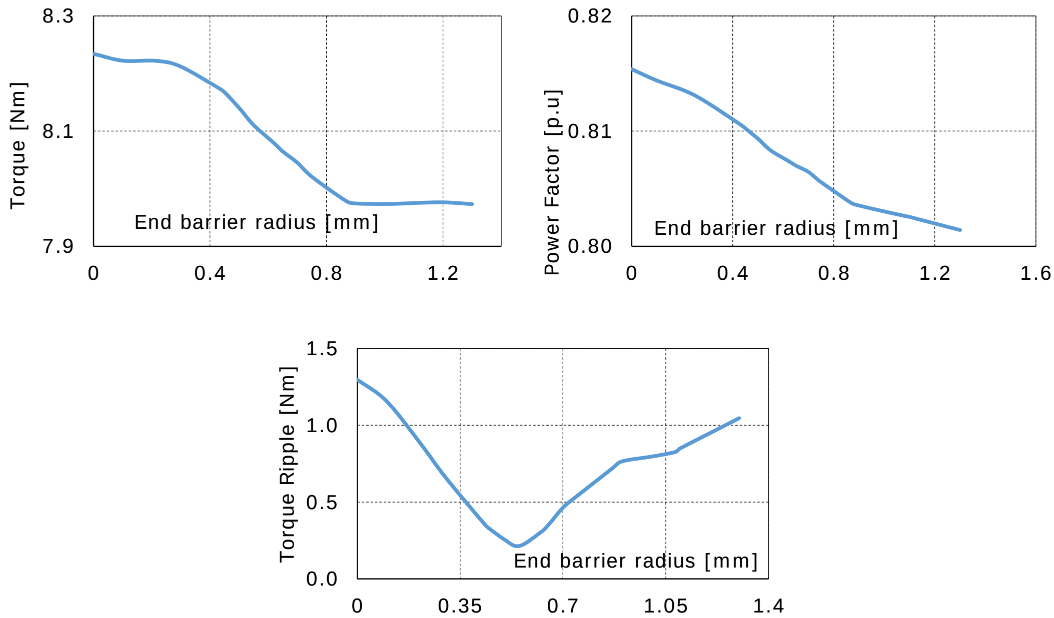

Figure 4-34: Analysis XV – Torque, power factor and torque ripples with respect to the barrier end radius

4.9 Conclusion

In this section, numerous methods are introduced for SynRM performance optimisation. A generic algorithm for multi-variable and single variable optimisation, especially for SynRM is discussed in details. A novel optimisation topology specially designed for multi-barrier SynRM is prepared for this study. It has been used for various optimisation processes including torque ripples optimisation. The study has developed numerous design techniques to alter the design parameters during parameterisation and optimisation. Moreover, novel methods are developed to inter-connect design parameters hence, optimisation variables can be minimised for effective optimisation.

Torque, power factor and torque ripples are investigated via single-objective optimisation as well as together by multi-objective optimisation. The three single-objective optimisations and multi-objective optimisation together revealed a high-performance machine with significantly improved power factor and torque compared with the base design. The torque and power factors are increased by 18 % and 15.3 % respectively compared with base design. As never before, the multi-objective optimisation method is utilised for three optimisation targets torque, power factor and torque ripples. It is proven to be effective for SynRM design. The results reveal all three parameters can be optimised for better performance if it is properly utilised.

The optimisations reveal that a SynRM can be optimised for high machine performance if it is appropriately optimised. In addition, a novel torque ripples minimisation method is proposed for primitive designs, and it analyses various machine features. The study reveals that the torque ripples of SynRM can be minimised below acceptable level by optimisation rather than approaching complicated arrangements.

Part II: Permanent Magnet Assisted Synchronous Reluctance Machines

5 PMSYNRM: ANALYSIS AND OPTIMISATION

5.1 Introduction

As discussed in chapters 2, 3 and 4, the torque density and power factor of a SynRM can be improved, but the machine still suffers due to low power factor (even though it has been improved by almost 20 % compared with base design, as found in the study presented in Chapter 3 and Chapter 4). It has been suggested recently that the power factor and torque ripples of SynRM can be improved by adding PMs, as discussed in section 1.5 [51, 116]. Unlike other PM machines, PMSynRM does not require high-grade rare-earth permanent magnet to improve its performance. Thus, special high-performance machines should only be designed with rare-earth permanent magnets such as neodymium while general PMSynRM can use ferrite magnets to enhance performances. It is essential to understand magnet properties in order to select the right type of magnet for this type of machine. This section begins with investigating the available magnets and its properties.

In addition, the machine efficiency is quite high at flux weakening region and at low load, which make them a competitive in electric vehicle application which is further discussed in section 5.11.2. Due to missing rotor coils, the temperature rise is quite low. Thus, demagnetisation is no longer a challenge with even neodymium magnets. Moreover, the machine cost can be further reduced in size by using ceramic magnets. The quantity of PM usage in this machine is significantly lower compared with other PM machines such as SPM and IPM. In some cases, in order to avoid having empty barrier spaces in the rotor, ceramic magnets can be filed to improve the power. PMSynRM has shown incredible torque density in the constant torque and also in the constant power region.

In subsequent sections of this chapter, the PM assisted design is reviewed, discussed, simulated, and optimised. Firstly, a PM assisted design on a linear flux barrier is discussed with magnet direction, quantity and placement using neodymium magnets to understand its characteristics. Then the study focuses on high-grade rare-earth magnets (neodymium) and placement for machine performance. Then, the study focuses on the optimisation of PMSynRM using two advanced optimisation techniques. The first technique optimises the PMs in an optimised SynRM, while the second technique introduces a novel optimisation process for both PMSynRM and SynRMs. Finally, the study focuses on PMSynRM and SynRM operational regions MTPA and field-weakening regions.

5.2 Permanent Magnets used in Electrical Machines

The cost of rare-earth neodymium magnets had been the major issue in the applications in electrical machines. The prices of rare-earth magnets have decreased rapidly over the years, and they are quite economical to be used in many industrial applications. Figure 5-1 shows the prices of rare-earth magnets over the last decade or so. The rare-earth magnets had gone through the sudden boom and burst except for Alnico magnets. The search for another machine with high performance comparable to PM machines, at the same time that is not susceptible to the market surge, intensely begins during the period. As a result, some researchers pursued high-performance synchronous machine while others search for high-performance brushless machine [21].

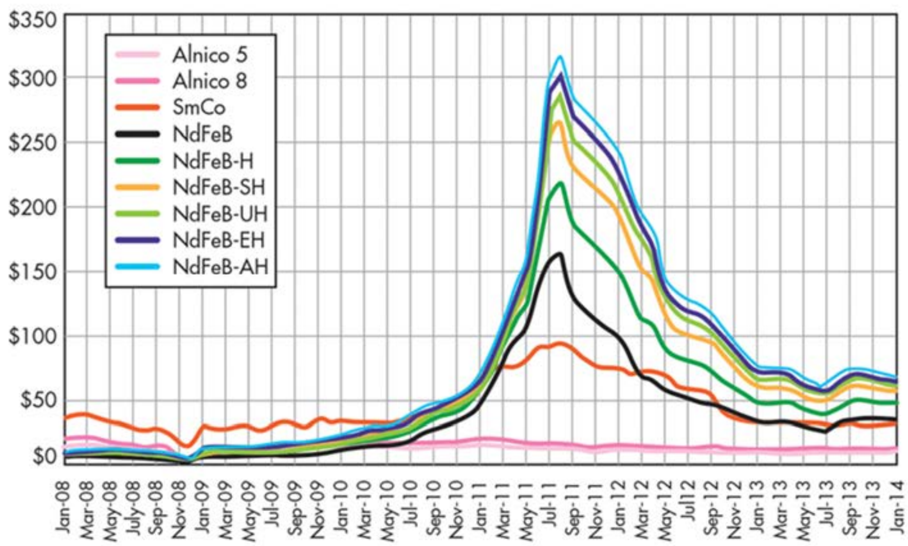

Figure 5-1: Cost of rare-earth permanent magnets in between 2010 and 2013

There are a few different types of ferromagnetic materials that have been used in electrical machines. The well-known and widely used magnets are ferrite magnets or ceramic magnets (Fe_3O_4 and Fe_2O_3). It the most widely used magnet in the world because of lower cost, high-temperature up to $250°C$ and high corrosion resistance. However, its magnetic strength is not high enough compared with rare-earth magnets.

Alnico ($AlNiCo$) magnets have been mass-produced over a century, and the process has not radically changed since then. It is also a permanent magnet made of aluminium, nickel, and cobalt as its name describes. It can also include iron and titanium depending on the magnetic strength requirement. Its properties of excellent stability under extreme temperature, high residual induction, high resistance to corrosion, makes it a better selection over ferrite magnets. On the other hand, it is hard and brittle, and machining is challenging in this composition. However, it can be used as permanent magnets as its alloys are ferromagnetic and high resistance to loss of magnetism.

Samarium cobalt ($SmCo$) is a rare-earth permanent magnet which has been in mass production since the early 1980s. It is made out of samarium and cobalt, but some grades would also include iron (Fe), copper (Cu) and other chemicals such as Zirconium (Zr) depending on the grade. It is manufactured using the method of reduction, melting and by process of bonding or sintering the raw material to form magnets. The relatively high magnetic strength (second only to neodymium), high-temperature performance up to $550°C$ and high resistance to corrosion make this magnet a popular choice.

The most popular and high-quality rare-earth magnet is a neodymium iron boron magnet ($NdFeB$). It is the most potent magnet to date and can attract over 1000 times its weight. Manufacturing of neodymium magnets is relatively complicated, and it involves high-end technology to strip casting, remove oxygen (very susceptible to oxidisation), jet milling, moulding, pressing (at almost $14{,}000\ psi$) sintering (at $200°C$ to $900°C$), machining, plating and magnetising (at the intensive magnetic field using 2400VDC/12ADC). Therefore, it is relatively expensive. Samarium cobalt qualities such as high magnetic strength, ultra-high resistance to demagnetisation, and high power to volume ratio make it one of the best rare-earth magnet. On the other hand, compromise in energy when used in high-temperature applications and inclination to corrosion require additional coating are some of the drawbacks of this magnet [185, 224].

5.2.1 Properties of permanent magnets

The quality (grade) of the magnet is determined by its energy density (BH_{max}). It is often used to denote the grade of a rare-earth magnet. The magnet is denoted, such as grade 48 or 48 MGOe (Mega Gauss Oersted). It is the BH_{max} of the magnet. Magnetic properties of commonly used magnets are given in Figure 5-2. As can be seen, the magnetic strength of neodymium magnet is quite high at low temperatures. However, its energy density reduces rapidly at temperatures above $80°C$. The Curie temperature of this magnet is around $150°C$. However, samarium cobalt ($SmCo$) can withstand high-temperatures. The temperature cannot increase above $75°C$ in electrical machines. As SynRM does not have rotor coils, the rotor's temperature is somewhat lower compared with the equivalent of induction motor.

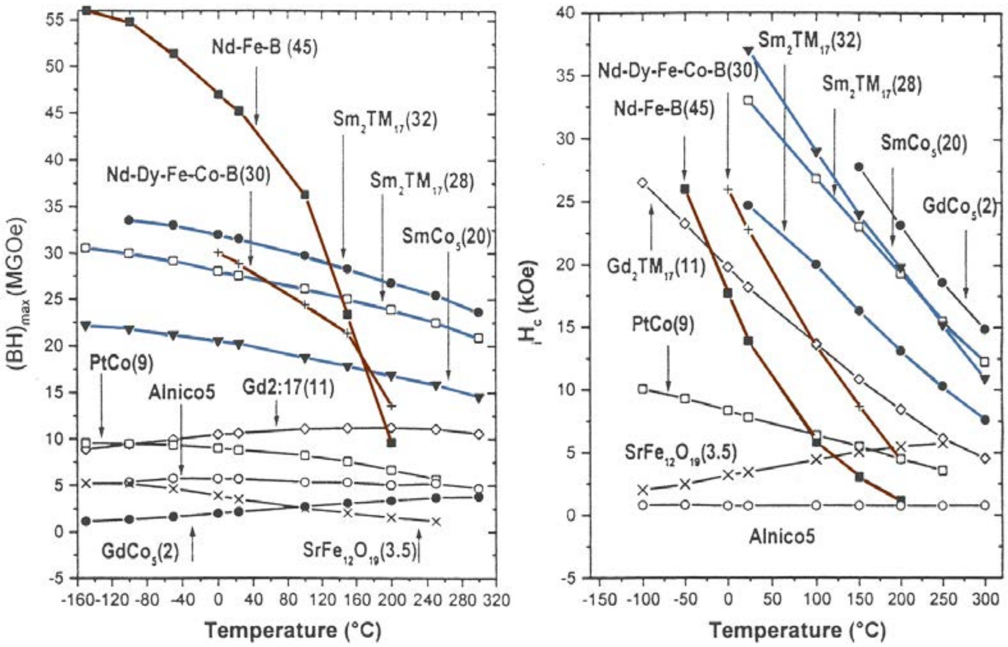

Figure 5-2: Energy density of commonly used permanent magnets (in MGOe and KGOe) (Curtesy: Arnold magnetic technologies)

Figure 5-3 shows the magnetic properties (second quadrant) for rare-earth, Alnico, and ceramic magnets. It is also called magnetic reversing or demagnetisation properties that define the strength of a permanent magnet. Although the neodymium magnets have higher retention magnetism, the other magnets are not that far. However, due to the low coercive field intensity, other magnets become susceptible to demagnetisation faster than that of rare-earth magnets as can be seen in the Figure 5-3. The other reason neodymium magnet is a good candidate for electrical machines is that its linearity and high reversible strength. Moreover, the coercive field intensity of neodymium and samarium cobalt is quite high.

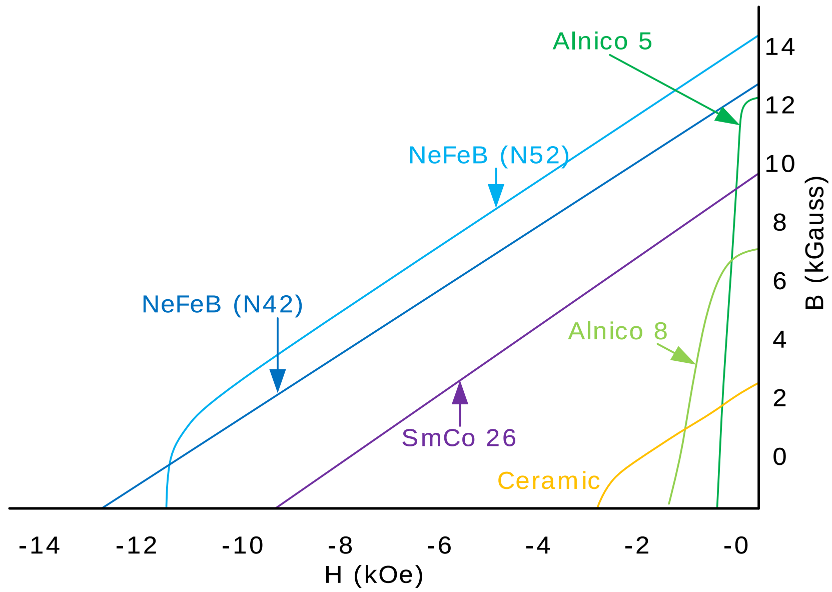

Figure 5-3: Reversible magnetic properties in the second quadrant of the hysteresis graph with retention and coercing

The high-grade rare-earth magnets are difficult to machine to obtain required tolerance. Therefore, the magnet size is quite essential to reduce magnet manufacturing cost in small range machines. Another critical feature to consider is that the magnet will have no air-gap between the magnet and the rotor segment in order to reduce leakage flux linkage. If there is an adequate air-gap between the magnet and barrier wall, it enables leakage flux.

5.3 Analytical Model of PMSynRM

An optimised SynRM can be used to achieve optimum PMSynRM. Typically, a PMSynRM is prepared by inserting PMs in a TLA SynRM. If the flux barriers are designed in such a way, PMs do not require any radial support. Hence, it can be axially supported by two proper end-press rings. It does not need any additional mechanical arrangement. Although PMs are used to enhance the performance of SynRM, there is another reason which achieving improved performance with less cost. Thus, it can deliver better performance per unit cost for other PM synchronous machines.

Figure 5-4 shows the phasor diagram with and without PMs in the SynRM. As discussed earlier, PMs are inserted in the negative Q axis direction, shown in the vector space. As a result, the resultant flux linkage is moved to the fourth quadrant and nearly $90°$ to I_s. The added PM flux linkage, in the negative Q axis, is given in Eq. (5.1) as a result, the induced DQ voltage (given in Eq. (5.2) is moved into the first quadrant from the second quadrant as can be seen in Figure 5-4. Thus, the angle between DQ current and voltage is reduced in comparison to an equivalent SynRM as in Eq. (5.3). Consequently, it improves the power factor.

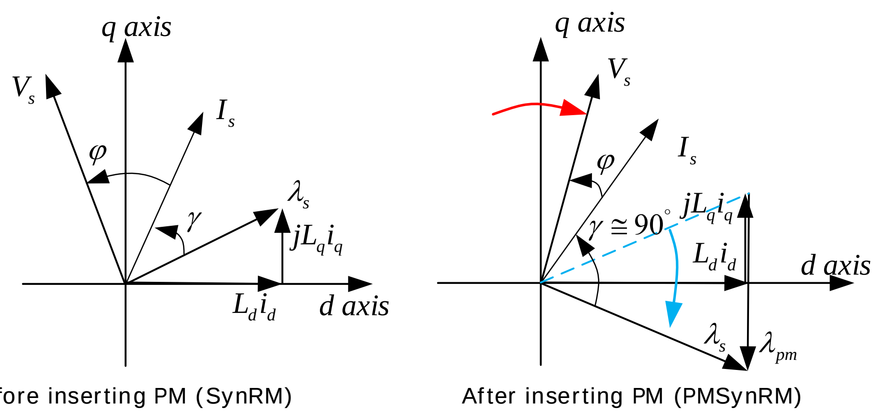

Figure 5-4: Changes in the magnetic model of a PMSynRM when PM inserted

$$\lambda_s = \begin{bmatrix} L_d & 0 \\ 0 & L_q \end{bmatrix} i_d i_q + \begin{bmatrix} \lambda_{pm} \\ 0 \end{bmatrix} \tag{5.1}$$

$$\begin{gathered} V_s = j.\omega\lambda_s + R_s i_{dq} + \frac{\partial \lambda_{dq}}{\partial i_{dq}} . \frac{di_{dq}}{dt} \\ V_s \cong j.\omega\lambda_s \end{gathered} \tag{5.2}$$

$$\varphi = 90^\circ - \gamma \tag{5.3}$$

Where V_r the resistive voltage can be ignored

The Eq.(5.4) shows the developed torque as a function of the torque angle. Due to the torque angle closer to $90°$, the torque is close to its maximum as given in (5.5).

$$T_{PMSynRM} = \frac{3}{2}\frac{p}{2}\left(|\lambda_s||i_s|\right)\bullet\sin(\gamma) \tag{5.4}$$

The current and the magnitude of flux linkage are not affected. The developed torque is increased to its maximum just by adding enough PMs. This is the limiting factor a further addition of PMs will not yield extra torque [225]. The design shall be refined to have higher currents by other means such as reducing the number of turns to increase the torque of the machine further.

$$T_{PMSynRM} = \frac{3}{2}\frac{p}{2}\left(|\lambda_s||i_s|\right) \quad ; \ \sin(\gamma) \cong 1 \tag{5.5}$$

5.4 PMSynRM Phasor Diagram

From the analysis, the PMSynRM's steady-state vector diagram can be drawn as in Figure 5-5.

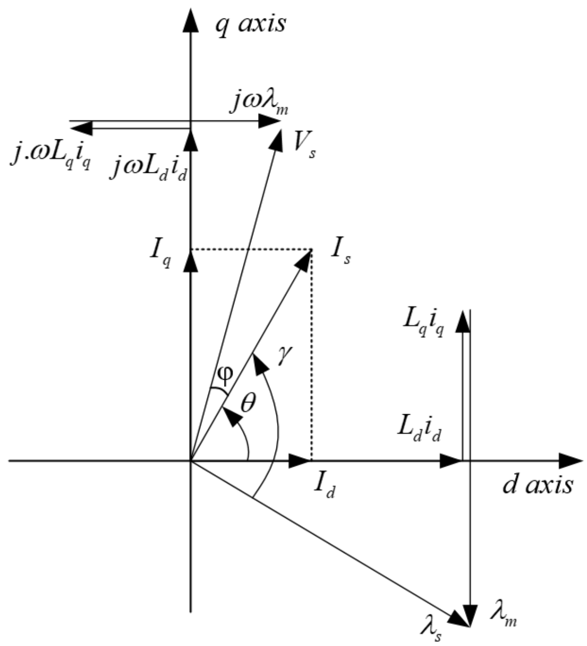

Figure 5-5: Steady-state phasor diagram of PMSynRM in DQ frame

Due to the addition of PMs, the power becomes constant in the flux weakening region, as shown in Figure 5-6 in the blue line.

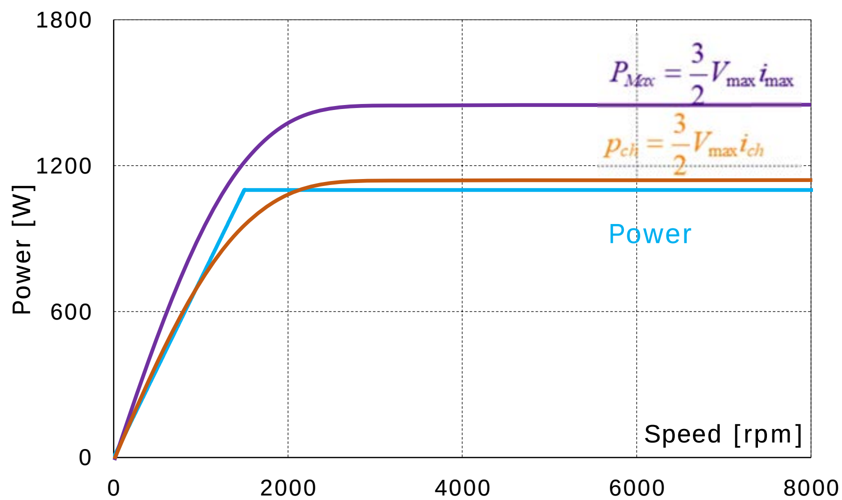

Figure 5-6: Characteristic and a maximum power of PMSynRM in the flux weakening region

When the Q axis current changes its direction (i_q), the PM torque components remains the same, but the reluctance torque component is changed. On the other hand, when the D axis current changes its direction (i_d) both reluctance and PM torque components are changed as in Eq. (5.6). The analytical MTPA is no longer lies at $45°$ for PMSynRM.

$$T_{PMSynRM} = \frac{3}{2}\frac{p}{2}\left((L_d - L_q)i_d i_q + \lambda_{pm} i_d\right) \tag{5.6}$$

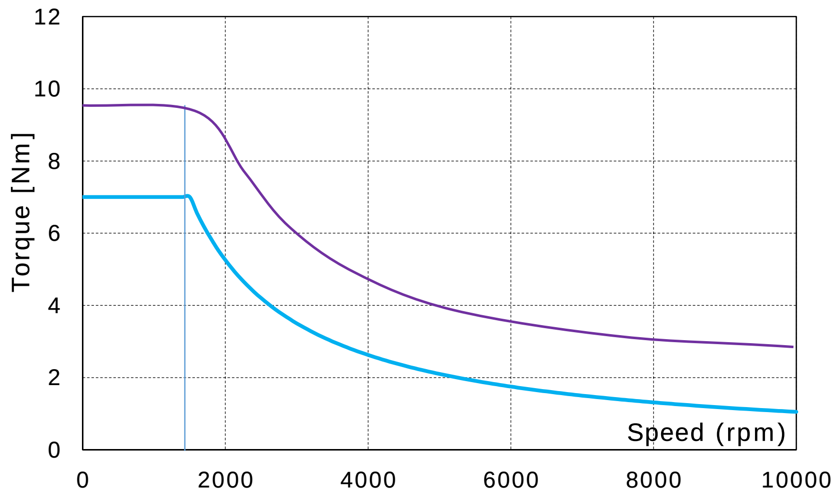

Figure 5-7: Torque speed curve of SynRM and PMSynRM

The power factor of a PMSynRM can be derived as Eq. (5.7) using the phasor diagram. In the case of PMSynRM, the current angle $\theta = \gamma - \delta$.

$$pf = \frac{\cos(\theta)\left(\left(\xi - 1\right)\sin(\theta) - \frac{\lambda_m}{L_q i}\right)}{\sqrt{\xi^2 \cos^2(\theta) + \left(\sin(\theta) + \frac{\lambda_m}{L_q i}\right)^2}} \tag{5.7}$$

Thus, the power of a SynRM can be significantly increased by merely adding PMs along the negative Q axis direction, as shown in Eq. (5.7). The resultant magnetic flux is shifted to the fourth quadrant, and the voltage vector is moved to the first quadrant while the current vector is not affected, as shown in the phasor diagram in Figure 5-8. Now the next design question is, what is the correct amount of PM flux linkage? The machine characteristics shall be defined in order to determine the amount of PM flux correctly. Regardless of the magnitude of added PM flux linkage, the machine power is increased. Therefore, the machine characteristics are significantly impacted by the addition of the PMs. The following section defines the magnitude of the PM flux.

5.5 Optimum PM Flux Linkage

As we already know the characteristics of SynRM, it is relatively easy to define the PM assisted designs characteristic. The only difference between the two machines is the added PM flux in the negative Q axis for PMSynRM. The magnitude of the PM flux is essential to minimise the PM quantity, optimise the cost and machine performance. As per the phasor diagram, if the base SynRM's performance is weak, the quantity and quality of PM (PM flux) need to be high, as shown in Figure 5-8. If the load angle is higher, it requires high PM flux. Therefore, the first and far most step in designing the PMSynRM is obtaining a fine SynRM before defining the PM flux.

The PM quantity is then determined by the flux needed at characteristic operation. The characteristic operation is the rated realistic operation, as shown in Figure 5-9. The PM flux is given by Eq. (5.8). The quantity of PM selected so as it follows the characteristic current condition at maximum speed. In this state, the power is constant in the flux weakening region. [226, 227].

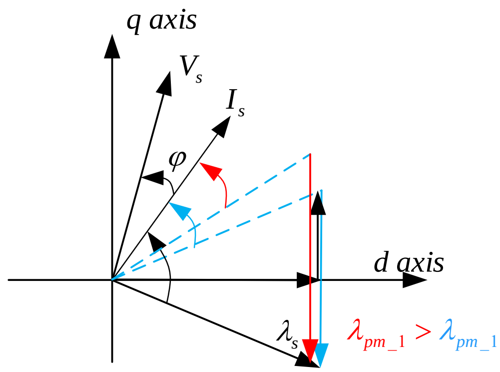

Figure 5-8: A good and poor performance of SynRM's influence on the quantity of PM

The characteristic operation and maximum operating conditions of PMSynRM are defined in Figure 5-9. It shows the PM flux selection in terms of characteristic current where $\lambda_{mq,i_{ch}}$ is Q axis flux generated at flux weakening condition (current angle is $90°$). PMs shall be inserted to compensate the Q axis flux. The characteristic current i_{ch} is the Q axis current at flux weakening conditions that define the required PM flux, as shown in Figure 5-9

$$i_{ch} = \frac{\lambda_{pm}}{L_{mq}} \qquad (5.8)$$
$$\lambda_{pm} = L_{mq} i_{ch}$$

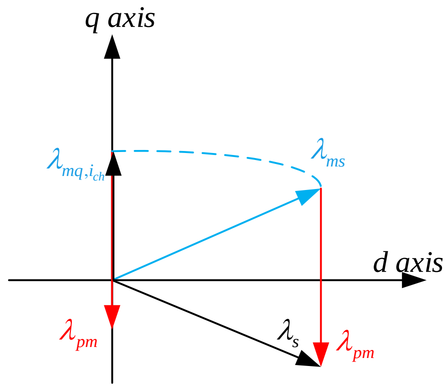

Figure 5-9: PM flux characterisation

Thus, the PM flux in a PMSynRM is determined using Eq. (5.8) for MTPA and field-weakening operation. The quantity and grade of the PM should be selected in such a way that the flux linkage is just enough to develop the characteristic current. The characteristic power of PMSynRM is determined by Eq.(5.9).

$$P_{ch} = \frac{3}{2} V_{\max} i_{ch} \tag{5.9}$$

5.6 The Basis of PM Assisted Design Simulation

Fractional symmetry method has been used for the above SynRM analyses. Thus, the processing time could be minimised for a symmetrical object in FEM tool. It should be re-assessed to ensure the symmetry method is still applicable because of different directions of PM flux in each quadrature. The fractional symmetry method is essential to understand the application of vectors in the FEM. The fractional symmetry method is applied to any vector component based on the number of fractions (for magnitude) and boundary conditions (for direction) on a symmetrical object. This method has been utilised for SynRM simulation about its symmetrical axes. However, it is important to ensure the method's usage for PMSynRM simulation as the machine has added PM flux vectors in a particular direction. Figure 5-10 shows one-fourth of the design in the first quadrature while second quadrature shows its mirror.

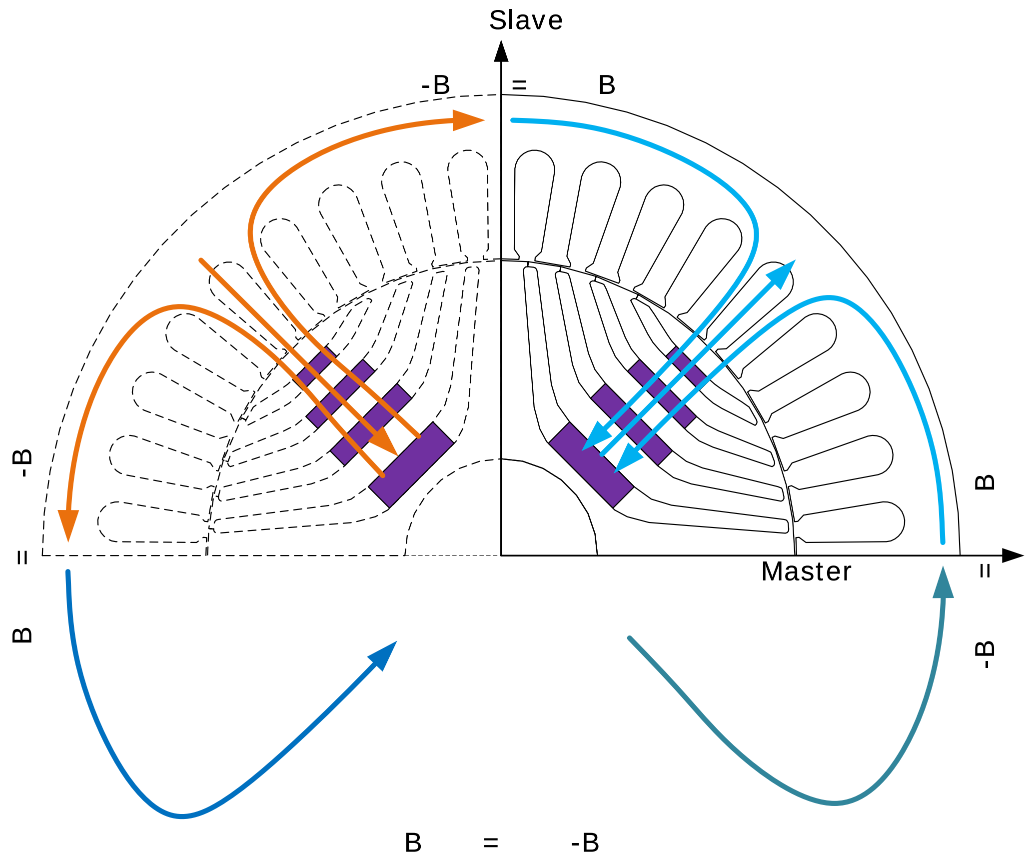

Figure 5-10: Applying fractional symmetry to PM assisted design

The flux directions are shown on the other two quadrature. The boundary condition defines the symmetry in the FEM tool in such a way that the next quarter is opposite of the considered quarter as shown by the labels. Then the FEM tool will automatically interpret the vector directions. The X and Y axes can be considered as a master and slave boundary conditions for the symmetry purpose. There are no additional PMs in SynRM, but it is quite a similar magnetic circuit, and easy to comprehend. However, in the case of PMSynRM, the added flux is directed towards specific directions using magnetic properties. Based on the graphical interpretation, the magnetic direction agrees with boundary condition in each quadrature and follow the fractional symmetry boundary condition. It is verified with simulation to make sure the fractional symmetry methods results match with a complete design.

The first case of PMSynRM is analysed using a linear-barrier to understand the PM flux analysis. The location, direction and quantities of the PMs are analysed with a focus on the machine performance. The second study focuses on optimising the PMs in a SynRM. Finally, a novel optimisation topology is investigated by optimising SynRM and PMs simultaneously to achieve the best PMSynRM.

5.7 Analysis of PM Assisted Design

In this section, an optimised SynRM with a linear-barrier is prepared, as shown in Figure 5-11. High-grade neodymium rare-earth permanent magnets are used for this analysis. The design AN-PMI_SynRM is selected as the base-design for all other PMSynRMs with the linear-barriers. The other eleven PM assisted designs to have different quantities of PMs and placement. PMs are added incrementally into the first four PM assisted designs, as shown in Figure 5-11 (AN-PMI_01 to AN-PM_04). The next four designs have PMs inserted along the intermediate axis incrementally (from AN-PMI_05 to AN-PMI_08).

The next three designs are randomly selected to see the difference in PM volume along the intermediate axis. The PMs are sized to match the barrier thickness with $\pm 0.05\,mm$ air-gap between the magnet and barrier walls. Thus, no additional support to hold the PMS is required. PMSynRM is supposed to have optimum PM quantity. If the PM volume is high, then its PM torque becomes dominant, and it becomes an interior permanent magnet (IPM). This investigation is intended to analyse the PM quantities and PM placement. Subsequent studies will perform the optimisation of the PM quantities.

The radial webs are removed from its equivalent SynRM for PM insertion. N52 neodymium magnets are selected for this simulation due to its high demagnetisation capability and reasonable temperature resistance for PMSynRM. This analysis does not focus on torque ripples analysis rather on the impact of high-grade rare-earth magnets. It focuses primarily on the added PM flux and its influence on the machine performance. The efficiency is also estimated by carefully modelling losses using magnetic steel and neodymium manufacturer data and stator winding details.

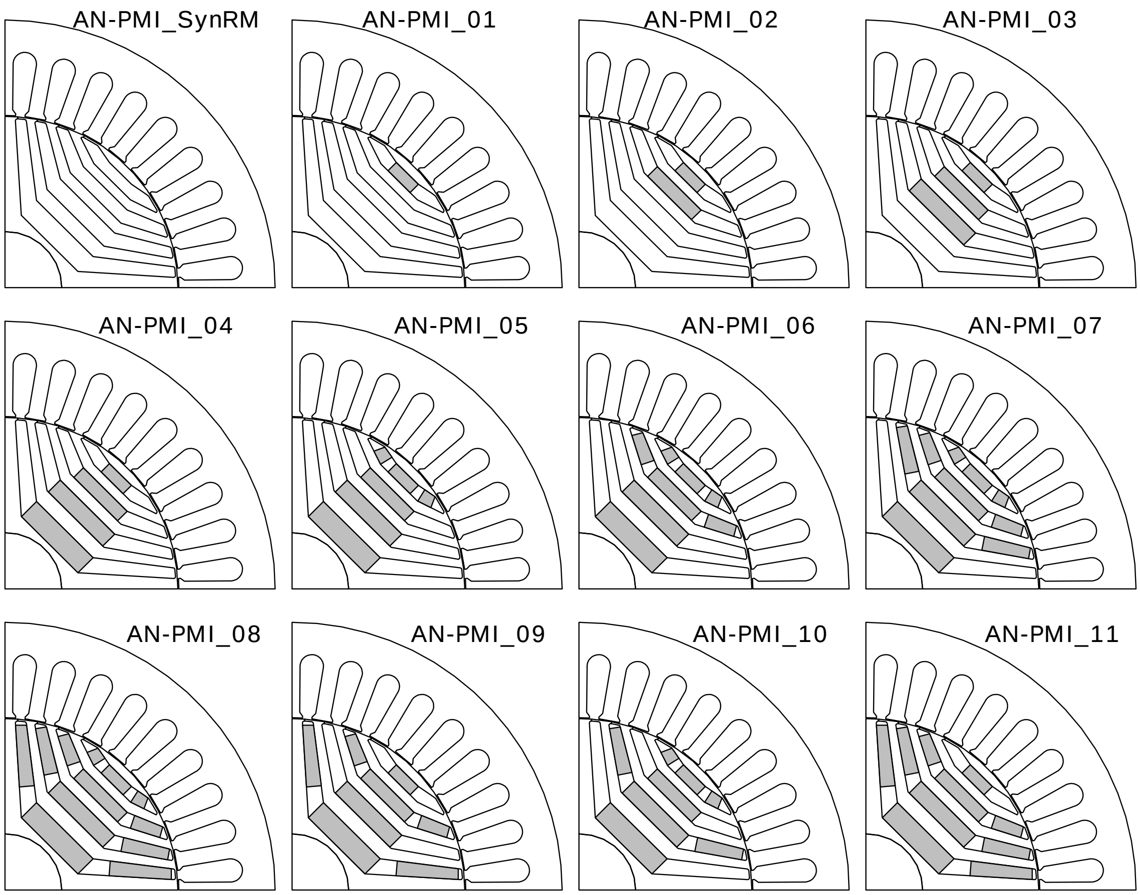

Figure 5-11: Analysis-PMI - PM arrangement in a linear-barrier SynRM

DQ voltage of each design is plotted with respect to the designs in Figure 5-12 and flux linkage is plotted in Figure 5-13. The design names are shortened to PMxx in the figure where xx represent the numerical number of each design. The design names are shortened to self-descriptive names in the graph for simplification. The DQ voltage of each design in Figure 5-12 shows the importance of having high-grade PMs. In a SynRM, the D axis voltage is in the negative range, which increases the angel between voltage and current, resulting in low power factor (refer to Figure 2-9 in Chapter 2). The addition of PM in design AN-PMI_01, although it is a PM assisted design, does not have PM assisted characteristics. Its

D axis voltage is still in the negative range, and the resultant flux linkage has also not moved to the fourth quadrant, and its power factor is slightly increased.

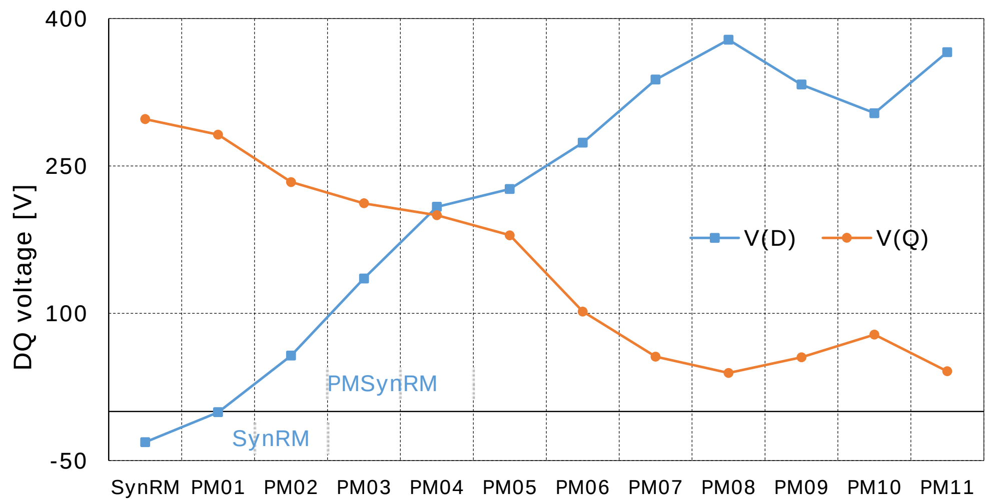

Figure 5-12: Analysis-PMI - DQ voltages of the designs

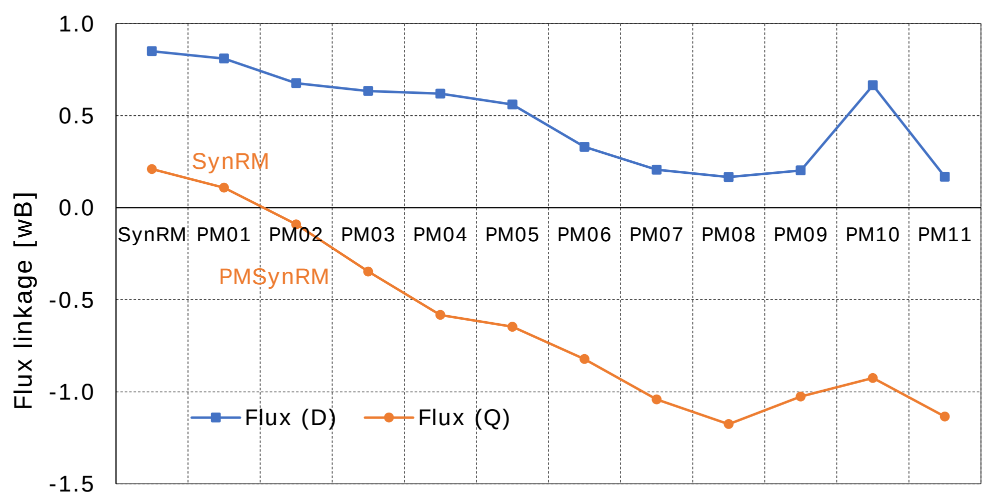

Figure 5-13: Analysis-PMI - Flux linkages of the designs

The phasor diagrams of SynRM and PMSynRM designs AN-PM_01, AN-PM_02 and AN-PM_04 are illustrated in Figure 5-14. A PM assisted design should have DQ voltages in the first quadrant while the resultant flux linkage in the fourth quadrant. In the case of PM_01 machine characteristics, although improved, but not enough to meet its characteristic current and required machine performance. The added PM flux is not enough to move the D axis voltage into the first quadrature. On the other hand, AN-PM_02 has both D and Q voltages in the first quadrant, which makes it a complete PM assisted design. The other PM assisted designs (as indicated in Figure 5-12 and Figure 5-13) have positive DQ voltage with flux linkage in the fourth quadrant.

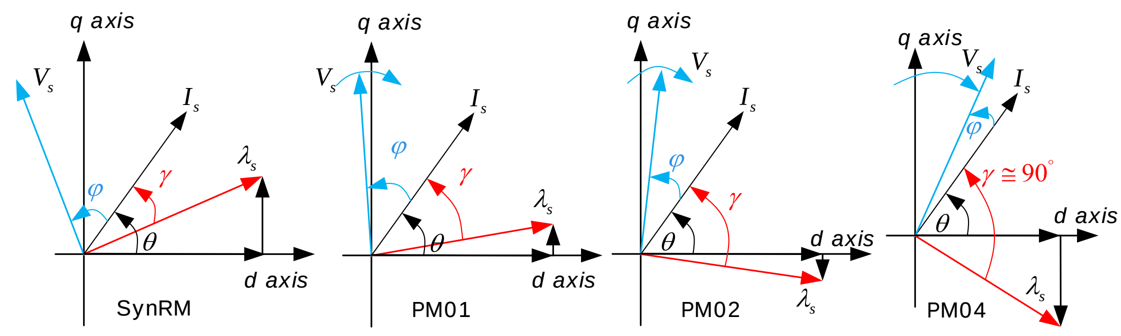

Figure 5-14: Analysis-PMI - Vector diagram of four designs

The induced Q axis flux linkage of AN-PMI_01, is just above 0 Wb. However, the next design AN-PMI_02 has just under 0 Wb. Although, it has PMSynRM characteristics, its performances are not quite high as other PMSynRM with high PMs. The impact of PM flux on the resultant flux linkage can be seen in the phasor diagram in Figure 5-14. Except for the first design, all other designs have the characteristics of the PMSynRM, although the characteristic current of each design is different due to the difference in resultant flux linkage. The design with more PMs (AN-PMI_08) has higher D axis voltage and lower Q axis voltage, but both are positive voltages. On the other hand, the magnitude of the D axis flux linkage is reduced while the Q axis is increased in the fourth quadrature to have the same total flux linkage vector magnitude. The design AN-PMI_10 shows quite different DQ voltage changes and flux linkage changes. The change is due to the direction of the flux path for the particular PM arrangement.

The addition of PMs along the intermediate axes drags the resultant flux into the fourth quadrant as expected. However, its arrangement is essential in achieving a high-performance machine. The steady-state voltage, current and flux linkage vectors of four designs are shown in Figure 5-14. AN-PMI_01 has weak characteristics similar to a SynRM, as shown in the figure. However, as can be seen, due to the added PM, its power factor is increased in each design.

The power factors of all the designs are plotted in Figure 5-15. The power factors of designs AN-PMI_01 to AN-PMI_04 has increased with the addition of PMs. The Designs AN-PMI_01 to PMI_04 have shown 5.5 %, 7.5 %, 8 % and 9.1 % more power factor compared with the base SynRM, respectively. Figure 5-16 shows the torque of each design. The torque of a PMSynRM is directly proportional to its torque angle γ as in Eq. (5.4) for an ideal machine with no saturation. The increase in PM quantity has certainly increased the angle between the current vector and flux linkage vector. However, it cannot be assumed the same for the designs with PMs along intermediate axes.

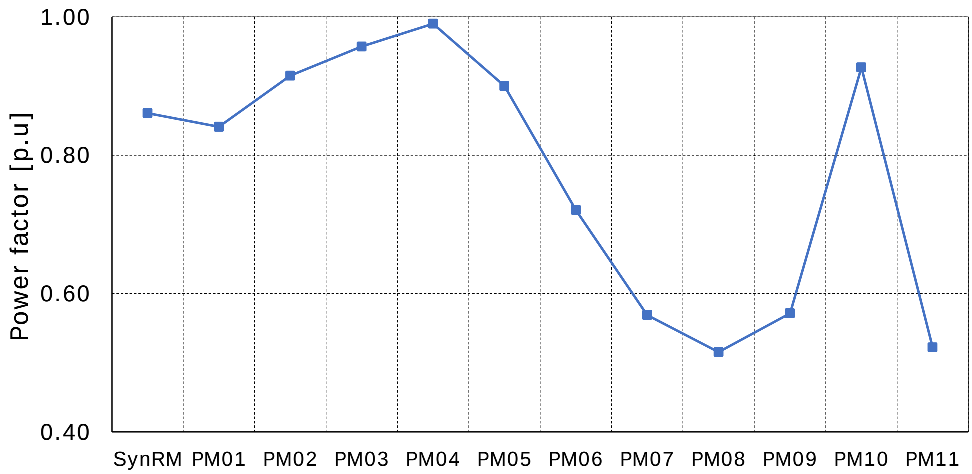

Figure 5-15: Analysis-PMI -Power factor of the designs

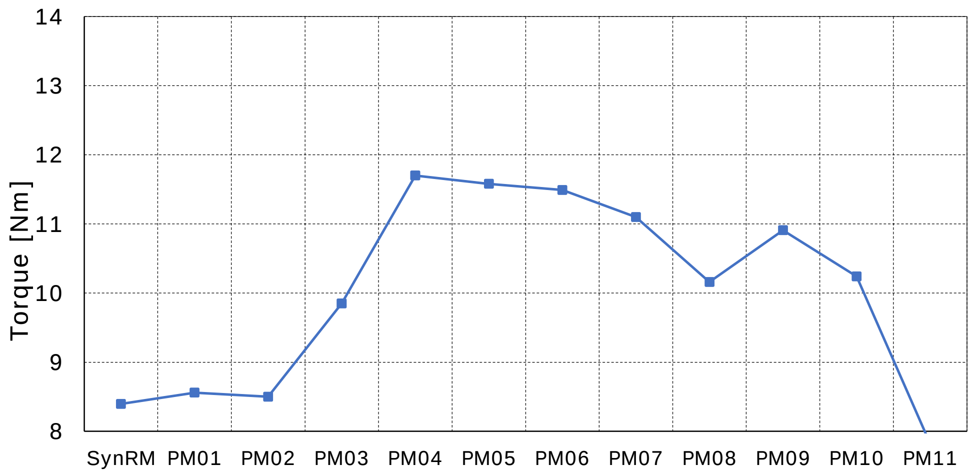

Figure 5-16: Analysis-PMI -Torque of the designs

The addition of PMs increases the efficiency of PMSynRM compared with equivalent SynRM. The core losses of all the models from the investigation are plotted in Figure 5-17. The DQ frame currents are slightly impacted due to the PM flux. The magnetic current i_d drives the core loss as already discussed in section 3.8. Besides, the added PM flux increase the core saturation depending on its location. The combination of increased i_d and core saturation influences the core-loss in each design. The results of each design are produced at its MTPA (concerning the current angle of maximum torque). Thus, the i_d current is different in each design resulting in different core losses and the efficiencies.

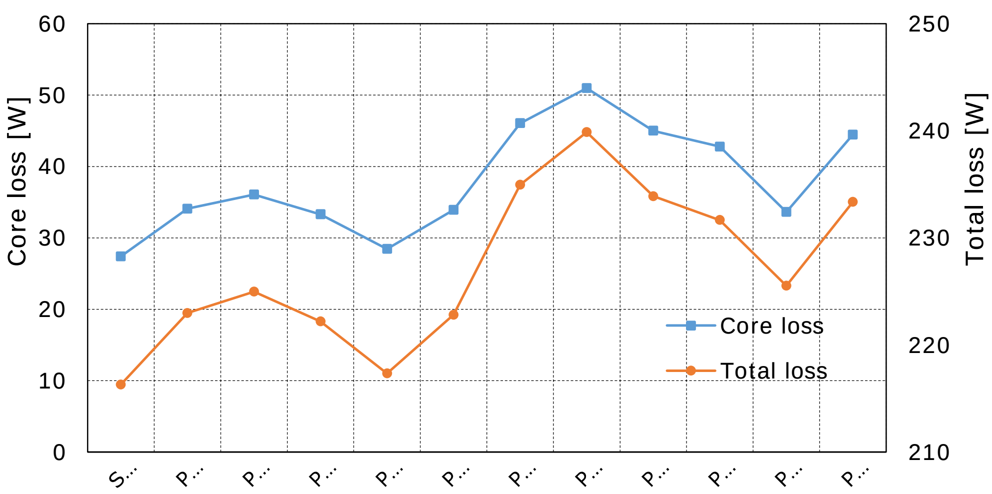

Figure 5-17: Analysis-PMI - Core and total losses of the designs

The core loss defines the difference in efficiencies of a PMSynRM and its equivalent SynRM. It can be seen in the efficiency plot in Figure 5-18, where the efficiencies have dropped for the first two designs and then increased for the next two designs. The design AN-PMI_04's efficiency is increased by 1.9 % compared with its equivalent SynRM while the design AN-PMI_02's efficiency is dropped by 1.05 %. The efficiencies of other designs from AN-PMI_05 to 11 is not consistent and quite low compared with the design AN-PMI_04 as the PM flux saturates core segments.

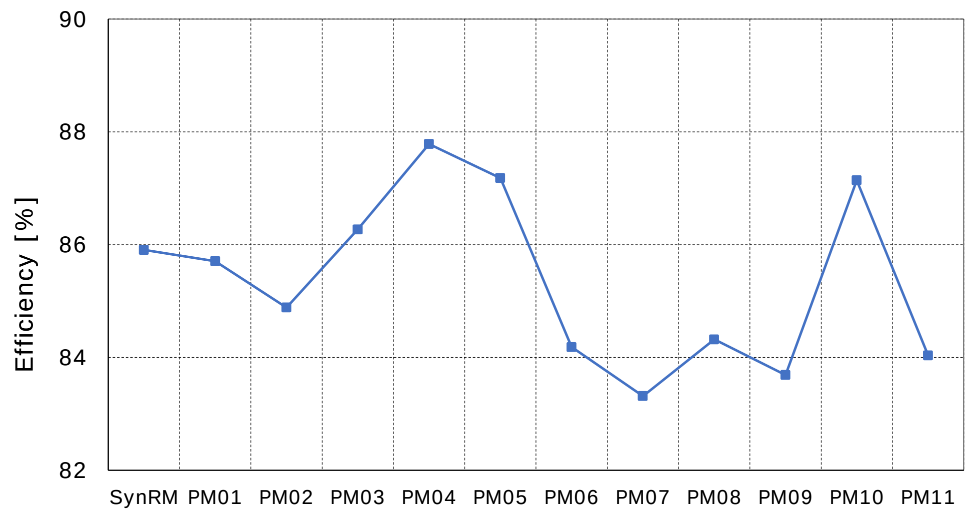

Figure 5-18: Analysis-PMI - Efficiency of the PMSynRM designs

The design AN-PMI_10 with PMs along the intermediate axes have resulted in higher power factor and torque compared with similar PMSynRMs. A comprehensive optimisation study is performed in the subsequent section to understand the high-performance machine with PMs along intermediate axes.

The study deals with various configurations of PMs in a SynRM with linear-barriers and compares the machine performance and operational characteristics for each configuration. As shown earlier, an increased quantity of PMs in SynRM is not a recommended practice due to costly PMs. The high volume of PMs would make it a PM machine instead of PMSynRM. The optimisation of PM volume is necessary to yield the best performance. The optimisation of PMs in an optimised SynRM and optimisation of a PMSynRM as a whole object using primitive design are discussed later in section 5.9 and 5.10, respectively. Before to optimisation, the characteristics of PMSynRM are discussed and investigated.

5.8 Characteristics of PMSynRM

5.8.1 PM Flux Linkage

PMSynRM is distinguished by its ability to saturate the ribs (and webs if there is one in the design) from SynRM. The SynRM is predominantly controlled using current controllers due to its linear relationship with torque in the MTPA (discussed in section 2.8 and 5.11). Thus, a PMSynRM should be controlled by the same current controller with slight changes in the algorithm, as discussed in section 5.11. If the machine uses the current controller, it is quite simple to saturate rotor ribs in a controlled manner if the saturation model is accounted for in the control algorithm. Thus, the impact of saturation due to supplied current and current angle needs to be understood. The rotor ribs can be saturated even before introducing current if enough high-grade PMs are used. The current angle is a critical control parameter in the operation of the machine.

Q-Axis Inductance

In a typical PMSynRM, PMs are placed in Q axis, and ribs are in the circumference. Due to the alignment of PM flux direction and increase in current, the flux is directed through the ribs. The ribs saturate faster at lower currents, though it results in reduced efficiency. Figure 5-19 shows the saturation in the ribs of a PM assisted design. In saturation state, further flux through the ribs is reduced, thus less flux for further increasing currents. Therefore, the machine saliency increases with increasing current. The subsequent investigation is carried out by keeping the current angle constant at MTPA and varying the supplied current from 0 to 8 A.

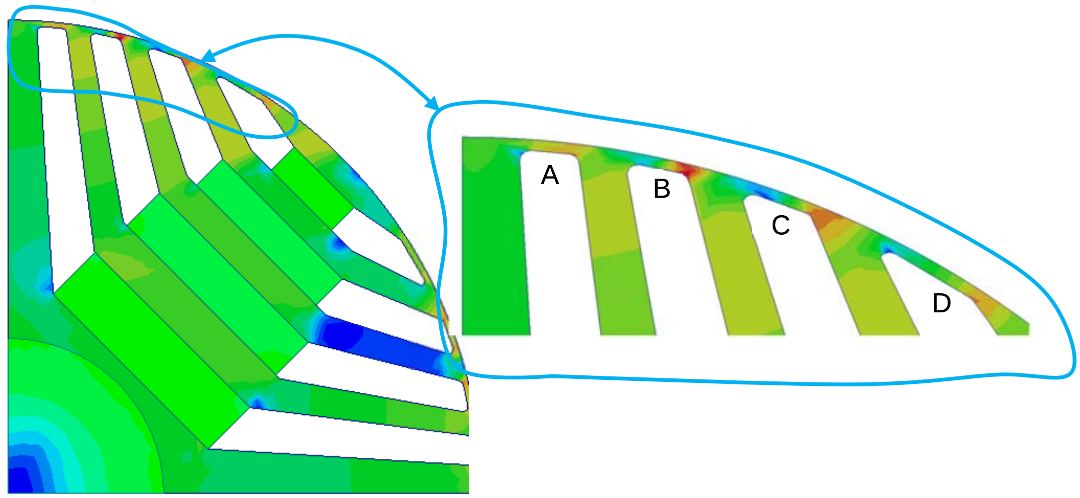

Figure 5-19: Analysis-PMI – Saturation in the ribs of a PM assisted design

Figure 5-20 shows the comparison of the DQ flux linkages of PMSynRM and equivalent SynRM. D axis flux linkage of PMSynRM is similar to equivalent SynRM at low currents, while it becomes lower at higher current than that of SynRM. However, F_d of PMSynRM increases above that of SynRM's at currents above (7.5 A). On the other hand, F_q of PMSynRM is in the negative range. However, there is no saturation on the Q axis flux because the magnets have already saturated the ribs. The rate of change in Q axis flux linkage with respect to current is quite low compared with the D axis, similar to SynRM. The initial Q axis flux linkage with added PMs is -0.8 Wb and increases gradually with the supplied current. It can be seen, and due to the high PM flux in the Q axis, the ribs are saturated even before the current applied. The machine's resultant flux linkage is in negative range and linear with the current.

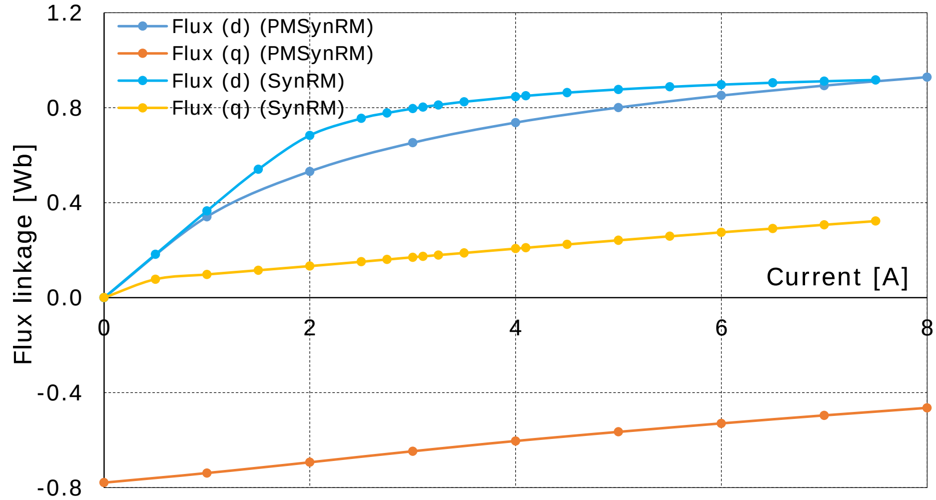

Figure 5-20: Analysis-PMI – DQ flux linkage of SynRM and PMSynRM with respect to supply current

The flux linkage characteristics for varying current angles (during control) is vital to understand the machine's behaviour. Figure 5-21 shows the flux linkage with a simultaneous change in currents and current angles for the same PMSynRM. The D and Q flux linkages are marked as F_d and F_q for easy identification with associated currents. The simulation for the current of $0\,A$ shows the machine characteristics at standstill condition. At this stage, the D axis flux is zero, but the Q axis flux is in the negative region but not affected by the change in the current angle and remains constant. It validates the notion that the saturation in the ribs has already occurred even before the current is applied.

The D axis flux linkage increases non-linearly with currents while the change in Q axis flux shows rather linear change as the Q axis does not saturate with the change in current. The high saturation region is indicated above 70° current angle in the figure. The D axis flux linkage decreases with the current while Q axis flux increases for increasing current angle. The increase in the current angle will reduce the flux with constant current and voltage. Thus, the resultant flux decreases gradually with increasing current angle regardless of the current magnitude. It is the technique used to control the machine at higher speeds, termed as field-weakening as discussed in 2.8.

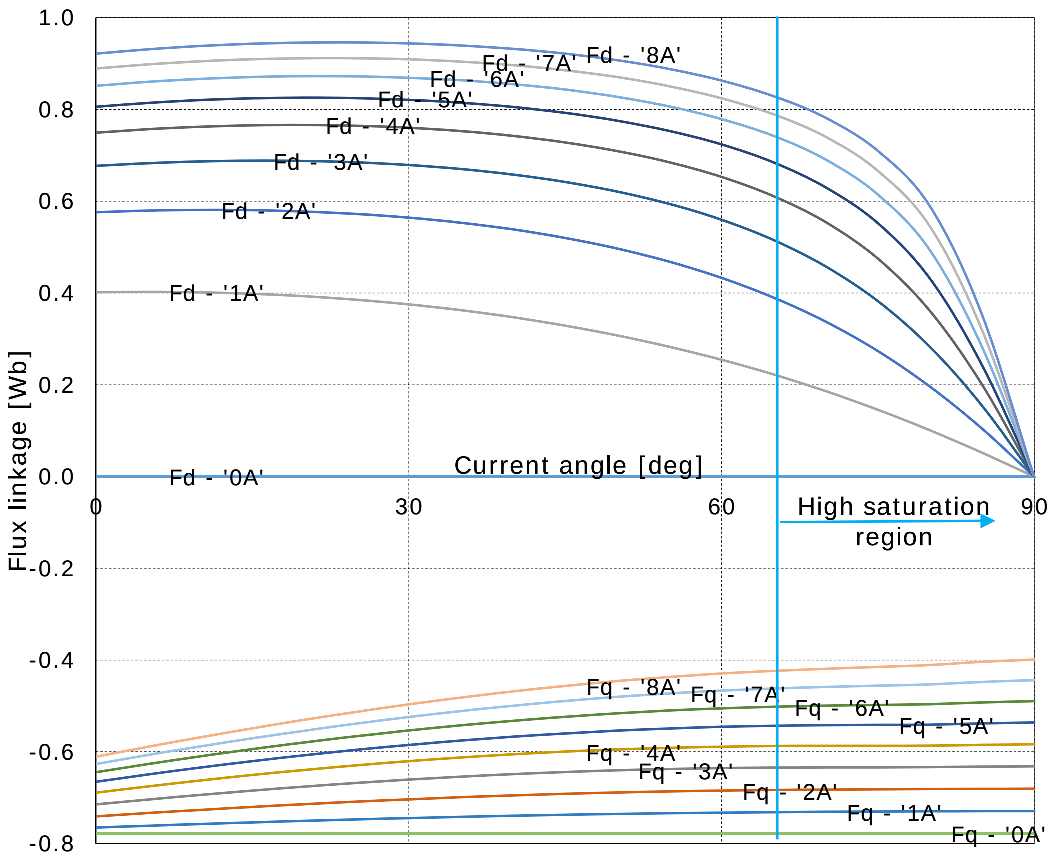

Figure 5-21: Analysis-PMI - DQ Flux linage of PMSynRM as a function of the current and current angle

The field-weakening philosophy will be discussed in the subsequent section. In order to yield the best out of this PMSynRM, the machine shall be operated between $30°$ to $65°$ in MTPA. If the machine is operated at a higher current and current angle, the saturation and cross saturation will be significantly high, and the efficiency of the machine will be low.

5.8.2 D and Q Inductances and Saliency

The above investigation is further extended to study D and Q inductances. A practical PMSynRM is simulated throughout the study. This section investigates the inductances for varying currents and current angles to find the optimal operating region of a PMSynRM and compared with equivalent SynRM. The results are plotted in Figure 5-22 (a) for SynRM and (b) for PMSynRM.

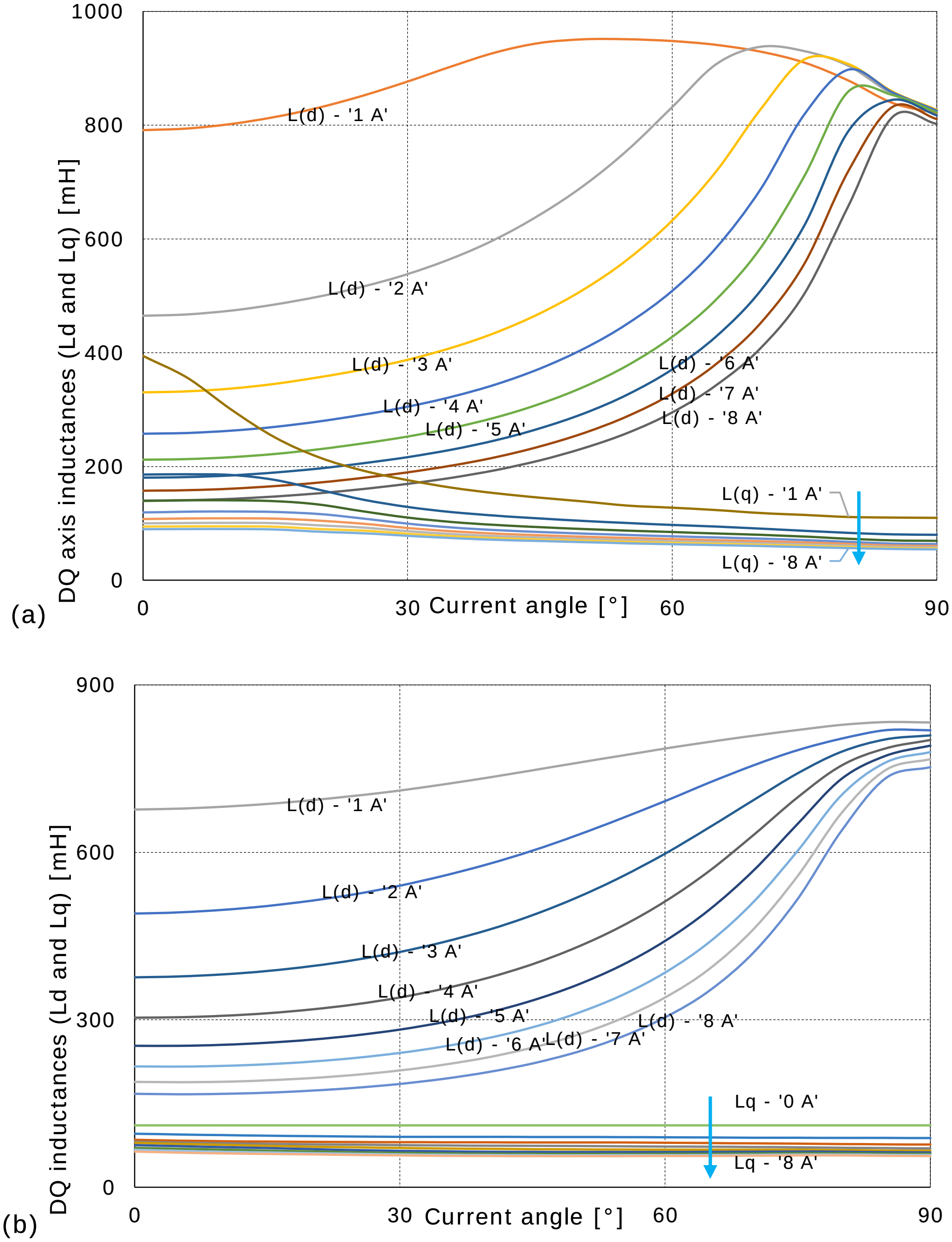

Figure 5-22: Analysis-PMI – (a) DQ inductances of SynRM as a function of current and current angle (b) DQ inductances of PMSynRM as a function of the current angle

The L_q of SynRM decreases with increasing currents as the ribs are not fully saturated, especially at low current angles. Thus, the ribs act as a passage for the Q axis flux to pass through. The L_q in PMSynRM is nearly constant with current angle and experiences little change with increasing current as the ribs are already saturated in PMSynRM. Thus, it does not experience any change with either current or current angle.

The magnitude of D axis inductance L_d of a SynRM is reduced with increasing currents and at low current angles. It then increases with the current angle to a particular current angle before it decreases again. The maximum L_d of each current is obtained at various current angles. The maximum D axis inductances for currents of 1, 2 and 3 A are obtained at around $53°$, $71°$ and $74°$, respectively in the case of SynRM. It suggests that the optimum machine performance of this machine lies within a narrow range current angle. Similarly, L_d gradually decreases for increasing currents and increases with current angles for PMSynRM. It keeps on increasing with the current angle before reading maximum at of around $90°$ of the operating regions regardless of the current levels.

Figure 5-23 shows the saliency ratios of both SynRM and PMSynRM. The saturated saliency of SynRM increases with the current angle to its maximum and then it drops again. Whereas in the case of PMSynRM, the saliency ratio gradually increases with the current angle. Although PMSynRM has higher saliency ratio at lower currents and current angles, SynRM has higher saliency ratios for high currents and current angles. It is the critical performance factor of a SynRM and PMSynRM operation. Further investigation is continued to understand the operational machine performances in the subsequent sections.

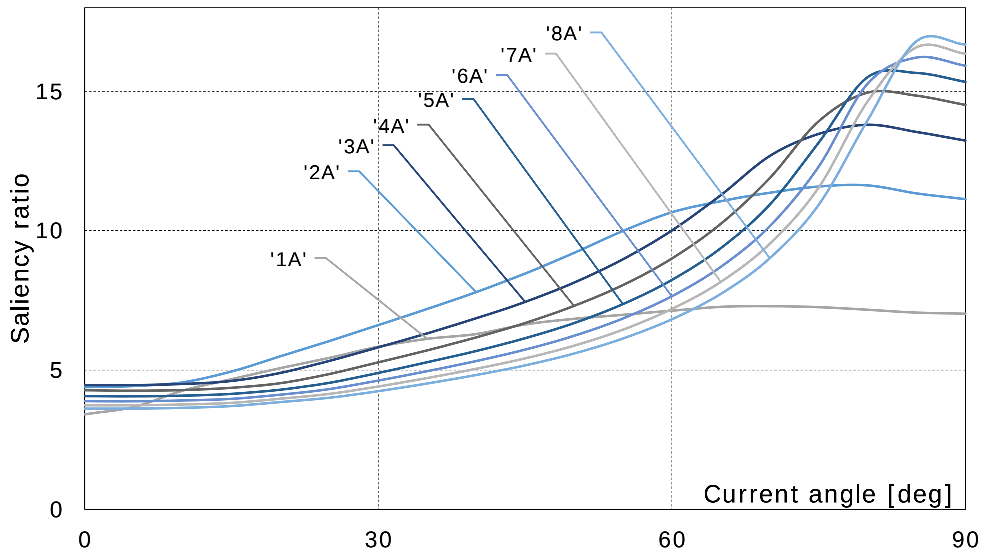

(a)

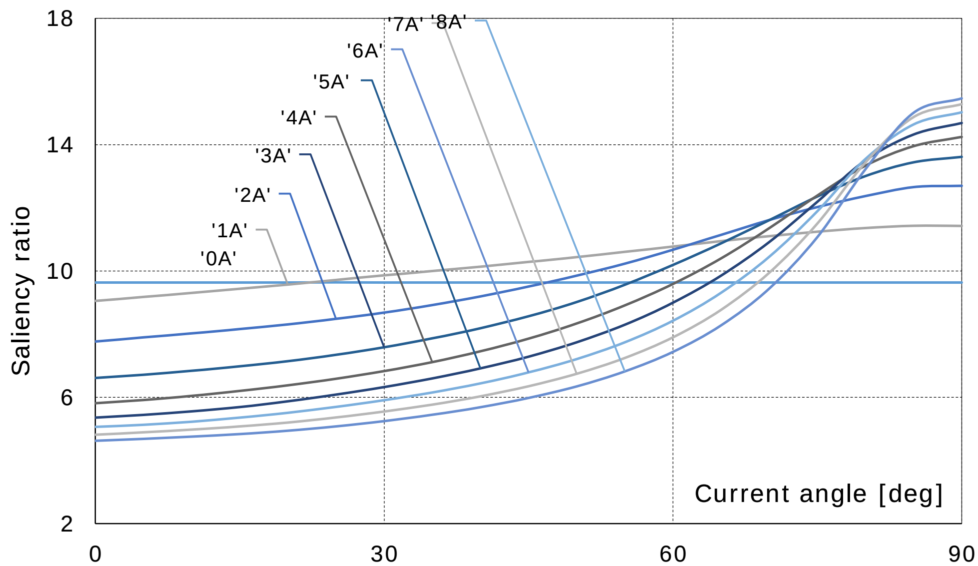

(b)

Figure 5-23: Analysis-PMI – (a) Saliency ratio of SynRM as a function of current and current angle and (b) Saliency ratio of PMSynRM as a function of the current and current angle

5.8.3 The power factor of PMSynRM

The power factor of PMSynRM is studied in this section using the same PMSynRM shown in Figure 5-19. As discussed earlier in section 5.4, the performance of PM assisted design is not directly proportional to its saliency ratio as in the case of SynRM. The power factor of PMSynRM is given by Eq. (5.7). It is worth noting that MTPA of SynRM and PMSynRM are different. The current angle at maximum torque is $65°$ in the case of SynRM, and it is at $42°$ in the case of PMSynRM (for this particular PM configuration). The MTPA of PMSynRM will be discussed further in subsequent sections. The power factor of PMSynRM and equivalent SynRM are obtained from FEM simulations and compared, as shown in Figure 5-24. The power factor of SynRM is higher at lower currents compared with PMSynRM for MTPA. The power factor of PMSynRM is higher for currents above 1.5 A and stays above 0.97 $p.u$ for increasing currents. The high-grade and volume of PM increase the PM flux in the Q axis, which results in torque angle $\gamma \cong 90°$ ($\varphi = 90° - \gamma$), as shown in Figure 5-5.

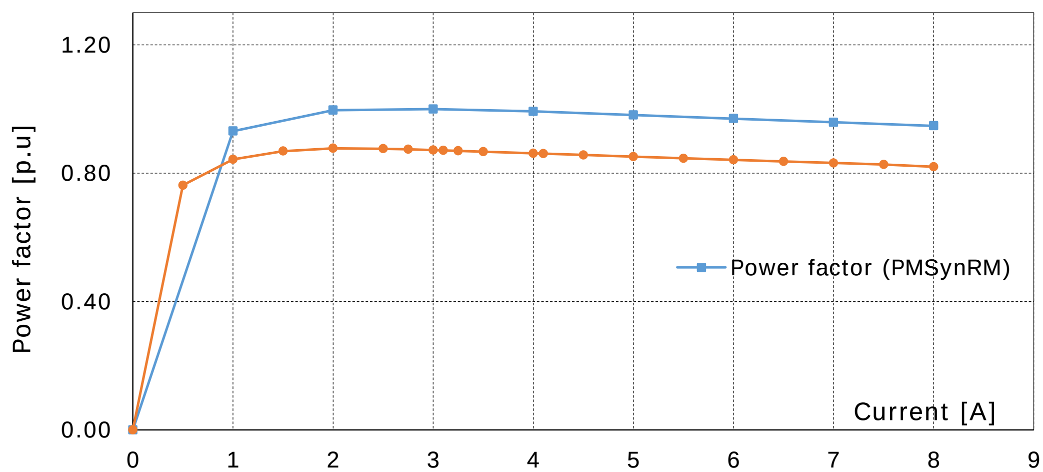

Figure 5-24: Analysis-PMI – Comparison of power factor of PMSynRM and SynRM (at current angle $65°$)

The following study compares the power factor of SynRM and PMSynRM with respect to current and current angles. The Power factor of SynRM is given in Figure 5-25(a) and PMSynRM results are plotted in Figure 5-25(b). The saturation effects in SynRM shifts the maximum power factor with high current angles (between $65°$ and $80°$).

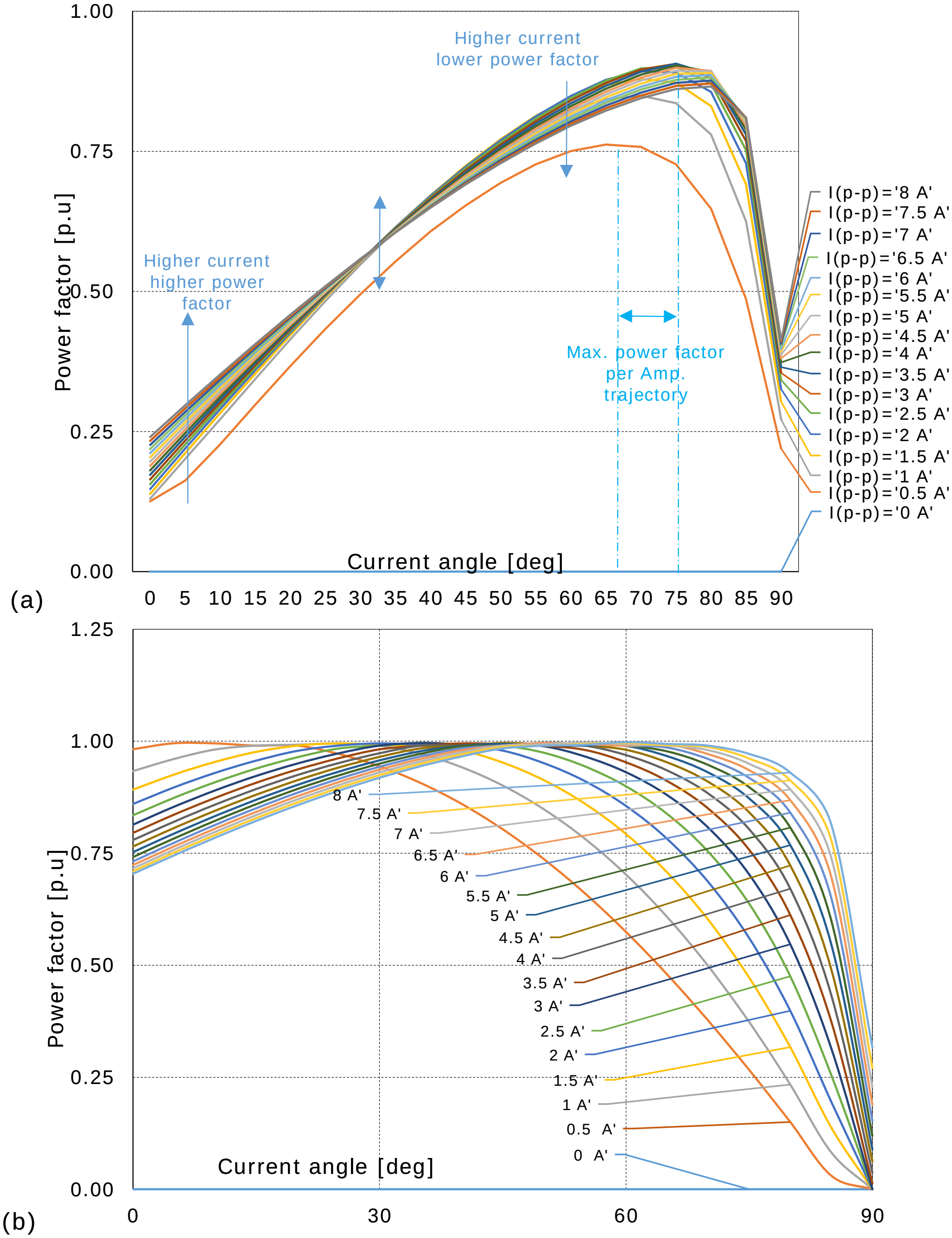

Figure 5-25: Analysis-PMI – (a) Power factor of SynRM as a function of current and current angle (b) Power factor of PMSynRM as a function of the current and current angle

However, in PMSynRM, the un-saturated power factor is obtained at lower current angles low as $15°$, and saturated power factor is at around $60°$ depending on the PM flux and supplied current, as shown in Figure 5-25(b).

This following section investigates four PMSynRM's with incremental PM flux discussed in section 5.7 and shown in Figure 5-11 for the maximum power factor trajectory. As can be seen from the phasor diagram in Figure 5-5, the higher the PM flux, the higher the torque angle γ. However, as ($\varphi = 90° - \gamma$), hence the higher PM flux will reduce the current angle for maximum power factor. It is verified by simulation as follows. Figure 5-26 shows the investigation results. As can be seen in Figure 5-11, the quantity of PMs increases with the designs (AN-PMI_01 to 04). The results show that increasing PM flux moves the maximum power factor per ampere trajectory to lower current angle, as shown in Figure 5-26. Thus, it can be concluded that PMSynRMs with different PM quantities have different characteristics.

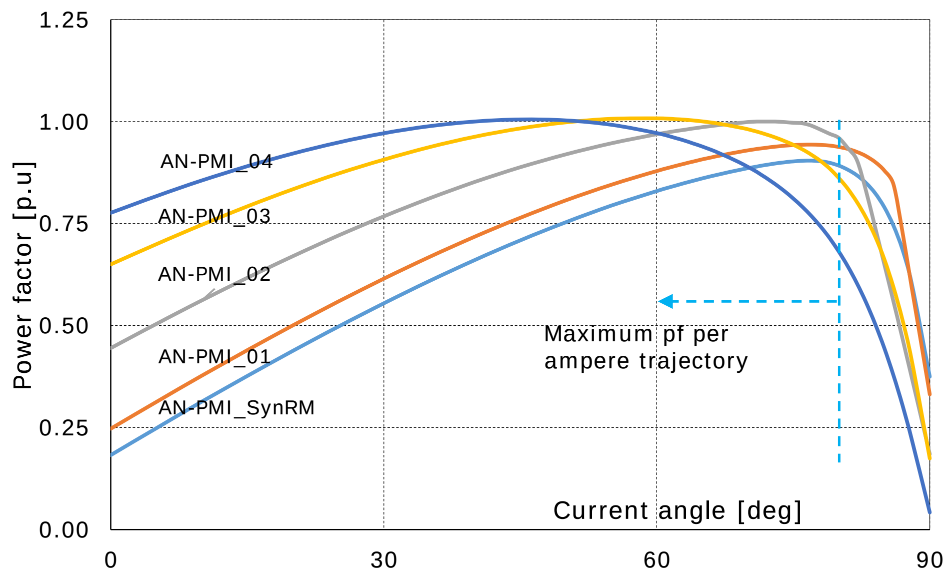

Figure 5-26: Analysis-PMI – Power factor of PMSynRM for varying PM fluxes.

5.8.4 PM and Reluctance Torque

The PMSynRM has two torque components, reluctance and PM torques. Although the same SynRM is used to make PMSynRM, the reluctance torque of the PMSynRM is not the same as the SynRM as the saturation in the ribs are affected by added PMs (high saturation). Therefore, the final reluctance torque in the PMSynRM slightly increased compared with its equivalent SynRM. On the other hand, the addition of PMs brings PM torque component as given in Eq. (5.6). The added PMs saturates the ribs. Thus, the reluctance torque is increased (assumed tangential ribs are not modified for adding PMs). Therefore, the addition of PM can increase the reluctance torque of the SynRM as well as PM torque. Hence, it is not easy to segregate the reluctance torque from a PMSynRM or PM torque, and considered as a single torque. The total PMSynRM torque is, in general, around 30+ % higher than that of the SynRM's torque.

The simulation results for the SynRM (at $65°$ MTPA) and PMSynRM (at $42°$ MTPA) are given in Figure 5-27. The PMSynRM displays 36 % more torque than that of SynRM at rated current 4.1 A for this particular design. In PMSynRM, the same torque of SynRM can be achieved at a current 3 A, with 26 % reduction in the current. The lines in Figure 5-27 indicate the rated conditions of SynRM and equivalent of PMSynRM. It is a critical design decision about whether to reduce the current by adding PMs or saving cost by minimising PMs.

The saturation of the ribs at lower currents is visible in SynRM, but in PM assisted design as discussed earlier, the saturation is already occurred due to high PM flux. Therefore, the torque has a linear relationship with the supplied current at a constant current angle. Thus, the control of this machine is much easier than an induction machine. Therefore, the efficiency of the PMSynRM is higher than that of equivalent SynRM, discussed in the subsequent sections.

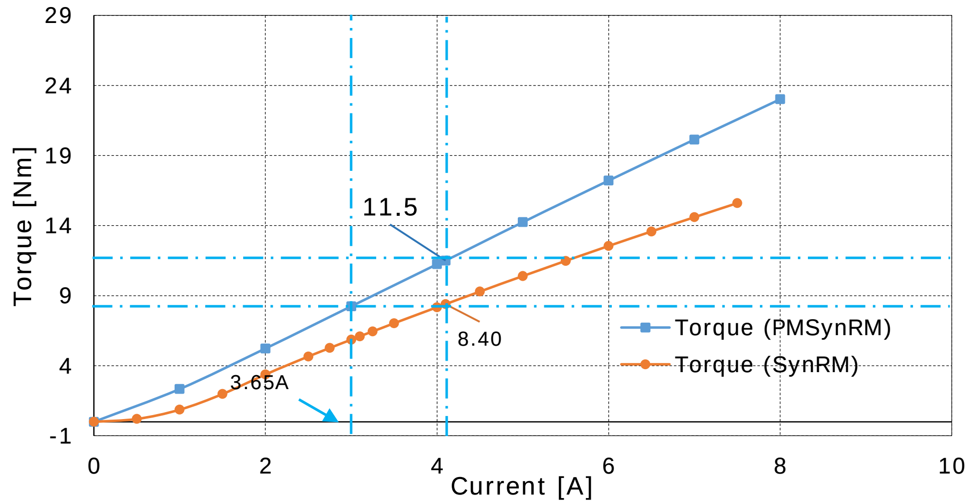

Figure 5-27: Analysis-PMI – PMSynRM and SynRM machine torque as a function of supplied current (at current angle $65°$)

The following study is conducted to understand the torque characteristic of the same PMSynRM estimated with respect to current and current angle and plotted in Figure 5-28. MTPA trajectories of PMSynRM and equivalent SynRM are indicated in the figure.

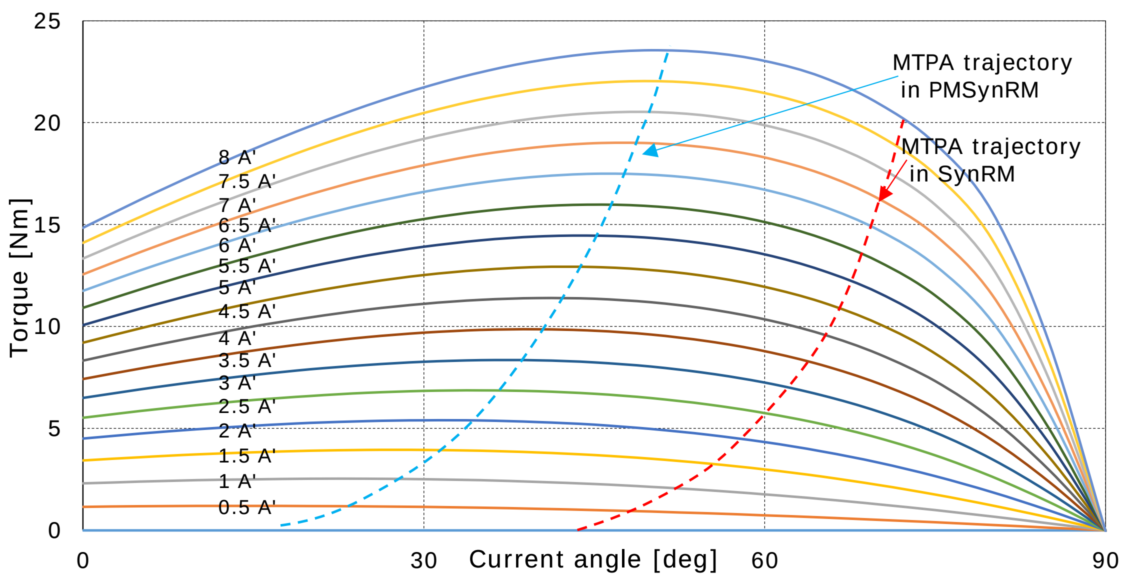

Figure 5-28: Analysis-PMI – PMSynRM's torque with respect to the current and current angle

The maximum torque of the PMSynRM is not obtained at $45°$ due to the added PM flux, unlike SynRM. In this case, the MTPA trajectory follows the lower current angle compared to an equivalent SynRM, as shown in Figure 3-66. The MTPA of this particular PMSynRM is at rated current is $42°$ whereas SynRM's is at $65°$. The change in PM flux is simulated for the four designs from section 5.7 to understand the torque MTPA trajectory with respect to the quantity of PM flux. The results are plotted in Figure 5-29. The simulation is performed at the rated conditions with current angle $42°$.

As can be seen, the increase in PM quantity (PM flux) lowers the MTPA current angle. Additional PMs, not only, lower the current angle but also increase the initial torque (no-load condition). At no-load condition, the SynRM does not develop any torque, but the PMSynRM with high PM flux (AN-PMI_03 and 04) produce significantly high torque of almost 6 and 8.3 Nm. It must be noted that the machine's core is magnetised by D axis current at this stage. The rotor core has been under magnetic stress due to high current at a high current angle, *i.e.* due to high Q axis current. Hence, the PM torque is reduced gradually while the reluctance torque increases as shown in the figure.

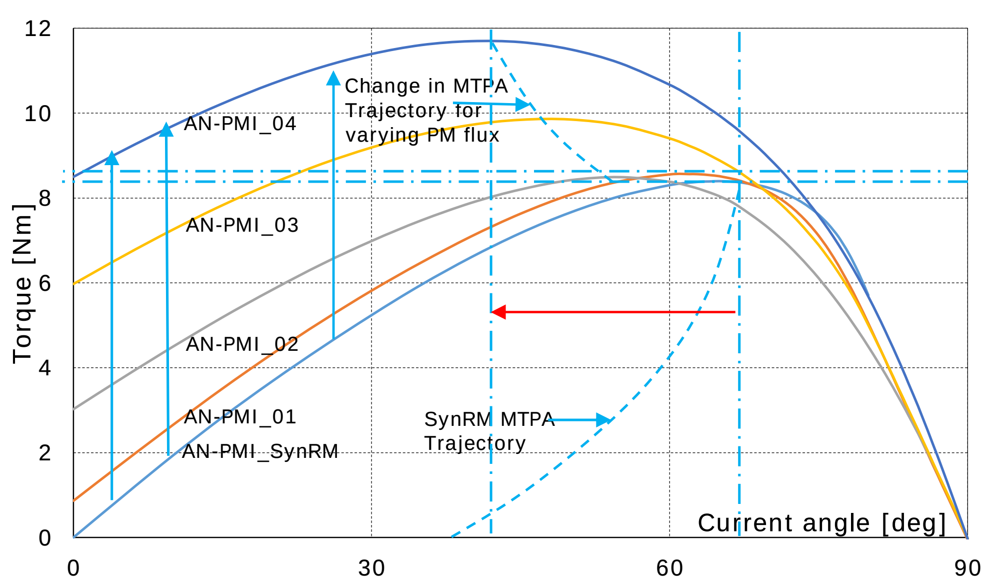

Figure 5-29: Analysis-PMI – PM and reluctance torque as a function of current angle for various PM quantities

The torque as a function of D and Q currents are shown in Figure 5-30. The torque is not only linear with supplied current and current angle but also with DQ currents.

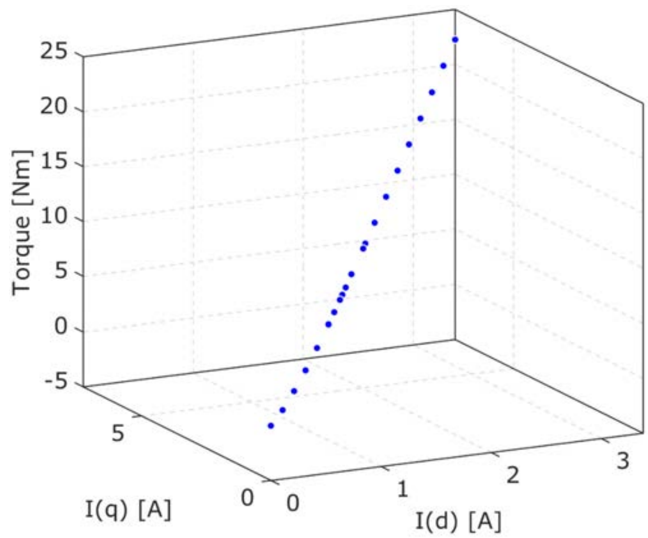

Figure 5-30: Analysis-PMI – PMSynRM's torque with respect to DQ currents (at the current angle 65°)

The investigation has revealed an important characteristic, *i.e.* the linear relationship of the torque with DQ current. This finding makes this machine a perfect candidate for current control. Its high torque density at no-load and linearity with torque can make this machine to be started with high loads. In addition, the characteristics allow this machine to be precisely controlled at the lower speed.

5.9 PM Optimisation in SynRM

This section deals with the overall performance of a PMSynRM by optimising the quantity and placement of the PMs in optimised SynRM's as discussed in sections 4.7 and 5.7 but without radial webs. Two SynRM rotor designs are selected for this analysis, one with the linear-barrier (Figure 5-12) and the other with the hyperbolic barrier. Firstly, the linear design is optimised with PMs along the Q axis direction. Then the hyperbolic design is tested with PMs along both Q and intermediate axes to compare the performance.

5.9.1 Optimisation Topology for PMSynRM

The topology of PM optimisation is designed to analyse the width of PMs in the barriers. The width of PMs along the Q axis is increased from 0 mm to its maximum along the barrier's linear section using an optimisation variable δ_n^j and δ_n^i, as shown in Figure 5-31 (a). The topology is designed with the linear-barrier section being straight to PM's maximum length in each barrier. By using this technique, a PM's existence can be decided by the optimiser. At maximum width ($\delta_{n_{max}}^i$), all PMs have occupied the linear sections of the barrier cavity, as shown in Figure 5-31(b). The barrier near the circumference is completely filled with PMs and not included in the second optimisation.

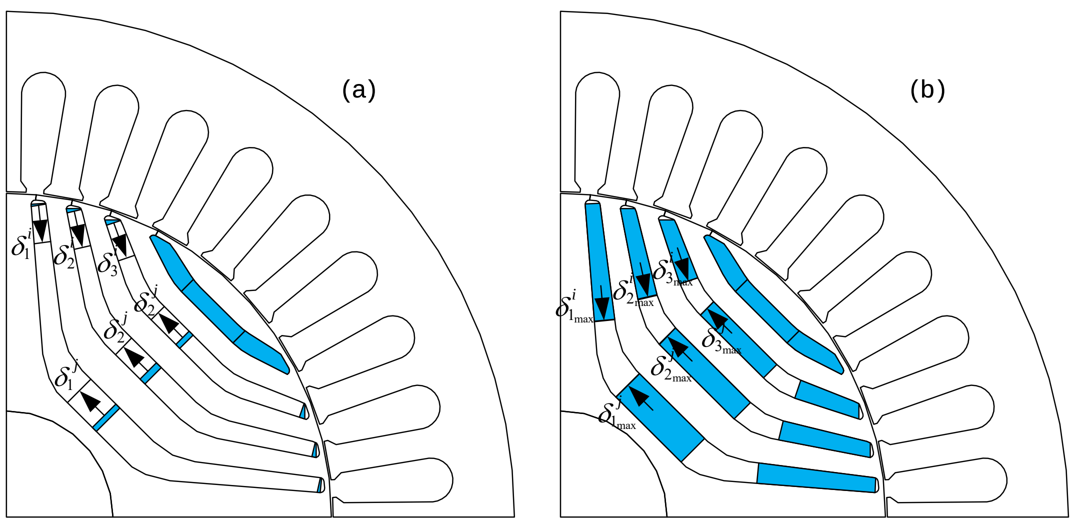

Figure 5-31: Analysis PMII - PM optimisation topology

The first optimisation in the following section uses the linear-barrier design with PMs only along the Q axis. The total number of optimisation variables selected for the first optimisation is only three (δ_1^j , δ_2^j and δ_3^j) whereas the second optimisation has six variables as in Figure 5-31. The maximum width of each barrier is limited only by the length of the straight section of the barriers. It is essential to have straight edge PMs to preserve magnetic coordinates for optimisation as the length is changed during the optimisation process.

5.9.2 Optimisation for Maximum Torque, Power Factor and Torque Ripples

The optimisation targets three performance parameters torque, torque ripples and power factor with the same weight. As discussed in the above analytical and FEM analyses section 5.3, the added PMs increases torque and power factor of the machine. However, the torque ripples were not analysed in the earlier studies. It is one of the critical parameters as PM fluxes can result high in ripples. The increase in ΔL_{dq} due to the PM flux is directed towards the ribs along the circumference. This optimisation topology is designed to achieve optimum PM width for improved performance in all three performance parameters, *i.e.* torque, torque ripples and power factor.

5.9.3 Optimisation I – PMSynRM with Linear-Barriers

Multi-Objective optimisation is performed with objectives as in Table 5-1. The optimisation uses the same topology described in section 5.9.1 but without PMs in the intermediate axis. All three parameters are equally treated with the same optimisation weight. The target torque of the previous study was 10 Nm, but optimiser found higher than the target. Thus, it is assigned slightly more (10.5 Nm) for this study so that optimiser will search in a broader range. The power factor of the previous study was above 0.95 $p.u$, thus it can’t be used as an optimisation driving parameter. Therefore, torque ripples are selected as optimisation driving parameter and set 10 %. The optimised design is shown in Figure 5-32 (AN-PMII_OT01) along with the model AN-PMI_04 for comparison purpose.

Table 5-1: Multi-Objective Optimisation targets

Parameters	**Target**
Torque	> 10.5 Nm
Power factor	> 0.95 p.u
Torque ripple	< 12 %

The design AN-PMI_04 has PMs to the complete straight section of each barrier along the Q axis, whereas the optimised design AN-PMII_OT01 has optimised PMs in various width along each barrier, as shown in Figure 5-32. The cross-section area of each PMs on both designs are listed in Table 5-2. As can be seen, the quantity of PM 3 is more than that of the PM 2 in the optimised design.

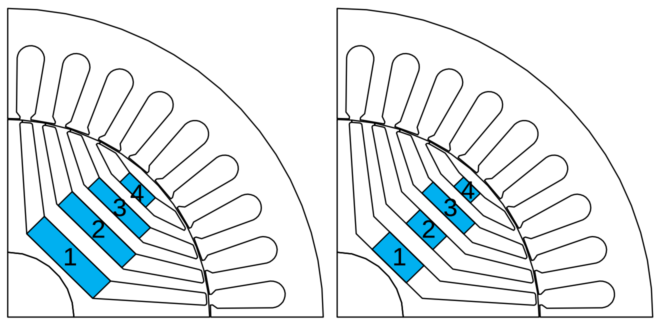

Figure 5-32: Analysis PMII – The design AN-PMI_04 and Optimised PMSynRM with linear-barrier

By optimising the quantities of the PMs in this way, the flux lines along the ribs through to air-gap and stator teeth are smoothed to achieve lower torque ripples with higher performance. The optimised design requires nearly half of PMs compared with AN-PMI_04 even with better performance.

Table 5-2: Comparison of PM quantities in optimised and non-optimised design

PM ID	Area of PMs $[mm^2]$	
	AN-PMI_04	**AN-PMII_OT01**
1	120.45	62.18
2	91.33	38.42
3	59.44	48.51
4	25.8	16.73
Total	297.02	165.84

The performances of the base SynRM, AN-PMI_04 and AN-PMII_OT01 are summarised in Table 5-3 at its MTPA. Its torque density is 39 % more than that of SynRM while its power factor is 13 % more than that of SynRM. Although the optimised design achieves high torque and power factor, the torque ripple is the main difference between just adding PMs to an optimised SynRM and optimising PMs. The torque ripples of AN-PMI_04 are not acceptable as it is almost 50 % of the machine's average torque whereas the optimised design has less than 10 %.

Table 5-3: SynRM and PMSynRM parameters

Parameter	SynRM_01	AN-PMI_04	AN-PMII_OT01
Torque [Nm]	8.3	11.56	11.59
Power factor [p.u]	0.85	0.97	0.96
Efficiency [%]	85.91	89.59	89.91
Torque ripple [Nm]	1.45	**5.42**	1.19

5.9.4 Efficiency

In PMSynRM, the supplied voltage is reduced at rated current to develop the same torque due to the added PMs. Therefore, the input power drawn by a PMSynRM is lower than that of SynRM to develop the same torque. The core loss is slightly increased in PMSynRM, but the other losses are not significantly affected by the addition of PMSynRM. As a result, the machine efficiency is higher than that of SynRM. In the above case, in both PMSynRM the efficiency is increased by almost 4.6 % compared with equivalent SynRM as listed in Table 5-3.

5.9.5 Optimisation II – PMSynRM with Hyperbolic Barriers

The above study has confirmed that PMs can enhance the performance of a SynRM. However, the torque ripples of the optimised machine are rather higher than an optimised SynRM. Although the torque ripples of the optimised design, which is around 10.5 % of the torque, can still be acceptable for many applications, however, it can be further minimised. The flux follows the hyperbolic pattern in the rotor space 0. However, the linear-barriers are used as part of the study in the previous case because of the straight barrier section where PMs can be easily accommodated. It is one of the primary reasons for slightly higher torque ripples. The following study is conducted to investigate a PMSynRM with hyperbolic barriers with PMs also along the intermediate axis.

The optimised SynRM from section 4.7 is modelled to suit PMs along the Q axis with slightly thicker ribs (0.75 mm), as shown in Figure 5-33. It is then investigated with PMs (similar to the AN-PMI_04) along the linear section of barrier (in design AN-PMII_OT02). As discussed earlier, the design with PMs in the intermediate axis have shown significantly improved performance. It is revisited here to investigate it further. It is optimised with PMs in both negative Q and intermediate axes using the above optimisation topology. The novel topology is designed to eliminate PMs if not required in a particular barrier during automated optimisation. The optimiser can find the best PM flux characteristic for defined requirements. The optimised PMSynRM with intermediate axis PMs (AN-PMII_OT03) is also shown in Figure 5-33. PM quantities of both designs are given in Table 5-4.

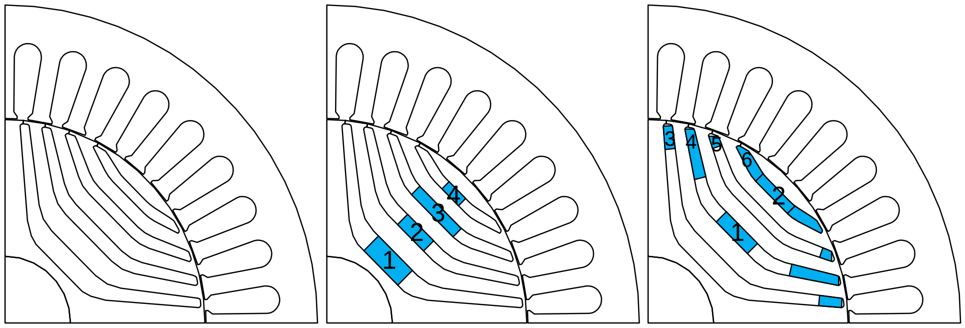

Figure 5-33: Analysis PMII – The SynRM_02, and optimised designs AN-PMII_OT02 and AN-PMII_OT03

The PMs quantities (area) given in Table 5-4 for PMs 3 to 6 are total area and its equivalent counterpart in the same pole pair. Although the design AN-PMII_OT02 looks quite similar to AN-PMII_OT01, the volume of PM is not the same. These two designs cannot be compared as the former has a 4.7 % more torque density for 57 % reduction in PM volume. It is to be noted that AN-PMII_OT01 has high insulation ratio compared with AN-PMII_OT02, *i.e.* its barrier thickness is larger and hence high PM volume. Hence, it has high PM flux resulting in high power factor.

Table 5-4: Comparison of PM quantities in two PMSynRM

PMs	**Area of PMs [mm^2]**	
	AN-PMII_OT02	**AN-PMII_OT03**
1	51.57	32.8
2	27.42	23.81
3	35.71	23
4	12.32	53.82
5	N/A	11
6	N/A	36.4
Total	127.02	180.83

The machine parameters are given in Table 5-5. AN-PMII_OT02 has gained 38.2 % more torque compared with equivalent SynRM and power factor of 0.96 $p.u$. Its torque ripples are slightly higher compared with the SynRM. The torque ripples are reduced to 8.3 % of the average torque of the machine. Torque per PM ratio of AN-PMII_OT02 is 0.082 compared with AN-PMI_04 has only 0.033. The results show that while torque density and power factor of AN-PMII_OT02 are quite comparable to AN-PMII_OT01, but its torque ripples are reduced. It shows the effectiveness of the hyperbolic barrier compared with a linear-barrier design.

Table 5-5: Performance comparison of the three designs

Parameter	SynRM	AN-PMII_OT02	AN-PMII_OT03
Torque [Nm]	8.33	11.51	11.07
Power factor [p.u]	0.82	0.96	0.93
Efficiency [%]	86.16	89.91	89.81
Torque ripple [Nm]	0.89	0.97	0.92

The optimisation of PMs in the intermediate axis are investigated further. PMs along the intermediate axis can have a high impact on the machine performance based on the studies in section 5.7 and references [107, 125]. Therefore, the next optimisation is conducted utilising the same topology as mentioned earlier in section 5.9.1. The optimiser finds the best solution, as shown in Figure 5-33 (AN-PMII_OT03). It eliminates PM from the first barrier for the given objectives. The optimised design has slightly lower torque density and power factor compared with AN-PMII_OT02, but the torque ripples are reduced. The PM quantity of this design is quite high compared with AN-PMII_OT02.

5.10 Optimisation of PMSynRM

The quantity of PMs is optimised on an already optimised SynRM in previous sections. It is the recommended process in designing PMSynRM. This section discusses a novel method to optimise PMSynRM as one single object. Although a hyperbolic barrier design is used in this optimisation, any design is possible in this process.

5.10.1 Optimisation of PMSynRM

The SynRM topology used in section 4.3.1 and PM optimisation topology used in section 5.9.1 are combined to investigate the PMSynRM optimisation with four hyperbolic barriers but without radial webs. By combining the two topologies, a design is developed to have a high degree of freedom in changing rotor and PM dimensions (optimisation parameters) during optimisation. PMs are only placed along the Q axis for this investigation. As a result, nine optimisation variables are selected for multi-objective optimisation. In this topology, when SynRM design parameters are altered during automated optimisation, the PMs dimensions are also altered in such a way that can fit into the new barriers of the new SynRM. It is achieved by designing a PM larger than that of the barrier and subtracting it from the rotor so the when the rotor dimensions are changed, the PM can change the shape.

The subtraction is stored in the design memory. Hence, when the SynRM design parameters are altered, the subtraction automatically adjusts the PM dimensions to suit to the new parameters. As the initial PM is larger than that of the barrier, it can still fit in. Thus, the initial PM design is the critical element in this topology. Two possible designs are shown in Figure 5-34, the PMs are almost not-existing, and in the second one in the first one, PMs are configured by the optimiser. As can be seen, when the design parameters of the SynRM are altered, the PMs change with it.

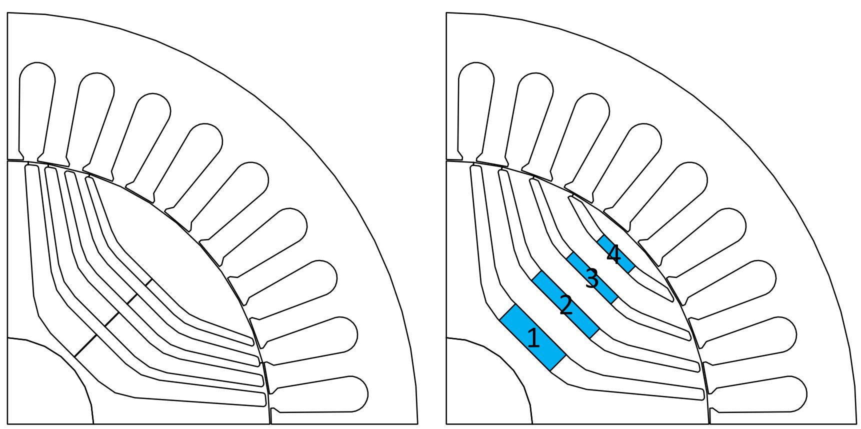

Figure 5-34: Analysis PMIV – Two designs by varying the optimisation parameters

Optimisation variables

The domains of the optimisation variables (r, δ_n^j *and* R_{b_n} $(n = \{1,2,3,4\})$ are selected to accommodate the PMs along the straight section of the barriers. The PMs do not intersect the barrier during the optimisation process. The width of each PM is selected in such a way PM non-existence can be depicted if the optimiser is looking for such a scenario as well as it can be stretched all the way to the end of the straight section of the barrier.

Performance Parameters

The multi-objective optimisation is performed with the same objectives given in Table 5-1. The best four optimised designs are given in Figure 5-35 from left to right. There is not much difference between the four designs. All four designs have similar insulation ratio, barriers are equally distributed along with the rotor space, and the volume of the PMs are quite similar. The area of the PMs is plotted against the model in Figure 5-36. It can be seen that the quantity of each PMs in each design is quite similar. The design names are shortened and given as OPT01 to OPT04 in the figures.

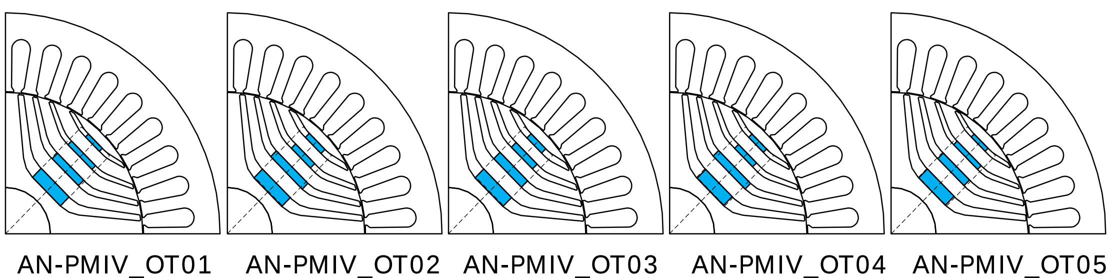

Figure 5-35: AN-PMIV – Optimised PMSynRM designs (the finest four designs are given from left to right)

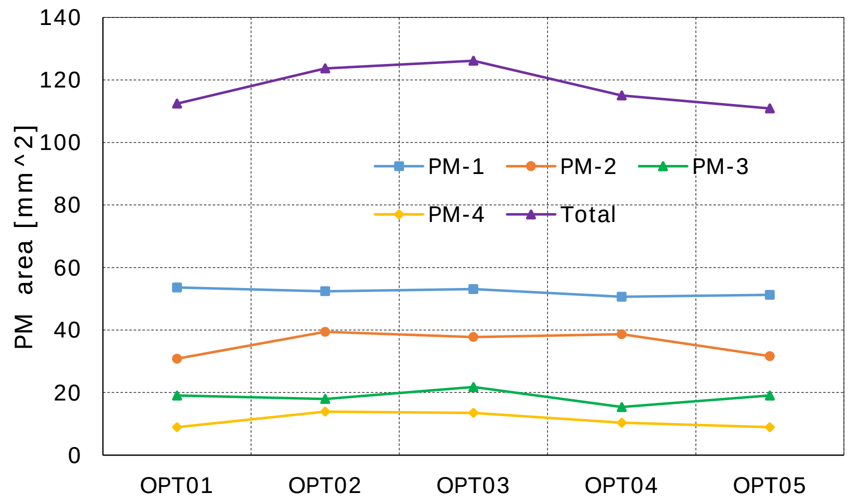

Figure 5-36: PM quantity of the four designs

The torques and power factors of the four PMSynRM and equivalent SynRM are plotted in Figure 5-37. The difference in torque is quite small between the various designs that confirm the validity of the optimisation. Although AN-PMIV_OT01 has less PMs than AN-PMIV_OT02 and AN-PMIV_OT03, its torque density is higher than the rest of the designs. The differences in torque between PMSynRM and equivalent SynRM of the four designs are 37.2 %, 33.2 %, 33.5 % and 34.81 %. All three optimisation objectives determine the best design, and AN-PMIV_OT02 has 2 % higher torque density compared with the best design.

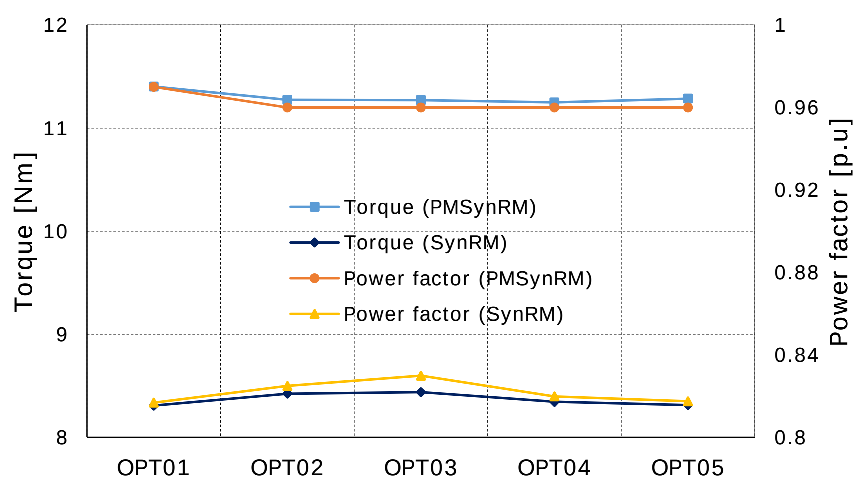

Figure 5-37: Torque and power factor of the four designs

On the other hand, the power factors of the four PMSynRMs are 18.7 %, 16.3 %, 15.6 % and 17.51 % higher than that of equivalent SynRM. The torque ripples of the four PMSynRM and SynRM are plotted in Figure 5-38. The efficiency of the PMSynRM is more or less the same between the different designs and about 3 % higher than equivalent SynRM.

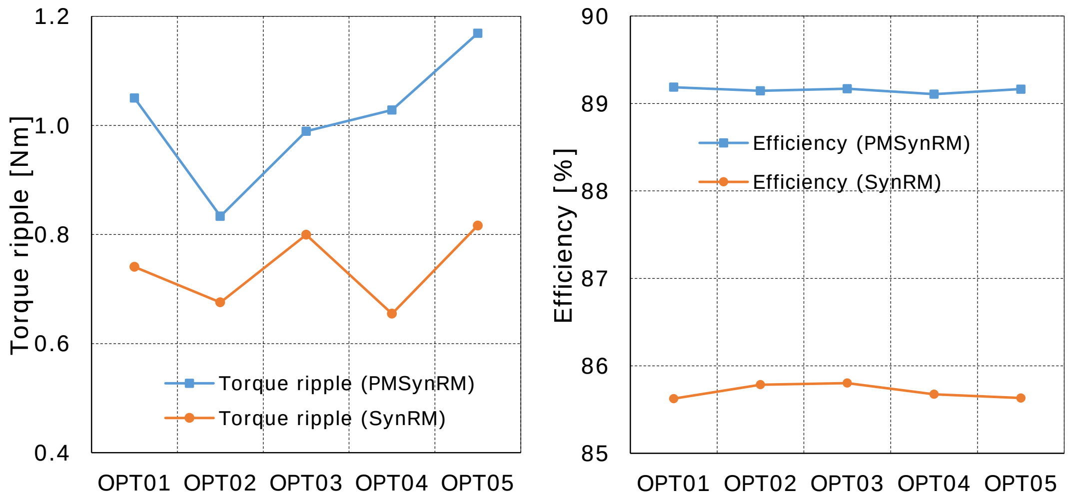

Figure 5-38: Torque ripple and Efficiency of the four designs

The above study has shown that the optimisation of PMSynRM as a whole object yields the best machine with low torque ripples. On the other hand, the optimisation for PM has also resulted in a machine with relatively high torque and power factor compared with equivalent SynRM's characteristics. However, it is always good to optimise PMSynRM as a whole so that it can yield the best machine.

5.10.2 Optimised Torque

The torque of the optimised design is calculated with respect to current, current angle and D and Q currents. Figure 5-39 shows the torque with respect to D and Q current map in a 2D space in, and its 3D version is plotted in Figure 5-40. PMSynRM requires a higher load current to produce positive torque as can be seen in Figure 5-41 due to the PM flux in the negative Q direction. The machine has significant torque (developed) at its rated condition. The high torque density of the machine requires the machine to be started with a controller under no-load condition. The rated and overload high torque density regions are marked in Figure 5-39. It shows the machine has significantly high torque for lower i_d and higher i_q, especially the SynRM. The rated and high torque region are marked in blue colour and overload condition region is marked by red colour in the figure. The blue lines in the figure show the overload and high torque regions.

In a SynRM, the optimum torque and highly efficient operating region are around at lower Id (between 1 and 3 A), as shown in Figure 5-41. However, in the case of PMSynRM, the region is quite larger as can be seen in Figure 5-40. The simulation results reveal that both machines can be operated at lower D current for high torque and vice versa is also true to a certain extent.

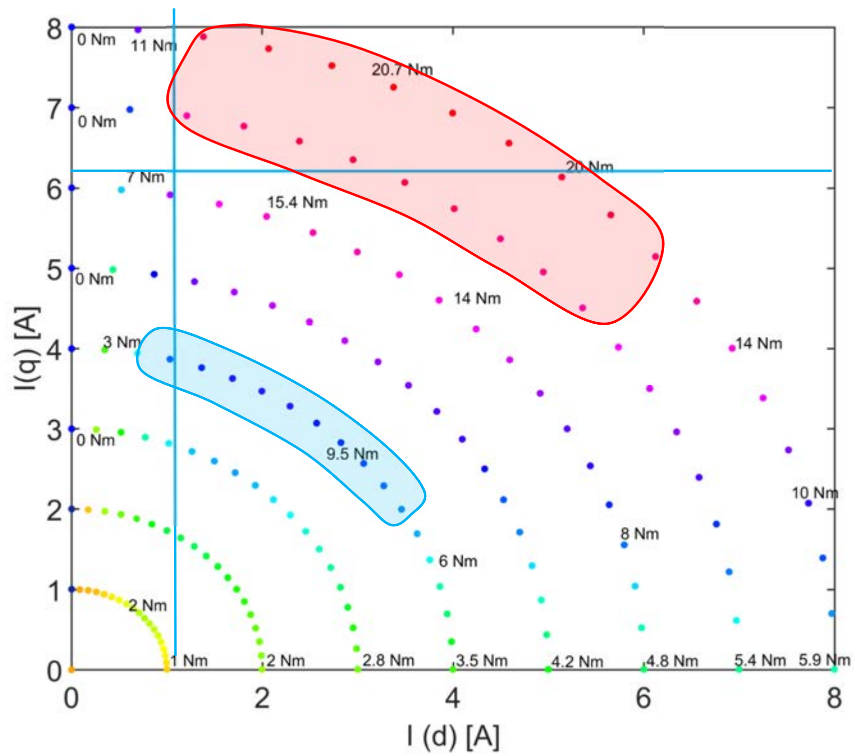

Figure 5-39: Torque of PMSynRM with respect to DQ current in 2D space

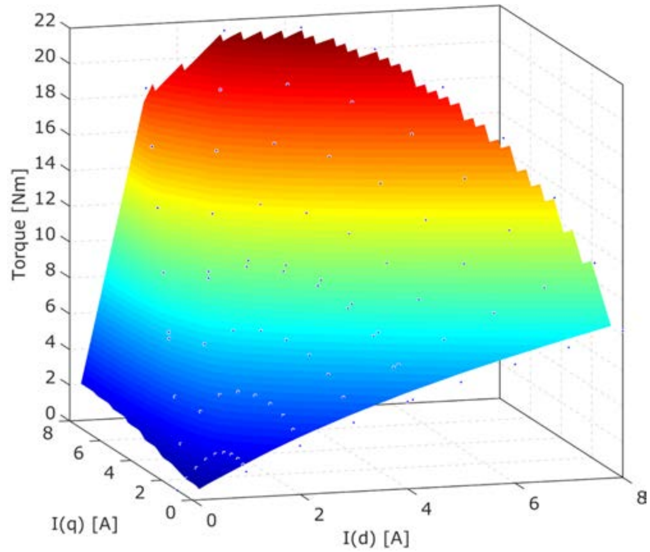

Figure 5-40: Torque of PMSynRM with respect to DQ currents in 3D space

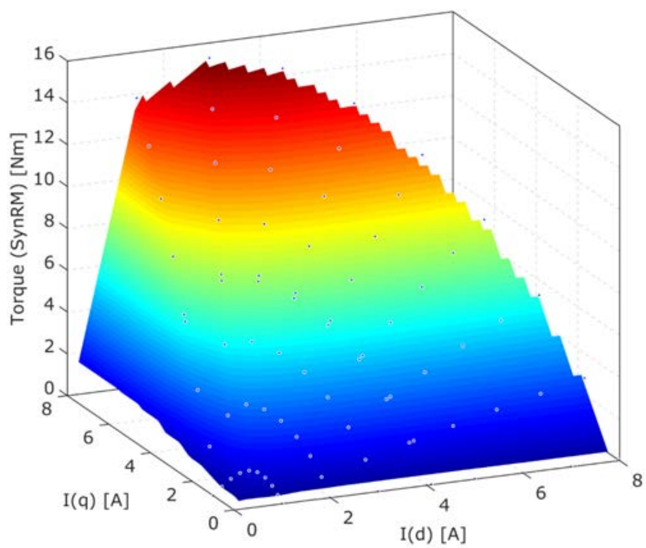

Figure 5-41: Torque of SynRM with respect to DQ currents in 3D space

The added PMs has not only saturated the ribs but also helps to improve the reluctance torque by saturated ribs. Therefore, the saliency ratio of the PMSynRM is increased, resulting in high torque density. Thus, it is essential to ensure that added PM flux does not have a negative impact on the D axis flux path. The increased PM flux may have weaken the reluctance torque due to cross-coupling [228]. The additional PM flux increases the saturation of steel segments and reduces reluctance torque. It is further analysed in section 5.11. The addition of PMs also introduces cogging torque.

5.10.3 Optimised Power Factor

The power factor of optimised PMSynRM is evaluated using FEM and plotted in Figure 5-42, and equivalent SynRM machine's power factor is plotted in Figure 5-43 in 3D space with respect to DQ currents. The power factor of PMSynRM is quite high in comparison with equivalent SynRM as expected shown in Figure 5-42 and Figure 5-43. The SynRM has quite low power factor even at no-load conditions, whereas PMSynRM has a high-power factor for the same conditions. At the same time, PM assisted design show high power factor for certain conditions, especially for MTPA. As discussed in section 5.3, it is apparent the PM flux narrows the angle between voltage and current vectors. The power factor improvement depends on the magnitude of the PM flux as discussed in section 5.5.

The high-power factor (above 0.95 $p.u$) is obtained even at low i_d. The PMSynRM has wider high-power factor range in comparison to SynRM. The PMSynRM with wider region of an optimum power factor can be controlled for high torque and power factor as both have similar MTPA trajectory.

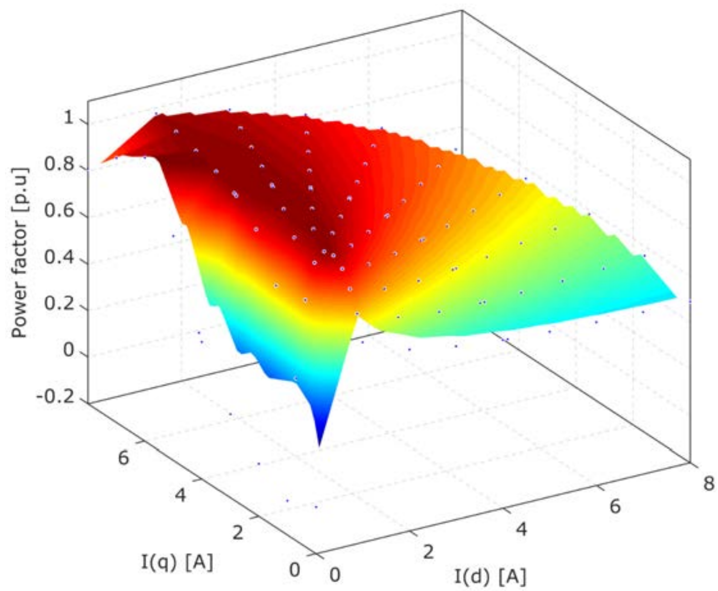

Figure 5-42: Power factor of PMSynRM (neodymium) with respect to DQ currents in 3D space

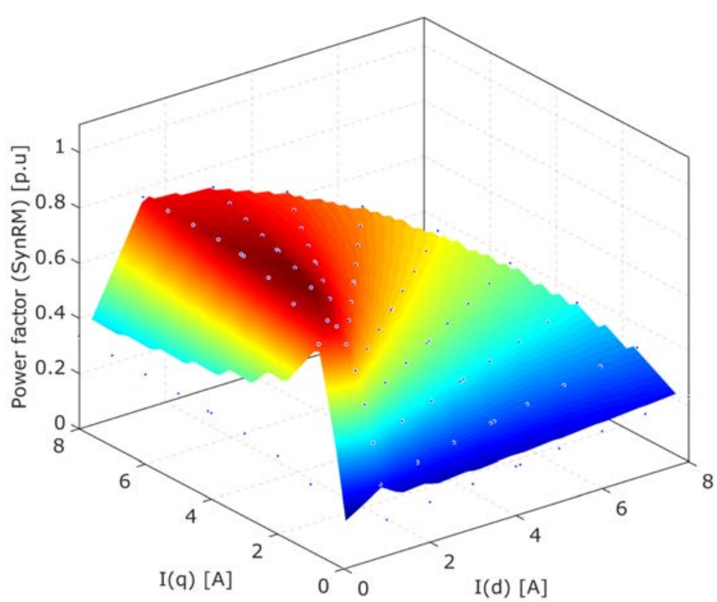

Figure 5-43: Power factor of SynRM with respect to DQ currents in 3D space

5.10.4 Cross Saturation Effects on PMSynRM Performance

The PMs increase the saturation effects in the PMSynRM core, especially the cross-saturation due to the PM flux directed into the steel segments towards the intermediate axis in a PM assisted machine. In the case of SynRM, the saturation drifts the MTPA angle (θ) higher than the theoretical value of $45°$. The supplied current enhances the saturation effect and compensate F_d. It is the same in the case of PMSynRM. However, in the case of PMSynRM, the resultant flux is not just current introduced flux but combined with PM flux. Therefore, the drifts in MTPA is not significant as SynRM, which is analysed in section 5.8.4.

This study investigates the cross-saturation in PMSynRM, the saturation caused by inter-axes. D and Q Flux linkages at various current angles are plotted for cross saturation in Figure 5-44 and Figure 5-45. The D axis flux has high cross saturation due to an increase in Q axis current. The broken blue line in both figures shows each $10°$ steps in the incremental direction. As can be seen in Figure 5-44, the D axis flux saturates quite high for low current angles compared with high current angles for increasing i_q. On the other hand, the added PM flux has saturated the ribs even before the current is introduced to the machine which increases the reluctance in the Q axis. Thus, Q axis flux linkages do not significantly saturate as can be seen in Figure 5-45.

The MTPA of the optimised design is around $42°$, which shows the design will experience high cross saturation if the Q axis current is increased. D & Q axis flux linkages are evaluated at rated condition ($42°$) for the same design and plotted in Figure 5-46 and Figure 5-47. The results show the saturation impact on pf due to D axis flux linkage, while the Q axis flux linkage is not significantly affected by the saturation.

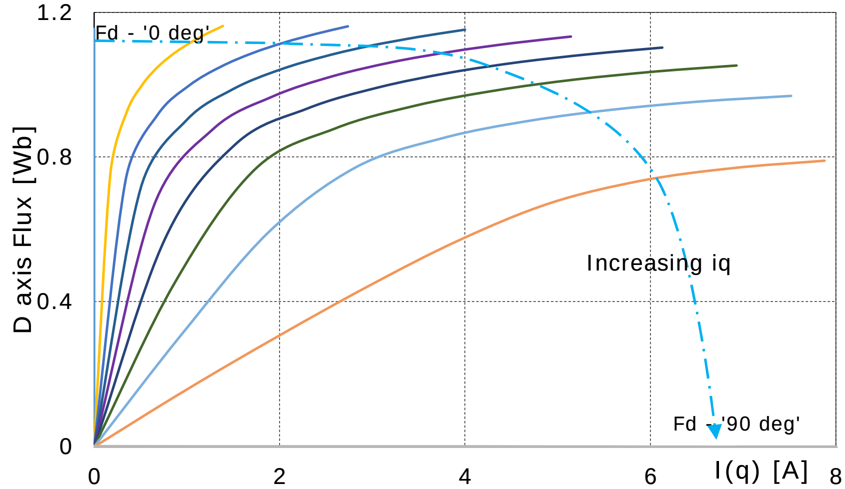

Figure 5-44: D axis Flux linkage of PMSynRM with respect to its cross current (i_q)

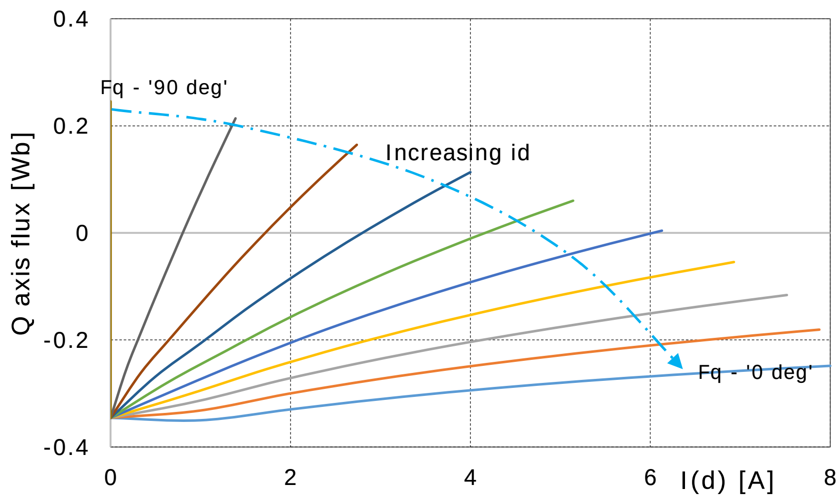

Figure 5-45: Q axis Flux linkage of PMSynRM with respect to its cross current (id)

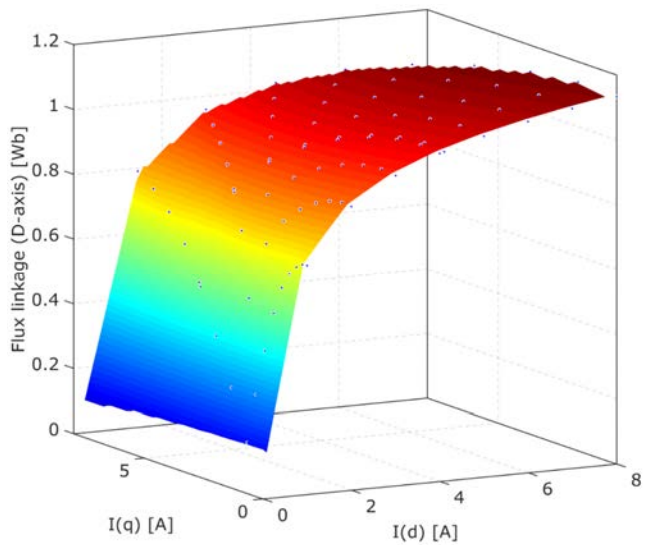

Figure 5-46: D axis flux linkage of PMSynRM with respect to DQ currents in the 3D space

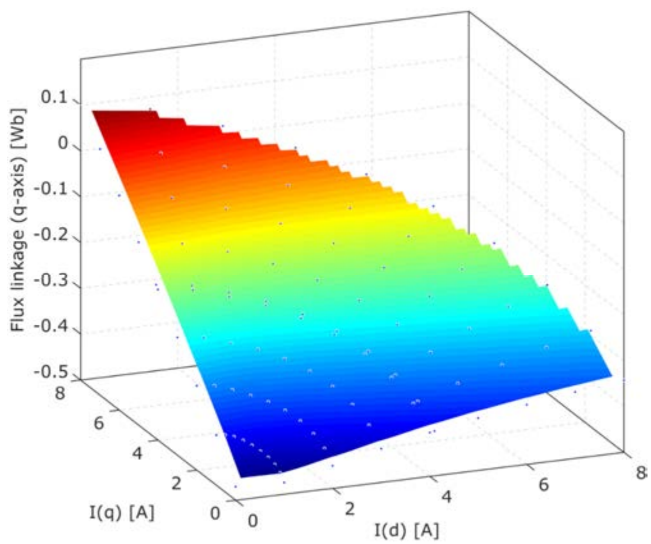

Figure 5-47: Q axis flux linkage of PMSynRM with respect to DQ currents in the 3D space

5.10.5 Efficiency

The losses and efficiency of SynRM are investigated in details in section 2.5.3 and 5.10.5. The difference in losses between a SynRM and PMSynRM is due to the induced cross-saturation effects and core loss due to PM materials. This section analyses the input power, core loss, total loss, output power in order to determine the efficiency of the optimised design. The motor input and shaft output powers are evaluated at steady-state and plotted in Figure 5-48, as discussed in section 3.4. The analysis performed over the same current limit that is used in the previous analysis. The simulation is performed at MTPA for high torque density. As can be seen, the high output power is obtained at low i_d and high i_q.

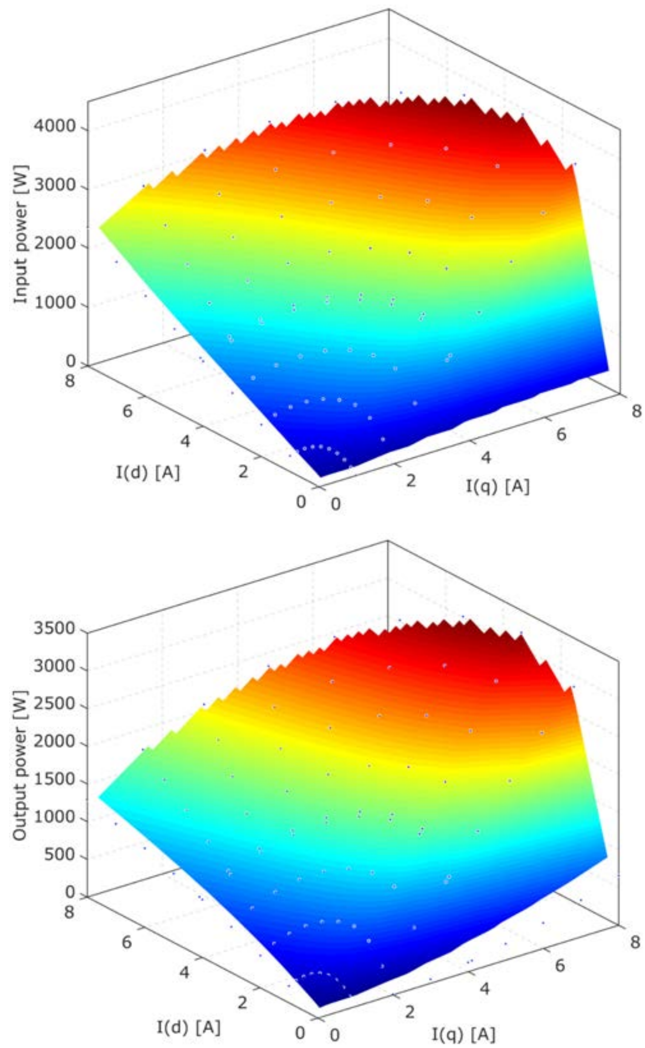

Figure 5-48: Input and output powers of PMSynRM with respect to DQ currents in 3D space

Core Loss Analysis in PMSynRM

The core-loss in SynRM is studied in detail in section 3.8. As already discussed, the operational difference between SynRM and PMSynRM is the added PM flux. It has slightly altered the machine MTPA and DQ currents. As discussed, the core-loss is depended on DQ current. The core-loss as a function of DQ currents are investigated, and the simulation results are shown in Figure 5-49. It is high for high magnetising current i_d as can be seen in Figure 5-49. Q axis current i_q does not affect it.

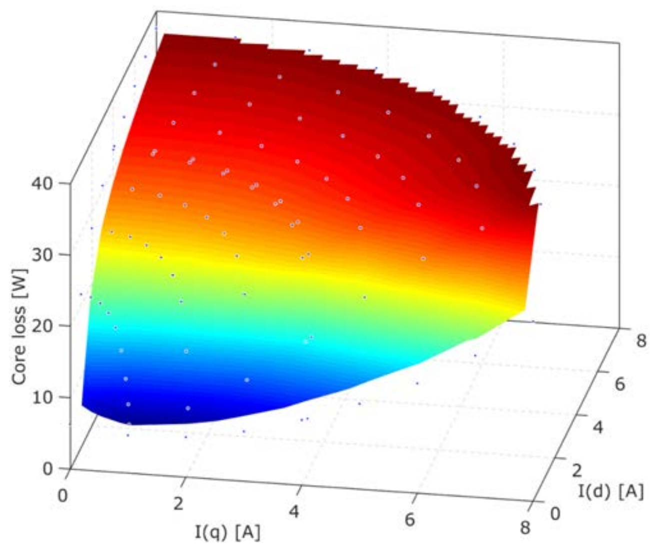

Figure 5-49: Core-Loss of PMSynRM with respect to DQ currents in the 3D space

The other losses such as winding loss and stranded loss are similar to equivalent SynRM counterparts. Therefore, the total loss is investigated for PMSynRM and shown in Figure 5-50 with respect to DQ currents. The core-loss is quite insignificant compared with total losses. It is visible in the figure that the losses are increasing with load current i_q as expected.

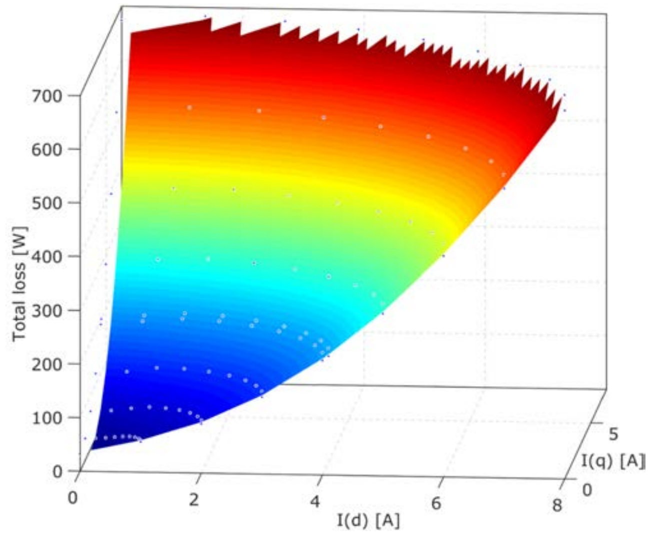

Figure 5-50: Total loss of PMSynRM with respect to DQ currents in 3D space

The initial SynRM is designed for 7 Nm, 1.1 kW at rated conditions. However, the optimisation of the SynRM and addition of PMs increased machine performance. The efficiency of base SynRM is 81.4 %, while the final optimised design has an efficiency of 89.2 %. The high-efficiency region can be seen in Figure 5-51, which is for low to medium DQ currents. The high currents increase saturation, thus resulting in wastage of energy. However, in the case of optimised design, the ribs are already saturated, and the core segments are properly designed. Thus, the saturation effects are minimised for high current in this design to improve its efficiency, as shown in Figure 5-51.

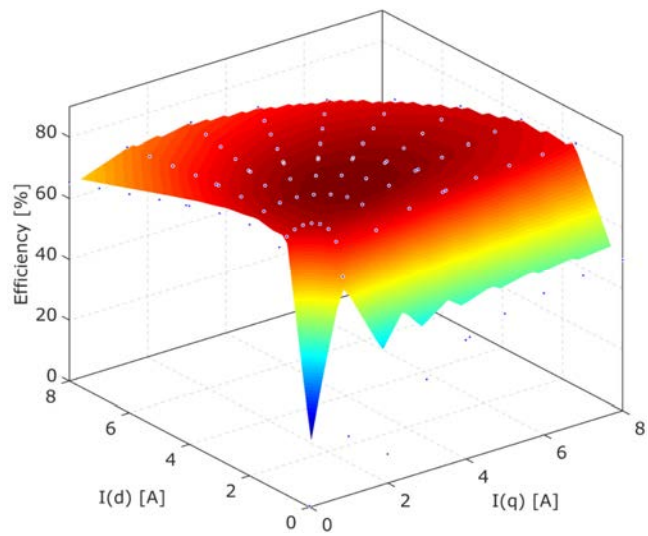

Figure 5-51: Efficiency of PMSynRM with respect to DQ currents in 3D space

5.11 Control and Operation of PMSynRM

The SynRM is controlled in two operating conditions, maximum torque per ampere and field-weakening similar to induction machine control. The control of SynRM is discussed in detail in section 2.8. This section analyses the field-weakening characteristics of SynRM and PMSynRM using existing strategy in FEM tool. Both SynRM and PMSynRM, similar to the induction machine, are controlled using MTPA strategy in the constant torque region. It is the best option for a constant torque region due to its linearity. However, when speed goes beyond nominal speed, the inverter cannot increase the voltage above the maximum available value. In order to run the motor above the rated speed, the field-weakening strategy shall be employed in the same way as DC or an induction machine. The strategy weakens the flux linkage in the air-gap while keeping the maximum voltage by reducing the supplied current, as shown earlier in Figure 2-18 and Figure 2-19.

In this type of machine, the D axis flux is the magnetising flux, and therefore it is weakened with respect to speed. The strategy has been used even in PM machines, called flux weakening. The flux is controlled by referencing it to the inverse of machine speed as given in Eq. (2.65) [6, 12, 229-232]. While the speed is increased, the torque producing capability of the machine is reduced. In order to get the optimum performance at high speed, the current angle is controlled in such a way that can yield the maximum torque for each speed points in the field-weakening region. This is studied in the following section using FEM tool.

5.11.1 Torque-Speed Characteristics of SynRM and PMSynRM

In this section, the PMSynRM with various PM quantities and equivalent SynRM and are studied for its constant torque and field-weakening capabilities with MTPA and constant voltage constant current control strategy. The control of the current angle in the high-speed region is essential to yielding the maximum torque. The increased current angle will alone not yield the maximum torque as there is an optimum point for maximum torque. Therefore, the maximum torque current angle is obtained in the field-weakening region to optimise the performance of the machine in this region.

It is achieved by implementing the constant voltage constant current control strategy in Ansys's macro for SynRM and PMSynRM. The sinusoidal current supply is used for the entire simulation. Ansys's existing design script that was developed for the PM machine has been modified to include SynRM and PMSynRM topologies. The script is developed to search for optimal operating points using sophisticated optimiser tool automatically. Figure 5-52 shows the SynRM and other five PMSynRM design that are studied for field-weakening control. The PMSynRM is the optimised one as per section 5.10 but with changing the number of PMs in the barriers. The rated machine configuration such as voltage and current used for the transient simulation are already given in Table 3-1 with speed up to 12000 rpm is selected for the simulation.

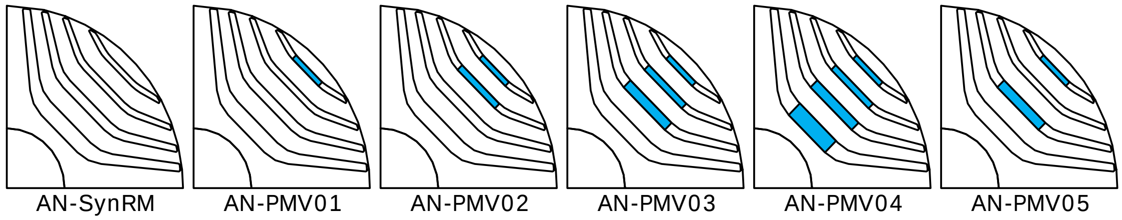

Figure 5-52: Analysis PMV – designs are chosen for constant torque constant power region analysis

The torque-speed curves of the simulation are given in Figure 5-53 for the six designs. As can be seen, all six designs are consistent in terms of the constant torque (MTPA) and field-weakening capability regions. AN-PMV04, with the highest volume of PM, shows high torque characteristics in the MTPA region as discussed earlier in the section 5.11 with 34.5 % more torque than equivalent SynRM. AN-PMV01 has 10 % more torque density than that of the SynRM in the MTPA region and has slightly higher torque density through an increase in speed. The SynRM drops torque density for speed between base speed and 1:2 speed region before it almost settles at 16 % of its rated torque around the 1:4 speed region. It depends only on reluctance torque which is reduced by decreased air-gap flux.

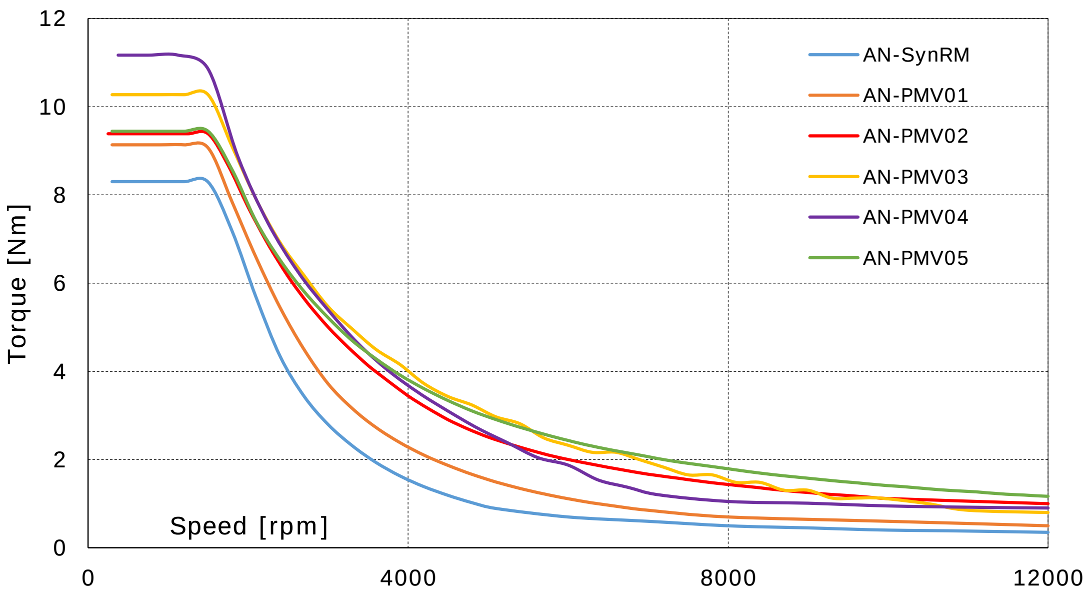

Figure 5-53: Analysis PMV – Torque-speed curves of SynRM and PMSynRM in the field-weakening region

AN-PMV01 also shows similar change with speed as SynRM but with little higher torque than SynRM. Its torque characteristics are quite similar to the SynRM due to lack of PM flux in the air-gap, as discussed in section 5.7. On the other hand, AN-PMV02 and AN-PMV05 have nearly the same amount of PM but in different barriers, as shown in Figure 5-52. They have similar torque characteristics in the MTPA region. The two designs show quite different torque characteristics with increasing speed, especially above 3000 rpm. AN-PMV05 shows significantly high torque for increasing speed compared with AN-PMV02. Although both designs have almost the same volume of PMs, AN-PMV05 has one PM piece away from the air-gap while AN-PMV02 has both closer to the air-gap. As already discussed in section 3.6.8, the area closer to circumference has high flux density and susceptible to saturation. In the case of AN-PMV02, both PMs are almost within the same area, which makes different demagnetisation level for the two designs.

Although AN-PMV03 has quite a high volume of PMs and 13 % more torque density compared with AN-PMV02 in the MTPA region, very similar torque characteristics between 2000 rpm and 6700 rpm before its torque reduces further compared with AN-PMV02. It shows the importance of having PMs at an optimum location for high-speed applications. The design AN-PMV04 with highest PM volume results in torque drop with increasing speed above base speed. It follows the torque curve of AN-PMV03 up to the speed region 1:2 before it drops lower than AN-PMV02 at 1:3. The increase in speed and current angle in the field-weakening region plays a significant part in the demagnetisation.

In conclusion, the study finds that PMSynRM can be designed to have a significantly high speed of up to 1:7 by adequately optimising the design with magnets in the right location. The PMSynRM should be designed with less barriers and bigger PMs for a high-speed application with quality field-weakening characteristics to reduce the demagnetisation.

5.11.2 Field-Weakening Characteristics of PMSynRM

In this section, the machine performance of a selected PMSynRM (AN-PMV05) is analysed in both MTPA and field-weakening regions. Firstly, the DQ flux weakening is plotted in Figure 5-54. As already mentioned, F_d is the magnetising flux in both SynRM and PMSynRM. As can be seen in Figure 5-54 (a), the D axis flux is directly proportional to the machine torque. It is rather compromised in order to increase the speed. On the other hand, the Q axis flux is increased with maximum torque and speed.

(a)
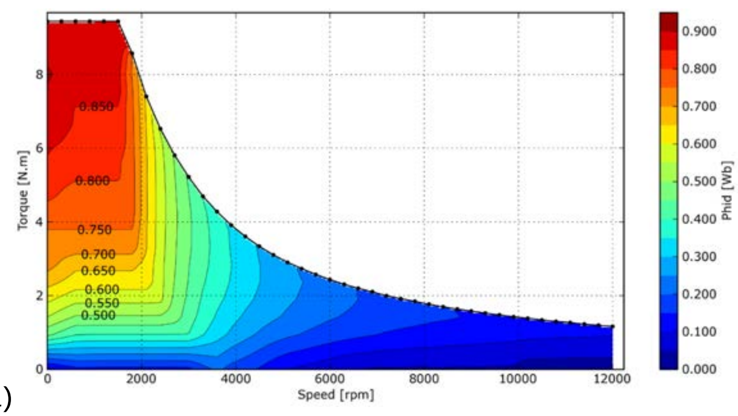

(b)
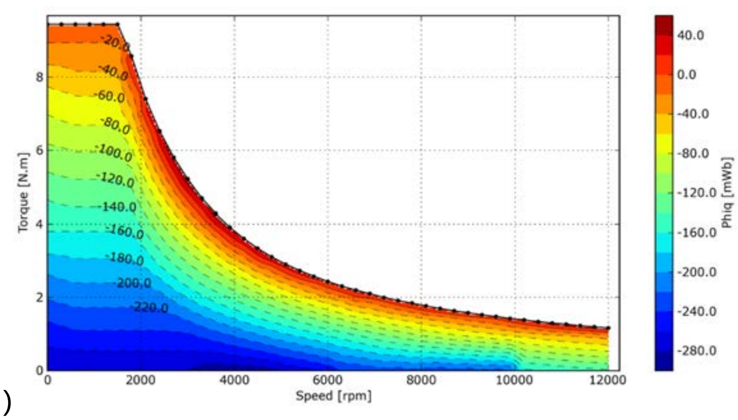

Figure 5-54: DQ Flux of AN-PMV05 in the field-weakening region

The DQ currents throughout the field-weakening region are plotted in Figure 5-55 with a similar pattern as fluxes. As already shown in Eq. (2.1) and (2.62), the magnetic axis flux is proportional to its current, i.e. the magnetic current controls the flux. As discussed earlier in section 2.5.1, i_d and i_q are magnetising and torque developing currents, respectively. In order to yield maximum torque even during the field-weakening process, the i_q should be at its maximum, as shown in Figure 5-55 (b). The only way to maintain maximum i_q is by increasing the current angle as already discussed in section 2.8 and demonstrated in Figure 2-18.

The higher i_q can be seen along the maximum torque locus in Figure 5-55(b). The D axis current is not drawn above 2.10 A while Q axis current is drawn to its maximum, which shows the effectiveness of the control topology. The torque-speed as a function of current angles are plotted in Figure 5-56. The current angle of maximum torque at MTPA region is between $55°$ and $60°$. It is around $80°$ to $85°$ for speed regions between 1:2 and 1:4 and above 85° from speed regions beyond 1:5.

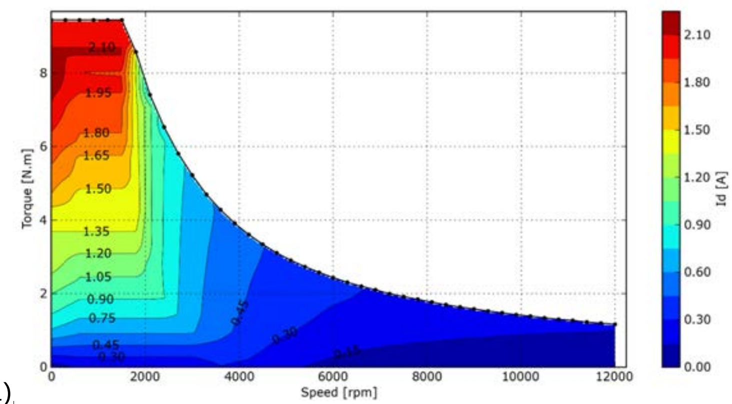

(a)

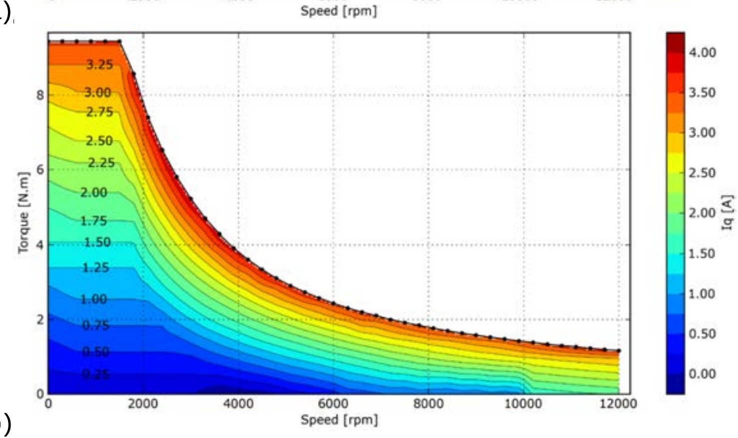

(b)

Figure 5-55: DQ Currents of AN-PMV05 in the field-weakening region

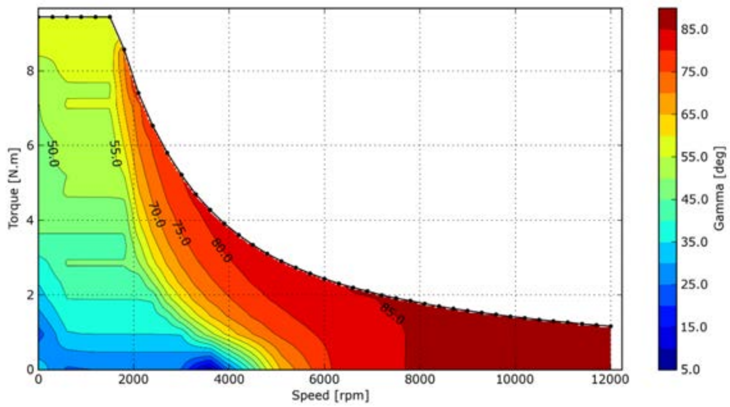

Figure 5-56: Current angle of AN-PMV05 in the field-weakening region

Figure 5-57 shows the power factor of the design with respect to torque and speed. The power factor of PMSynRM is also discussed in section 5.8.3 and its characteristic is plotted in Figure 5-25. Based on the power factor study, the maximum power factor of PMSynRM (AN-PMV04) lies around $65°$ to $75°$ depending on the PM volume and arrangement. The maximum power factor is not significantly affected by the current angle, unlike the maximum torque, which changes with the current angle. It has already accounted the leakage inductance (power factor is calculated using L_d and L_q, whereas the torque is calculated using L_{md} and L_{mq}) which is discussed in section 2.5.2.

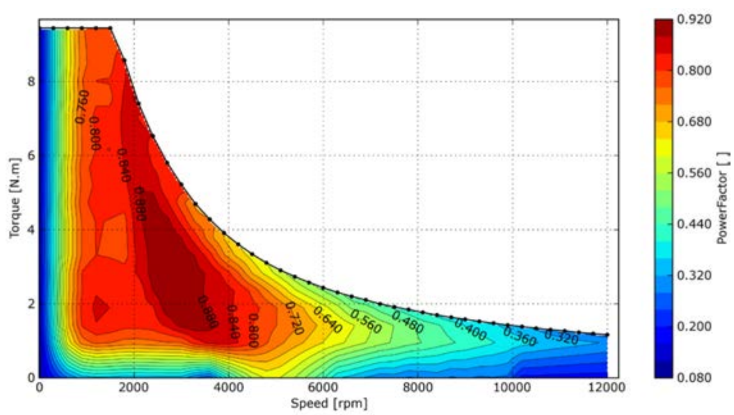

Figure 5-57: Power factor of AN-PMV05 in the field-weakening region

The input and output power in the field-weakening region is plotted in Figure 5-58, and its losses are plotted in Figure 5-59. The input power increases with speed up to 3.28 kW, as shown in Figure 5-58(a). However, the machine output is only 1.65 kW at the same speed, as shown in Figure 5-58(b). As already discussed in sections 3.8 and 0 the core loss depends on the core volume and supplied current.

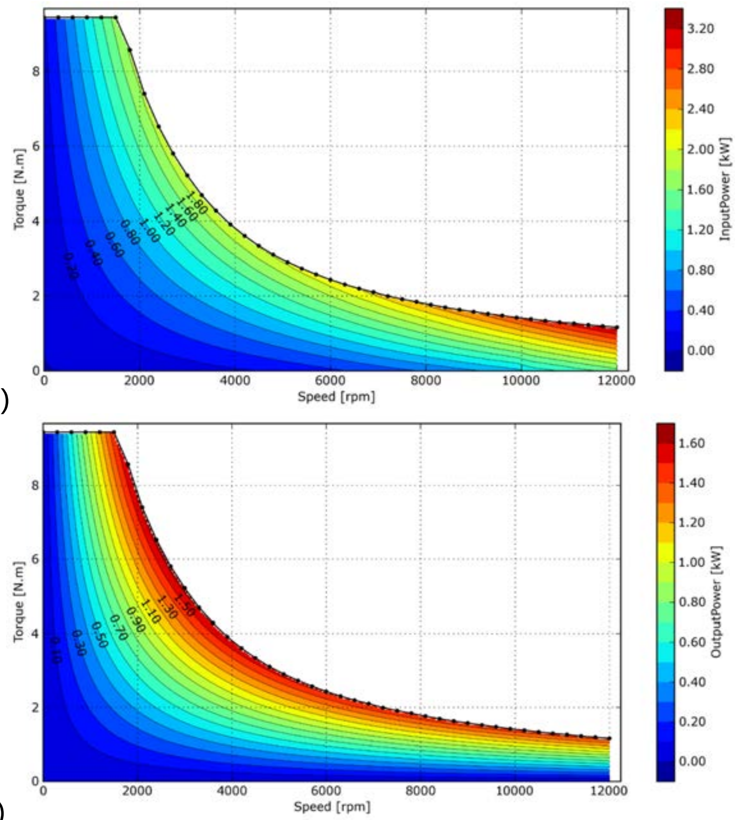

(a)

(b)

Figure 5-58: Input and output power of AN-PMV05 in the field-weakening region

In this case, the core of the machine is not changed. However, the current has been at its maximum, especially i_q at high speed which causes high core loss, as shown in Figure 5-59(a). At the same time, the mechanical loss is also significant at high-speed, as shown in Figure 5-59(b). On the other hand, the winding loss (shown in Figure 5-59(c)) is the property of stator winding only as there are no coils present on the rotor coil which follows the supplied current. The total loss of the machine is plotted in Figure 5-59(d). It shows the high loss is at high-speed region due to the high core-loss and winding loss.

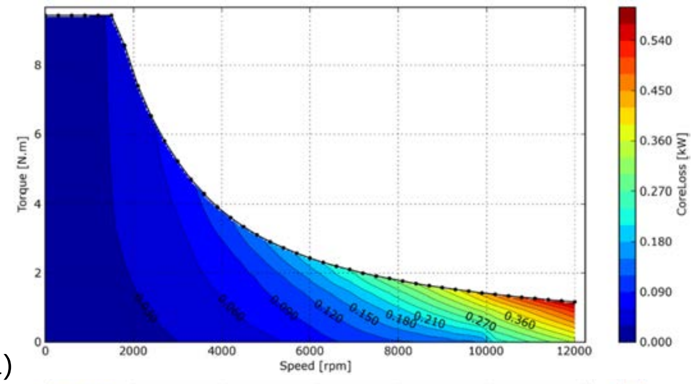

(a)

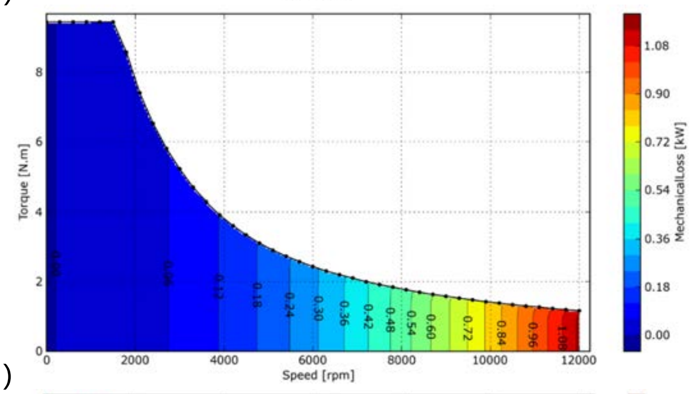

(b)

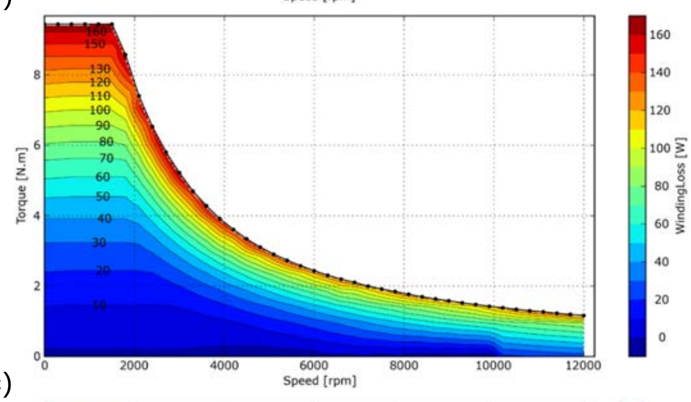

(c)

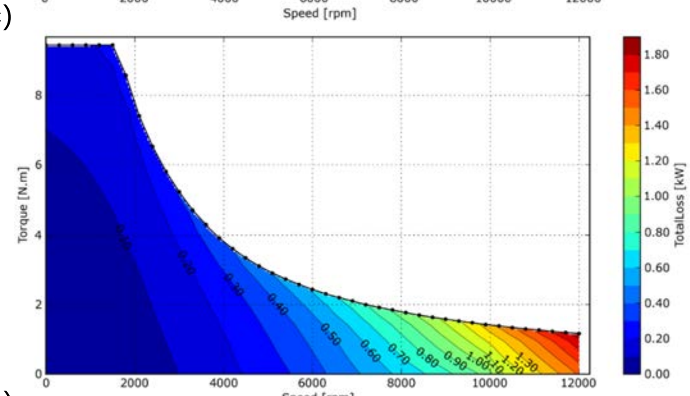

(d)

Figure 5-59: Losses of AN-PMV05 in the field-weakening region

The supplied current and voltage of the design is plotted in Figure 5-60. A high stator current is used at high torque region in MTPA, and flux-weakening where i_d and i_q are high. On the other hand, the voltage is constant in the flux weakening regions, as shown in Figure 5-60(b) where some numerical noises are also present due to the non-linearity.

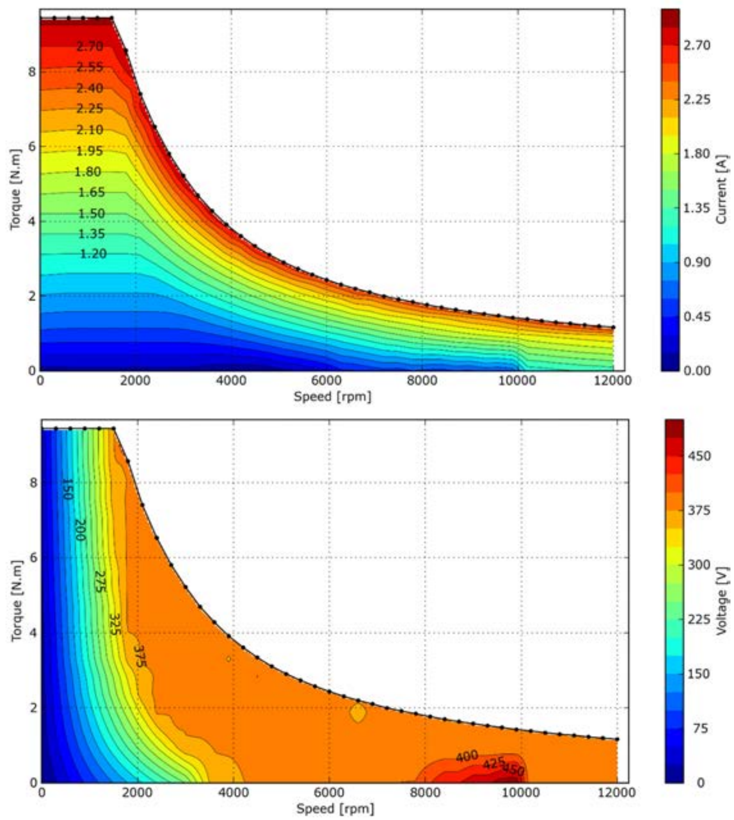

Figure 5-60: Supplied Current and Voltage of AN-PMV05 in the field-weakening region

Based on the above findings, the efficiency can be estimated in the field-weakening region as in Figure 5-61. The high efficiency of above 85 % is recorded partially in MTPA region and partially in 1:2 region. The study finds that the efficiency of machine is considerably low at low speed and high speed, especially the region beyond 1:3.

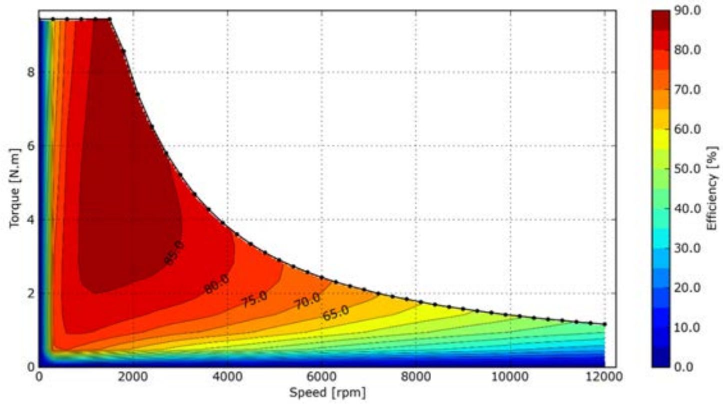

Figure 5-61: Efficiency of AN-PMV05 in the field-weakening region

The performance parameters are summarised and plotted in $p.u$ space in Figure 5-62. It shows the areas where the machine can yield the best performance in various aspects. The machine uses the supplied power efficiently in both MTPA as well as in field-weakening regions. On the other hand, the machines optimum power factor lies around 1:2 regions. Thus, the machine shall be operated in this region for better efficiency and low reactive power.

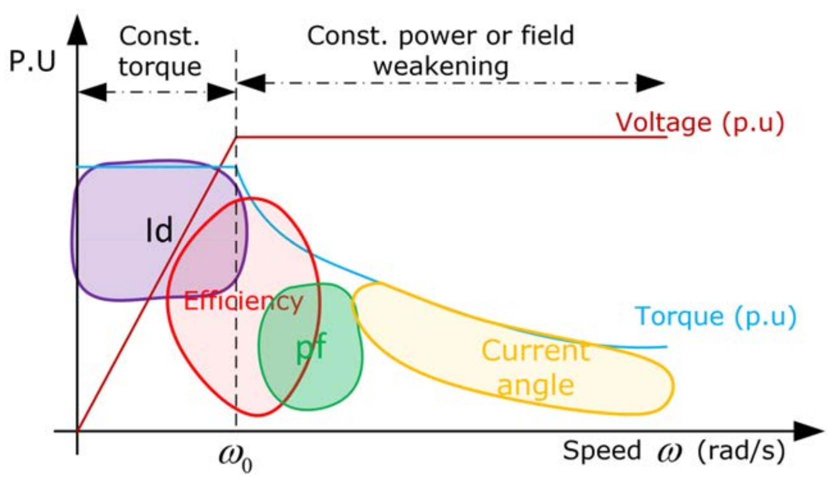

Figure 5-62: Summary of performance parameters as $p.u$ values in the field weakening region for PMSynRM

5.12 Conclusion

A comprehensive investigation of PMSynRM is presented in this chapter. Properties of magnets for electrical machines are discussed in detail, especially the suitability of rare-earth neodymium magnets for the electrical machine is investigated with its temperature and demagnetisation characteristics. A detailed analytical model of PMSynRM is developed using SynRM's phasor diagram, and properties such as magnetic flux, voltage, torque angle and load angle are explicitly studied. The machine performance parameters torque, power factor and torque ripples are analytically modelled. MTPA and flux-weakening characteristics of the machine analytically investigated.

The characteristic current and flux of the PMSynRM are defined to determine the optimum quantity of the PM. The simulation techniques of for PMSynRM is demonstrated graphically for fractional design simulation. PMSynRM with various PM quantities are simulated, and their characteristics are demonstrated via phasor diagrams. The saturation and cross-saturation in PMSynRM are discussed with simulation results, and its effects of performance parameters are studied. Cross-saturation on flux linkages with changing current and current angle is demonstrated by numerous FEM simulations. The saliency of PMSynRM with respect to current and current angle is investigated, and the impact of saturations on saliency is also investigated. An optimum operational point for maximum saliency is found and demonstrated.

The hybrid capability of PMSynRM with reluctance and PM torques are comprehensively studied. The difference between the two torques is analytically discussed and backed by FEM simulation results. The torque of PMSynRM with various PM quantities broadly analysed for two types of barriers. In the meantime, the power factor is analytically modelled, and its impact due to added PMs are systematically investigated and graphically established. The techniques to improve power factor is systematically investigated the findings are backed up by simulations results.

A novel topology is developed to optimise the PMSynRM with PMs in more than one barrier. A hyperbolic barrier design is prepared for the optimisation of PMs, and its results are investigated. A novel topology is developed to optimise PMSynRM as a whole object that can yield the best of the PMSynRM and find low torque ripples. The optimised designs from both topologies demonstrated high torque, power factor and low torque ripples. Torque and power factor of almost 39 % and 13 % is achieved by optimised design, respectively. Moreover, the torque ripples can be minimised below 8 % by optimising the machine as a whole. The efficiency of the machine also can be improved by almost 8 %.

The machine operational characteristics are studied for both MTPA and flux-weakening regions. The torque-speed curves as a function of various machine parameters discussed using highly advanced machine design toolkit. The analyses found that PMSynRM can be controlled better at a lower speed due to its initial torque density as well as have higher torque in the flux weakening region. The primary two setbacks of SynRM is no longer an issue with added PMSynRM.

6 OPTIMISED DESIGNS AND EXPERIMENTAL ANALYSES

6.1 Introduction

The simulated results are experimentally verified in this section via numerous prototypes. Altogether, ten prototypes have been fabricated as part of this study. Six of them are SynRM rotors, two of them are PMSynRM, one out of the two is optimised SynRM from section 4.7 and section 5.9, and the other one is PMSynRM rotor with linear-barrier. The other two prototypes are used for experimental verification of torque ripples studied in section 4.8. Figure 6-1 shows all ten prototypes. A flexible rotor assembly is prepared to reuse the same shaft assembly for PMSynRM so that different PM configuration is possible.

Figure 6-1: Prototypes that are prepared for this thesis experiments

6.1.1 Experimental Rotors and Rotor Assembly

As already discussed, air-gap length should be minimised as low as possible for high performance, especially for high efficiency. The study aims to have a 0.25

mm air-gap length, which has been utilised in the simulations. In order to achieve 0.25 mm air-gap length, a highly precise and low-tolerance technology is needed. Thus, the prototypes are manufactured using medium speed wire cutting method with 0.01 mm tolerance. Electrical steel M400-50A is used with 0.50 mm lamination thickness for all prototypes. The wire cutting process of a SynRM is shown in Figure 6-2.

Figure 6-2: Wire cutting process of a SynRM prototype

An existing stator is used for the experiments, while the entire rotor assembly is prepared to align the stator. The rotors are mounted using an insulation ring on both sides with end-press ring assembled by heat press at the right end. The end insulation rings, end-press rings and shaft are separately prepared for each SynRM rotor assembly as they are heat pressed for high mechanical integrity and safety except for the PMSynRM rotors. The PMSynRMs require multiple configurations of PMs, hence it requires a flexible assembly so that it can be reused. The PMSynRM rotor shafts are prepared with end threads and lock nuts for minimum required safety instead of heat-pressing, as shown in

Figure 6-3. The insulation end rings, end-press rings, lock nuts, bearing and its clip are also shown in the Figure 6-3.

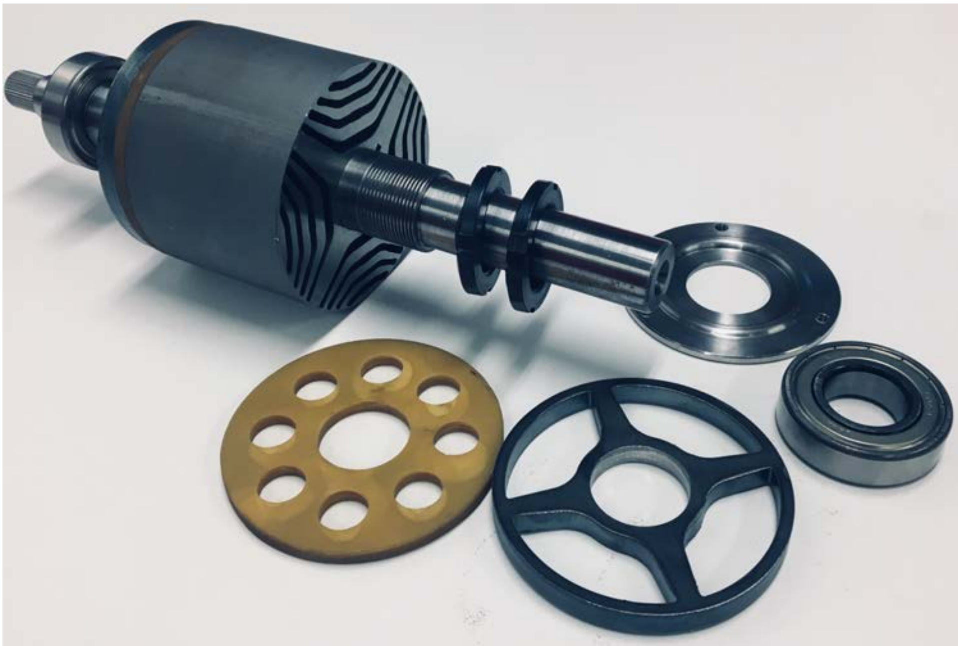

Figure 6-3: Flexible rotor assembly for multiple rotor and PM configurations

The figure shows an optimised SynRM mounted on the shaft. This type of assembly allows to change the configuration of PMs and rotor. The lock nuts deliver high integrity and safety to the rotor assembly at high-speed application while the non-drive end is heat pressed. The safety has been given high priority during the experiments. The prototypes are fabricated with an air-gap length of 0.25 mm to suit the already available stator shown in Figure 3-2. The six prototypes prepared for experimental study of SynRM characteristics for various barrier shapes, location and dimensions are shown in Figure 6-4. The designs are optimised for two types of barriers, hyperbolic arc (marked as “R”) and hyperbolic non-arc (marked as “N”). Although, the designs are optimised for torque, power factor and torque ripples, torque and power factor are given high significant. It uses a primitive design method specially developed as part of this thesis. It employs unsaturation-ring between the shaft and first barrier that allows optimiser for a wider range in searching for final design. The last two designs (WSU-4B-CO-

R-SynRM and WSU-4B-CO-N-SynRM) are equipped with circumferential cut-off (grooved).

(I) WSU-3B-R-SynRM (II) WSU-3B-N-SynRM

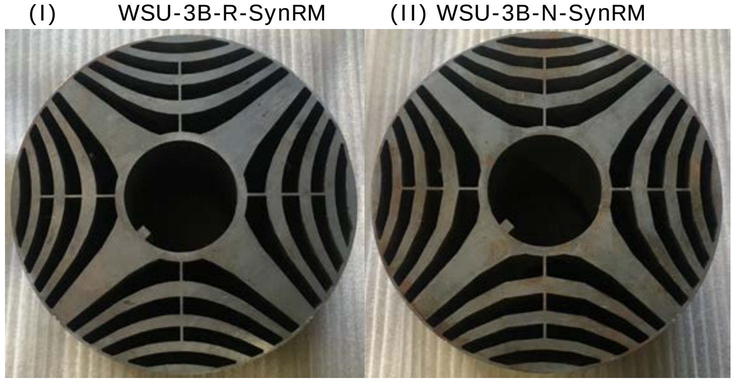

(III) WSU-4B-R-SynRM (IV) WSU-4B-N-SynRM

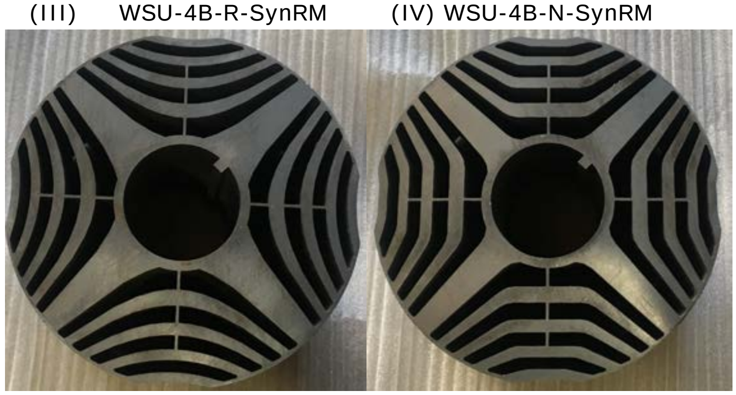

(V) WSU-4B-CO-R-SynRM (VI) WSU-4B-CO-N-SynRM

Figure 6-4: SynRM prototypes with three and four barriers and circumferential cut-off

The linear-barrier PMSynRM that is used for investigation of characteristics of PMSynRM is shown in Figure 6-5 (WSU-4B-OP-L-PMSynRM). The two designs, as shown in the figure are fabricated to hold PMs in the slots. Thus, additional mechanical arrangements are avoided for PMs. The PM slots (as can be seen in Figure 6-5) have 0.25 mm extended depth in the barriers which are accounted in the experimental studies and FEM simulation results. The cut-off is optimised, with keeping all other rotor dimensions same as other four designs. The final optimised SynRM that is studied in section 4.7, which is also used for section 5.9 for PMSynRM, which is shown in Figure 6-5 (WSU-4B-OP-N-PMSynRM). The end rings shown in Figure 6-3, are designed in such a way that it can hold the PMs from leaving the rotor during high-speed application.

(VII) WSU-4B-OP-N-PMSynRM (VIII) WSU-4B-OP-L-PMSynRM

Figure 6-5: Optimised SynRM and PMSynRM prototypes

Two rotors from the torque ripple optimisation in section 4.8, are also prototyped and shown in Figure 6-6. The rotors are also made of electrical steel M400-50A with lamination thickness of 0.50 mm and stacking factor of 0.95. All rotors, except the PMSynRM designs, have ribs and webs of 0.50 mm.

(IX) WSU-4B-TR-N-SynRM (X) WSU-4B-TR-G-SynRM

Figure 6-6: Torque ripple Optimised prototypes

6.2 Locked rotor test

The locked rotor test is conducted for experimental verification of the saliency ratio. DC resistance of the stator coil is measured, and calculated resistances are compared with direct measurement from the terminals prior to the lock rotor test. The DC resistance and stator end coil details such as leakage inductance, end coil dimensions are vital parameters as the same stator is modelled in FEM tool for highly accurate results. For a balanced system, the R_a, R_b and R_c are equal and hereafter called R_s. Likewise, L_a, L_b and L_c are equal and called L. As it is relatively challenging to measure the leakage inductance, it is calculated by feeding the other measured values into FEM (into RMXprt tool). The DC resistance and leakage inductance are important parameters in modelling an accurate simulation as given in Eq. (2.10)

The topology used for the experiment is given in Figure 6-7. In order to experimentally measure the inductances, an AC supply is used. The rotor is locked in D axis as shown and the supplied voltage is changed from 0 to 150 VAC/50Hz. The i_d is measured and the DC resistance can be calculated using Eq. (6.1). The impedance Z_d can be calculated using Eq. (6.2). Similarly, the equivalent of the Q axis can be measured by locking the rotor in the Q axis.

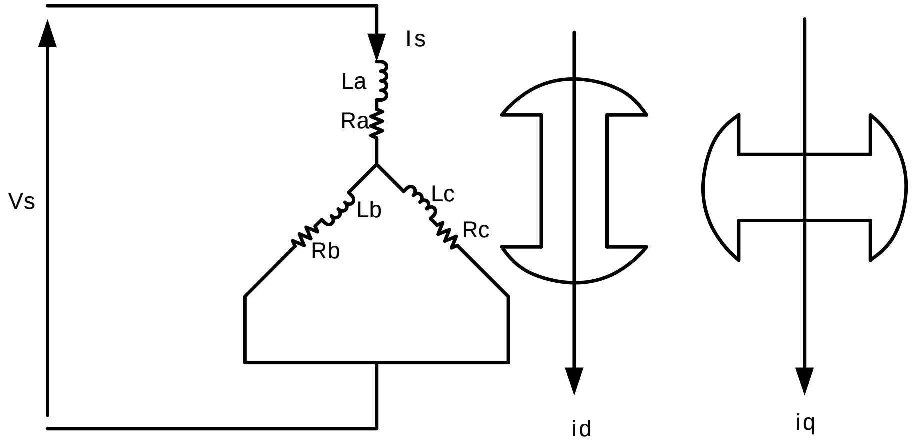

Figure 6-7: Locked rotor test arrangement for D and Q axis

$$R_{tot} = \frac{3R_s}{2} \tag{6.1}$$

$$Z_d = \frac{V_s}{i_d}$$
$$Z_q = \frac{V_s}{i_q} \tag{6.2}$$

The total reactance of the terminal can be experimentally calculated by applying underlying electrical AC network Eq. (6.3), while the inductance is calculated as given in Eq. (6.4). The D and Q axis inductances can be calculated for each rotor in the same way for various supplied voltages.

$$X_d = \sqrt{{Z_d}^2 - {R_s}^2}$$
$$X_q = \sqrt{{Z_q}^2 - {R_q}^2} \tag{6.3}$$

$$X_d = 2\pi f L_d$$
$$X_q = 2\pi f L_q \tag{6.4}$$

When the rotor is locked in D axis as shown in the figure, the supplied current is equivalent to D axis current ($I_s = i_d$), and when it is locked in the Q axis, the current is equivalent to Q axis current ($I_s = i_q$). The rotor is naturally aligned to D axis when the current is applied. The rotor should be rotated 90° electrically to lock it in Q axis position. The saliency of the machine can be experimentally measured as discussed above. The measured saliency ratios of the six designs are shown in Figure 6-8. The saliency ratio of each design changes with voltage but the change is high for design WSU-4B-CO-N-SynRM (Rotor-VI) compared with other designs due to the groove as discussed in section 3.9.

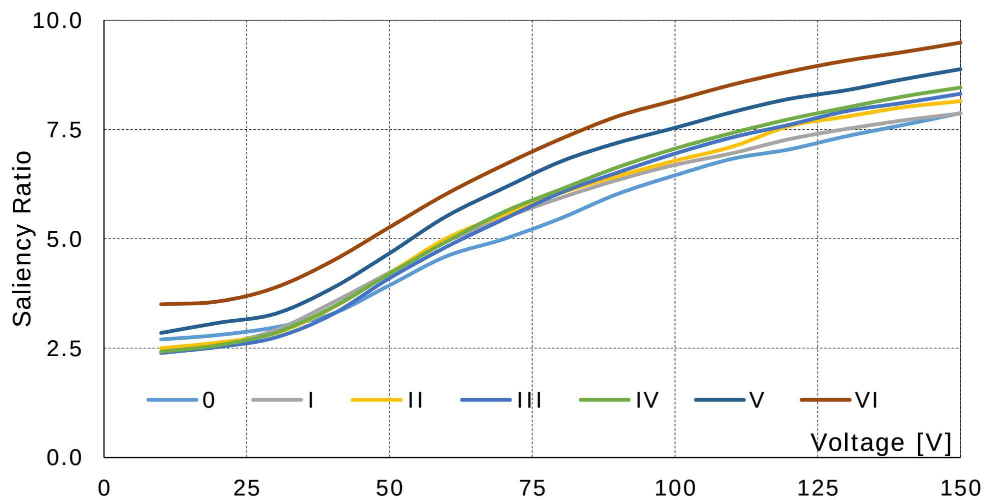

Figure 6-8: Saliency ratio of the six design from lock rotor test (0 -base design)

As discussed in section 2.6 the saliency ratio of a non-linear rotor is depended on supplied current. As can be seen in Figure 6-8, the saliency ratio of all seven designs increase with current. It saturates the ribs and webs (for applicable designs) resulting in no further flux through them. The analytical finding, and FEM simulated findings in section 3.6 closely match the experimental verification. The design WSU-4B-CO-N-SynRM is employed with the optimum (natural flux path) barrier designed in section 3.5.1 and cut-off at circumference shows significantly high saliency ratio of 9.6 at rated condition (MTPA). The theory of saturating ribs and webs for high saliency ratio discussed in section 2.6 and 2.7 is validated by the locked rotor experiment. The saliency ratio is increased for higher currents due to the saturation of ribs and webs as can be seen. The experiment also validates the theory of having higher barriers yields high saliency ratio, discussed in 3.6.5.

The two cut-off designs (WSU-4B-CO-R-SynRM and WSU-4B-CO-N-SynRM) show a high saliency ratio out of all the six designs. The machine performance of cut-off designs is further discussed in the subsequent experiments. All six designs exceeded the base SynRM's saliency ratio at rated condition even though it has higher saliency ratio than the designs II, III and IV at initial condition.

6.3 Test System

A block diagram of the test setup is shown in Figure 6-9. ABB's ACS-880 drive controller is used as the test machines drive in this setup. The ACS-880' real-time data is acquired via serial communication (via RS-232) by wiring it to the test PC. A power analyser is also used in the downstream of the drive so that the ACS-880's data samples can be verified. The power analyser's real-time data acquisition is established using RS485 serial communication back to the same test PC (PC-01), which is communicating to ACS-800. The test machines are coupled using a custom-made coupler with a dynamometer. A DC servo motor of 15 kW is selected as a load and generator for the dynamometer test setup. The torque, speed and power of the test machine are measured by a torsional sensor located on the DC motor shaft side as shown in the figure. It is wired to the TS3000 (data acquisition device), and the TS300 is wired to a test PC (PC-02) along with DC motor controller via RS-484 communication to read the measured values.

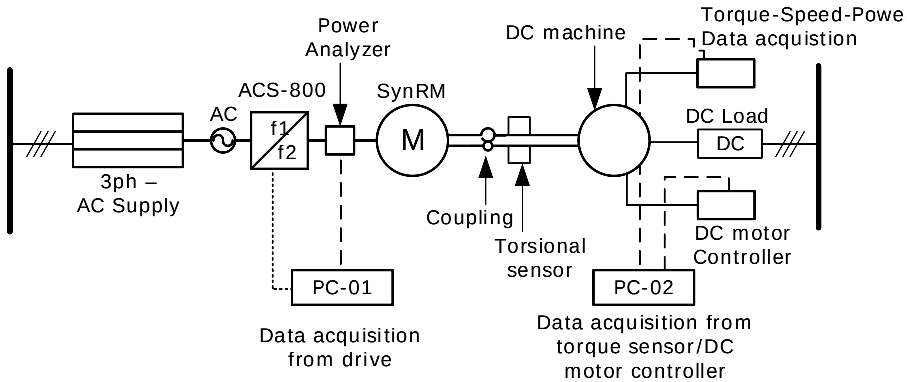

Figure 6-9: Block diagram of SynRM experiment

The experimental setup is shown in Figure 6-10. The test arrangements are custom made particularly the present research. ACS-800 and power analyser with its wiring arrangements are shown in Figure 6-10(a). The entire test arrangement with test motor, dynamometer, controllers, and test PCs are shown in Figure 6-10(b).

(a)

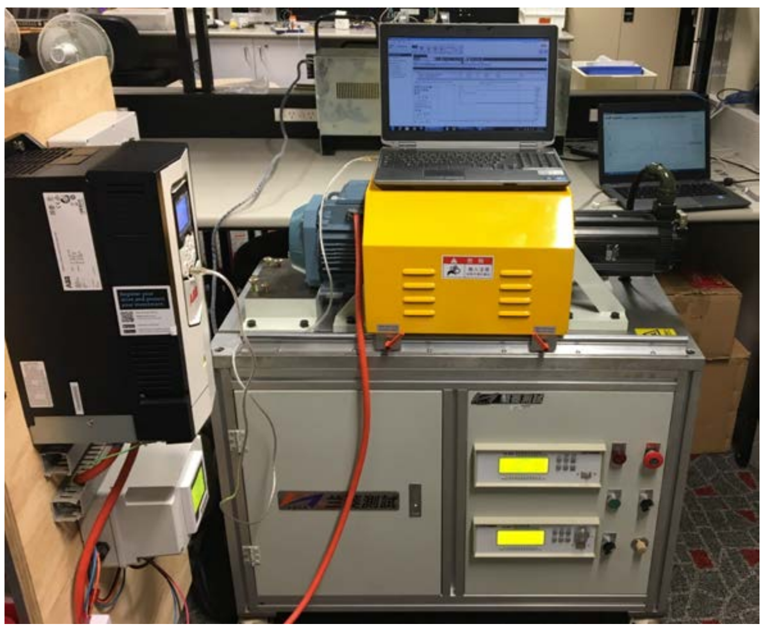

(b)

Figure 6-10: (a) ACS-880 drive controller setup (b) Dynamometer test setup used for the prototype experiments

6.4 SynRM Experiments

The rated condition for the below experiments is defined by the base machine's nameplate rating, as given in Table 3-1. The rated four-pole machine speed in a 50 Hz supply is 1500 rpm and supplied line voltage is considered 380 VAC throughout the experiments. The full load current of the machine based on the nameplate rating is 2.9 A. Therefore, the machine rated condition is considered as 1500 rpm, 380 VAC and 2.9 A. Thus, the average torques (full load torque) and machine power factors of prototypes (rated torque of the machine at the base machine full load current) are measured at supply current is at 2.9 A.

The six SynRMs have been experimentally tested and compared with respective FEM simulation results using an exact test condition. The new test system has been calibrated prior to each test in order to maintain consistency. The FEM and measured torques of all six designs and base machine (named "0" in the figure) are shown in Figure 6-11. The experimental results closely align with the FEM results discussed in section 3.6 as well as the analytical prediction that the higher the number of barriers, the higher the torque density. FEM results are closely matching the experimental readings.

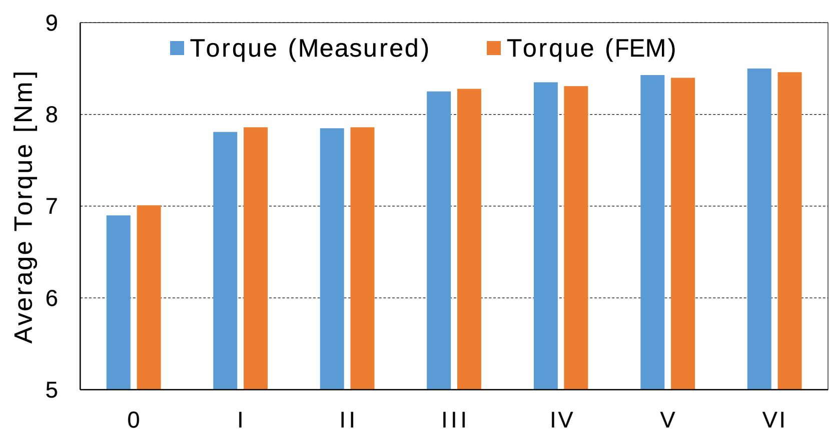

Figure 6-11: Measured and FEM torque of SynRM at rated condition

The power factors of all the designs at rated condition are plotted in Figure 6-12. As can be seen, the difference between FEM discussed in section 3.6 and measured results is slightly higher compared with torque. The power factor is calculated via external arrangements such as power analyser reading, drive reading and multi-meter measurements. The addition of their tolerances is slightly higher in comparison to the torsional sensor, which is direct reading in the case of torque measurement. The measured power factors are closely following the FEM results.

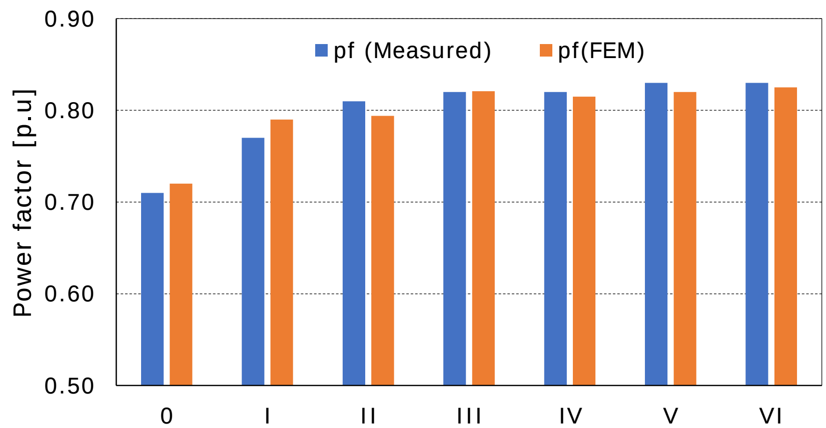

Figure 6-12: Measured and FEM power factor of SynRM at rated condition

The efficiency of all the prototypes at the rated condition is shown in Figure 6-13. Like power factor, efficiency also has a slightly higher difference between FEM and measured values, but it closely follows the FEM results for all six designs. The study shows that a small range of SynRM can be design with relatively high efficiency of almost 86 % which is almost 4 % increase compared with the base machine.

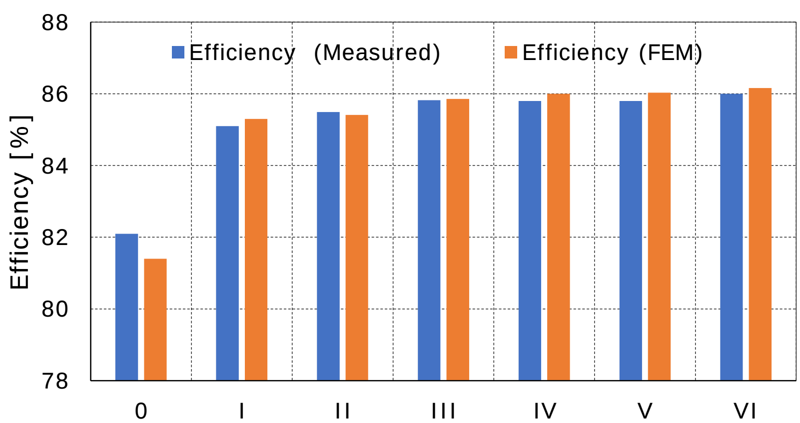

Figure 6-13: Measured and FEM efficiency of SynRM at rated condition

The saliency ratios of all the designs are shown in Figure 6-14 at rated condition. The cut-off design with hyperbolic barriers has relatively high saliency ratio. The designs with high number of barriers produce high saliency ratio regardless of the barrier shape. Hyperbolic barrier designs produce high saliency in each case, thus resulting in high performance. This validates the study results about the shape of the flux guides in section 3.5. As discussed in the FEM analysis section 3.6.5, the higher the barriers, the higher the reluctance in the Q axis. It has been experimentally proven in this study.

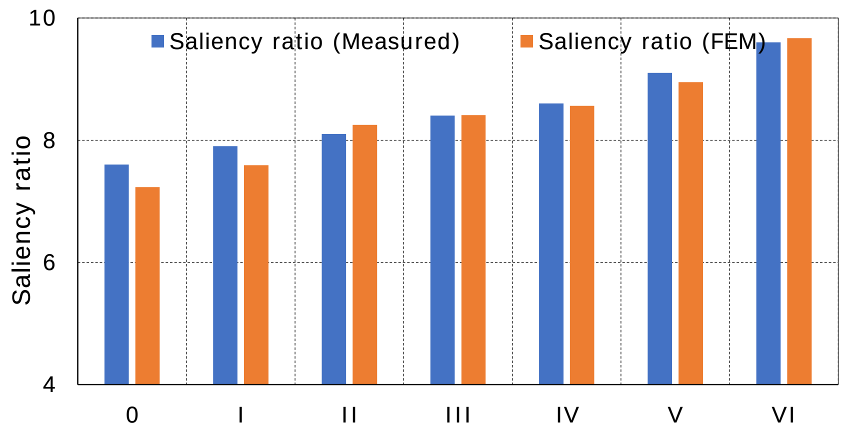

Figure 6-14: Measured and FEM saliency ratio of SynRM at rated condition

The pull-out torque of each design is experimentally tested at rated speed as part of the performance verification. The test results are given in Figure 6-15. Pull-out torque is evaluated by steadily increasing the load while the speed is constant. The pull-out torque of a machine at a certain speed is the maximum torque that the machine can withstand and stay in synchronism without pulling out. Thus, it is rather apparent to identify the point where the machine synchronism is lost by pulling out, as can be seen in figures from Figure 6-15 through to Figure 6-20.

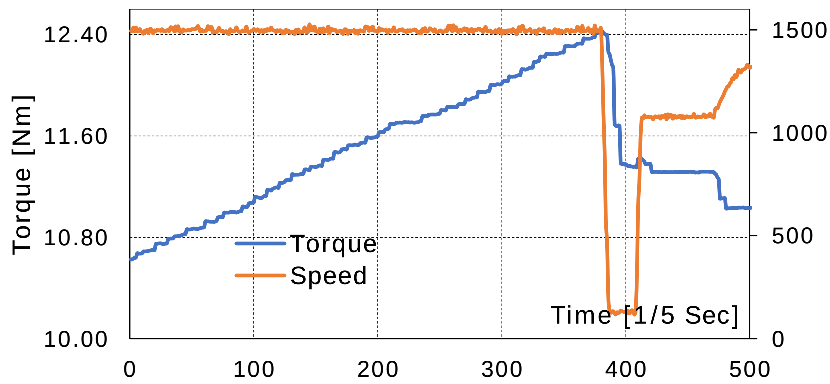

Figure 6-15: Design I: Pull-out torque test results

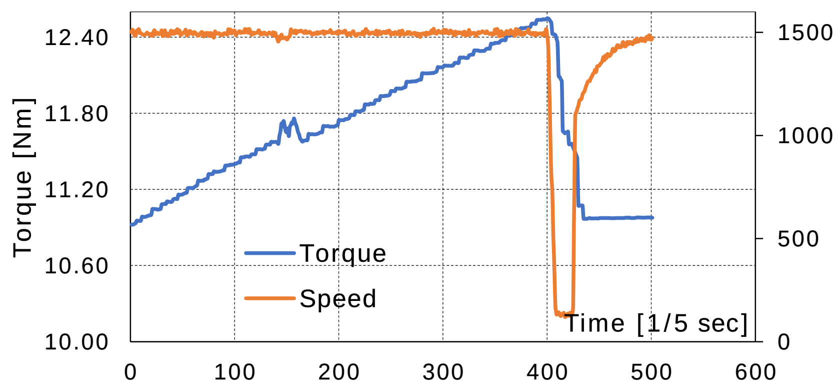

Figure 6-16: Design II: Pull-out torque test results

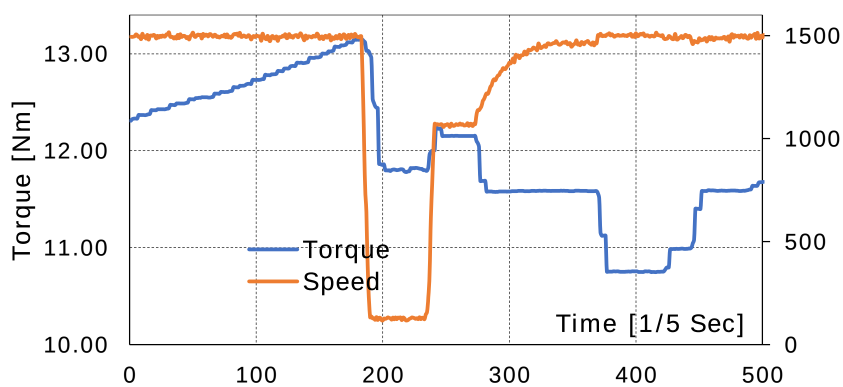

Figure 6-17: Design III: Pull-out torque test results

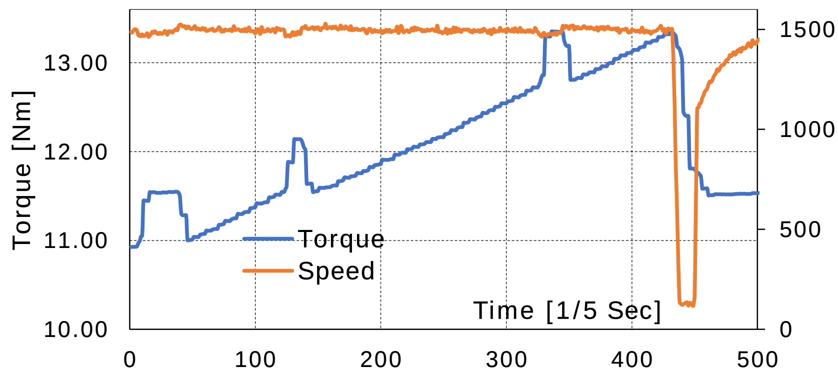

Figure 6-18: Design IV: Pull-out torque test results

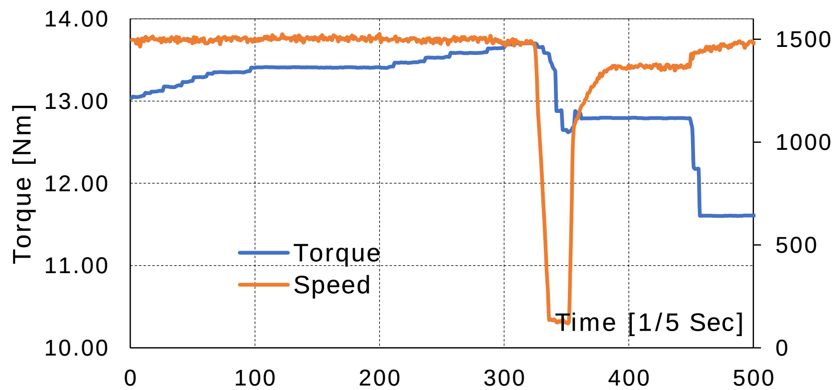

Figure 6-19: Design V: Pull-out torque test results

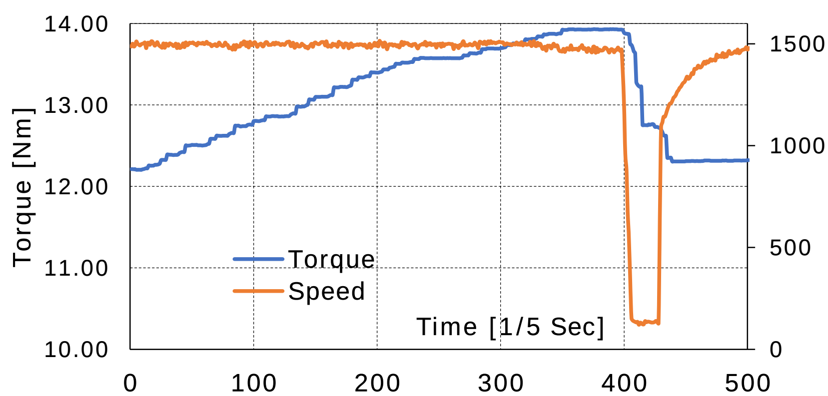

Figure 6-20: Design VI: Pull-out torque test results

The test results are shown in Figure 6-21. The hyperbolic arc designs have slightly higher pull-out torques except in the case of four barrier designs (designs

II, IV and VI). The results show that the machines produce great pull-out torque capability of almost 180 to 190 % of its torque.

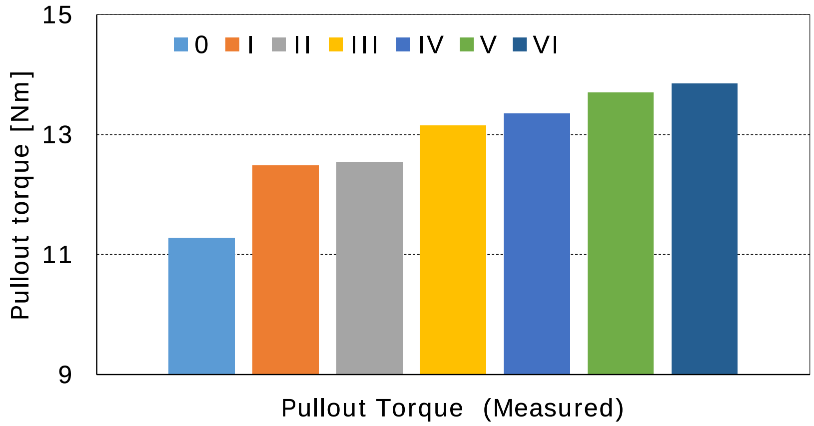

Figure 6-21: Measured pull-out torque of SynRM

The output power of each design at rated conditions are plotted in Figure 6-22. The cut-off designs (V and VI) produces the highest power compared to all other designs by almost 22 % more compared with the base design. The study shows that by proper design and optimisation, not only torque, and power factor but also the machine efficiency and output power can be significantly improved.

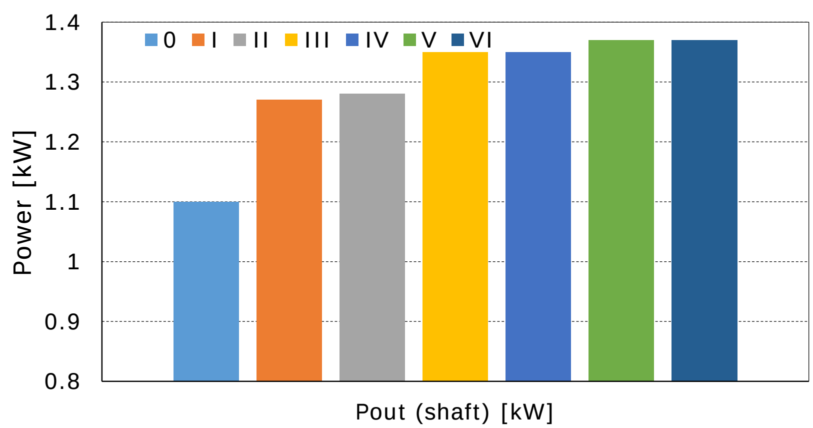

Figure 6-22: Measured output power of SynRM

6.5 PMSynRM Experiments

The linear barrier PMSynRM design discussed in section 5.7 is experimentally tested in this section using the same PM arrangement. Prototype WSU-4B-OP-L-PMSynRM (VIII) is used with the same quantities of PMs as studied (PM 1 to 4) for this analysis, as shown in Figure 6-23. As can be seen, the design VIII-04 has relatively high volume of PM, thus higher PM torque. Due to the addition of PM, the machine inertia is increased in this machine compared with equivalent SynRM. It takes slightly high starting torque start the machine.

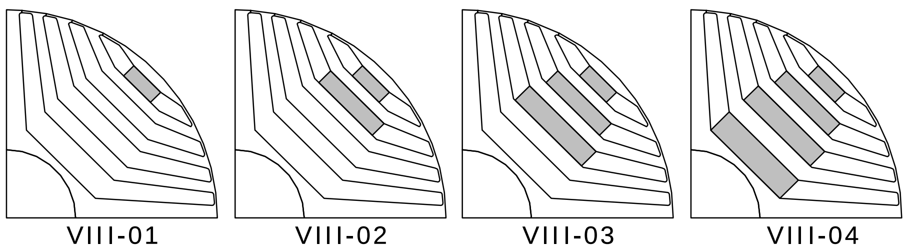

Figure 6-23: Linear-barrier PMSynRM designs with various PM quantities for experiments

The average torques of all the designs (SynRM is called VIII-00 in the figure) at the rated condition (defined in section 6.4) are shown in Figure 6-24. The measured torques are closely following the FEM torques obtained in section 5.8.4. The design VIII-04 has significantly high PMs compared with the other three designs which also shows high torque.

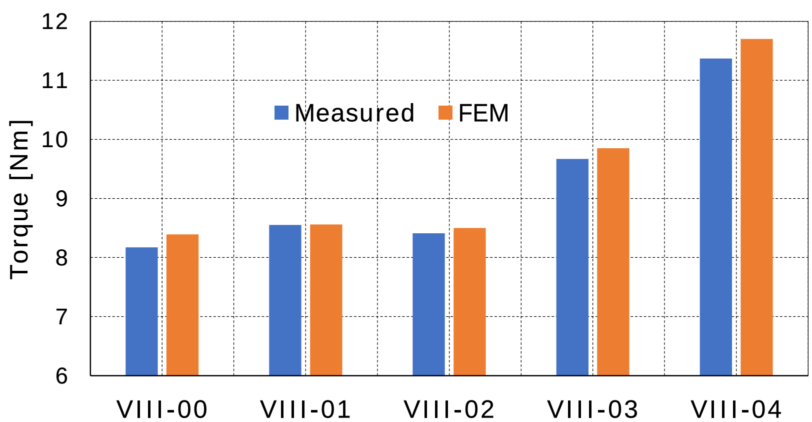

Figure 6-24: Measured and FEM torque of PMSynRM at rated condition

The power factors at the rated condition (defined in section 6.4) are shown in Figure 6-25. The SynRM used for this experiment is an optimised design with linear barriers to contain PMs. Thus, its measured power factor is slightly higher (11 %) than that of the base design. As discussed in section 5.4, addition of PM increases the power factor of the machine. It is experimentally observed where the FEM and measured readings are quite similar.

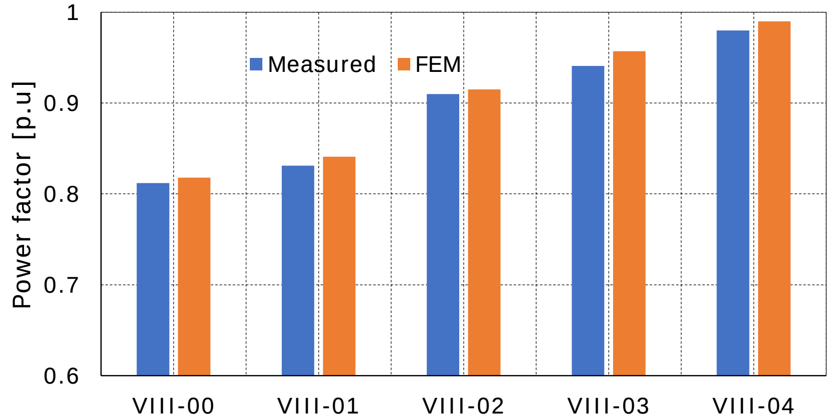

Figure 6-25: Measured and FEM power factor of PMSynRM at rated condition

The PMSynRM pull-out torques of the above designs are plotted in Figure 6-26. The pull-out torque of SynRM is almost 180-190 % of its average torque. Whereas, in the case of PMSynRM, it is not quite the same. As can be seen, pull-out torques of machines VIII-01, VIII-02, VIII-03 and VIII-04 are 183 %, 173 %, 177 %, and 169 % of the rated torque, respectively.

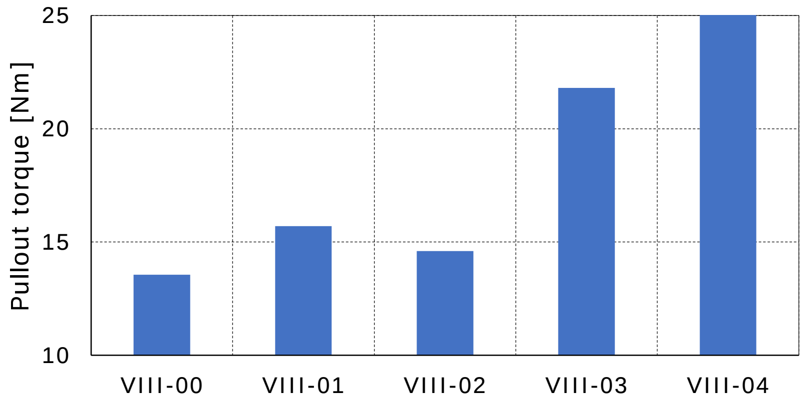

Figure 6-26: Measured and FEM pull-out torque of PMSynRM at rated condition

The efficiencies of the experimental designs at rated condition are plotted in Figure 6-27. The experimental efficiencies are slightly higher than that of the FEM. It is primarily attributed to the tolerances of the test equipment. However, the differences between FEM and measured results are still within 1 % and consistent in all cases. The experimental study verifies that the FEM simulation results are closely matching the measured results.

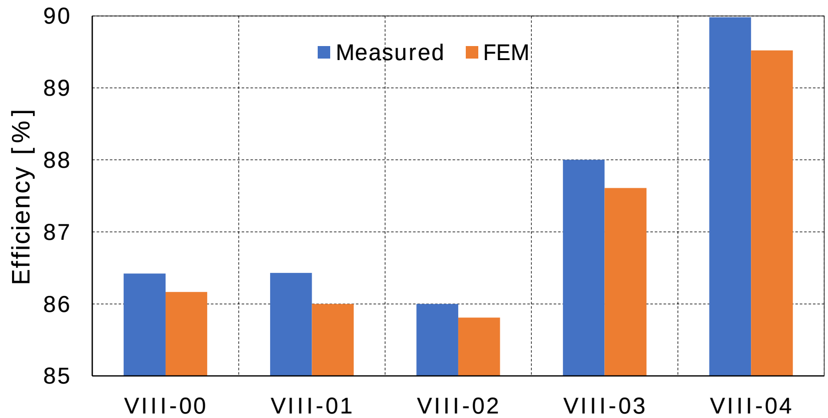

Figure 6-27: Measured and FEM efficiency of PMSynRM at rated condition

6.6 Optimised PMSynRM Experiments

The PMSynRM (WSU-4B-OP-N-PMSynRM) studied in section 5.9 and shown in Figure 6-4 is experimentally tested. The optimised designs AN-PMII_OT02 and AN-PMII_OT03 share the same SynRM configuration. However, this section experimentally investigates only the design AN-PMII_OT02. The tests are carried out at rated condition defined in section 6.4. The torques of all the designs are shown in Figure 6-27. As can be seen, the measured torques are quite close to the FEM results. The measured torque of the PMSynRM is increased by 38 % compared with its equivalent SynRM.

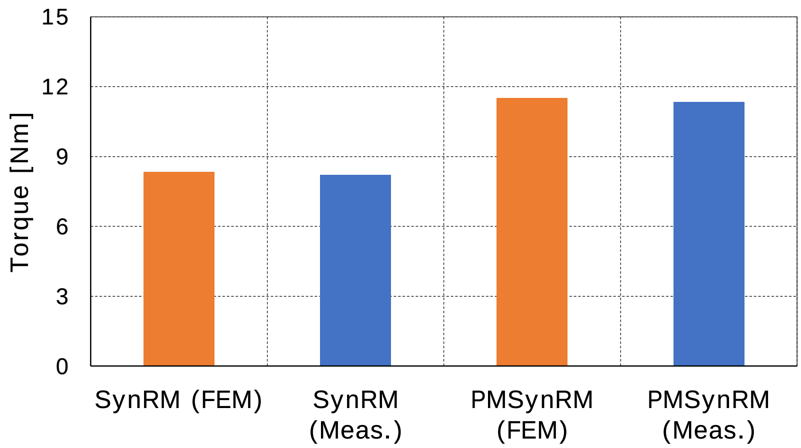

Figure 6-28: Measured and FEM torque at rated condition

The power factors of the optimised PMSynRM and its equivalent SynRM are plotted in Figure 6-29. The results verify that the performance of a SynRM can be significantly improved with PMs. The measured power factor of the optimised PMSynRM is increased by almost 14 % compared to its equivalent SynRM without PMs.

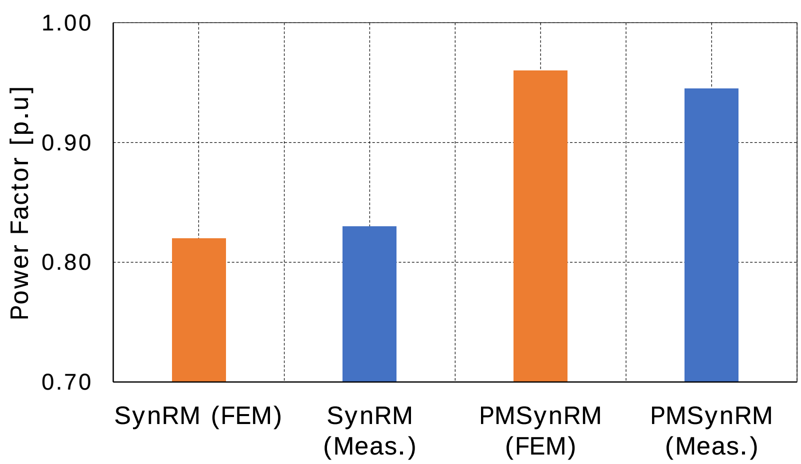

Figure 6-29: Measured and FEM power factor at rated condition

The efficiency of the optimised PMSynRM is shown in Figure 6-30 at rated conditions. It is increased by 3.8 % compared with equivalent but optimised SynRM. As discussed in section 5.10.5, efficiency of these machine naturally higher than that of SynRM and it is experimentally verified.

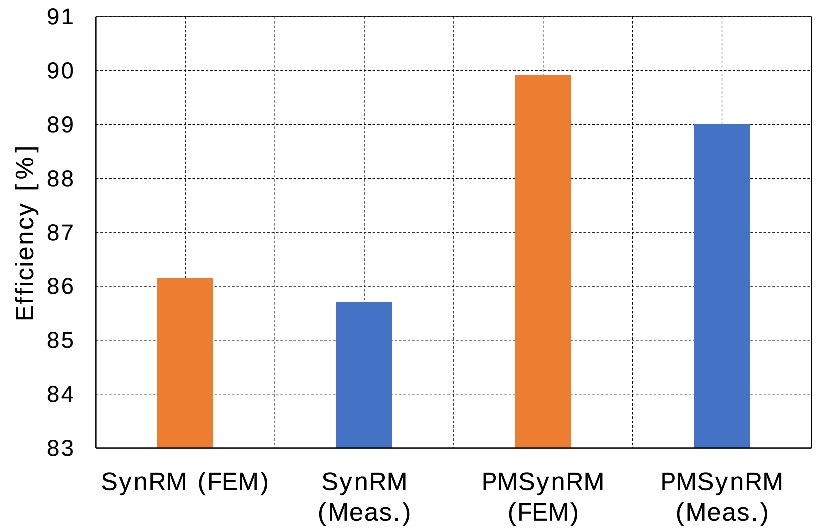

Figure 6-30: Measured and FEM efficiency at rated condition

The instantaneous torque of PMSynRM and SynRM are recorded at various speeds to study the torque ripples of the two machines which are plotted in Figure 6-31 and Figure 6-32. The torque sensor captures the real-time torque pulsation at various speed. However, the sampling rate of the torque sensor is not as high as FEM step time. The sampling rate of the test system is 0.2 seconds, whereas the simulation time step is 0.000333 seconds. Thus, the captured pulsation is not expected to show the ripples captured by FEM. However, the real-time torque ripples, shown in the figure is enough to determine the instantaneous machine torque in an application.

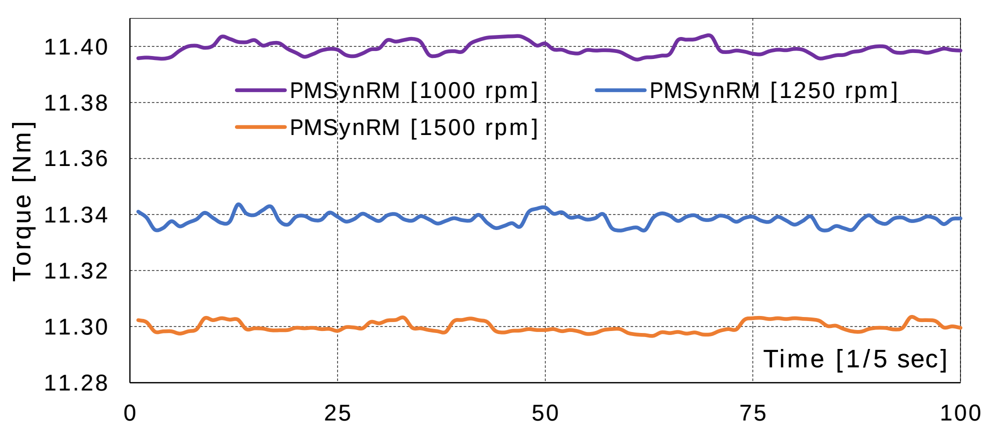

Figure 6-31: Real-time torque ripples of PMSynRM at three different speeds

The torque ripples of PMSynRM at all three speeds are less than 0.5 % of the average torque. The torque ripples of SynRM at the same three speeds are plotted in Figure 6-32. The torque at 1500 rpm experiences slightly higher ripples compared with other two speeds, but still within 0.5 % of the average torque of the machine.

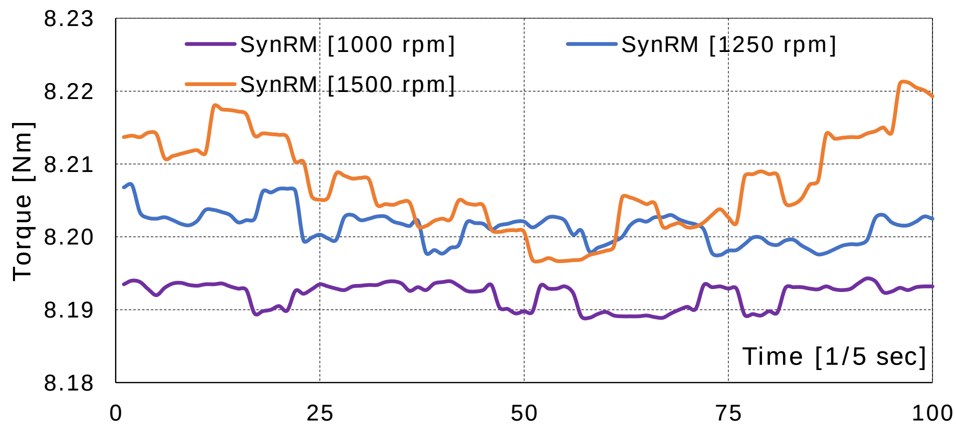

Figure 6-32: Real-time torque ripples of SynRM at three different speeds

The investigation verifies experimentally that an optimised PMSynRM with high-grade rare-earth permanent magnet can considerably improve the performance of a SynRM. Moreover, the machine can also be designed to run with less torque ripples as shown. The PMSynRM is designed without radial webs to have PMs in the middle of the barriers (Figure 6-5). Thus, its tangential ribs are slightly increased to balance the mechanical integrity.

6.7 SynRM for Low Ripples

Both OPT-A and OPT-C from section 4.8, are prototyped for experimental verification using medium wire cutting technology so that 0.25 mm air-gap can be achieved, as shown in Figure 6-6. Electrical steel JFE50JN400 is used for the prototype to achieve high anisotropy. As discussed in section 6.6, the sampling rate of the test system is not high enough to capture tiny torque spikes exposed by FEM simulation. However, it can capture the practical torque pulsations that affects the machine performance in a real-world application. The instantaneous torques of both designs at three different speeds are plotted in Figure 6-33.

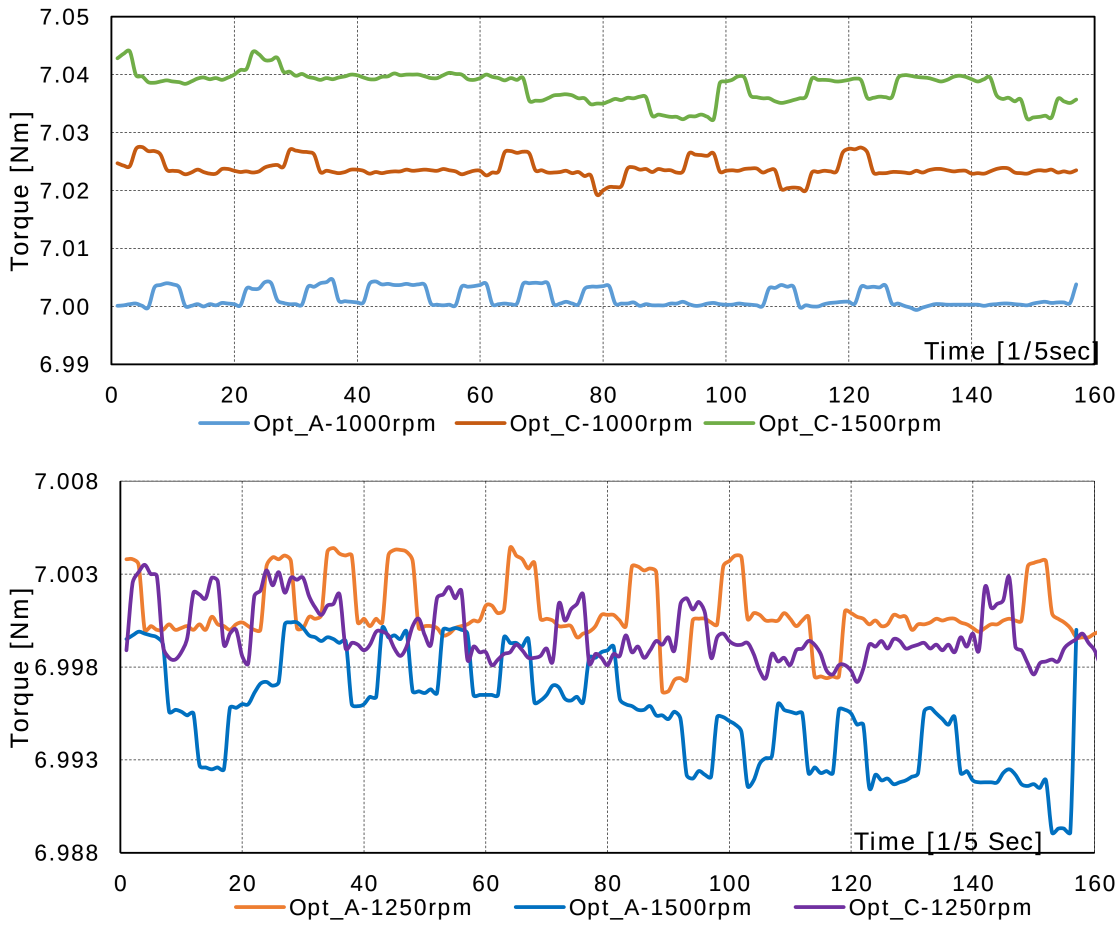

Figure 6-33: Real-time torque ripples of optimised SynRM at three different speeds

The design OPT-A shows torque ripples of 0.0113 Nm, whereas the design OPT-C shows 0.0101 Nm at 1500 rpm speed both are too low and in the torque sensor's tolerance range. Design OPT-A shows slightly higher ripples effect at higher speed compared with design OPT-C as can be seen in the figure. Whereas, the design OPT-C shows smooth operation at both lower and higher speeds. Both designs more or less have similar ripples at 1000 rpm. As mentioned, the sampling rate of the test bench is quite low to capture the same ripples shown by FEM though the test bench utilises state of the art torque sensor and cutting-edge controller. The tiny torque pluses occur within microseconds should not affect the operation of the machine. What matter is the practical torque ripples that are picked up by the torque sensor, as shown in Figure 6-33. Both designs show outstanding performance with respect to the ripples.

Based on OPT-A and OPT-C results it is confirmed that having more barriers increases the torque density of SynRM. It helps to minimise the ripples if barriers are placed at optimum locations. Thus, higher number of barriers can result in better machine performance. On the other hand, it dies have drawbacks. If the number of barriers is increased, it increases the saturation and core losses in the rotor core. Consequently, it reduces the overall efficiency. In SynRM, the recommended number of barriers per pole is generally defined by the number of stator slots. The definition in Eq. (3.9) provides a generic but quite broad in deciding the number of barriers. Therefore, the number of barriers shall be verified by FEM simulation and optimisation for the excellent performance of the machine.

6.8 Conclusion

The significant research findings are prototyped to validate the simulation study results. Six SynRM prototypes, two PMSynRM prototypes and two SynRM prototypes to test torque ripples effects are fabricated as part of this study. Lock rotor tests are performed to experimentally measure the saliency ratio by injecting currents. The results show the impact of saturation on machine saliency ratio as discussed earlier in the analytical and simulation studies. The test results also show that if the ribs and webs are saturated as early as possible, the saliency ratio can be increased at operation.

Experimental results of the six SynRM designs validates the simulation study results. The test results show that increasing barriers certainly increases the machine performance. Furthermore, it also reveals that rotor dimensions of a SynRM can be optimised to have relatively high performance without external arrangements. The study also found that a SynRM can be designed with optimum grove size to significantly improve the machine performance with relatively low torque ripples. Finally, the SynRM experiments also validate the barrier profile proposed by the study in section 3.5 can have high performance. Moreover, the study also found that 3.9 % more efficiency compared with the base machine which is a significant achievement.

The two PMSynRM studies reveal that not only torque and power factor but also other performances such as efficiency and output power of a SynRM can be considerably increased by adding rare-earth PMs. The torque, power factor and efficiency of a SynRM are increased by 38 %, 13 %, and 3.8 % respectively by inserted PMs. Moreover, the efficiency of the PMSynRM is increased by 6.9 % compared with base machine. It means not only relatively high cost savings for the end user, but also less emission to the environment due to the optimum usage power. Finally, the experiment results of torque ripples backup the FEM simulation results from section 4.8.3. The unconventional SynRM prototypes show that SynRM can be designed to have very low torque ripples below 1 % of the machine rated torque. However, it is achieved by slightly compromising machine average torque.

7 CONCLUSION AND RECOMMENDATION FOR FUTURE WORKS

7.1 Conclusion

This thesis has focused primarily on machine performance improvement of both SynRMs and PMSynRMs. The detailed analytical models of both machines are developed and presented with completed phasor diagrams. The machines operating principles have been comprehensively studied and illustrated with the help of graphs and vector diagrams for better understanding. The reluctance theory concept, both for axially laminated and transversally laminated structures and their impact on machine performance, are described with details and illustrated. The machine performance parameters such as torque, power factor, torque ripples and efficiency are well defined analytically and in a simulation environment for both machines. The impact of saturation, cross saturation in the non-linear structures is demonstrated with various simulations and the results presented in chapter 3.

Both SynRMs and PMSynRMs are modelled with a highly advanced FEM program using primitive design methods. The average solutions of SynRM and PMSynRM performance parameters are defined for post-processing of the simulation results. The machine parameters are investigated using the average solution on numerous rotor dimensions, and the results are presented in this thesis. The optimisation techniques have been employed in this study to obtain the best optimal machine performance. Numerous optimisation algorithms, for single-objective and multi-objective optimisation, have been discussed and employed on various design topologies that can be automated during optimisation, and detailed in chapter 4 and 5.

The torque ripples are also given considerable attention in this study. A comprehensive investigation focusing on barrier dimensions, barrier shapes and barrier end profile is presented. Two optimised designs from torque ripples investigation are prototyped and the simulation results are experimentally verified in chapter 6. Ten prototypes for SynRM and PMSynRM experimental verification are fabricated for this study using high-grade electrical steel and medium wire-cutting technology. These prototypes are tested experimentally to verify the theoretical results and discussed in chapter 7. The rare-earth neodymium magnets are also fabricated to suit the optimised designs. A new test system (dynamometer) is prepared solely for this study using a DC servo motor, as presented in section 6.3. The prototypes are tested extensively, and the results are presented along with simulation results in chapter 7.

7.1.1 Important findings

The study finds an optimum flux barrier shape using natural flux path for high performance. The study developed a new multi-barrier arrangement for SynRM from numerous simulations, and parameterisation in section 3.5. The study uses a commercial off the shelf SynRM as a basis to compare the results. The optimised SynRM (in section 4.7) exceeds the torque of the base machine by 17 %, the power factor by 15 %, and the efficiency by 5.8 %. Moreover, a new method is developed to optimise SynRM for torque ripples. The first SynRM with hyperbolic barrier type developed via means of optimisation techniques and the second model is found by replacing the hyperbolic barrier with a circular barrier to achieve low torque ripples. The hyperbolic barrier SynRM shows 3.2 % torque ripples, while the circular barrier design shows 1.1 %, as presented in chapter 3.

The study also investigated PMSynRM with new topologies to optimise the machine in two ways, the first one to optimise PMs in an already optimised SynRM and the second one is optimising the PMSynRM as a whole object using a novel topology developed just for this study. Both machines have shown much improved performance. The optimised PMSynRM yields torque of 38 %, the power factor of 17 % and efficiency of 4.3 % more of its equivalent SynRM as presented in chapter 5.

7.2 Recommendation for Future Works

Although the torque ripples have been investigated in detail in this thesis, it focuses primarily on the rotor dimensions. It allows the torque ripples in SynRM to be minimised with minimum structural change in the machine without radically changing cost of manufacturing. Although other methods such as skewing, fractional winding, step skewing and asymmetrical flux barriers are also discussed in this thesis but they are not investigated. Each method as shown in section 4.8 requires investigation to minimise the ripples effects in these machines. The simulations and experiments were investigated with sinusoidally fed excitation. The ripples effect can be further investigated for various control algorithms that can minimise the influence of flux harmonics during the operating condition.

This study has investigated both SynRM s and PMSynRMs machines in detail. The one area that requires further investigation is the control of the machines using a specific controller that is specifically designed for these machines. The ASC-880 is capable of driving SynRM, and it can be tuned for specific SynRM using the advance inbuilt functions. However, the function injects current to identify the saliency of the machine, and it alone may not be enough to properly understand the machine characteristics as it has been discussed throughout this thesis. In addition, the MTPA region of a PMSynRM is completely changed when the quantities of PMs and configuration are changed. Thus, it requires a dedicated controller that can be programmed online for a specific machine.

References

[1] (2015). *Energy-efficiency with electric drive systems*. Available: https://cemep.eu/data/CEMEP_Brochure_Energy_Efficiency_with_Drive_Systems_2015_4.pdf

[2] (2014). *Primium efficiency motor selection and application guide*. Available: https://www.energy.gov/sites/prod/files/2014/04/f15/amo_motors_handbook_web.pdf

[3] ABB. (2019). *Searching for cost efficient efficiency (Drives ed.)*. Available: https://new.abb.com/drives/media/cost-efficient-efficiency

[4] I. Boldea, "Direct torque and flux control (dtfc) of ac drives," *Control in Power Electronics,* Acedamic Press Series in Engineering pp, 301-349, 2002.

[5] J. K. Kostko, "Polyphase reaction synchronous motors," *Journal of the American Institute of Electrical Engineers,* vol. 42, no. 11, pp, 1162-1168, 1923.

[6] R. E. Betz, R. Lagerquist, M. Jovanovic, T. J. E. Miller, and R. H. Middleton, "Control of synchronous reluctance machines," *IEEE Transactions on Industry Applications,* vol. 29, no. 6, pp, 1110-1122, 1993.

[7] M. J. Kamper and A. F. Volsdhenk, "Effect of rotor dimensions and cross magnetisation on ld and lq inductances of reluctance synchronous machine with cageless flux barrier rotor," *IEE Proceedings - Electric Power Applications,* vol. 141, no. 4, pp, 213-220, 1994.

[8] R. Lagerquist, I. Boldea, and T. J. E. Miller, "Sensorless-control of the synchronous reluctance motor," *IEEE Transactions on Industry Applications,* vol. 30, no. 3, pp, 673-682, 1994.

[9] M. H. Nagrial and M. A. Rahman, "Operation and characteristics of self-excited reluctance generator," in *Conference Record of the IEEE Industry Applications Society Annual Meeting*, pp, 55-58 vol.1, 1988.

[10] T. J. E. Miller, C. Cossar, and A. J. Hutton, "Design of a synchronous reluctance motor drive," in *Conference Record of the IEEE Industry Applications Society Annual Meeting*, pp, 122-127 vol.1, 1989.

[11] E. Muljadi, T. A. Lipo, and D. W. Novotny, "Power factor enhancement of induction machines by means of solid-state excitation," *IEEE Transactions on Power Electronics,* vol. 4, no. 4, pp, 409-418, 1989.

[12] T. A. Lipo, "Synchronous reluctance machines-a viable alternative for ac drives?," *Electric Machines and Power Systems,* vol. 19, no. 6, pp, 659-671, 1991.

[13] T. J. E. Miller, A. Hutton, C. Cossar, and D. A. Staton, "Design of a synchronous reluctance motor drive," *Industry Applications, IEEE Transactions on,* vol. 27, no. 4, pp, 741-749, 1991.

[14] J. Malan, M. J. Kamper, and P. N. T. Williams, "Reluctance synchronous machine drive for hybrid electric vehicle," in *Industrial Electronics. Proceedings. ISIE. IEEE International Symposium on*, vol. 2, pp, 367-372 vol.2, 1998.

[15] J. J. Germishuizen, F. S. V. d. Merwe, K. V. d. Westhuizen, and M. J. Kamper, "Performance comparison of reluctance synchronous and induction traction drives for electrical multiple units," in *Industry Applications Conference. Conference Record of the 2000 IEEE*, vol. 1, pp, 316-323 vol.1, 2000.

[16] S. Guenther and W. Hofmann, "Multi-objective tradeoffs in the design optimization of synchronous reluctance machines for electric vehicle application," in *IEEE International Electric Machines & Drives Conference (IEMDC)*, pp, 1715-1721, 2015.

[17] N. Bianchi, S. Bolognani, E. Carraro, M. Castiello, and E. Fornasiero, "Electric vehicle traction based on synchronous reluctance motors," *IEEE Transactions on Industry Applications,* vol. 52, no. 6, pp, 4762-4769, 2016.

[18] M. Degano, M. DiNardo, M. Galea, C. Gerada, and D. Gerada, "Global design optimization strategy of a synchronous reluctance machine for light electric vehicles," in *8th IET International Conference on Power Electronics, Machines and Drives (PEMD)*, pp, 1-5, 2016.

[19] R. Rouhani, S. E. Abdollahi, and S. A. Gholamian, "Torque ripple reduction of a synchronous reluctance motor for electric vehicle applications," in *9th Annual Power Electronics, Drives Systems and Technologies Conference (PEDSTC)*, pp, 386-391, 2018.

[20] L. S. Ari Tammi. (2011) Synchronous reluctance motor & drive package low voltage motors and drives. *ABB Internal training material* [Internal training material].

[21] Gianmario P. e. al., *The rediscovery of synchronous reluctance and ferrite permanent magnet motors* (Springer briefs in electrical and computer engineering). Switzerland: Springer International Publishing, p. 142, 2016.

[22] P. H. Trickey, "Performance calculations on polyphase reluctance motors (synchronous motors without field excitation)," *Transactions of the American Institute of Electrical Engineers,* vol. 65, no. 4, pp, 191-193, 1946.

[23] C. H. Crouse, "A design method for polyphase reluctance synchronous motors," *Transactions of the American Institute of Electrical Engineers,* vol. 70, no. 1, pp, 957-962, 1951.

[24] K. Burian, "Pulling-into-step of reluctance synchronous motors," *IEEE Transactions on Power Apparatus and Systems,* vol. 84, no. 5, pp, 349-352, 1965.

[25] D. A. Staton, W. L. Soong, C. Cossar, and T. J. E. Miller, "Unified theory of torque production in switched and synchronous reluctance motors," in *Sixth International Conference on Electrical Machines and Drives (Conf. Publ. No. 376)*, pp, 67-72, 1993.

[26] D. A. Staton, W. L. Soong, and T. J. E. Miller, "Unified theory of torque production in switched reluctance and synchronous reluctance motors," *IEEE Transactions on Industry Applications,* vol. 31, no. 2, pp, 329-337, 1995.

[27] M. E. Talaat, "Steady-state and transient synthesis of 3-phase reluctance motors (synchronous motors without field excitation)," *Transactions of the American Institute of Electrical Engineers,* vol. 70, no. 2, pp, 1963-1970, 1951.

[28] M. E. Talaat, "Optimum synthesis of 3-phase reluctance motors," *Electrical Engineering,* vol. 71, no. 2, pp, 141-141, 1952.

[29] G. R. Slemon, "Equivalent circuits for cylindrical-rotor, reluctance, and salient-rotor synchronous machines," *Transactions of the American Institute of Electrical Engineers. Part III: Power Apparatus and Systems,* vol. 81, no. 3, pp, 219-224, 1962.

[30] P. J. Lawrenson and L. A. Agu, "A new unexcited synchronous machine," *Electrical Engineers, Proceedings of the Institution of,* vol. 110, no. 7, p. 1275, 1963.

[31] P. J. Lawrenson and L. A. Agu, "Reluctance machines," *Electronics and Power,* vol. 10, no. 8, pp, 264-265, 1964.

[32] P. J. Lawrenson and L. A. Agu, "Theory and performance of polyphase reluctance machines," *Proceedings of the Institution of Electrical Engineers,* vol. 111, no. 8, pp, 1435-1445, 1964.

[33] W. Fong, "Change-speed reluctance motors," *Electrical Engineers, Proceedings of the Institution of,* vol. 114, no. 6, pp, 797-801, 1967.

[34] C. Lin, "Characteristics of reluctance machines," *Transactions of the American Institute of Electrical Engineers,* vol. 70, no. 2, pp, 1971-1977, 1951.

[35] C. Lin, "Equivalent circuits of reluctance machines," *Transactions of the American Institute of Electrical Engineers. Part III: Power Apparatus and Systems,* vol. 71, no. 1, pp, 1-9, 1952.

[36] T. A. Lipo and P. C. Krause, "Stability analysis of a reluctance-synchronous machine," *IEEE Transactions on Power Apparatus and Systems,* vol. PAS-86, no. 7, pp, 825-834, 1967.

[37] A. F. Anderson, A. J. O. Cruickshank, P. J. Lawrenson, and S. R. Bowes, "Stability of reluctance machines," *Proceedings of the Institution of Electrical Engineers,* vol. 118, no. 9, pp, 1289-1290, 1971.

[38] V. B. Honsinger, "Steady-state performance of reluctance machines," *Power Apparatus and Systems, IEEE Transactions on,* vol. PAS-90, no. 1, pp, 305-317, 1971.

[39] I. Boldea and S. A. Nasar, "Thrust and normal forces in a segmented-secondary linear reluctance motor," *Proceedings of the Institution of Electrical Engineers,* vol. 122, no. 9, pp, 922-924, 1975.

[40] C. M. Ong and T. A. Lipo, "Steady-state analysis of a current source inverter/reluctance motor driveꟷ part ii: Experimental and analytical results," *IEEE Transactions on Power Apparatus and Systems,* vol. 96, no. 4, pp, 1152-1155, 1977.

[41] B. J. Chalmers and A. S. Mulki, "Design and performance of reluctance motors with unlaminated rotors," *Power Apparatus and Systems, IEEE Transactions on,* vol. PAS-91, no. 4, pp, 1562-1569, 1972.

[42] A. Nicolaide, P. J. Lawrenson, and R. M. Mathur, "Asynchronous performance of reluctance machines allowing for irregular distributions of rotor conductors," *Proceedings of the Institution of Electrical Engineers,* vol. 119, no. 12, pp, 1731-1732, 1972.

[43] A. C. Williamson, "Calculation of saturation effects in segmented-rotor reluctance machines," *Proceedings of the Institution of Electrical Engineers,* vol. 121, no. 10, pp, 1127-1133, 1974.

[44] P. J. Lawrenson and L. A. Agu, "Low-inertia reluctance machines," *Proceedings of the Institution of Electrical Engineers,* vol. 111, no. 12, pp, 2017-2025, 1964.

[45] A. J. O. Cruickshank, R. W. Menzies, and A. F. Anderson, "Axially laminated anisotropic rotors for reluctance motors," *Electrical Engineers, Proceedings of the Institution of,* vol. 113, no. 12, pp, 2058-2060, 1966.

[46] P. J. Lawrenson and S. K. Gupta, "Fringe and permeance factors for segmented-rotor reluctance machines," *Proceedings of the Institution of Electrical Engineers,* vol. 118, no. 5, pp, 669-674, 1971.

[47] P. J. Lawrenson and S. R. Bowes, "Stability of reluctance machines," *Proceedings of the Institution of Electrical Engineers,* vol. 118, no. 2, pp, 356-369, 1971.

[48] P. J. Lawrenson and S. K. Gupta, "Developments in the performance and theory of segmental-rotor reluctance motors," *Electrical Engineers, Proceedings of the Institution of,* vol. 114, no. 5, pp, 645-653, 1967.

[49] I. Boldea, Z. X. Fu, and S. A. Nasar, "High-performance reluctance generator," *IEE Proceedings B - Electric Power Applications,* vol. 140, no. 2, pp, 124-130, 1993.

[50] D. A. Staton, T. J. E. Miller, and S. E. Wood, "Maximising the saliency ratio of the synchronous reluctance motor," *Electric Power Applications, IEE Proceedings B,* vol. 140, no. 4, pp, 249-259, 1993.

[51] W. L. Soong, D. A. Staton, and T. J. E. Miller, "Design of a new axially-laminated interior permanent magnet motor," *IEEE Transactions on Industry Applications,* vol. 31, no. 2, pp, 358-367, 1995.

[52] W. Fong and J. S. C. Htsui, "New type of reluctance motor," *Electrical Engineers, Proceedings of the Institution of,* vol. 117, no. 3, pp, 545-551, 1970.

[53] A. Wexler, "Finite-element field analysis of an inhomogeneous, anisotropic, reluctance machine rotor," *IEEE Transactions on Power Apparatus and Systems,* vol. PAS-92, no. 1, pp, 145-149, 1973.

[54] A. J. O. Cruickshank, A. F. Anderson, and R. W. Menzies, "Theory and performance of reluctance motors with axially laminated anisotropic rotors," *Electrical Engineers, Proceedings of the Institution of,* vol. 118, no. 7, pp, 887-894, 1971.

[55] S. Chandrasekhara Rao, "Dynamic performance of reluctance motors with magnetically anisotropic rotors," *Power Apparatus and Systems, IEEE Transactions on,* vol. 95, no. 4, pp, 1369-1376, 1976.

[56] D. A. Staton, T. J. E. Miller, and S. E. Wood, "Maximising the saliency ratio of the synchronous reluctance motor," *IEE Proceedings B - Electric Power Applications,* vol. 140, no. 4, pp, 249-259, 1993.

[57] I. Boldea, Z. X. Fu, and S. A. Nasar, "Performance evaluation of axially-laminated anisotropic (ala) rotor reluctance synchronous motors," *IEEE Transactions on Industry Applications,* vol. 30, no. 4, pp, 977-985, 1994.

[58] F. N. Isaac, A. A. Arkadan, A. A. Russell, and A. El-Antably, "Effects of anisotropy on the performance characteristics of an axially laminated anisotropic-rotor synchronous reluctance motor drive system," *IEEE Transactions on Magnetics,* vol. 34, no. 5, pp, 3600-3603, 1998.

[59] A. A. Arkadan and A. A. Russell, "Effects of converter excitation on the performance of axially laminated anisotropic synchronous reluctance motor drives," *IEEE Transactions on Magnetics,* vol. 35, no. 3, pp, 1865-1868, 1999.

[60] F. N. Isaac, A. A. Arkadan, and A. El-Antably, "Characterization of axially laminated anisotropic-rotor synchronous reluctance motors," *IEEE Transactions on Energy Conversion,* vol. 14, no. 3, pp, 506-511, 1999.

[61] L. Q. Zhou, J. H. Zhu, and C. L. Gu, "A direct torque control scheme of ala synchronous reluctance machine and its dsp-based implementation," in *31st Annual Conference of IEEE Industrial Electronics Society, . IECON.*, p. 6 pp., 2005.

[62] L. Q. Zhou, "Direct torque control of ala synchronous reluctance machine based on modified integrator," in *Power Conversion Conference - Nagoya*, pp, 271-274, 2007.

[63] A. A. Arkadan, M. N. ElBsat, and M. A. Mneimneh, "Particle swarm design optimization of ala rotor synrm for traction applications," *IEEE Transactions on Magnetics,* vol. 45, no. 3, pp, 956-959, 2009.

[64] Z. Wei, "Analysis of magnetic circuit on ala rotor synchronous reluctance motor," in *International Conference on Electrical Machines and Systems*, pp, 1-4, 2011.

[65] R. Saxena, G. Banerji, A. Srivastava, and H. Rawat, "Performance analysis of axially laminated anisotropic synchronous reluctance motor," in *7th WSEAS International Conference on Electric Power Systems, High Voltages, Electric Machines*, Venice, Italy, 2007.

[66] C. L. Gu, L. R. Li, K. R. Shao, and Y. Q. Xiang, "Anisotropic finite element computation of high density axially-laminated rotor reluctance machine," *IEEE Transactions on Magnetics,* vol. 30, no. 5, pp, 3679-3682, 1994.

[67] B. J. Chalmers and L. Musaba, "Design and field-weakening performance of a synchronous reluctance motor with axially laminated rotor," *IEEE Transactions on Industry Applications,* vol. 34, no. 5, pp, 1035-1041, 1998.

[68] K. Young Hyun, L. Jung Ho, and L. Jin Kyoung, "Optimum design of axially laminated anisotropic rotor synchronous reluctance motor for torque density and ripple improvement," in *Computation in Electromagnetics (CEM), 9th IET International Conference on*, pp, 1-2, 2014.

[69] F. Martin, D. Singh, U. Aydin, L. Daniel, L. Bernard, P. Rasilo, and A. Belahcen, "Magneto-mechanical analysis of an axially laminated synchronous reluctance machine," in *XXII International Conference on Electrical Machines (ICEM)*, pp, 1861-1867, 2016.

[70] M. Muteba, B. Twala, and D. V. Nicolae, "Effect of double-triple winding layout on axially-laminated anisotropic rotor synchronous reluctance motors," in *XXII International Conference on Electrical Machines (ICEM)*, pp, 279-284, 2016.

[71] W. Zhao, F. Xing, X. Wang, T. A. Lipo, and B. Kwon, "Design and analysis of a novel pm-assisted synchronous reluctance machine with axially integrated magnets by the finite-element method," *IEEE Transactions on Magnetics,* vol. 53, no. 6, pp, 1-4, 2017.

[72] D. A. Staton, T. J. E. Miller, and S. E. Wood, "Optimisation of the synchronous reluctance motor geometry," in *Fifth International Conference on Electrical Machines and Drives (Conf. Publ. No. 341)*, pp, 156-160, 1991.

[73] M. H. Nagrial, "Analysis and performance of variable reluctance (vr) torque coupler," in *Proceedings IEEE Conference on Industrial Automation and Control Emerging Technology Applications*, pp, 136-139, 1995.

[74] M. H. Nagrial and S. M. R. Sadri, "Magnetic circuit analysis of flux guided reluctance motor using finite element method," in *Proceedings of International Conference on Power Electronics and Drive Systems. PEDS*, pp, 628-633 vol.2, 1995.

[75] M. H. Nagrial, "Finite element analysis and design of variable reluctance (vr) torque coupler," in *Proceedings of Second International Conference on Power Electronics and Drive Systems*, vol. 1, pp, 252-254 vol.1, 1997.

[76] S. M. R. Sadri and M. Nagrial, "Multi-flux guided rotor for variable speed reluctance motors," in *Proceedings of Second International Conference on Power Electronics and Drive Systems*, vol. 1, pp, 275-279 vol.1, 1997.

[77] M. H. Nagrial, "Developments of sensorless synchronous reluctance drive systems," in *Multi Topic Conference. IEEE INMIC. Technology for the 21st Century. Proceedings. IEEE International*, Lahore, Pakistan, Pakistan, pp, 104-110, 2001.

[78] I. Marongiu and A. Vagati, "Improved modelling of a distributed anisotropy synchronous reluctance machine," in *Conference Record of the IEEE Industry Applications Society Annual Meeting*, pp, 238-243 vol.1, 1991.

[79] T. Mohanarajah, J. Rizk, A. Hellany, and M. Nagrial, "Optimisation of flux barrier parameters in synchronous reluctance machines," in *Energy Conversion (CENCON), 2015 IEEE Conference on*, pp, 299-304, 2015.

[80] A. Vagati, G. Franceschini, I. Marongiu, and G. P. Troglia, "Design criteria of high performance synchronous reluctance motors," in *Industry Applications Society Annual Meeting., Conference Record of the IEEE*, Houston, TX, USA, USA, pp, 66-73 vol.1, 1992.

[81] A. Vagati, M. Pastorelli, G. Francheschini, and S. C. Petrache, "Design of low-torque-ripple synchronous reluctance motors," *IEEE Transactions on Industry Applications,* vol. 34, no. 4, pp, 758-765, 1998.

[82] A. Fratta and A. Vagati, "A reluctance motor drive for high dynamic performance application," *IEEE Transactions on Industry Applications,* vol. 28, no. 4, pp, 873-879, 1992.

[83] A. Vagati, G. Franceschini, I. Marongiu, and G. P. Troglia, "Design criteria of high performance synchronous reluctance motors," in *Conference Record of the 1992 IEEE Industry Applications Society Annual Meeting*, pp, 66-73 vol.1, 1992.

[84] A. Fratta, G. P. Troglia, A. Vagati, and F. Villata, "Evaluation of torque ripple in high performance synchronous reluctance machines," in *Conference Record of the 1993 IEEE Industry Applications Conference Twenty-Eighth IAS Annual Meeting*, pp, 163-170 vol.1, 1993.

[85] A. Vagati, "The synchronous reluctance solution: A new alternative in ac drives," in *Industrial Electronics, Control and Instrumentation. IECON., 20th International Conference on*, vol. 1, pp, 1-13 vol.1, 1994.

[86] A. Vagati, A. Fratta, G. Franceschini, and P. Rosso, "Ac motors for high-performance drives: A design-based comparison," *IEEE Transactions on Industry Applications,* vol. 32, no. 5, pp, 1211-1219, 1996.

[87] A. Fratta, G. P. Troglia, A. Vagati, and F. Villata, "Evaluation of torque ripple in high performance synchronous reluctance machines," in *Industry Applications Society Annual Meeting., Conference Record of the IEEE*, pp, 163-170 vol.1, 1993.

[88] T. Mohanarajah, M. Nagrial, A. Hellany, and J. Rizk, "Torque ripple improvement in synchronous reluctance machines," presented at the EECON 2018, Colombo, Sri Lanka. 2018.

[89] A. Vagati, M. Pastorelli, and G. Franceschini, "High-performance control of synchronous reluctance motors," *IEEE Transactions on Industry Applications,* vol. 33, no. 4, pp, 983-991, 1997.

[90] X. B. Bomela and M. J. Kamper, "Effect of stator chording and rotor skewing on average torque and torque ripple of reluctance synchronous machine," in *IEEE Africon. 5th Africon Conference in Africa (Cat. No.99CH36342)*, vol. 2, pp, 687-690 vol.2, 1999.

[91] M. Sanada, K. Hiramoto, S. Morimoto, and Y. Takeda, "Torque ripple improvement for synchronous reluctance motor using an asymmetric flux barrier arrangement," *IEEE Transactions on Industry Applications,* vol. 40, no. 4, pp, 1076-1082, 2004.

[92] R. R. Moghaddam, F. Magnussen, and C. Sadarangani, "Novel rotor design optimization of synchronous reluctance machine for low torque ripple," in *International Conference on Electrical Machines*, pp, 720-724, 2012.

[93] T. Lange, B. Kerdsup, C. Weiss, and R. W. D. Doncker, "Torque ripple reduction in reluctance synchronous machines using an asymmetric rotor structure," in *7th IET International Conference on Power Electronics, Machines and Drives (PEMD)*, pp, 1-5, 2014.

[94] A. Takbash, M. Ibrahim, and P. Pillay, "Torque ripple reduction of a variable flux motor," in *IEEE Energy Conversion Congress and Exposition (ECCE)*, pp, 1-7, 2016.

[95] R. R. Moghaddam, F. Magnussen, and C. Sadarangani, "Novel rotor design optimization of synchronous reluctance machine for high torque density," in *Power Electronics, Machines and Drives (PEMD), 6th IET International Conference on Electrical Machines*, pp, 1-4, 2012.

[96] E. Howard, M. J. Kamper, and S. Gerber, "Asymmetric flux barrier and skew design optimization of reluctance synchronous machines," *IEEE Transactions on Industry Applications,* vol. 51, no. 5, pp, 3751-3760, 2015.

[97] S. Taghavi and P. Pillay, "A novel grain-oriented lamination rotor core assembly for a synchronous reluctance traction motor with a reduced torque ripple algorithm," *IEEE Transactions on Industry Applications,* vol. 52, no. 5, pp, 3729-3738, 2016.

[98] S. Taghavi, "Design of synchronous reluctance machines for automotive applications," Ph.D, Electrical and Computer Engineering, Concordia University, Montreal, Quebec, Canada, 2015.

[99] C. Yun-Chul and L. Jung-Ho, "Rotor & stator design on torque ripple reduction for a synchronous reluctance motor with a concentrated winding using rsm," in *International Conference on Electrical Machines and Systems (ICEMS)*, pp, 1216-1221, 2007.

[100] L. N. Langue, G. Friedrich, S. Vivier, and K. E. K. Benkara, "Optimization of synchronous reluctance machines for high power factor," in *XXII International Conference on Electrical Machines (ICEM)*, pp, 1976-1982, 2016.

[101] Y. Wang, D. Ionel, D. G. Dorrell, and S. Stretz, "Establishing the power factor limitations for synchronous reluctance machines," *IEEE Transactions on Magnetics,* vol. 51, no. 11, pp, 1-4, 2015.

[102] R. R. Moghaddam, F. Magnussen, C. Sadarangani, and H. Lendenmann, "New theoretical approach to the synchronous reluctance machine behavior and performance," in *Electrical Machines, ICEM 18th International Conference on*, Vilamoura, Portugal, pp, 1-6, 2008.

[103] G. Bacco and N. Bianchi, "Choice of flux-barriers position in synchronous reluctance machines," in *IEEE Energy Conversion Congress and Exposition (ECCE)*, pp, 1872-1879, 2017.

[104] T. Mohanarajah, J. Rizk, M. Nagrial, and A. Hellany, "Design of synchronous reluctance motors with improved power factor," in *11th IEEE International Conference on Compatibility, Power Electronics and Power Engineering (CPE-POWERENG)*, pp, 340-345, 2017.

[105] H. C. Liu, I. G. Kim, Y. J. Oh, J. Lee, and S. C. Go, "Design of permanent magnet-assisted synchronous reluctance motor for maximized back-emf and torque ripple reduction," *IEEE Transactions on Magnetics,* vol. 53, no. 6, pp, 1-4, 2017.

[106] T. Zhou and J. Shen, "Cogging torque and operation torque ripple reduction of interior permanent magnet synchronous machines by using asymmetric flux-barriers," in *20th International Conference on Electrical Machines and Systems (ICEMS)*, pp, 1-6, 2017.

[107] T. Mohanarajah, J. Rizk, M. Nagrial, and A. Hellany, "Permanent magnet optimization in pm assisted synchronous reluctance machines," in *IEEE 27th International Symposium on Industrial Electronics (ISIE)*, pp, 1347-1351, 2018.

[108] E. Poskovic, C. Babette, N. Bianchi, and L. Ferraris, "The study of permanent magnet assisted reluctance machine with the adoption of ndfeb bonded magnets," in *International Symposium on Power Electronics, Electrical Drives, Automation and Motion (SPEEDAM)*, pp, 274-279, 2018.

[109] J. Juergens, A. Fricassè, L. Marengo, J. Gragger, M. D. Gennaro, and B. Ponick, "Innovative design of an air cooled ferrite permanent magnet assisted synchronous reluctance machine for automotive traction application," in *XXII International Conference on Electrical Machines (ICEM)*, pp, 803-810, 2016.

[110] S. Stipetic, D. Zarko, and M. Kovacic, "Optimised design of permanent magnet assisted synchronous reluctance motor series using combined analytical & finite element analysis based approach," *IET Electric Power Applications,* vol. 10, no. 5, pp, 330-338, 2016.

[111] A. K. M. Arafat, S. S. R. Bonthu, S. Dharmasena, and S. Choi, "Torque ripple minimization under unbalanced phase resistance in a five-phase permanent magnet assisted synchronous reluctance motor," in *IEEE International Electric Machines and Drives Conference (IEMDC)*, pp, 1-7, 2017.

[112] F. Chai, H. Hu, and L. Geng, "Theoretical analysis of torque performance in permanent magnet-assisted synchronous reluctance motor," in *20th International Conference on Electrical Machines and Systems (ICEMS)*, pp, 1-6, 2017.

[113] J. Baek, S. S. R. Bonthu, S. Kwak, and S. Choi, "Optimal design of five-phase permanent magnet assisted synchronous reluctance motor for low output torque ripple," in *IEEE Energy Conversion Congress and Exposition (ECCE)*, pp, 2418-2424, 2014.

[114] J. Baek, S. S. R. Bonthu, and S. Choi, "Design of five-phase permanent magnet assisted synchronous reluctance motor for low output torque ripple applications," *IET Electric Power Applications,* vol. 10, no. 5, pp, 339-346, 2016.

[115] S. S. R. Bonthu, M. T. B. Tarek, and S. Choi, "Optimal torque ripple reduction technique for outer rotor permanent magnet synchronous reluctance motors," *IEEE Transactions on Energy Conversion,* vol. 33, no. 3, pp, 1184-1192, 2018.

[116] R. Vartanian, H. A. Toliyat, B. Akin, and R. Poley, "Power factor improvement of synchronous reluctance motors (synrm) using permanent magnets for drive size reduction," in *Twenty-Seventh Annual IEEE Applied Power Electronics Conference and Exposition (APEC)*, Orlando, FL, USA, pp, 628-633: IEEE, 2012.

[117] Z. Zhengming and E. A. Ahmed, "Optimization of added permanent magnet amount in synchronous reluctance machines for high performance," *Tsinghua Science and Technology,* vol. 3, no. 3, pp, 1137-1142, 1998.

[118] L. Jung Ho, K. Jung Chul, and H. Dong Seek, "Effect analysis of magnet on Id and Iq inductance of permanent magnet assisted synchronous reluctance motor using finite element method," *IEEE Transactions on Magnetics,* vol. 35, no. 3, pp, 1199-1202, 1999.

[119] H. W. D. Kock and M. J. Kamper, "Dynamic control of the permanent magnet-assisted reluctance synchronous machine," *IET Electric Power Applications,* vol. 1, no. 2, pp, 153-160, 2007.

[120] M. Barcaro, N. Bianchi, and F. Magnussen, "Permanent-magnet optimization in permanent-magnet-assisted synchronous reluctance motor for a wide constant-power speed range," *IEEE Transactions on Industrial Electronics,* vol. 59, no. 6, pp, 2495-2502, 2012.

[121] P. Guglielmi, B. Boazzo, E. Armando, G. Pellegrino, and A. Vagati, "Permanent-magnet minimization in pm-assisted synchronous reluctance motors for wide speed range," *IEEE Transactions on Industry Applications,* vol. 49, no. 1, pp, 31-41, 2013.

[122] A. Kallaste, T. Vaimann, and A. Belahcen, "Design of permanent magnet assisted synchronous reluctance machine," in *Electric Power Engineering (EPE), Proccedings of the 15th International Scientific Conference on*, pp, 579-582, 2014.

[123] E. S. Calvo and D. Potoradi, "Synchronous reluctance motors with and without permanent magnets for high performance low cost electrical drives," in *Electric Drives Production Conference (EDPC), 5th International*, pp, 1-7, 2015.

[124] K. Yamazaki, S. Tamiya, K. Utsuno, K. Shima, T. Fukami, and M. Sato, "Rotor shape optimization for output maximization of permanent-magnet-assisted synchronous machines," *IEEE Transactions on Industry Applications,* vol. 51, no. 4, pp, 3077-3085, 2015.

[125] T. Mohanarajah, J. Rizk, M. Nagrial, and A. Hellany, "Comparative analysis of synchronous reluctance machines with and without permanent magnets," in *IEEE International Conference on Power System Technology (POWERCON)*, pp, 1-6, 2016.

[126] T. M. Jahns and W. L. Soong, "Pulsating torque minimization techniques for permanent magnet ac motor drives-a review," *IEEE Transactions on Industrial Electronics,* vol. 43, no. 2, pp, 321-330, 1996.

[127] B. Gaussens, J. Boisson, A. Abdelli, L. Favre, and D. Bettoni, "Torque ripple mitigation of pm-assisted synchronous reluctance machine : Design and optimization," in *20th International Conference on Electrical Machines and Systems (ICEMS)*, pp, 1-6, 2017.

[128] M. Barcaro and N. Bianchi, "Torque ripple reduction in fractional-slot interior pm machines optimizing the flux-barrier geometries," in *International Conference on Electrical Machines*, pp, 1496-1502, 2012.

[129] L. Jung Ho and H. Dong Seek, "Hysteresis analysis for the permanent magnet assisted synchronous reluctance motor by coupled fem and preisach modelling," *IEEE Transactions on Magnetics,* vol. 35, no. 3, pp, 1203-1206, 1999.

[130] S. Morimoto, M. Sanada, and Y. Takeda, "Performance of pm-assisted synchronous reluctance motor for high-efficiency and wide constant-power operation," *IEEE Transactions on Industry Applications,* vol. 37, no. 5, pp, 1234-1240, 2001.

[131] H. Murakami, Y. Honda, Y. Sadanaga, Y. Ikkai, S. Morimoto, and Y. Takeda, "Optimum design of highly efficient magnet assisted reluctance motor," in *Conference Record of the IEEE Industry Applications Conference. 36th IAS Annual Meeting (Cat. No.01CH37248)*, vol. 4, pp, 2296-2301 vol.4, 2001.

[132] P. Guglielmi, M. Pastorelli, G. Pellegrino, and A. Vagati, "Position-sensorless control of permanent-magnet-assisted synchronous reluctance motor," *IEEE Transactions on Industry Applications,* vol. 40, no. 2, pp, 615-622, 2004.

[133] P. Niazi and H. A. Toliyat, "Online parameter estimation of permanent-magnet assisted synchronous reluctance motor," *Industry Applications, IEEE Transactions on,* vol. 43, no. 2, pp, 609-615, 2007.

[134] P. Niazi, H. A. Toliyat, D. H. Cheong, and J. C. Kim, "A low-cost and efficient permanent-magnet-assisted synchronous reluctance motor drive," *IEEE Transactions on Industry Applications,* vol. 43, no. 2, pp, 542-550, 2007.

[135] P. Niazi, H. A. Toliyat, and A. Goodarzi, "Robust maximum torque per ampere (mtpa) control of pm-assisted synrm for traction applications," *IEEE Transactions on Vehicular Technology,* vol. 56, no. 4, pp, 1538-1545, 2007.

[136] I. Boldea, L. Tutelea, and C. I. Pitic, "Pm-assisted reluctance synchronous motor/generator (pm-rsm) for mild hybrid vehicles: Electromagnetic design," *IEEE Transactions on Industry Applications,* vol. 40, no. 2, pp, 492-498, 2004.

[137] P. Guglielmi, G. Giraudo, G. M. Pellegrino, and A. Vagati, "P.M. Assisted synchronous reluctance drive for minimal hybrid application," in *Conference Record of the IEEE Industry Applications Conference. 39th IAS Annual Meeting.*, vol. 1, pp, 1-306, 2004.

[138] I. Boldea, C. I. Pitic, C. Lascu, G. D. Andreescu, L. Tutelea, F. Blaabjerg, and P. Sandholdt, "Dtfc-svm motion-sensorless control of a pm-assisted reluctance synchronous machine as starter-alternator for hybrid electric vehicles," *IEEE Transactions on Power Electronics,* vol. 21, no. 3, pp, 711-719, 2006.

[139] A. K. Chakali, H. A. Toliyat, and H. Abu-Rub, "Observer-based sensorless speed control of pm-assisted synrm for direct drive applications," in *IEEE International Symposium on Industrial Electronics*, pp, 3095-3100, 2010.

[140] L. Chen, J. Wang, P. Lombard, P. Lazari, and V. Leconte, "Design optimisation of permanent magnet assisted synchronous reluctance machines for electric vehicle applications," in *International Conference on Electrical Machines*, pp, 2647-2653, 2012.

[141] E. Carraro, M. Morandin, and N. Bianchi, "Traction pmasr motor optimization according to a given driving cycle," *IEEE Transactions on Industry Applications,* vol. 52, no. 1, pp, 209-216, 2016.

[142] N. Bianchi, H. Mahmoud, and S. Bolognani, "Fast synthesis of permanent magnet assisted synchronous reluctance motors," *IET Electric Power Applications,* vol. 10, no. 5, pp, 312-318, 2016.

[143] N. Bianchi, E. Fornasiero, M. Ferrari, and M. Castiello, "Experimental comparison of pm-assisted synchronous reluctance motors," *IEEE Transactions on Industry Applications,* vol. 52, no. 1, pp, 163-171, 2016.

[144] N. Bianchi, S. Bolognani, D. Bon, and M. D. Pre, "Rotor flux-barrier design for torque ripple reduction in synchronous reluctance and pm-assisted synchronous reluctance motors," *IEEE Transactions on Industry Applications,* vol. 45, no. 3, pp, 921-928, 2009.

[145] E. Carraro, M. Degano, and N. Bianchi, "Permanent magnet volume minimization in permanent magnet assisted synchronous reluctance motors," in *Eighth International Conference and Exhibition on Ecological Vehicles and Renewable Energies (EVER)*, pp, 1-4, 2013.

[146] N. Bianchi, E. Fornasiero, and W. Soong, "Optimal selection of pm flux linkage in a pm assisted synchronous reluctance machine," in *International Conference on Electrical Machines (ICEM)*, pp, 1341-1347, 2014.

[147] E. Fornasiero, N. Bianchi, and W. L. Soong, "Analysis of torque versus current capability of reluctance and interior pm machines under limited current and flux-linkage operation," in *IEEE Energy Conversion Congress and Exposition (ECCE)*, pp, 4162-4169, 2014.

[148] T. Matsuo and T. A. Lipo, "Rotor design optimization of synchronous reluctance machine," *IEEE Transactions on Energy Conversion,* vol. 9, no. 2, pp, 359-365, 1994.

[149] C. Babetto, G. Bacco, and N. Bianchi, "Synchronous reluctance machine optimization for high-speed applications," *IEEE Transactions on Energy Conversion,* vol. 33, no. 3, pp, 1266-1273, 2018.

[150] N. Safin, V. Kazakbaev, V. Prakht, and V. Dmitrievskii, "Calculation of the efficiency and power consumption of induction ie2 and synchronous reluctance ie5 electric drives in the pump application based on the passport specification according to the iec 60034-30-2," in *25th International Workshop on Electric Drives: Optimization in Control of Electric Drives (IWED)*, pp, 1-5, 2018.

[151] T. Mohanarajah, J. Rizk, M. Nagrial, and A. Hellany, "Finite element analysis and design methodology for high-efficiency synchronous reluctance motors," *Electric Power Components and Systems,* 2018.

[152] T. Mohanarajah, J. Rizk, M. Nagrial, and A. Hellany, "Analysis and design of high-performance synchronous reluctance machine," in *IEEE 12th International Conference on Compatibility, Power Electronics and Power Engineering (CPE-POWERENG-2018)*, pp, 1-6, 2018.

[153] Siemens. (2016) The new synchronous-reluctance drive system with simotics and sinamics. *Siemens AG Process Industries and Drives*. 12.

[154] E. C. F. Lovelace, "Optimization of a magnetically saturable interior permanent-magnet synchronous machine drive," Electrical Engineering and Computer Science, Massachusetts Institute of Technology, 2000.

[155] A. Vagati, M. Pastorelli, F. Scapino, and G. Franceschini, "Cross-saturation in synchronous reluctance motors of the transverse-laminated type," in *Conference Record of IEEE Industry Applications Conference. Thirty-Third IAS Annual Meeting (Cat. No.98CH36242)*, vol. 1, pp, 127-135 vol.1, 1998.

[156] E. Capecchi, P. Guglielmi, M. Pastorelli, and A. Vagati, "Position sensorless control of transverse-laminated synchronous reluctance motors," in *Conference Record of the IEEE Industry Applications Conference. Thirty-Fifth IAS Annual Meeting and World Conference on Industrial Applications of Electrical Energy (Cat. No.00CH37129)*, vol. 3, pp, 1766-1773 vol.3, 2000.

[157] A. Vagati, M. Pastorelli, F. Scapino, and G. Franceschini, "Impact of cross saturation in synchronous reluctance motors of the transverse-laminated type," *IEEE Transactions on Industry Applications,* vol. 36, no. 4, pp, 1039-1046, 2000.

[158] E. Capecchi, P. Guglielmi, M. Pastorelli, and A. Vagati, "Position-sensorless control of the transverse-laminated synchronous reluctance motor," *IEEE Transactions on Industry Applications,* vol. 37, no. 6, pp, 1768-1776, 2001.

[159] P. Guglielmi, M. Pastorelli, and A. Vagati, "Impact of cross-saturation in sensorless control of transverse-laminated synchronous reluctance motors," *IEEE Transactions on Industrial Electronics,* vol. 53, no. 2, pp, 429-439, 2006.

[160] G. Pellegrino, E. Armando, P. Guglielmi, and A. Vagati, "A 250kw transverse-laminated synchronous reluctance motor," in *Power Electronics and Applications, 2009. EPE '09. 13th European Conference on*, pp, 1-10, 2009.

[161] S. M. Taghavi and P. Pillay, "A mechanically robust rotor with transverse laminations for a wide-speed-range synchronous reluctance traction motor," *IEEE Transactions on Industry Applications,* vol. 51, no. 6, pp, 4404-4414, 2015.

[162] V. B. Honsinger, "The inductances Id and Iq of reluctance machines," *Power Apparatus and Systems, IEEE Transactions on,* vol. PAS-90, no. 1, pp, 298-304, 1971.

[163] V. B. Honsinger, "Steady-state performance of reluctance machines," *IEEE Transactions on Power Apparatus and Systems,* vol. PAS-90, no. 1, pp, 305-317, 1971.

[164] O. Sugiura and Y. Akiyama, "Precise method for measuring xd and xq based on slip test of synchronous machines," in *Conference Record of the IEEE Industry Applications Conference Twenty-Eighth IAS Annual Meeting*, pp, 155-162 vol.1, 1993.

[165] T. Mohanarajah, J. Rizk, M. Nagrial, and A. Hellany, "Optimisation of flux barrier parameters in synchronous reluctance machines," in *IEEE Conference on Energy Conversion (CENCON)*, pp, 299-304, 2015.

[166] A. Vagati, A. Canova, M. Chiampi, M. Pastorelli, and M. Repetto, "Design refinement of synchronous reluctance motors through finite-element analysis," *IEEE Transactions on Industry Applications,* vol. 36, no. 4, pp, 1094-1102, 2000.

[167] R. R. Moghaddam and F. Gyllensten, "Novel high-performance synrm design method: An easy approach for a complicated rotor topology," *IEEE Transactions on Industrial Electronics,* vol. 61, no. 9, pp, 5058-5065, 2014.

[168] N. Bianchi, S. Bolognani, D. Bon, and M. D. PrÉ, "Torque harmonic compensation in a synchronous reluctance motor," *IEEE Transactions on Energy Conversion,* vol. 23, no. 2, pp, 466-473, 2008.

[169] N. Bianchi, S. Bolognani, D. Bon, and M. D. Pre, "Rotor flux-barrier design for torque ripple reduction in synchronous reluctance motors," in *Conference Record of the IEEE Industry Applications Conference Forty-First IAS Annual Meeting*, vol. 3, pp, 1193-1200, 2006.

[170] D. Yan, C. Xia, L. Guo, H. Wang, and T. Shi, "Design and analysis for torque ripple reduction in synchronous reluctance machine," *IEEE Transactions on Magnetics,* pp, 1-5, 2018.

[171] G. Todorov and B. Stoev, "Parameters and torque ripple of synchronous reluctance motors with different rotor topology," in *20th International Symposium on Electrical Apparatus and Technologies (SIELA)*, pp, 1-4, 2018.

[172] J. Bao, J. Paulides, K. Boynov, and E. Lomonova, "Torque ripple minimization of variable flux reluctance machines by rotor skewing," in *IEEE International Magnetics Conference (INTERMAG)*, pp, 1-2, 2017.

[173] M. Barcaro, T. Pradella, and I. Furlan, "Low-torque ripple design of a ferrite-assisted synchronous reluctance motor," *IET Electric Power Applications,* vol. 10, no. 5, pp, 319-329, 2016.

[174] A. Vagati, M. Pastorelli, G. Franceschini, and C. Petrache, "Design of low-torque-ripple synchronous reluctance motors," in *Industry Applications Conference, 1997. Thirty-Second IAS Annual Meeting, IAS '97., Conference Record of the 1997 IEEE*, vol. 1, pp, 286-293 vol.1, 1997.

[175] I. Boldea, N. Muntean, and S. A. Nasar, "Robust low-cost implementation of vector control for reluctance synchronous machines," *Electric Power Applications, IEE Proceedings,* vol. 141, no. 1, pp, 1-6, 1994.

[176] S. Bolognani, L. Peretti, and M. Zigliotto, "Online mtpa control strategy for dtc synchronous-reluctance-motor drives," *Power Electronics, IEEE Transactions on,* vol. 26, no. 1, pp, 20-28, 2011.

[177] A. Guagnano, G. Rizzello, F. Cupertino, and D. Naso, "Robust control of high-speed synchronous reluctance machines," *IEEE Transactions on Industry Applications,* vol. 52, no. 5, pp, 3990-4000, 2016.

[178] T. Lubin, H. Razik, and A. Rezzoug, "Magnetic saturation effects on the control of a synchronous reluctance machine," *IEEE Transactions on Energy Conversion,* vol. 17, no. 3, pp, 356-362, 2002.

[179] T. Matsuo and T. A. Lipo, "Field oriented control of synchronous reluctance machine," in *Power Electronics Specialists Conference. PESC Record., 24th Annual IEEE*, Seattle, WA, USA, USA, pp, 425-431, 1993.

[180] X. Zhang and G. H. B. Foo, "A robust field-weakening algorithm based on duty ratio regulation for direct torque controlled synchronous reluctance motor," *IEEE/ASME Transactions on Mechatronics,* vol. 21, no. 2, pp, 765-773, 2016.

[181] A. P. Goncalves, S. M. A. Cruz, F. J. T. E. Ferreira, A. M. S. Mendes, and A. T. D. Almeida, "Synchronous reluctance motor drive for electric vehicles including cross-magnetic saturation," in *IEEE Vehicle Power and Propulsion Conference (VPPC)*, Coimbra, Portugal, pp, 1-6, 2014.

[182] E. Carraro and N. Bianchi, "Design and comparison of interior permanent magnet synchronous motors with non-uniform airgap and conventional rotor for electric vehicle applications," *IET Electric Power Applications,* vol. 8, no. 6, pp, 240-249, 2014.

[183] A. K. M. Arafat and S. Choi, "Active current harmonic suppression for torque ripple minimization at open-phase faults in a five-phase pma-synrm," *IEEE Transactions on Industrial Electronics,* vol. 66, no. 2, pp, 922-931, 2019.

[184] L. Ge, X. Zhu, W. Wu, F. Liu, and Z. Xiang, "Design and comparison of two non-rare-earth permanent magnet synchronous reluctance motors for ev applications," in *20th International Conference on Electrical Machines and Systems (ICEMS)*, pp, 1-5, 2017.

[185] M. Expert. (2018). Https://www.First4magnets.Com.

[186] M. H. Nagrial and S. M. R. Sadri, "Axially-laminated cum flux-guided reluctance motors with improved performance," in *Proceedings of Second International Conference on Power Electronics and Drive Systems*, vol. 1, pp, 188-192 vol.1, 1997.

[187] A. Boglietti, A. Cavagnino, M. Pastorelli, and A. Vagati, "Experimental comparison of induction and synchronous reluctance motors performance,"

in *Fourtieth IAS Annual Meeting. Conference Record of the Industry Applications Conference.*, Kowloon, Hong Kong, China, vol. 1, pp, 474-479 Vol. 1, 2005.

[188] A. N. Hanekom, "A torque ripple analysis on reluctance synchronous machines," Magister Technologiae Department of Electrical Engineering, Cape Peninsula University of Technology, Cape Town, 2006.

[189] Y. Kano, T. Kosaka, and N. Matsui, "Magnetization characteristics analysis of srm by simplified non-linear magnetic analysis," in *Proceedings of the Power Conversion Conference-Osaka (Cat. No.02TH8579)*, vol. 2, pp, 689-694 vol.2, 2002.

[190] K. Kim and S. Jeon, "Analysis on correlation between cogging torque and torque ripple by considering magnetic saturation," *IEEE Transactions on Magnetics,* vol. 49, no. 5, pp, 2417-2420, 2013.

[191] T. J. E. Miller, M. I. McGilp, and M. Olaru, "Finite elements applied to synchronous and switched reluctance motors," in *IEE Seminar on Current Trends in the Use of Finite Elements (FE) in Electromechanical Design and Analysis (Ref. No. 2000/013)*, pp, 3/1-3/4, 2000.

[192] V. Bilyi, D. Gerling, and D. Bilyi, "Flux barrier design method for torque ripple reduction in synchronous reluctance machines," in *IEEE Transportation Electrification Conference and Expo, Asia-Pacific (ITEC Asia-Pacific)*, pp, 034-039, 2016.

[193] H. Mahmoud, "Synchronous reluctance machines: Eccentricity analysis and design criteria," Ph.D., Department of Industrial Engineering, University of Padova, Padova 2017.

[194] R. R. Moghaddam, "Synchronous reluctance machine design," Msc, Department of Electrical Engineering Electrical Machines and Power electronics, KTH Royal Institute of Technology, Stockholm, Sweden, 2007.

[195] F. Reiter and T. Stuart, "Composite powder metal synchronous reluctance machine," in *IEEE International Electric Machines and Drives Conference. IEMDC'03.*, vol. 1, pp, 523-527 vol.1, 2003.

[196] Ansys. (2018). *Https://www.Ansys.Com/products/electronics/ansys-maxwell*.

[197] D. Meeker. (2018, 2018). *Http://www.Femm.Info/wiki/homepage*.

[198] I. Corporation. (2018). *Https://www.Mentor.Com/products/mechanical/infolytica*.

[199] A. Vagati, "Synchronous reluctance electrical motor having a low torque-ripple design," United States Patent 5,818,140, 1998.

[200] G. Pellegrino, F. Cupertino, and C. Gerada, "Automatic design of synchronous reluctance motors focusing on barrier shape optimization," *IEEE Transactions on Industry Applications,* vol. 51, no. 2, pp, 1465-1474, 2015.

[201] F. Cupertino, G. Pellegrino, and C. Gerada, "Design of synchronous reluctance motors with multiobjective optimization algorithms," *IEEE Transactions on Industry Applications,* vol. 50, no. 6, pp, 3617-3627, 2014.

[202] M. Šebest, V. Hrabovcová, and P. Makyš, "Optimization of the reluctance synchronous motor with barriers rotor," in *ELEKTRO*, pp, 374-378, 2016.

[203] N. Bianchi, D. Durello, and E. Fornasiero, "Multi-objective optimization of a pm assisted synchronous reluctance machine, including torque and sensorless detection capability," in *6th IET International Conference on Power Electronics, Machines and Drives (PEMD)*, pp, 1-6, 2012.

[204] G. C. Tenaglia and L. Lebensztajn, "A multiobjective approach of differential evolution optimization applied to electromagnetic problems," *IEEE Transactions on Magnetics,* vol. 50, no. 2, pp, 625-628, 2014.

[205] M. D. Nardo, G. L. Calzo, M. Galea, and C. Gerada, "Design optimization of a high-speed synchronous reluctance machine," *IEEE Transactions on Industry Applications,* vol. 54, no. 1, pp, 233-243, 2018.

[206] T. Mohanarajah, J. Rizk, M. Nagrial, and A. Hellany, "Design optimisation of flux barrier synchronous reluctance machines," in *Intl Aegean Conference on Electrical Machines & Power Electronics (ACEMP), 2015 Intl Conference on Optimization of Electrical & Electronic Equipment (OPTIM) & Intl Symposium on Advanced Electromechanical Motion Systems (ELECTROMOTION)*, pp, 58-62, 2015.

[207] T. Mohanarajah, M. Nagrial, A. Hellany, and J. Rizk, "Effect of saturation on performance of synchronous reluctance machines," in *IEEE International Conference on Power and Energy (PECon)*, pp, 802-807, 2016.

[208] J. R. M. Nagrial, A.Hellany, "Analysis and performance of high efficiency synchronous reluctance machines," *International journal of energy and environment,* vol. 2, no. 2, pp, 247-254 2011.

[209] T. A. Huynh, M. Hsieh, K. Shih, and H. Kuo, "Design and analysis of permanent-magnet assisted synchronous reluctance motor," in *20th International Conference on Electrical Machines and Systems (ICEMS)*, pp, 1-6, 2017.

[210] E. Armando, P. Guglielmi, G. Pellegrino, M. Pastorelli, and A. Vagati, "Accurate modeling and performance analysis of ipm-pmasr motors," *IEEE Transactions on Industry Applications,* vol. 45, no. 1, pp, 123-130, 2009.

[211] S. Talebi, P. Niazi, and H. A. Toliyat, "Design of permanent magnet-assisted synchronous reluctance motors made easy," in *IEEE Industry Applications Annual Meeting*, pp, 2242-2248, 2007.

[212] M. Barcaro, N. Bianchi, and F. Magnussen, "Rotor flux-barrier geometry design to reduce stator iron losses in synchronous ipm motors under fw operations," *IEEE Transactions on Industry Applications,* vol. 46, no. 5, pp, 1950-1958, 2010.

[213] Y. Lu, J. Li, R. Qu, J. Sun, M. Ge, and H. Xu, "Magnetic stress and vibration analysis of the permanent magnet assisted synchronous reluctance machines," in *IEEE International Electric Machines and Drives Conference (IEMDC)*, pp, 1-7, 2017.

[214] M. Dems, K. Komeza, and J. Lecointe, "Influence of massive ferromagnetic shaft on the distribution of electromagnetic field and magnetising current for two- and four-pole induction motors at frequencies of 50 and 200 hz," *IET Electric Power Applications,* vol. 12, no. 9, pp, 1407-1416, 2018.

[215] C. Yicheng and P. Pillay, "An improved formula for lamination core loss calculations in machines operating with high frequency and high flux density excitation," in *Conference Record of the IEEE Industry Applications Conference. 37th IAS Annual Meeting (Cat. No.02CH37344)*, vol. 2, pp, 759-766 vol.2, 2002.

[216] H. Ghorbani and B. Majidi, "A comparative study on synchronous reluctance and pm-synchronous reluctance machine torque using fem analysis," in *9th Annual Power Electronics, Drives Systems and Technologies Conference (PEDSTC)*, pp, 128-132, 2018.

[217] K. C. Kim, J. S. Ahn, S. H. Won, J. P. Hong, and J. Lee, "A study on the optimal design of synrm for the high torque and power factor," *IEEE Transactions on Magnetics,* vol. 43, no. 6, pp, 2543-2545, 2007.

[218] B. Nikbakhtian, S. Talebi, P. Niazi, and H. A. Toliyat, "An analytical model for an n-flux barrier per pole permanent magnet-assisted synchronous reluctance motor," in *IEEE International Electric Machines and Drives Conference*, pp, 129-136, 2009.

[219] M. Muteba, B. Twala, and D. V. Nicolea, "Based 3d finite element analysis of a synchronous reluctance motor with sinusoidal rotor shape," in *2017 IEEE International Electric Machines and Drives Conference (IEMDC)*, pp, 1-7, 2017.

[220] C. Donaghy-Spargo, "Electromagnetic-mechanical design of synchronous reluctance rotors with fine features," *IEEE Transactions on Magnetics,* vol. PP, no. 99, pp, 1-1, 2017.

[221] M. D. Nardo, M. Degano, M. Galea, C. Gerada, M. Palmieri, F. Cupertino, N. Bianchi, and D. Gerada, "End barrier shape optimizations and sensitivity analysis of synchrnous reluctance machines," in *IECON - 41st Annual Conference of the IEEE Industrial Electronics Society*, pp, 002914-002919, 2015.

[222] A. Fratta, G. P. Toglia, A. Vagati, and F. Villata, "Ripple evaluation of high-performance synchronous reluctance machines," *IEEE Industry Applications Magazine,* vol. 1, no. 4, pp, 14-22, 1995.

[223] N. Bianchi, M. Degano, and E. Fornasiero, "Sensitivity analysis of torque ripple reduction of synchronous reluctance and interior pm motors," *IEEE Transactions on Industry Applications,* vol. 51, no. 1, pp, 187-195, 2015.

[224] S. Constantinides, "Magnet selection," in "Arnold Magnetic Technologies," October 15-17 2003.

[225] W. L. Soong and T. J. E. Miller, "Field-weakening performance of brushless synchronous ac motor drives," *IEE Proceedings - Electric Power Applications,* vol. 141, no. 6, pp, 331-340, 1994.

[226] A. Vagati, B. Boazzo, P. Guglielmi, and G. Pellegrino, "Design of ferrite-assisted synchronous reluctance machines robust toward demagnetization," *IEEE Transactions on Industry Applications,* vol. 50, no. 3, pp, 1768-1779, 2014.

[227] E. Armando, P. Guglielmi, M. Pastorelli, G. Pellegrino, and A. Vagati, "Performance of ipm-pmasr motors with ferrite injection for home appliance washing machine," in *IEEE Industry Applications Society Annual Meeting*, pp, 1-6, 2008.

[228] R. R. Moghaddam, "Synchronous reluctance machine (synrm) in variable speed drives (vsd) applications," Ph.d, Department of Electrical Engineering Electrical Machines and Power electronics, KTH Royal Institute of Technology, Stockholm, Sweden, 2011.

[229] A. Varshney and B. Singh, "Direct torque controlled synchronous reluctance motor drive for pv array fed water pumping," in *IEEMA Engineer Infinite Conference (eTechNxT)*, pp, 1-6, 2018.

[230] A. Yousefi-Talouki, P. Pescetto, and G. Pellegrino, "Sensorless direct flux vector control of synchronous reluctance motors including standstill, mtpa, and flux weakening," *IEEE Transactions on Industry Applications,* vol. 53, no. 4, pp, 3598-3608, 2017.

[231] G. H. B. Foo and X. Zhang, "Robust direct torque control of synchronous reluctance motor drives in the field-weakening region," *IEEE Transactions on Power Electronics,* vol. 32, no. 2, pp, 1289-1298, 2017.

[232] M. Hinkkanen, H. A. A. Awan, Z. Qu, T. Tuovinen, and F. Briz, "Current control for synchronous motor drives: Direct discrete-time pole-placement design," *IEEE Transactions on Industry Applications,* vol. 52, no. 2, pp, 1530-1541, 2016.